As conventional electronics approaches its fundamental limits, novel concepts of ultrafast quantum control have been sought after. *Lightwave electronics* has opened the door to a new regime, where the oscillating carrier wave of intense light pulses can be used to control electrons faster than a cycle of light. In this thesis, intense single- and few-cycle light pulses in the terahertz (THz) spectral regime are utilized to coherently control the electron's spin as well as its translational motion on the femtosecond timescale (1 fs = 10^{15} s) and with minimal energy dissipation. The presented results offer a promising route towards future ultrafast, low-loss information technology based on coherent lightwave control.

First, low-energy THz pulses are utilized to coherently switch the electron's most important quantum attribute – its spin – between two stable states separated by a potential barrier, in the fastest and least dissipative way. This is achieved by coupling spins in the prototypical antiferromagnetic thulium orthoferrite ($TmFeO_3$) with the locally enhanced THz electric field of custom-tailored antenna structures. The single-cycle THz pulses abruptly change the magnetic anisotropy and trigger a large-amplitude ballistic spin motion. The observed dynamics hallmark a novel regime of ultrafast all-coherent spin control throughout the entire phase space. This sets the stage for practical spin memories operating at THz clock rates, and ultimately low dissipation close to the Landauer limit.

In a second set of experiments, the electric field of intense single- and few-cycle THz waveforms is used to ballistically accelerate Dirac electrons in the surface band of the topological insulator bismuth telluride (Bi_2Te_3). Simultaneously, the lightwave-driven dynamics is traced by time- and angle-resolved photoemission spectroscopy (ARPES). For the first time, even strong light-matter interaction, involving THz-driven intraband and interband dynamics, can be resolved directly in the band structure and on a subcycle timescale. The novel subcycle THz-ARPES studies will help answering key open questions of lightwave electronics and may pave the way to dissipation-free, topological-insulator-based lightwave-driven electronic devices with optical clock frequencies.

Universität Regensburg
Institut für Experimentelle und Angewandte Physik
Lehrstuhl Prof. Dr. Rupert Huber

STEFAN SCHLAUDERER

MINIMALLY DISSIPATIVE LIGHTWAVE-CONTROL OF SPIN AND CHARGE

MINIMALLY DISSIPATIVE LIGHTWAVE-CONTROL OF SPIN AND CHARGE

STEFAN SCHLAUDERER

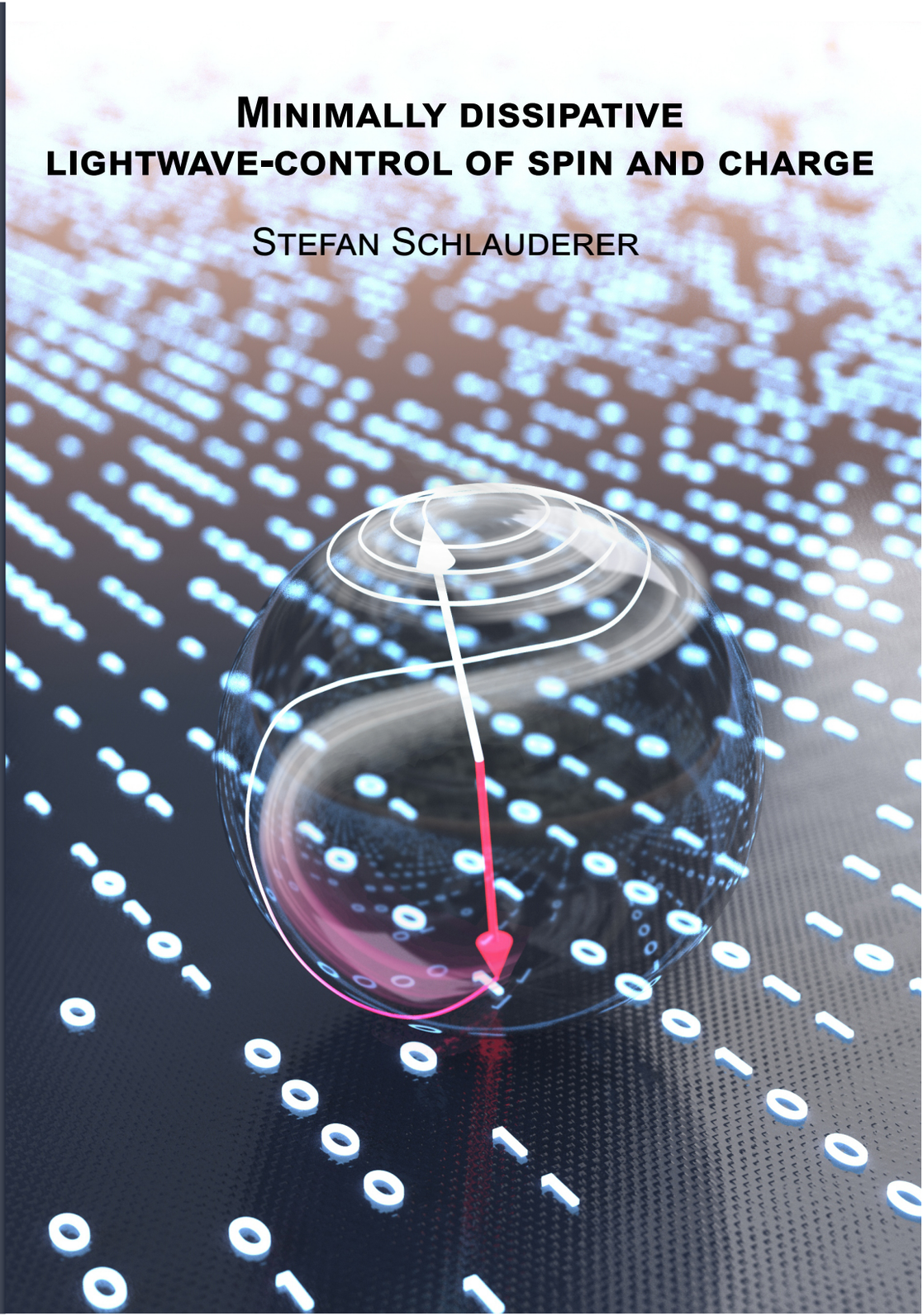

Cover: Utilizing ultrashort light pulses facilitates extremely economical switching of spins within only a few picoseconds from one stable orientation (red arrow) to another (white arrow). This concept enables ultrafast information storage with optimal energy efficiency.

Minimally dissipative lightwave-control of spin and charge

Dissertation
zur Erlangung des Doktorgrades der Naturwissenschaften
(Dr. rer. nat.)
der Fakultät für Physik der Universität Regensburg

vorgelegt von
Stefan Schlauderer
aus Regensburg
im Jahr 2021

Das Promotionsgesuch wurde eingereicht am: 04.11.2020.

Die Arbeit wurde angeleitet von: Prof. Dr. Rupert Huber.

Prüfungsausschuss:	Vorsitzender:	Prof. Dr. Klaus Richter
	1. Gutachter:	Prof. Dr. Rupert Huber
	2. Gutachter:	Prof. Dr. Jörg Wunderlich
	weiterer Prüfer:	Prof. Dr. Franz J. Gießibl

Das Promotionskolloquium fand am 25.03.2021 statt.

Contents

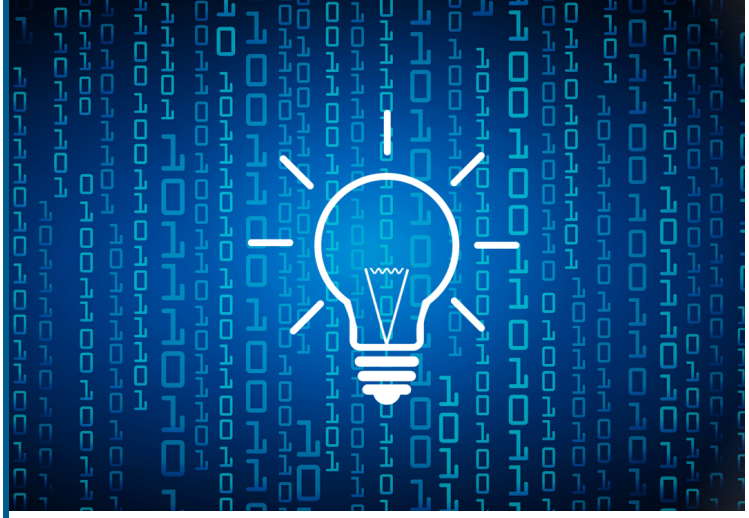

1 Introduction

Everything's impossible until someone does it.

— Bruce Wayne, Batman

Within the last decades, mankind experienced a society-transforming digital revolution. This ongoing development still calls for ever faster and more energy efficient information technology. Similar to the steam engine, which had been the backbone of the industrial revolution, the development of compact solid-state-based electronic devices has been the driving force of this digitalization. The starting point of the modern semiconductor era was the invention of the transistor in 1947 by J. Bardeen, W.H. Brattain, and W.B. Shockley [Bar48], for which they received the Nobel Prize in Physics in 1956. After the development of the integrated circuit in 1958 by Jack Kilby [Kil64, Kil76], for which he was awarded the Nobel Prize in Physics in 2000, a true race for miniaturized electronic circuits started. In 1965, Gordon Moore, one of the co-founders of the technology company *Intel*, quantified the escalating pace of said race. He predicted that the number of transistors per integrated circuit chip would double roughly every two years [Moo65]. For more than 50 years, this famous prediction dubbed *Moore's law* dictated not only the exponential rise of technological progress, it also acted as the driving force of social change, productivity, and economic growth [Key06]. By now, computers and processors have reached every facet of our daily life.

Beyond that, the rate of data generation grows exponentially, whereas emerging smart technologies like 5G networking, neural networks, artificial intelligence, and

autonomous driving are gasping for ultimately fast and least-dissipative information technologies. The progress in extreme ultraviolet lithography in recent years has allowed for an ongoing miniaturization of electronic circuitry. Nonetheless, the achievable device density is limited by the width of the gate dielectric, which recently reached the few nanometer scale [Mar14]. Moreover, a further up-scaling of the clock rates of contemporary electronic processors is hampered by the large dissipative losses associated with the incoherent electron dynamics on these short timescales. Thus, it seems that conventional electronic devices based on metal-oxide-semiconductor field-effect transistors (MOSFETs) approach their fundamental physical limits [Mar14]. It becomes increasingly apparent that future high-speed information processing technologies cannot be a simple improvement of already existing technologies. To cope with the advanced requirements of modern challenges like 'Big Data' or the 'Internet of Things', it requires groundbreaking innovations concerning both the underlying material platform and the general concept of information processing [Mar14, Sha20].

A promising route to increasing the computing capabilities of electronic devices by a massive scale-up of clock frequencies is to exploit the alternating electromagnetic fields of a lightwave. This concept of *lightwave electronics* [Chi01, Sch13, Sch14, Vam14, Hig14, Hoh15, Gar16, Lan17, Liu17, Yos17, Lan18b, Rei18b], has facilitated the observation of long-sought-after quantum phenomena such as dynamical Bloch oscillations [Gol08, Ghi11, Sch14], quasiparticle collisions [Zak12, Lan16, Ban17, Lan18b] as well as all-optical band structure reconstruction [Vam15, Bor20], and ultrafast atomic videography [Coc16, Von18, Nic18, Rei18b]. Utilizing the oscillating electric field of light as an ultrafast bias voltage to switch on and off electric currents, would allow for electronic devices operating at optical clock rates. The finite band mass and ultrafast scattering in conventional dielectrics, however, limit the velocity and the excursion of the accelerated electrons. Thus, up to now, practical lightwave electronic devices are out of reach.

In recent years, a novel class of quantum materials, so-called *topological insulators*, whose electronic properties depend on the topology of the system, moved into the focus of research in condensed-matter physics [Moo10, Has10]. In particular, van der Waals layered three-dimensional topological insulators, experimen-

tally observed only in 2007 [Fu07b], may provide a new route towards future ultrafast memory and logic technologies with minimal energy dissipation [Tok17]. Just like an ordinary insulator, these materials, in their bulk form, feature an energy gap, which separates the highest occupied electronic band from the lowest empty band [Zha09, Xia09]. Owing to their nontrivial topological nature, however, conducting, gapless states emerge on the sample surface, which are protected by time-reversal symmetry [Has10, Van18]. Hence, these states are inherently robust against crystal defects or any (non-magnetic) impurities and feature very long scattering times on the order of one picosecond [Haj12, Rei14]. In combination with the associated linear, Dirac-like energy dispersion, resulting in a large Fermi velocity of the carriers, these properties facilitate ballistic charge transport in the conducting edge channel [Rei18b]. Consequently, topologically protected surface currents have an extremely low dissipation rate. Future lightwave-driven electronic devices based on three-dimensional topological insulators could exploit an all-coherent electron transfer at terahertz ($1\,\mathrm{THz} = 10^{12}$ Hz) clock rates and with minimal energy losses [Has10, Rei18b].

Simply increasing the processing speed of electronic devices only looks at one side of the medal. Obviously, the ability to create and process more and more information also requires ever faster and more energy efficient methods of writing and recording data [Ole18, Kim19]. Whereas for a long time, the research on ultrafast magnetization dynamics focused on ferromagnetic memories [Bac98, Bac99, Ger02, Tud04, Bau17], recently, the material class of antiferromagnets gained tremendous attention [Kim09, Kam11, Bai16a, Bai16b, Wad16, Jun16, Stu17, Něm18, Ole18]. Owing to the strong exchange interaction of the antiferromagnetically coupled sublattices, the frequency of antiferromagnetic resonances is in the terahertz range [Kir10, Kam13, Bai16a]. Thus, magnetization dynamics in antiferromagnets are orders of magnitude faster than in ferromagnetic materials [Kim09, Pas13, Něm18]. Furthermore, the vanishing net magnetic moment renders ultrafast antiferromagnetic memories robust against magnetic-field perturbations and inhibits unintentional magnetic crosstalk between neighboring devices completely [Wad16, Jun16].
In general, writing information on a magnetic data storage device is achieved by local switching of the magnetization. Microscopically, the binary information is en-

coded in the orientation of the magnetic moment, the spin of the electron [Coe09]. Although the two spin states of a magnetic bit have equal energies, which in principle entails switching between these states with no energy dissipation, manipulating the magnetization on shorter and shorter timescales comes with a fundamental predicament: performing a task more rapidly usually costs more energy [Kim19]. Nonetheless, utilizing ultrashort light pulses to control the magnetic order of a material constitutes a promising solution for future low-loss spin memories with ultimate speed [Kam11, Bai16a, Stu17, Ole18, Kim19, Ved20]. According to the Landauer principle [Lan61], the lowest theoretical limit of energy dissipation for manipulating one bit of information is defined by $Q = k_{\mathrm{B}} T \ln 2$, where T is the temperature and k_{B} denotes the Boltzmann constant. This can be seen as a result of inelastic scattering of a quasiparticle of energy Q, such as a collective spin excitation. At or below room temperature, Q is of the order of meV, which - by the uncertainty principle - entails picosecond timescales for minimally dissipative switching. Consequently, ultrashort light pulses in the terahertz spectral window with meV photon energies and sub-picosecond pulse durations promise not only ultimately fast but also least-dissipative magnetic control [Kam11, Bai16a, Bai16b].

The experiments presented in this thesis will show how intense single- and few-cycle light pulses in the terahertz spectral regime can coherently control the electron's spin [Sch19] as well as its translational motion [Rei18b] on the femtosecond timescale ($1\,\mathrm{fs} = 10^{15}$ s) and with minimal energy dissipation. In this way, the experiments offer a path towards future ultrafast information technology with minimal energy losses.

The topic of chapter 2 is the lightwave-driven minimally dissipative spin control, which is achieved by coupling spins in the prototypical antiferromagnetic thulium orthoferrite ($TmFeO_3$) with the locally enhanced THz electric field of custom-tailored antenna structures. As described in section 2.1, the magnetic anisotropy potential of this material may be modified by THz electric dipole transitions between crystal field-split states of the electronic ground state of the thulium ions. Thus, within the duration of only one picosecond ($1\,\mathrm{ps} = 10^{12}$ s), low energy THz light pulses abruptly change the magnetic anisotropy, which initiates coherent magnetization dynamics. Section 2.3, introduces the custom-tailored optical antenna structures,

which selectively enhance the electric field component of the intense single-cycle THz pulses, generated by tilted-pulse-front optical rectification (see section 2.2). In the antenna near-field region, the large THz-induced displacive and impulsive anisotropy torques ballistically navigate the spins over the potential barrier separating two stable states. As shown in section 2.4, the temporal and spectral fingerprints of this all-coherent spin switching into adjacent potential minima can be identified by tracing the THz-induced spin dynamics on a subcycle timescale. With the help of the numerical simulations presented in section 2.5, the experimental findings can be directly linked to the microscopic spin dynamics. Beyond that, the switchable states can be selected by an external magnetic bias (see section 2.6). As discussed in section 2.7, the low dissipation, which is on the order of 1 µeV per spin, and the antenna's subwavelength spatial definition facilitate scalable low-loss spin memories operating at THz clock rates.

In chapter 3, the electron's translational motion is coherently controlled on ultrashort timescales. To achieve this goal, the carrier wave of intense THz pulses is used as an ultrafast bias voltage to accelerate electrons in their band structure (see section 3.1). Thereby, the electrons are driven through the entire Brillouin zone, which leads to the observation of dynamical Bloch oscillations in the semiconductor gallium selenide [Sch14], and completely flips the valley pseudospin in a monolayer of the transition metal dichalcogenide tungsten diselenide within only a few femtoseconds [Lan18b]. Nonetheless, the corresponding limited real space excursions hamper the development of actual lightwave-driven electronic devices.

In section 3.2, the novel material class of topological insulators and, in particular, the peculiar electronic properties of the three-dimensional topological insulator bismuth telluride (Bi_2Te_3) are described. In combination with the concept of lightwave acceleration, this novel material class opens up a realistic parameter space for dissipation-free lightwave-electronic devices. To understand the relevant complex microscopic quantum motion, the lightwave-induced electron dynamics in the topological surface state of Bi_2Te_3 are recorded by angle-resolved photoemission spectroscopy directly in the band structure and with subcycle time resolution (see section 3.3). The acceleration of Dirac states by intense single- and few-cycle THz waveforms leads to a strong redistribution of electrons in momentum space. As shown in section 3.4, the ballistic, inertia-free surface currents induced by a multi-THz pulse with an elec-

tric peak field amplitude in excess of $1\,\mathrm{MV\,cm^{-1}}$ reach peak densities as large as $28.3\,\mathrm{A\,cm^{-1}}$, with ballistic mean free paths of several nanometers. Future electronic devices based on three-dimensional topological insulators may allow for a ballistic, dissipation-free electron transfer up to optical clock frequencies.
Furthermore, with the help of the novel experimental setup established in this chapter, microscopic electron dynamics can be systematically studied under strong lightwave bias directly in the band structure and on a subcycle timescale. This directly traces lightwave-driven intra- and interband dynamics in the band structure itself, which will help answering key open questions of lightwave electronics. Section 3.5 gives a short outlook on high-order harmonic generation in the topological surface state of Bi_2Te_3, which can be directly linked to the observed strong-field control of Dirac electrons in the band structure.
Finally, in chapter 4, the results presented in this thesis are briefly summarized and future prospects of time- and momentum resolved studies of coherent lightwave-driven carrier dynamics throughout the entire Brillouin zone are discussed.

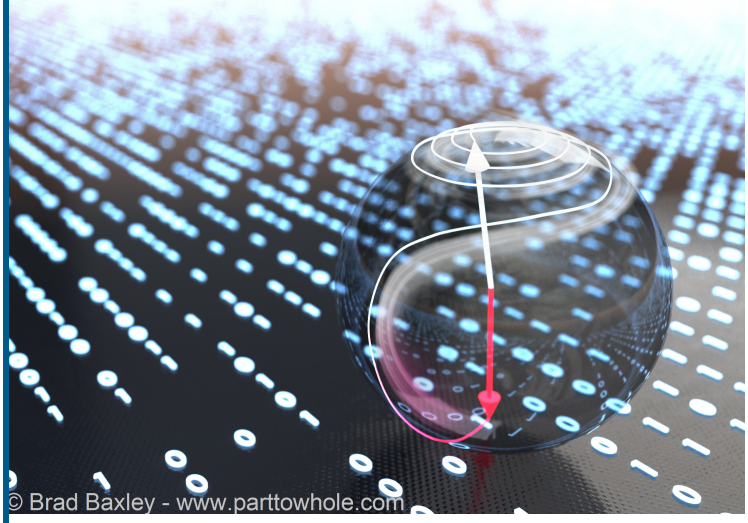

2

Terahertz-driven, all-coherent spin switching

Controlling magnetization with ultimate speed and minimal energy loss is a major building block of future information processing technologies. The shortest known stimulus to control the magnetization of a material are ultrashort laser pulses. Consequently, all-optical recording bears the potential for ultimately fast magnetic memories [Kim19]. Experimentally, the ultrafast spin control with light has come a long way from the first discovery of subpicosecond laser-induced spin dynamics by Beaurepaire *et al.* [Bea96] in 1996, to all-optical non-thermal recording by Stupakiewicz *et al.* [Stu17] just a few years ago. In ferromagnets, the fastest way to control the magnetization is through a precessional motion in an external magnetic field [Bac98, Bac99, Ger02]. As this most direct and purely magnetic interaction mechanism between spins and a magnetic field is fully understood theoretically, it has been possible to determine fundamental limits for the deterministic switching time between two magnetic states [Bac04, Tud04].

However, the desire for yet faster magnetic control triggered an extensive search for alternative coupling mechanisms of light and magnetic excitations, leading to the exploration of a vast range of magnetically ordered materials. These experiments revealed e.g. the possibility of magnetic switching using electric-field induced strain [Kat04], heating [Kim04, Ost12], spin-transfer torques [Wad16, Ole18, Sie19], modifications of the exchange coupling [Men15, Mik15], or via light-induced changes of

the magnetic anisotropy [Gam09, Kim18, Stu17]. Thereby, in particular, the class of antiferromagnets - initially designated as "interesting but useless" [Née70] owing to their zero net magnetic moment - has recently gained enormous attention since it possesses the capability for ultimately fast magnetic writing speed [Wad16, Jun16, Něm18, Kim19].

In ferromagnets, the spin dynamics are governed by the Landau-Lifshitz-Gilbert equation and only allow spin motion during the external stimulus [Coe09, Kim09]. Conversely, in antiferromagnets, the exchange interaction between the spins lead to an inertial behavior that allows for switching times much shorter than the precessional period [Ney02, Kim04, Kim09, Stu17, Kim20]. Despite their importance for the field of ultrafast magnetism, all experiments using light pulses in the visible and near-infrared spectral range face an ultimate disadvantage: Photons in this spectral range feature energies on the order of eV, whereas the typical energy scale of magnetic excitations in antiferromagnets is in the meV range. As a consequence of this huge energy mismatch, ballistic spin switching across a local potential minimum at the limit of minimal energy dissipation is highly challenging. According to the Landauer principle [Lan61], ultrashort light pulses in the terahertz spectral window with meV photon energies and sub-picosecond pulse durations are the most promising candidates for ultimately fast and also least-dissipative magnetic control [Kam11, Bai16a, Bai16b]. Up to now, the available peak electric fields in the frequency range around 1 THz which are on the order of $1\,\mathrm{MV\,cm^{-1}}$, however, have limited the maximum spin excursion far below critical values needed for a complete spin reversal.

In this chapter, intense single-cycle THz pulses, for the first time, coherently navigate spins over a potential barrier into a new stable spin state. This goal is achieved by coupling spins in antiferromagnetic $TmFeO_3$ with the locally enhanced THz electric field of custom-tailored optical antenna structures. Within their duration of 1 ps, the low energy THz pulses abruptly change the magnetic anisotropy and trigger a large-amplitude ballistic spin motion that leads to coherent spin switching with minimal energy dissipation. The results have been published in *Nature* [Sch19].

2.1 Light-induced anisotropy control in rare-earth orthoferrites

In oxides containing both $3d$ and $4f$ ions like orthoferrites [Sri95], manganites [För11], garnets [Bel75], or ferroborates [Vas06, Pop09], the orbital wavefunctions are strongly coupled to the magnetic anisotropy. Consequently, changing the orbital state of the electron, e.g. by optical pumping, modifies the magnetic anisotropy as well as the equilibrium orientation of the spins, which can trigger coherent magnon oscillations. The material of choice for the experiments in this chapter is the prototypical antiferromagnet thulium orthoferrite ($TmFeO_3$). The magnetic and electronic properties of this and similar compounds like dysprosium orthoferrite ($DyFeO_3$) and holmium orthoferrite ($HoFeO_3$) have been extensively studied [Whi69, Bal85, Sri95]. As a result, rare-earth orthoferrites became a role model for the investigation of lightwave-induced, ultrafast magnetization dynamics [Kim04, Kim05, Per06, Kim09, De 11, Mik15, Bai16a, Gri18].

$TmFeO_3$ crystallizes in a distorted perovskite structure [Eib65, Lea68] and belongs to the orthorhombic space group D_{2h}^{16} [Sri95]. Four thulium (Tm^{3+}), four iron (Fe^{3+}) and 12 oxygen ions (O^{2-}) form a crystallographic unit cell (see Figure 2.1), which has a size of $a = 525\,\text{pm}$, $b = 557\,\text{pm}$ and $c = 758\,\text{pm}$ [Lea68]. Owing to the fully occupied shells and a resulting total spin $S = 0$, the oxygen ions are non-magnetic. Although the spin quantum number of the thulium ions is $S = 1$, the thulium spins show no magnetic order above a temperature of $\approx 4\,\text{K}$ [Mik14]. As a consequence, the iron spins dominate, below their Néel temperature of $\approx 650\,\text{K}$, the magnetic behavior of $TmFeO_3$. Figure 2.1 shows the crystal structure of the compound. The bronze spheres indicate the Tm^{3+} ions, whereas the iron ions are represented by the cyan spheres. The oxygen ions, which form octahedrons around the iron ions [Mar70], are not shown for clarity. Due to the antiferromagnetic superexchange coupling of oxygen and iron ions, the iron spins (cyan arrows) form two antiferromagnetically coupled magnetic sublattices $\mathbf{M}_1$ and $\mathbf{M}_2$ [Kim04, Mik14]. Additionally, the antisymmetric exchange interaction, also called Dzyaloshinskii-Moriya interaction [Mor60], between the rare-earth and the iron ions, leads to a slight canting of the two spin sublattices by 0.5°. This results in a small net ferromagnetic moment $\mathbf{F} = \mathbf{M}_1 + \mathbf{M}_2$ (Figure 2.1, violet arrow) in the x-z-plane [Tre65].

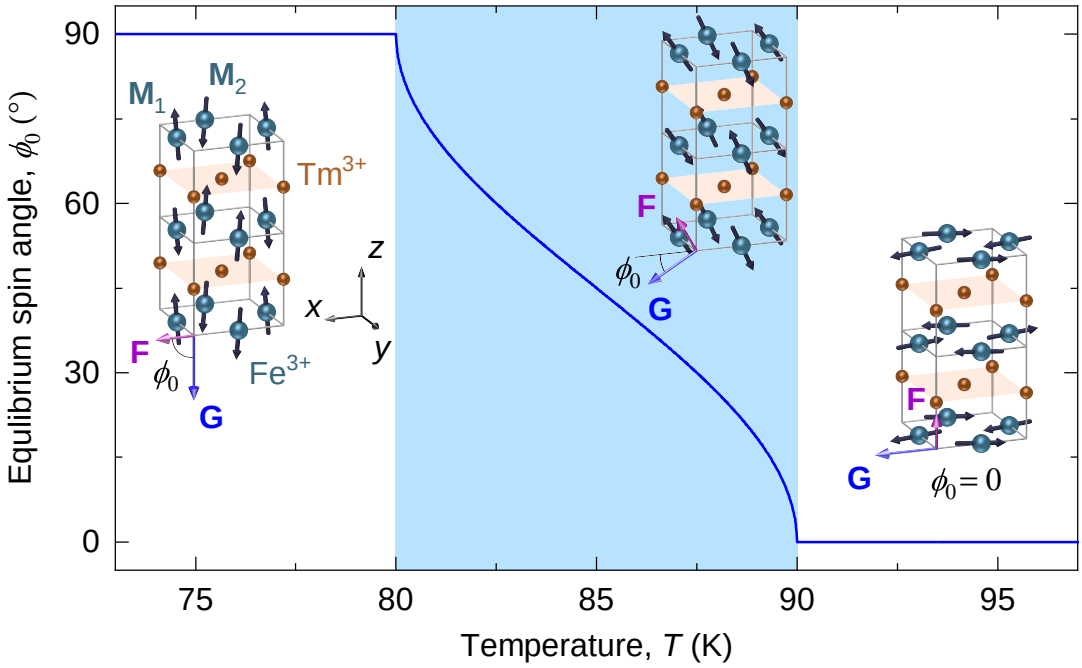

Figure 2.1 | Spin and lattice structure of $TmFeO_3$ in the magnetic phases Γ_2, Γ_{24} and Γ_4. Thulium ions (Tm^{3+}, bronze spheres) and iron ions (Fe^{3+}, cyan spheres). For clarity, the oxygen ions are not shown. The iron spins (cyan arrows) form two antiferromagnetic coupled sublattices $\mathbf{M}_1$ and $\mathbf{M}_2$, which are slightly canted by the Dzyaloshinkii-Moriya interaction. This results in a small net ferromagnetic moment $\mathbf{F} = \mathbf{M}_1 + \mathbf{M}_2$ (violet arrow) in the x-z-plane. The antiferromagnetic vector $\mathbf{G} = \mathbf{M}_1 + \mathbf{M}_2$ encloses an angle ϕ_0 with the crystallographic x-axis. In the Γ_2-phase below $T_1 \approx 80$ K, $\mathbf{G}$ is aligned along the crystallographic z-axis ($\phi_0 = 90°$). In the Γ_{24} transition phase (blue shaded area), ϕ_0 shifts continuously between 0° and 90°. In the Γ_4-phase above $T_2 \approx 90°$, $\mathbf{G}$ is oriented parallel to the crystallographic x-axis ($\phi_0 = 0°$.)

The crystal field splits the ground state of the paramagnetic rare-earth ion Tm^{3+} with the term symbol $^3H_6$ in a series of singlets spaced by a few meV [Sri95]. Thus, already below temperatures of $T \approx 100$ K, the different states are largely populated by thermal excitations. Experimentally, one can find three active transitions with transition frequencies around $R_1 = 0.6$ THz, $R_2 = 1.2$ THz, and $R_3 = 2.1$ THz [Muk91, Bai16a, Zha16]. Due to efficient exchange and dipolar interactions in $TmFeO_3$, a thermal re-population among the Tm^{3+} ground state multiplet can drive temperature-dependent spin reorientation phase transitions manifesting in different magnetic

phases [Sri95, Bai16a]. As shown in Figure 2.1, the Fe^{3+} spins in $TmFeO_3$ undergo such a second-order phase transition at $T_1 \approx 80\,\mathrm{K}$ and $T_2 \approx 90\,\mathrm{K}$. The temperature-dependent magnetic potential $W(T)$ is given by [Hor68, Kim04]:

$$W(T) = K_1(T)\ \sin^2\phi_0 + K_2\ \sin^4\phi_0, \tag{2.1}$$

where ϕ_0 defines the angle between the antiferromagnetic spin vector $\mathbf{G} = \mathbf{M}_1 - \mathbf{M}_2$ (Figure 2.1, blue arrow) and the crystallographic x-axis. $K_1(T)$ and K_2 are the anisotropy constants of second and fourth order, respectively. In equilibrium, this yields three magnetic phases depending on the lattice temperature T:

(a) For $T < T_1$, in the Γ_2 magnetic phase, the antiferromagnetic spin vector $\mathbf{G}$ is aligned along the crystallographic z-axis with a weak ferromagnetic moment $\mathbf{F}$ along the x-axis; $\phi_0 = 90°$.

(b) In the Γ_{24} transition phase (Figure 2.1, blue shaded area), between T_1 and T_2, the spin configuration continuously rotates in the x-z-plane as the magnetic potential changes with the thermal population of the Tm^{3+} crystal-field-split states. The temperature-dependent equilibrium spin angle $\phi_0(T)$ is given by

$$\phi_0(T) = \arcsin\sqrt{-\frac{K_1(T)}{2K_2}} = \arcsin\left(\frac{T - T_2}{T_2 - T_1}\right)^{\frac{1}{2}}. \tag{2.2}$$

(c) In the Γ_4 phase above T_2, the magnetic anisotropy leads to an alignment of the antiferromagnetically ordered spins along the crystallographic x-axis while the ferromagnetic spin vector $\mathbf{F}$ points in z-direction. The equilibrium spin angle ϕ_0 is 0°.

Microscopically, this second-order spin reorientation phase transition in $TmFeO_3$ can be described by the thermal re-population among the ground multiplet of Tm^{3+}. Due to a different exchange coupling of the orbital angular momentum of the Tm^{3+} ground state singlets to the Fe^{3+} spins, changing the population of the energy levels also modifies the strength and the direction of the magnetic anisotropy [Sri95, Kim04, Bai16a]. This, in turn, results in the temperature-dependent behavior of the antiferromagnetic spin vector $\mathbf{G}$ as depicted in Figure 2.1.

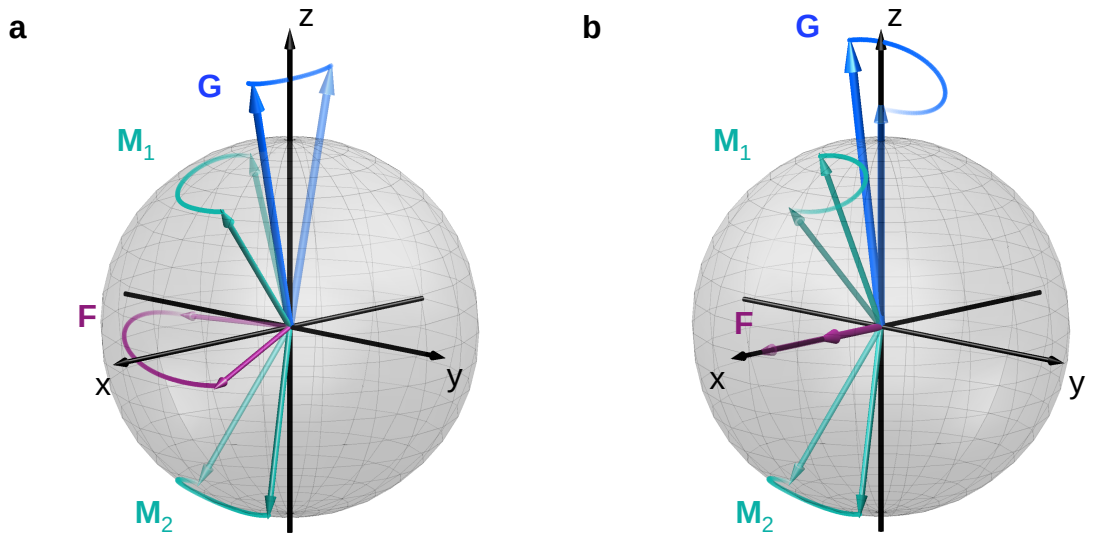

Figure 2.2 | Spin eigenmodes of $TmFeO_3$. **a**, Schematic illustration of the q-fm magnon mode in the Γ_2 magnetic phase. The ferromagnetic vector **F** precesses with a constant length around its equilibrium orientation, whereas **G** performs a fanning motion in the x-z-plane. **b**, The q-afm magnon mode causes an oscillatory motion of the length of the weak ferromagnetic moment **F** along the **x** axis. The antiferromagntic spin vector **G** moves in the y-z-plane while constantly changing its length. For clarity, the antiferromagnetic sublattices $\mathbf{M}_1$ and $\mathbf{M}_2$ as well as their canting due to the Dzyaloshinskii-Moriya interaction are shown on an exaggerated scale.

To reach a new equilibrium orientation, the Fe^{3+} spins have to perform a collective motion. Thereby, the magnetic structure of $TmFeO_3$ with two antiferromagnetically coupled magnetic sublattices supports two eigenmodes: the quasi-ferromagnetic (q-fm) magnon mode with a resonance frequency between 0.1 THz and 0.3 THz and the quasi-antiferromagnetic (q-afm) mode at $\approx$ 0.8 THz [Sri95, Mik14]. The underlying spin dynamics of the two magnon eigenmodes in the Γ_2 phase are shown in Figure 2.2. Whereas the q-fm magnon mode describes a precessional motion of the ferromagnetic spin vector **F** around its equilibrium position (Figure 2.2a), the q-afm mode leads to an oscillatory motion of the length of the vector **F** (Figure 2.2b). This can be explained by the characteristic phase between the motion of the two magnetic sublattices $\mathbf{M}_1$ and $\mathbf{M}_2$. For the q-fm mode, the y and z component of the antiferromagnetically coupled spins oscillate in phase, whereas their x components have a phase difference of 180°. This leads to the observed precessional motion of the vector **F**, whereas the antiferromagnetic vector **G** performs a fanning motion

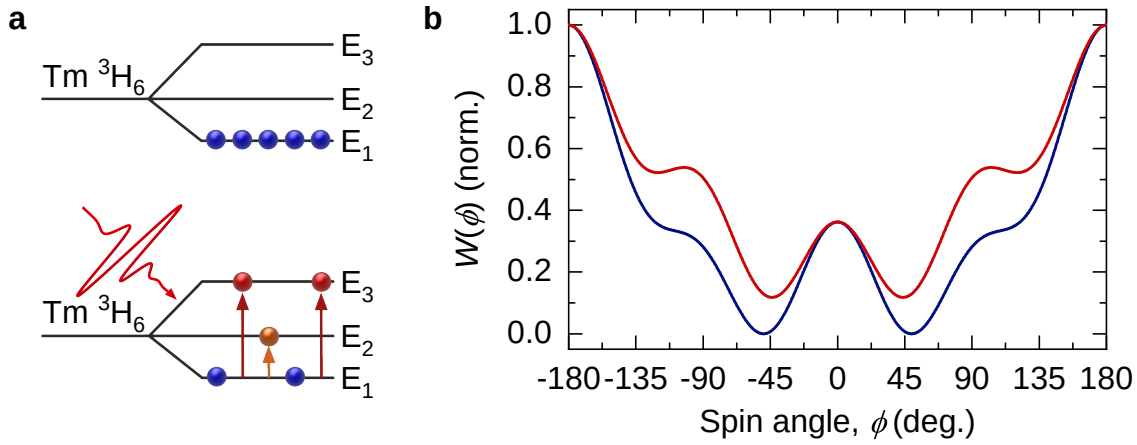

Figure 2.3 | Concept of THz-induced anisotropy changes. **a**, The crystal field splits the Tm^{3+} ground state with the term symbol $^3H_6$ into a set of singlet states. Transitions between the energy levels E_1, E_2 and E_3 can also be induced by an ultrashort THz pulse (red waveform). **b**, Normalized magnetic potential, $W(\phi)$, as a function of the spin angle, ϕ, at a lattice temperature of $T = 83.0$ K (blue curve). THz-induced electronic transitions in the $^3H_6$-Thulium ground state (term diagrams in **a**) abruptly modify the magnetic potential, which leads to a shift of the equilibrium spin angle, ϕ_0, and a reduced potential barrier between two stable spin states (red curve).

in the x-z-plane. As for the q-afm mode, the x and z components are oscillating in phase and the y components are moving out of phase. Thus, the weak ferromagnetic moment **F** does not precess, but its length oscillates along the x-axis. In this case, the antiferromagnetic spin vector **G** oscillates in the y-z-plane with a constantly varying length. As the temperature-dependent population of the Tm^{3+} ground state multiplet is accompanied by a change of the direction and strength of the magnetic potential, the resonance frequencies of both modes are also changing with temperature [Bai16a].

Besides thermal activation, also electromagnetic waves can be used to induce coherent magnetization dynamics [Kir10, Kam11]. As already shown, in particular, intense light pulses in the THz spectral range are a versatile tool to control spins in magnetically ordered materials, as they interface spin dynamics directly on their intrinsic energy scales [Kam11, Kam13, Bai16a, Bai16b]. Thereby, the magnetic field component of intense THz pulses can couple directly to the spins via the Zeeman

interaction, whereas the resulting amplitude of the induced spin dynamics scales linearly with the applied THz magnetic field [Kam11, Bai16b]. In the case of $TmFeO_3$, several transitions between the different singlet states within the Tm^{3+} ground state multiplet have non-zero electric dipole matrix elements [Bal85, Muk91]. In the Γ_{24} transition phase, the magnetic potential $W(\phi)$ strongly depends on the population of the Tm^{3+} ground state multiplet. Consequently, the electric-field component of intense THz pulses can be used to abruptly modify the magnetic potential (see Figure 2.3 and reference [Bai16a]). In Figure 2.3b, the blue curve shows the magnetic potential $W(\phi)$ in thermal equilibrium for a lattice temperature of $T = 83.0\,\mathrm{K}$. By resonant optical pumping of electronic transition at the frequencies $\nu = 0.6\,\mathrm{THz}$ ($E_1 \rightarrow E_2$), $\nu = 0.65\,\mathrm{THz}$ ($E_2 \rightarrow E_3$) and $\nu = 1.2\,\mathrm{THz}$ ($E_1 \rightarrow E_3$) [Zha16], both the equilibrium spin orientation ϕ_0 as well as the height of the potential barrier between the two stable spin states change (Figure 2.3b, red curve). This ultrafast modification of the magnetic potential results in an anisotropy torque that induces coherent magnon dynamics, whose amplitude scales quadratically with the applied THz electric field [Bai16a].
Despite this efficient coupling to the spin system, also Baierl *et al.* [Bai16a] could only obtain spin deflection angles of $\Delta\phi \approx 2.6°$ by applying THz peak electric fields of $1.0\,\mathrm{MV\,cm^{-1}}$. In this chapter, antenna-enhanced single-cycle terahertz pulses with peak electric near fields exceeding $25\,\mathrm{MV\,cm^{-1}}$ are utilized to completely switch spins between two adjacent minima of the magnetic potential.

2.2 THz high-field setup for subcycle probing of ultrafast magnetization dynamics

In general, electromagnetic waves in the THz spectral window are of particular interest for the investigation of numerous quasiparticles in solids, such as excitons [Poe15, Ste17, Mer19], magnons [Kam11, Bai16b, Bai16a], phonons [Kim12, Por14] and plasmons [Hub17]. Whereas weak THz fields allow the observation and characterization of these elementary processes, applying intense THz fields can lead to coherent control. In particular, THz waveforms with atomically strong peak electric fields have already been able to drive strong nonlinearities [Lei08, Jun12], induce novel

states of matter [Wan13], accelerate electrons ballistically throughout the entire Brillouin zone [Sch14, Hoh15, Lan16], or coherently flip the valley pseudospin [Lan18b]. Owing to the phase-stability of the applied THz waveforms, the induced dynamics could even be traced in absolute amplitude and phase on the femtosecond timescale. Despite these tremendous advances, the technologically most relevant quantum attribute of the electron - it's spin - has not been switchable on ultrafast timescales so far. The extremely stable THz high-field setup established in this chapter allows for switching spins in the prototypical antiferromagnet $TmFeO_3$ in the fastest and least-dissipative possible way, whereas the underlying magnetization dynamics can be probed with subwavelength spatial and subcycle temporal resolution in a highly stable cryogenic environment.

Figure 2.4 shows the experimental setup of the THz high-field source. The starting point is a commercial titanium-sapphire femtosecond laser oscillator in combination with a double-stage regenerative titanium-sapphire chirped pulse amplifier system. The oscillator generates near-infrared light pulses with a center wavelength of 793 nm at a repetition rate of 80 MHz. A Pockels cell then couples these pulses into the titanium-sapphire amplifier, where their pulse energy is enhanced according to the principle of chirped-pulse amplification [Str85]. With the help of a reflective diffraction grating configuration, the oscillator pulses get temporally stretched to avoid damage of the optical components during the amplification process. In the first stage, the light pulses travel 16 times through a regenerative cavity pumped by a frequency-doubled neodymium-doped yttrium lithium fluoride (Nd:YLF) laser with an average power of 30 W. The Pockels cell is modulated at a rate of 3 kHz, which defines the repetition rate, ν_{rep}, of the regenerative amplifier. The pulses then pass a single-pass amplifier, pumped by another Nd:YLF laser with an average power of 52 W to further boost the pulse energy. After recompression by diffraction gratings, the pulses feature a pulse energy of $E_{\mathrm{p}} = 5.5\,\mathrm{mJ}$ and a pulse duration of $\tau = 31\,\mathrm{fs}$. The spectrum has a center wavelength of $\lambda_{\mathrm{c}} = 807\,\mathrm{nm}$, while the full-width at half-maximum (FWHM) of the intensity is 39.5 nm (see Figure 2.4).

The near-infrared pulses from the titanium-sapphire amplifier are then guided to a custom-tailored THz source, that generates intense single-cycle THz pulses with a center frequency around 1 THz by optical rectification in a lithium niobate ($LiNbO_3$) nonlinear crystal. Thereby, optical rectification can be understood as difference-

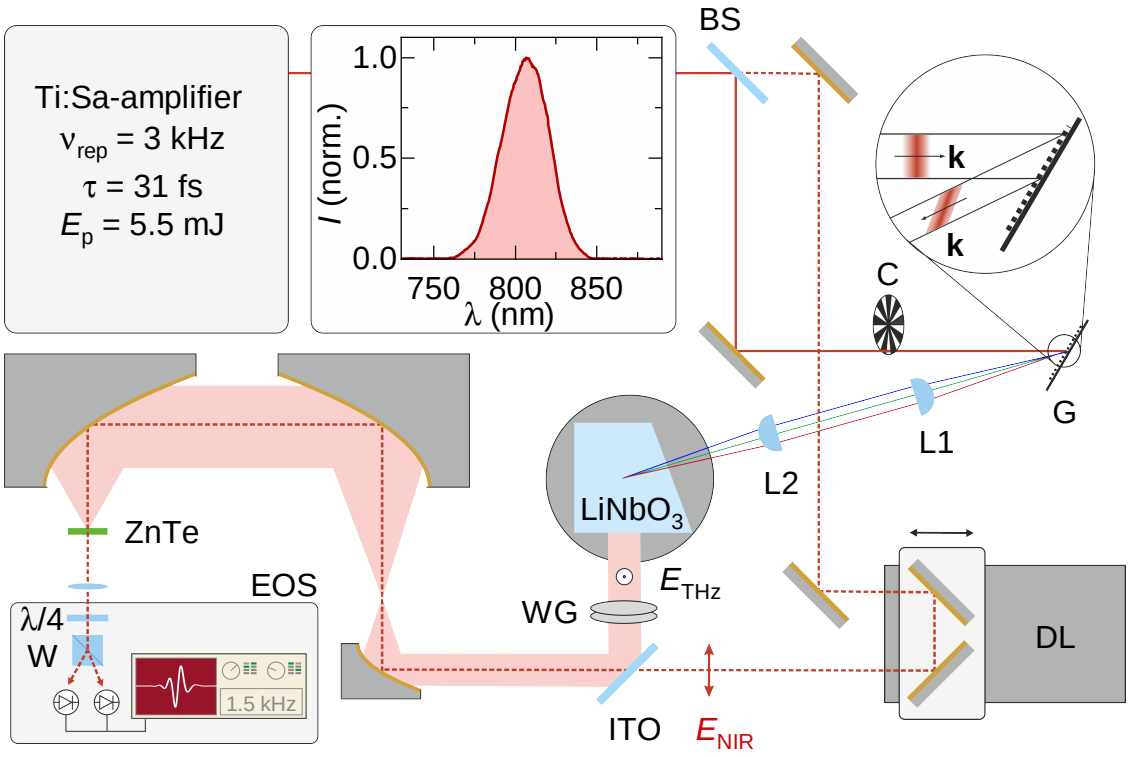

Figure 2.4 | Experimental setup for the generation of intense THz waveforms. a, Starting point is a Ti:sapphire laser system (center wavelength, 807 nm; pulse energy, 5.5 mJ; pulse duration, 31 fs; repetition rate, 3 kHz). A 99% beamsplitter divides the near–infrared beam in a weak probe arm (red dashed line) and a strong generation arm (red solid line), used for the THz generation. The grating (G), imprints a pulse front tilt onto the near-infrared beam and spatially separates the spectral components (blue, green and red lines). Two cylindrical lenses (L1 and L2) image and focus the laser pulses into a cryogenically cooled lithium niobate crystal ($LiNbO_3$), where the near-infrared light is converted to THz-radiation by optical rectification. A pair of wire-grid polarizers (WG) controls the intensity and the polarization state of the generated THz pulses. With the help of an indium-tin-oxide-coated fused silica window (ITO) the THz pulses and the near-infrared probe pulses are spatially superimposed. The delay line (DL) controls the temporal overlap. The THz-induced polarization changes are decoded with the help of a quarter-wave plate ($\lambda/4$), a Wollaston polarizer (W) and a pair of photodiodes and subsequently detected with a lock-in amplifier. E_{NIR}, is the near-infrared probe pulse polarization, E_{THz} indicates the polarization of the THz pulses.

frequency mixing within the spectrum of the same light pulse [Boy03]. Consequently, the generated THz pulses are inherently phase-stable [Cun02], which allows for a stroboscopic measurement of the ultrafast magnetization dynamics on a subcycle timescale. To reach the best conversion efficiency, the generated electromagnetic waves have to interfere constructively along the entire propagation length in the crystal. However, this condition is only fulfilled if the nonlinear polarization, induced by the fundamental near-infrared light, and the generated THz radiation propagate with the same velocity through the nonlinear medium. In the case of optical rectification this means that the group velocity $v_{\mathrm{group}}^{\mathrm{NIR}}$ and the phase velocity of the generated THz light $v_{\mathrm{phase}}^{\mathrm{THz}}$ have to be the same [Heb02, Boy03]:

$$v_{\mathrm{group}}^{\mathrm{NIR}} = v_{\mathrm{phase}}^{\mathrm{THz}}. \tag{2.3}$$

Owing to the natural dispersion of $LiNbO_3$, $v_{\mathrm{group}}^{\mathrm{NIR}}$ and $v_{\mathrm{phase}}^{\mathrm{THz}}$ differ by more than a factor of 2 [Heb04]. Nonetheless, the phase matching condition can be fullfilled by tilting the phase front of the near-infrared generation pulses by an angle χ [Heb02, Heb04]:

$$\chi = \arccos\left(\frac{v_{\mathrm{phase}}^{\mathrm{THz}}}{v_{\mathrm{group}}^{\mathrm{NIR}}}\right). \tag{2.4}$$

In this case, the phase difference between the two light pulses vanishes and they can interfere constructively over the entire interaction length. Here, the near-infrared phase front is tilted with respect to the wave vector $\mathbf{k}$ (Figure 2.4, inset) by the optical grating G. As the diffraction at the grating depends on the wavelength, the spectral components of the near-infrared pulses are spatially separated (Figure 2.4, blue, green, and red lines). Therefore, a lens telescope, consisting of two cylindrical lenses L1 and L2, collimates and then focuses the beam into the nonlinear crystal. To achieve the perfect tilt angle of $\chi = 63°$, the telescope has a magnification factor of 0.6, whereas the grating has a line density of $1800\,\mathrm{mm}^{-1}$ [Hir11]. A further boost of the conversion efficiency is achieved by cryogenically cooling the nonlinear $LiNbO_3$ crystal to a temperature of 77 K. This significantly narrows the transversal optical phonon with a frequency of 7.44 THz and therefore reduces the THz absorption in the crystal. The generated THz pulses have a pulse energy of up to $E_{\mathrm{p,THz}} = 1\,\mu\mathrm{J}$. In the actual experiment, the peak field strength and the polarization state of the

THz waveforms are controlled by a pair of wire-grid polarizers WG.
To be able to detect the THz-induced ultrafast magnetization dynamics with subcycle resolution, a small portion of 1 % of the near-infrared power is separated by the beamsplitter BS and then sent through a delay line DL. This allows for the variation of the temporal overlap between the THz pump and the near-infrared probe pulses. With the help of a fused silica window coated with indium tin oxide serving as a dichroic beam combiner, the near-infrared probe and THz pump beam are spatially superimposed. To reach the highest possible electric peak field, the THz pulses have to be focused down to the diffraction limit. Thus, a telescope, consisting of two parabolic mirrors, first enlarges the THz beam diameter, before a third parabolic mirror with a focal length of $f = 50\,\mathrm{mm}$ focuses the THz light onto the sample. The THz field amplitude in the sample focus was calibrated by measuring the THz power transmitted through a circular aperture. Thereby, the FWHM spot size of the THz beam can be determined to be 400 µm, which leads to a maximal THz peak electric field amplitude of $E_{\mathrm{THz}} = 1.0\,\mathrm{MV\,cm^{-1}}$.
By varying the temporal overlap between the near-infrared probe and the THz pump pulses, the absolute amplitude and phase of the phase-stable THz transients can be detected by means of electro-optic sampling [Wu95, Gal99, Sul20]. For this purpose, an electro-optic zinc telluride (ZnTe) detector crystal with a thickness of 6.5 µm, oriented in $\langle 110 \rangle$ direction, is placed in the sample focus. According to the electro-optic Pockels effect [Boy03], the oscillating THz electric field induces a transient birefringence, which is directly proportional to the applied field amplitude. Thus, the co-propagating near-infrared pulses exhibit a phase retardation of their polarization components, that depends on the instantaneous THz electric field. In the electro-optic sampling setup (Figure 2.4, EOS box) this polarization change induced by the THz field can be decoded with the help of a quarter-wave plate ($\lambda/4$), a Wollaston prism (WP), and two balanced silicon photodiodes, which are read out by a lock-in amplifier. If there is no THz field present, the quarter-wave plate translates the perfect linear polarization into a circular polarization state. This leads to equally strong signals onto the two photodiodes and thus, the difference between the two photocurrents is zero. If the near-infrared and the THz pulses overlap temporally, the THz-induced polarization change, however, leads to an unbalanced diode signal. Depending on the field polarity, this difference signal can be either posi-

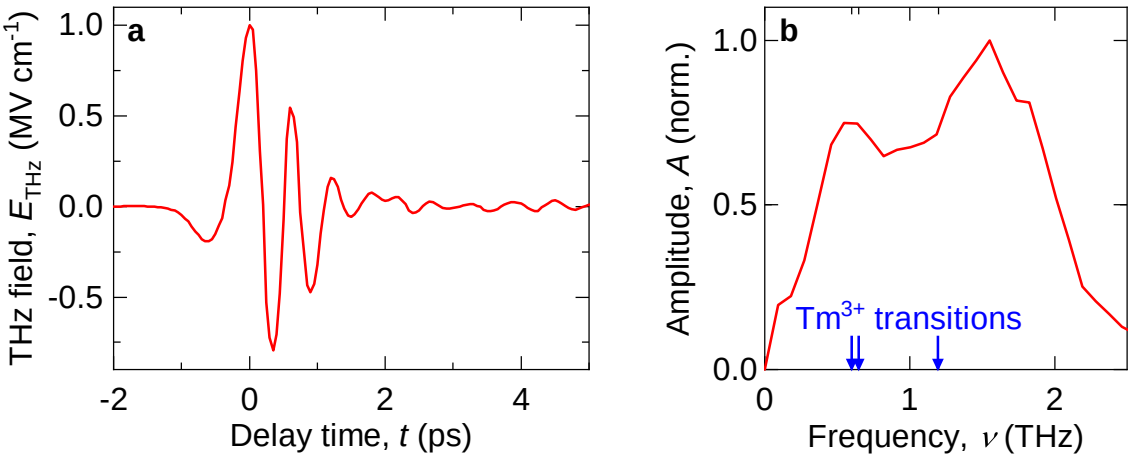

Figure 2.5 | Typical THz waveform generated by tilted-pulse-front optical rectification. **a**, Electro-optically detected THz field, E_{THz}, as a function of the delay time, t. **b**, Corresponding spectral amplitude of the THz transient shown in **a**. The blue arrows indicate the frequencies of the relevant ground state transitions in Tm^{3+}.

tive or negative. As the near-infrared pulses feature a pulse duration that is much shorter than a half cycle of the sampled waveform, the THz electric field can be seen as quasi-static during the duration of the probe pulse, which gives an unambiguous electro-optic signal. By varying the temporal overlap between the THz pump and near-infrared probe pulses, it is possible to stroboscopically detect the amplitude and phase of the THz electric-field profile simultaneously. Figure 2.5a shows the THz electric field, E_{THz}, as a function of the delay time, t, detected by electro-optic sampling. The waveform shows only a single oscillation within the FWHM intensity envelope (not shown). The corresponding amplitude spectrum (see Figure 2.5b) features frequency components between 0.1 THz and 2.5 THz. As this frequency range also includes the electronic transitions in the ground state multiplet of Tm^{3+} (see Figure 2.5b, blue arrows), these intense THz pulses with peak field amplitudes of up to $E_{\mathrm{THz}} = 1.0\,\mathrm{MV\,cm^{-1}}$ are perfectly suited to excite ultrafast magnetization dynamics in the prototypical antiferromagnet $TmFeO_3$.

In the actual experiment, the generated THz pulses are used to trigger a large-amplitude, coherent spin precession, which leads to THz-driven spin switching between two stable states. Thereby, the subsequent spin dynamics can be probed

on a subcycle timescale via the polarization rotation that is imprinted on the co-propagating near-infrared probe pulses by the magneto-optic Faraday effect [Kam11, Bai16a]. For this purpose, the ZnTe detector is replaced by a single crystal of $TmFeO_3$ with a thickness of 60 µm. The sample was cut perpendicularly to one of the crystal's optical axes, which lies in the y-z-plane at an angle of 51° with respect to the z-axis. Thus, the ferromagnetic vector $\mathbf{F}$ of the iron spins has a non-zero component parallel to the propagation direction of the near-infrared probe pulses $\mathbf{k}_{\mathrm{NIR}}$ (see also Figure 2.16). According to the magneto-optical Faraday effect, the transmission of linearly polarized light through such a magnetically ordered material results in a rotation of the polarization direction owing to circular birefringence [Coe09]. The THz-induced change of the magnetization, in particular, leads to a time-dependent rotation of the polarization, $\theta(t)$, that depends on the instantaneous orientation of the ferromagnetic vector $\mathbf{F}(t)$ at the delay time t [Kam11]:

$$\theta(t) = V\ d\ \langle \mathbf{k}_{\mathrm{NIR}} \cdot \mathbf{F}(t) \rangle. \tag{2.5}$$

Here, V is the magneto-optic Verdet constant, d is the thickness of the material and the last term denotes the projection of the time-dependent magnetization vector $\mathbf{F}(t)$ onto the $\mathbf{k}$-vector of the near-infrared probe pulses. Similar to the electro-optic sampling setup explained above, the THz-induced polarization rotation can be measured by subsequent optics consisting of a half-wave plate, a Wollaston prism, and two balanced silicon photodiodes. The time-dependent polarization rotation, $\theta(t)$, can be retrieved from the transient difference of the two photocurrents,

$$\frac{\Delta I(t)}{2I_0} = \theta(t), \tag{2.6}$$

where I_0 is the absolute signal on the photodiodes. The pulse duration of the near-infrared probe pulses of $\tau = 31$ fs is much shorter than the oscillation period of the excited magnon modes in $TmFeO_3$ (see section 2.1). Thus, by detecting the difference signal ΔI for different delay times, t, the THz-induced, coherent spin dynamics are traced stroboscopically with subcycle resolution. In previous experiments by Baierl *et al.* [Bai16a], THz pulses with a peak electric field of up to 1.0 MV cm^{-1} have been used to induce ultrafast magnon dynamics in $TmFeO_3$

with maximum spin deflection angles of 2.6°. In the present work, the advantages of the efficient electric-field control of the magnetic anisotropy in $TmFeO_3$ (see paragraph 2.1) are combined with the near-field enhancement in custom-tailored gold antennas. As a consequence, spins are coherently steered over the potential barrier between two metastable states, while the dynamics are observed directly on the femtosecond scale.

2.3 Electric near-field enhancement in custom-tailored optical antenna structures

Previous experiments have shown that it is possible to permanently switch the spin orientation in magnetically ordered materials using strong electric [Gam09, Wad16, Ole18, Stu17] and magnetic [Bac99, Ger02, Tud04] light fields. Yet, observing the underlying ultrafast spin dynamics on a subcycle timescale remained out of reach. Utilizing the magnetic and electric field components of intense THz pulses has however triggered coherent magnon dynamics which can be traced on the femtosecond timescale [Kam11]. In the frequency range of around 1 THz, the THz generation by tilted-pulse-front optical rectification usually limits the peak-electric-field amplitudes achievable with typical table-top laser sources to a few $\mathrm{MV\,cm^{-1}}$ [Hir11, Fül20]. As shown in previous studies by Baierl *et al.* [Bai16a, Bai16b], single-cycle THz waveforms with an electric peak field amplitude of $1\,\mathrm{MV\,cm^{-1}}$ can drive a nonlinear spin response, but only allow for spin deflection angles of a few degrees, which do not suffice for ultrafast THz-induced magnetic switching. Meanwhile, the near-field enhancement in custom-tailored antenna structures has been exploited to sculpt atomically strong THz waveforms, sufficient to drive non-perturbative nonlinearities, such as THz-induced phase transitions [Liu12] and interband Zener tunneling, with subdiffractional spatial definition [Lan14]. In this chapter, gold antenna structures are used to selectively enhance the electric field of the intense THz pulses generated in the high-field THz setup described in section 2.2. This leads to peak electric fields in the near field of the antenna on the order of $25\,\mathrm{MV\,cm^{-1}}$, enabling coherent spin control in the antiferromagnet $TmFeO_3$ throughout the entire phase space (see section 2.4 - 2.6).

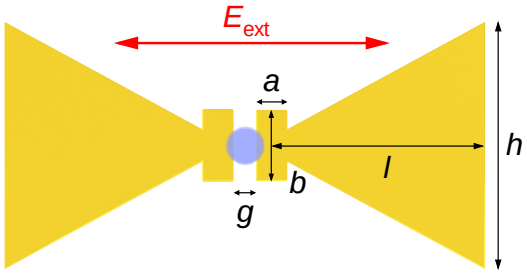

Figure 2.6 | Optical antenna scheme. The bowtie antenna is fully characterized by the parameters a, b, l, and h. Upon excitation by an external electromagnetic wave with an electric field E_{ext}, free carriers in the gold antenna get accelerated, which leads to a significant enhancement of the electric field in the antenna feed gap, g. Positioning the near-infrared probe pulse (blue circle) in the center of the antenna gap probes the THz-induced magnetization dynamics with subwavelength spatial resolution.

In the micro- or radiowave regime, antenna structures are a well-established scheme to control electromagnetic radiation on a subwavelength scale. Beyond that, in particular, in the THz and near-infrared spectral region custom-designed resonant circuits are utilized to precisely shape the magnetic and electric fields in the near field, which offers a large variety of applications ranging from extreme concentration and manipulation of light [Sch10, Nov11], nonlinear optics [Han09, Liu12, Lan14] to antenna-assisted high-harmonic generation [Kim08, Siv17, Liu18]. However, as the dimensions of the antenna structure are defined by their resonance frequency, applications in the optical range demand precise fabrication accuracies down to the nanometer scale. Nowadays, such small structures can for example be processed by electron- or ion-beam lithography [Pea81, Tse03], which makes the advantage of antennas accessible. Whereas conventional optical components like lenses or focusing mirrors only focus light down to the diffraction limit, in the near field of an optical antenna, field components of the electromagnetic wave can be concentrated and selectively enhanced on subdiffractional length scales [Nov11, Lan14]. Especially in the low THz spectral range around 1 THz, where the large wavelength limits the focusability of the light pulses, optical antenna structures are the ideal tool to realize high-field experiments. Bowtie antennas, e.g., allow for a selective enhancement and localization of the electric-field component of the applied electromagnetic wave [Fro04, Han09]. In the most straightforward geometry, these structures consist of two opposing tip-to-tip triangles made out of gold. Here, in order to have

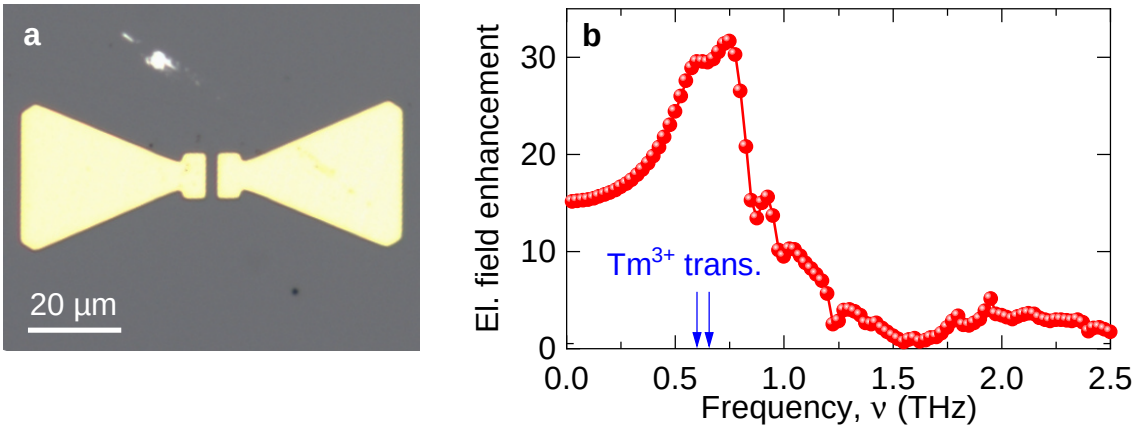

Figure 2.7 | Custom-tailored antenna structure on $TmFeO_3$. a, Microscope image of the gold bowtie antenna with a feed gap of 3.5 µm structured onto the $TmFeO_3$ sample with a thickness of 60 µm. Antenna gap $g = 3.5\,\mu m$, height $h = 39\,\mu m$, length $l = 39\,\mu m$. **b**, Electric-field enhancement in the center of the antenna structure shown in **a** as a function of the THz frequency, ν. The antenna resonance is centered at a frequency of 0.65 THz. The maximal electric-field enhancement factor of 31.6 is reached at a frequency of 0.75 THz. Blue arrows, relevant Tm^{3+} ground state transitions.

a well-defined near-field volume, two capacitive plates, whose size is determined by the parameters a and b, are added at the opposing tips of the two triangles (see Figure 2.6). The resonance of the structure is characterized by the length, l, and the height, h, of the two antenna lobes. If light polarized along the line between the two triangles excites the antenna structure as indicated in Figure 2.6, the free electrons in the gold film are accelerated. Depending on the polarity of the external driving field, E_{ext}, this leads to a charge accumulation on one or the other central capacitive plate. Due to the small distance between the two antenna lobes, a strong electric field inside the antenna feed gap, g, forms, similar to a parallel-plate capacitor.
In the experiments presented in this chapter, the antenna structures are supposed to enhance the electric-field component of the THz waveform (Figure 2.5a) such that the THz-induced change of the magnetic potential is sufficient to steer spins in $TmFeO_3$ over the potential barrier between two metastable magnetic states. Consequently, the bowtie antenna has to significantly enhance the spectral components that can resonantly drive the electronic transitions within the ground state multiplet of the Tm^{3+} ions (see section 2.1). Figure 2.7a shows a microscope image of

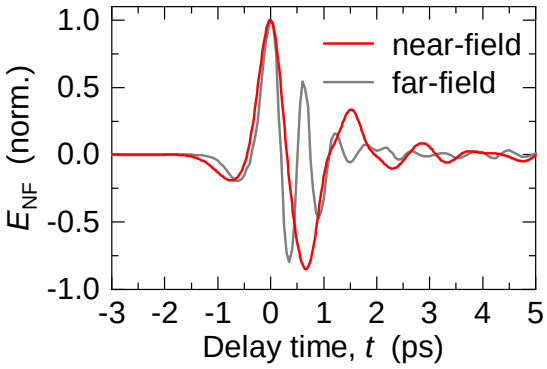

Figure 2.8 | Near-field transient. Calculated electric near-field, E_{NF},(red curve) in the center of the antenna gap as a function of the delay time, t, normalized to the experimentally detected THz field (gray curve).

the custom-tailored antenna structure processed on top of the 60-μm-thick $TmFeO_3$ crystal by electron-beam lithography of a poly(α-methylstyrene-co-α-chloracrylate methylester) resist, subsequent evaporation of 100 nm of gold, and lift-off. Further details of the fabrication procedure can be found in Appendix A. Guided by numerical finite element method (FEM) simulations in the frequency domain, the parameters l and h are optimized such that the bowtie antenna has a broad resonance peak centered around 0.65 THz. Thereby, the refractive index of $TmFeO_3$ is set to $n_{\mathrm{sub}} = 4.92$, while the gold structure is implemented as a perfect metal. For proper convergence, a grid resolution of $(100\,\mathrm{nm})^3$ is used. The antenna gap $g = 3.5\,\mu\mathrm{m}$, whereas the central capacitive plates feature a width of $a = 5.0\,\mu\mathrm{m}$ and a height of $b = 10.0\,\mu\mathrm{m}$. Figure 2.7b shows the near-field enhancement in the center of the antenna gap extracted from the FEM calculations for the frequency range covered by the spectrum of the THz driving waveform (see Figure 2.5). The full-width at half-maximum of the resonance peak, which is centered around 0.65 THz, includes the transitions $\mathrm{E}_1 \rightarrow \mathrm{E}_2$ and $\mathrm{E}_2 \rightarrow \mathrm{E}_3$ within the Tm^{3+} ground state multiplet (see Figure 2.7b, blue arrows). Thereby, the electric field is amplified by a factor of 29.5. Owing to interference effects in the substrate, however, the maximum of the electric-field enhancement is reached at 0.75 THz. At this frequency, the spectral amplitude is even 31.6 times larger than the corresponding far-field amplitude. For an antenna feed gap, g, of only 10 nm, it is even possible to reach enhancement factors on the order of 10^4 (see section 2.7). For this experiment, however, the fact that the THz-induced magnetization dynamics are simultaneously detected optically, limits a further miniaturization of the structure. In the sample focus (see Figure 2.4), the co-propagating femtosecond near-infrared probe pulse

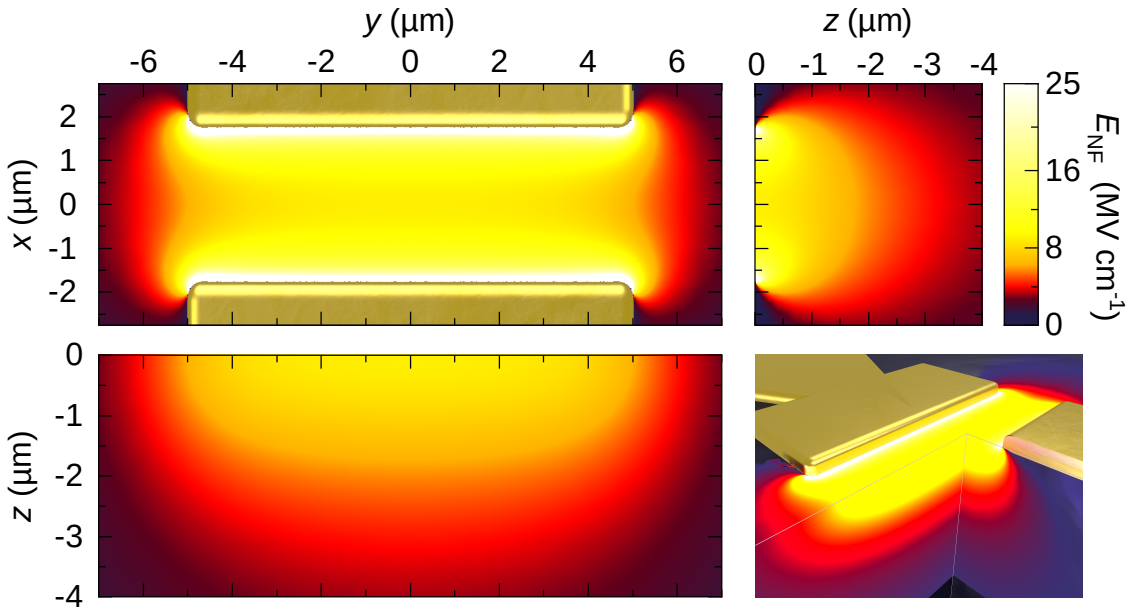

Figure 2.9 | Near-field characteristic in the antenna feed gap. Extracted peak near-field amplitude, E_{NF}, in the antenna feed gap calculated by finite-element method simulations for a real THz waveform with a peak-field amplitude of $E_{\mathrm{THz}} = 1.0\,\mathrm{MV\,cm^{-1}}$ in the x-y-, x-z-, and y-z-plane. In the center of the feed gap, E_{NF} readily exceeds $9.0\,\mathrm{MV\,cm^{-1}}$.

has a FWHM focus diameter of 6.0 µm. Thus, with a size of 3.5 µm, the antenna feed gap, g, is large enough, to transmit a large amount of the near-infrared beam while simultaneously maintaining the required electric-field enhancement. The local THz electric near-field waveforms (Figure 2.8, red curve) are calculated based on the measured far-field THz transient (Figure 2.8, gray curve) by employing the results of the FEM calculations as a complex-valued transfer function. Figure 2.9 shows the corresponding extracted peak electric near-field amplitudes, E_{NF}, in the x-y-, x-z- and y-z-plane for the strongest electro-optically detected THz waveform with a peak electric far field of $E_{\mathrm{THz}} = 1.0\,\mathrm{MV\,cm^{-1}}$. The area, where the electric near field exceeds the far-field amplitude, covers the whole antenna gap and reaches down to several micrometers. In the center of the antenna gap at $z = 0$, the electric-near-field amplitude, E_{NF}, readily exceeds $9.0\,\mathrm{MV\,cm^{-1}}$. Close to the metal plates, E_{NF} even goes beyond $25.0\,\mathrm{MV\,cm^{-1}}$. Thus, the custom-tailored antenna structures not only bypass the diffraction limit but also maximize the achievable THz amplitude,

which facilitates large-amplitude spin dynamics and ultimately steers spins over a potential barrier (see Figure 2.3) into a new stable state.

2.4 Ultrafast spin switching by near-field enhanced single-cycle THz pulses

The combination of a local near-field enhancement of metal antennas as described in the previous section and the advantages of nonlinear electric-field-induced anisotropy changes in the antiferromagnet $TmFeO_3$ allows for THz peak electric fields, which are sufficient for magnetic switching and even hold the potential for a coherent spin control throughout the entire phase space. Thereby, with the help of the THz high-field setup established in section 2.2, the corresponding ultrafast magnetization dynamics are traced with subwavelength spatial and subcycle temporal resolution.
For the experiments, monocrystalline $TmFeO_3$ with a thickness of 60 µm obtained by floating-zone melting is used. The sample was cut perpendicularly to one of the crystal's optical axes, which lies in the y-z-plane at an angle of 51° with respect to the z-axis. As shown in Figure 2.10a, the custom-tailored THz antennas with a feed gap of 3.5 µm and a resonance frequency of 0.65 THz (see Figure 2.7) were processed on top of the crystal such that the antenna gap is oriented parallel to the crystallographic x-axis. Consequently, the THz electric field is polarized perpendicular to the x-axis, which ensures the most effective excitation in the Tm^{3+} ground state multiplet [Sri95]. The whole structure is kept in a helium cryostat and cooled to temperatures in the Γ_{24} transition phase. For the measurements discussed in this section, a static bias field of $\mathbf{B}_{\mathrm{ext},0} = 100\,\mathrm{mT}$ from a permanent magnet is applied in the y-z-plane of the crystal at an angle of 39° relative to the z-axis, which defines the equilibrium spin orientation, ϕ_0, and ensures the restoring of the magnetization between subsequent laser pulses.
To test the efficiency of the antenna, the magneto-optical signal induced in $TmFeO_3$ ($T = 83.0\,\mathrm{K}$) with and without the near-field antenna is compared as a function of the pump-probe delay time, t (see Figure 2.10b). In the absence of the antenna, a THz pulse with an amplitude of $E_{\mathrm{THz}} = 1.0\,\mathrm{MV\,cm^{-1}}$ abruptly sets off coherent magnon oscillations, which decay exponentially within 40 ps (Figure 2.10b, black

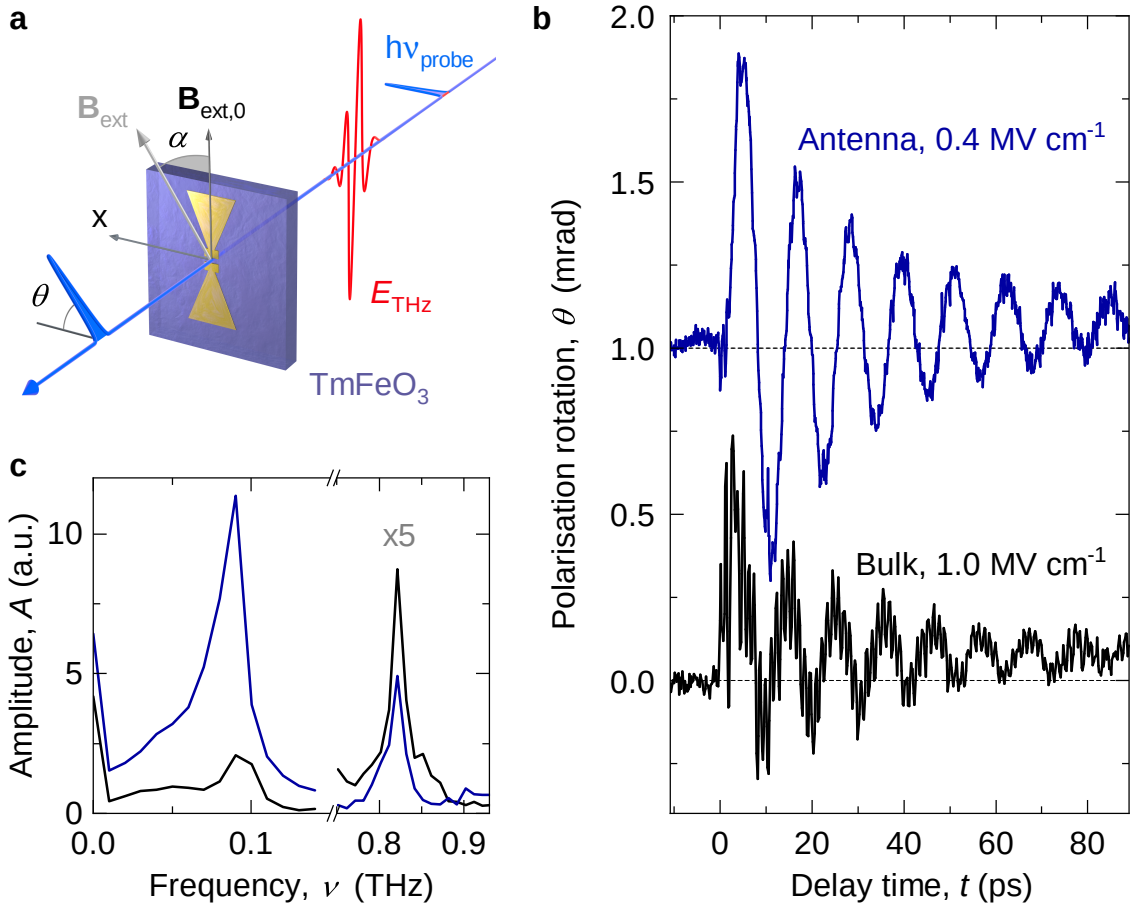

Figure 2.10 | Antenna-enhanced THz spin dynamics. **a**, Schematic of the gold bowtie antenna on $TmFeO_3$. The structure is excited from the backside by an intense THz electric field E_{THz} (red waveform). The THz-induced magnetization dynamics in the center of the feed gap is probed via the polarization rotation, θ, imprinted on the co-propagating near-infrared pulse ($h\nu_{\mathrm{probe}}$, blue). $\mathbf{B}_{\mathrm{ext,0}}$, orientation of the external magnetic bias field. For the experiments discussed in section 2.6, $\mathbf{B}_{\mathrm{ext}}$ is rotated by the angle, α, relative to the initial orientation $\mathbf{B}_{\mathrm{ext,0}}$. **b**, Experimentally detected polarization rotation signal, θ, as a function of the delay time, t, obtained for a peak electric THz field of $E_{\mathrm{THz}} = 1.0\,\mathrm{MV\,cm^{-1}}$ on the unstructured substrate (black curve) and when probing the gap of the bowtie antenna structure resonantly excited by a THz waveform with a peak electric far-field amplitude of $E_{\mathrm{THz}} = 0.4\,\mathrm{MV\,cm^{-1}}$ (blue curve, vertically offset by 1 mrad for better visibility). **c**, Corresponding amplitude spectra for the time domain data shown in **b** featuring two modes at 0.09 THz and 0.82 THz. The sample was kept at a lattice temperature of $T = 83.0\,\mathrm{K}$.

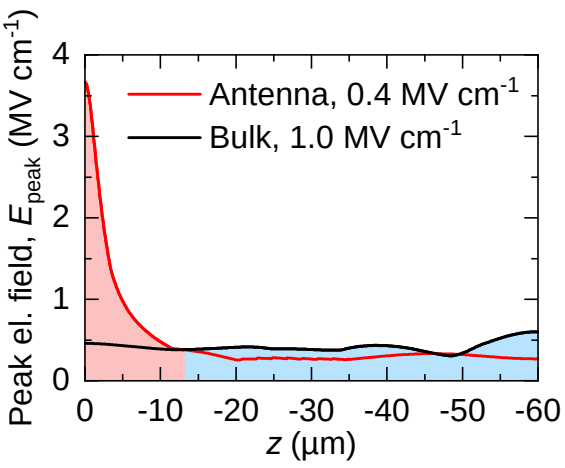

Figure 2.11 | Calculated electric near-field characteristics. Peak near-field amplitude, E_{peak}, as a function of depth, z, in the center of the antenna feed gap, for a THz far-field amplitude of $E_{\mathrm{THz}} = 0.4\,\mathrm{MV\,cm^{-1}}$ (red curve). The electric field distribution expected in the unstructured substrate for $E_{\mathrm{THz}} = 1.0\,\mathrm{MV\,cm^{-1}}$ is shown for comparison (black line). The near-field region of the antenna, where the electric field exceeds the value of the bulk structure, is indicated by the red-shaded area.

curve). The Fourier transformation of the time-domain data reveals a superposition of two frequency components centered at 0.09 THz and 0.82 THz (see Figure 2.10c) - the quasi-ferromagnetic (q-fm) and the quasi-antiferromagnetic (q-afm) mode (see section 2.1 and reference [Bai16a]), respectively. The maximum rotation angle of the probe polarization amounts to $\theta_{\mathrm{max}} = 0.5\,\mathrm{mrad}$. Numerical FEM calculations for the unstructured substrate and a THz far-field amplitude of $E_{\mathrm{THz}} = 1.0\,\mathrm{MV\,cm^{-1}}$ reveal a rather homogeneous peak electric field across the whole sample thickness of $E_{\mathrm{peak}} \approx 0.42\,\mathrm{MV\,cm^{-1}}$ (see Figure 2.11, black line). By assuming that also the polarization rotation originates from equal contributions across the entire sample thickness, the corresponding average magnetization deflection can be estimated to $\Delta\phi = 3.5°$ (see also Appendix B).

Now, positioning the probe pulse in the center of the antenna feed gap leads to a qualitatively different response. Here, a polarization rotation as high as $\theta_{\mathrm{max}} = 0.9\,\mathrm{mrad}$ is reached for a much weaker THz far field of $E_{\mathrm{THz}} = 0.4\,\mathrm{MV\,cm^{-1}}$ (Figure 2.10b, blue curve). In addition, the relative spectral amplitude of the q-fm mode is significantly enhanced, whereas the amplitude of the q-afm mode is suppressed. This behavior is expected since the q-fm mode is excited by the antenna-enhanced THz electric-field component, whereas the q-afm magnon can only be launched by Zeeman coupling to the THz-magnetic-field [Bai16a], which is not enhanced in the feed gap. Nonetheless, the amplitude of the q-fm magnon is remarkably high given the

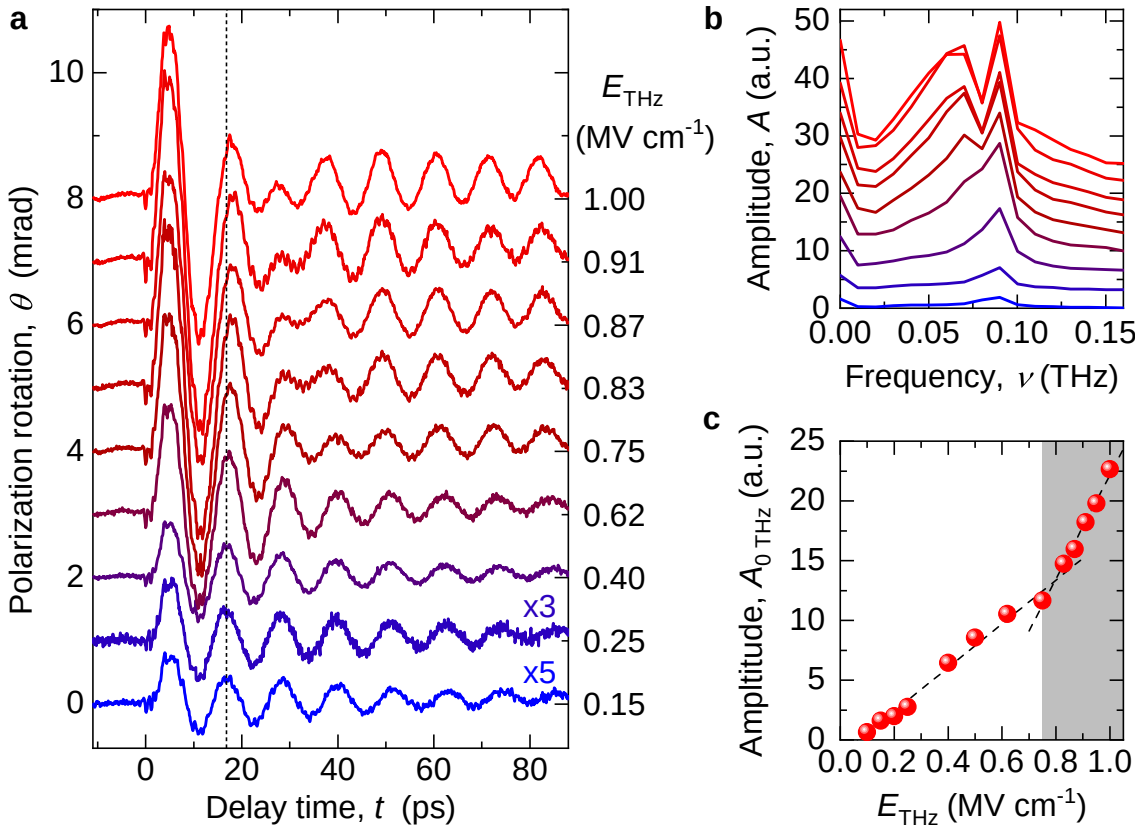

Figure 2.12 | THz-induced nonlinear spin dynamics. **a**, Polarization rotation, θ, probed in the center of the antenna feed gap for various far-field amplitudes, as a function of the delay time, t. For incident THz peak fields $E_{\mathrm{THz}} > 0.75\,\mathrm{MV\,cm^{-1}}$, the quasi-monochromatic oscillation is strongly distorted by a phase slip at delay times between 25 and 35 ps. The measurements are offset and scaled as indicated for clarity. Lattice temperature $T = 83.0\,\mathrm{K}$. **b**, Spectral amplitude of the time-domain data shown in **a**. The phase slip in the polarization rotation signal for the highest THz fields manifests in a splitting of the q-fm resonance. **c**, Spectral amplitude of the d.c. offset, $A_{0\ \mathrm{THz}}$, as a function of the THz far-field peak amplitude, E_{THz}. $A_{0\ \mathrm{THz}}$ increases monotonically with the THz field. Gray-shaded area: Spin-switching regime with increased slope of $A_{0\ \mathrm{THz}}$. Dashed lines, guides to the eye.

fact that the field enhancement is spatially confined to the evanescent near-field region (Figure 2.11, red shaded area) whereas the magneto-optical signal in the antenna-free case (Figure 2.10b, black curve) originates from the entire thickness of the $TmFeO_3$ substrate of 60 µm. In the center of the antenna feed gap, FEM calculations for a THz-far-field amplitude of $E_{\mathrm{THz}} = 0.4\,\mathrm{MV\,cm^{-1}}$ lead to a maximum

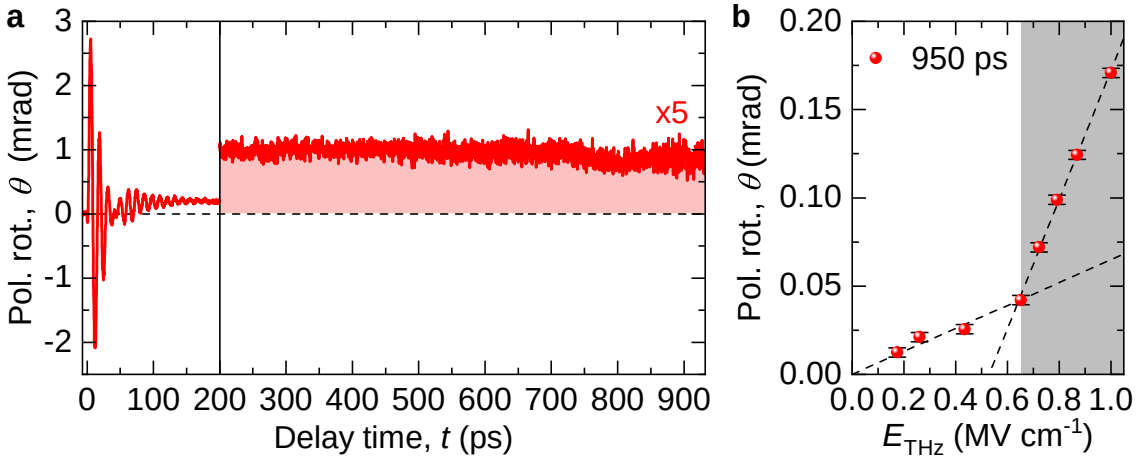

Figure 2.13 | Long-term evolution of the THz-induced magnetization dynamics. **a**, Polarization rotation, θ, measured in the center of the antenna feed gap as a function of the delay time, t, for a THz far-field amplitude of $E_{\mathrm{THz}} = 1.0\,\mathrm{MV\,cm^{-1}}$. The red-shaded area indicates the long-lived offset. **b**, Polarization rotation, θ, at a delay time of $t = 950\,\mathrm{ps}$ as a function of the THz electric peak field, E_{THz}. The data are extracted from time-resolved measurements in the feed gap of an antenna structurally similar to the one discussed in section 2.3 with a feed gap of 3.5 µm and a broad resonance around 0.65 THz, optimized to the Tm^{3+} ground state transitions. Lattice temperature, $T = 81.0\,\mathrm{K}$. In the spin switching regime, $E_{\mathrm{THz}} > 0.65\,\mathrm{MV\,cm^{-1}}$, the slope of the polarization rotation signal is significantly increased. Error bars, standard deviation of θ. Dashed lines, guides to the eye.

peak electric near-field amplitude of $E_{\mathrm{peak}} = 3.67\,\mathrm{MV\,cm^{-1}}$, whereas the antenna near-field region reaches to a depth of $z \approx 13\,\mu\mathrm{m}$ (Figure 2.11, red curve). A rough estimate (for details see Appendix B) shows that the spins in the antenna gap need to undergo a rotation by as much as $\Delta\phi = 24°$ in order to explain the observed signal strength. Hence, a further increase of the incident THz field may be able to cause complete spin switching.

Figure 2.12a shows the ultrafast polarization rotation probed in the antenna feed gap, for various far-field THz amplitudes between $E_{\mathrm{THz}} = 0.15\,\mathrm{MV\,cm^{-1}}$ and $E_{\mathrm{THz}} = 1.0\,\mathrm{MV\,cm^{-1}}$. For the lowest field, the spin dynamics resemble the q-fm precession sampled in the unstructured crystal (Figure 2.10b, black curve). For increasing fields, the oscillation amplitude grows. When the incident THz field exceeds $E_{\mathrm{THz}} = 0.75\,\mathrm{MV\,cm^{-1}}$, a qualitatively new behavior emerges. The period of the first full cycle of the magnetization oscillation is distinctly stretched (see vertical dashed

line in Figure 2.12a) while a pronounced beating feature occurs in the coherent polarization rotation signal for $25\,\mathrm{ps} < t < 35\,\mathrm{ps}$. Simultaneously, a long-lived offset of the Faraday signal develops, which persists up to nanoseconds (Figure 2.13). In the frequency domain (Figure 2.12b), these novel dynamics are associated with an asymmetric splitting of the q-fm magnon resonance superimposed on a broad spectral distribution, somewhat reminiscent of the spectral fingerprint of carrier-wave Rabi flopping [Müc01]. The long-lived offset manifests in a d.c. spectral component, $A_{0\,\mathrm{THz}}$, which grows more rapidly for $E_{\mathrm{THz}} > 0.75\,\mathrm{MV\,cm^{-1}}$ (Figure 2.12c and Figure 2.13b).
In the following section, a theoretical model, which describes the THz-induced spin dynamics microscopically, will identify the observed stretching of the first oscillation cycle, the beating of the Faraday signal, and the spectral splitting of the magnon resonance as the hallmarks of all-coherent non-perturbative spin trajectories between adjacent minima of the magnetic potential energy, whereas the long-lived offset directly reads out the switched spin state.

2.5 Simulation of ultrafast spin dynamics in the near field of optical antennas

The time-resolved pump-probe experiments in the last section lead to the observation of two magnon modes in $TmFeO_3$. Thereby, the selective enhancement of the THz electric field in the feed gap of a gold antenna caused a significant enhancement of the q-fm magnon mode and also revealed unprecedented features in the ultrafast polarization rotation above the threshold of $E_{\mathrm{THz}} = 0.75\,\mathrm{MV\,cm^{-1}}$. To investigate the origin of the observed stretching of the first oscillation cycle, the beating of the Faraday signal, and the spectral splitting of the q-fm magnon resonance it is crucial to track the THz-induced spin dynamics microscopically. The theoretical model presented in this section has been developed in close collaboration with *Alexey V. Kimel* from the Radboud University in Nijmegen, *Rostislav V. Mikhaylovskiy* from Lancaster University and *Anatoly K. Zvezdin* from the Prokhorov General Physics Institute and P.N. Lebedev Physical Institute of the Russian Academy of Sciences in Moscow.

Figure 2.14a shows the magnetic structure of $TmFeO_3$. As discussed in section 2.1 the slight canting between the two antiferromagnetically coupled sublattices $\mathbf{M}_1$ and $\mathbf{M}_2$ causes a weak ferromagnetic moment $\mathbf{F} = \mathbf{M}_1 + \mathbf{M}_2$ in the x-z-plane. The antiferromagnetic vector $\mathbf{G} = \mathbf{M}_1$ - $\mathbf{M}_2$ encloses an angle, ϕ, with the crystallographic x-axis. In the Γ_{24} transition phase, ϕ shifts continuously between 0° and 90° as the magnetic potential, $W(\phi)$, changes with the thermal population of the Tm^{3+} crystal field-split states (see also Figure 2.1). Consequently, the vectorial spin orientation can be mapped onto the angle ϕ between the antiferromagnetic vector $\mathbf{G}$ and the crystallographic x-axis. To understand the detected polarization rotation signal, one has to model the temporal evolution of ϕ in the vicinity of a THz pulse with the THz electric field $\mathbf{E}_{\mathrm{THz}} = \left(E_{\mathrm{THz,x}}, E_{\mathrm{THz,y}}, E_{\mathrm{THz,z}}\right)$ and a THz magnetic field $\mathbf{B}_{\mathrm{THz}} = \left(B_{\mathrm{THz,x}}, B_{\mathrm{THz,y}}, B_{\mathrm{THz,z}}\right)$. To unequivocally define the equilibrium spin orientation, ϕ_0, and to ensure the restoring of the magnetization between subsequent laser pulses, an additional weak external magnetic bias field $\mathbf{B}_{\mathrm{ext}} = \left(B_{\mathrm{ext,x}}, B_{\mathrm{ext,y}}, B_{\mathrm{ext,z}}\right)$ is applied. As shown in references [Kam11, Bai16b], spins can couple directly to the THz magnetic field via the Zeeman interaction. In centrosymmetric materials like $TmFeO_3$, an external electric field can also couple quadratically to the magnetic system [Bai16a]. The excitation of the q-fm magnon mode by an intense THz pulse can be described with the Langrangian function, L, of the spin angle, ϕ, and its time derivative, $\dot{\phi}$,

$$L = \frac{M_{\mathrm{Fe}}}{2\gamma^2 H_{\mathrm{E}}}\ddot{\phi}^2 - \frac{M_{\mathrm{Fe}}}{\gamma H_{\mathrm{E}}} B_{\mathrm{THz,y}}\dot{\phi} - W(\phi) - W_{\mathrm{el}}(\phi), \tag{2.7}$$

whereas the damping of the magnetic system is given by the Rayleigh function R with the Hilbert damping parameter β,

$$R = \frac{\beta M_{\mathrm{Fe}}}{2\gamma}\dot{\phi}^2. \tag{2.8}$$

Here, $M_{\mathrm{Fe}} = 1000$ e.m.u. cm^{-3} is the magnetization of a single Fe^{3+} sublattice, γ is the gyromagnetic ratio and $H_{\mathrm{E}} = 2{\cdot}10^7$ Oe is the effective field due to the d-d exchange interaction of the Tm^{3+} ions. The magnetic potential, $W(\phi)$, of $TmFeO_3$ under the influence of the THz magnetic field, $\mathbf{B}_{\mathrm{THz}}$, and the external bias field, $\mathbf{B}_{\mathrm{ext}}$, is given by [Bai16a]:

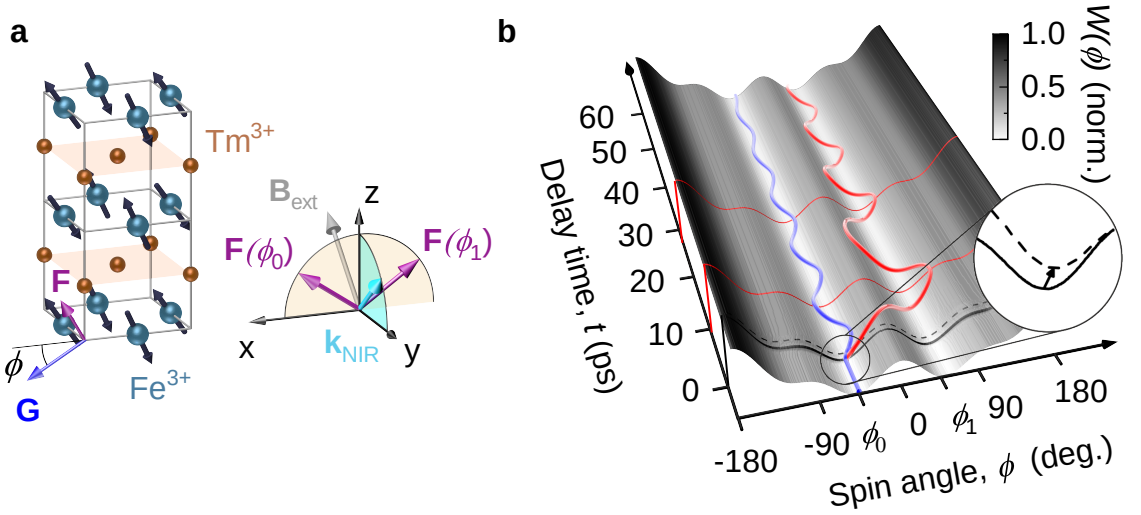

Figure 2.14 | Microscopic picture of ballistic spin motion. **a**, Spin and lattice structure of $TmFeO_3$ in the Γ_{24} phase ($T_1 < T < T_2$), showing the Fe^{3+} spins (cyan spheres and arrows), Tm^{3+} ions (bronze spheres), and the ferromagnetic moment, **F** (violet arrow). The antiferromagnetic vector, **G** (blue arrow), lies in the x-z-plane and encloses a finite angle of $0 < \phi < 90°$ with the x-axis. Switching the magnetic state from the equilibrium spin angle, ϕ_0, to the new equilibrium position, ϕ_1, causes a rotation of the ferromagnetic vector, **F**, in the x-z-plane. The wave vector of the probe pulse, $\mathbf{k}_{NIR}$ (light blue arrow), and the external magnetic field, $\mathbf{B}_{ext}$ (gray arrow), are oriented in the y-z-plane as indicated. **b**, Numerical simulation of THz-induced ballistic spin dynamics. Upon THz excitation, the magnetic potential, $W(\phi)$, is abruptly modified near a delay time of $t = 0\,\mathrm{ps}$ (magnified in inset). Near-field THz transients with peak amplitudes of $E_{NF} = 6.0\,\mathrm{MV\,cm^{-1}}$ abruptly induce large-amplitude spin oscillations in the same potential valley around the initial angle, ϕ_0 (blue trajectory). For a THz near-field of $E_{NF} = 10.0\,\mathrm{MV\,cm^{-1}}$, the spins reach the adjacent local minimum (red trajectory) at ϕ_1, where $\phi_1 \approx \phi_0 + 90°$, accumulating a phase retardation relative to spins oscillating around ϕ_0. The red cuts through the magnetic potential indicate the delay times $t = 9.7\,\mathrm{ps}$ and $27.2\,\mathrm{ps}$, respectively.

$$\begin{aligned} W(\phi) &= K_1(T)\sin^2\phi + K_2\sin^4\phi \\ &\quad -\frac{H_\mathrm{D}}{H_\mathrm{E}}M_\mathrm{Fe}\Big[(B_\mathrm{ext,z}+B_\mathrm{THz,z})\cos\phi - (B_\mathrm{ext,x}+B_\mathrm{THz,x})\sin\phi\Big], \end{aligned} \tag{2.9}$$

where $H_\mathrm{D} = 2{\cdot}10^5$ Oe is the Dzyaloshinskii field and the ratio $\frac{H_\mathrm{D}}{H_\mathrm{E}}$ defines the spin canting angle of the two magnetic sublattices due to the Dzyaloshinskii-Moriya interaction. The parameter $K_1(T) = 2K_2\frac{T-T_2}{T_2-T_1}$ for $T_1 < T < T_2$, where K_2 is a constant, sets the potential curvature by the frequency of the quasi-ferromagnetic mode $\omega^2_\text{q-fm} = \frac{1}{2}\omega_\mathrm{E}\omega_\mathrm{A}\sin^2\phi_0$, for a vanishing external magnetic bias field (see also paragraph 2.1). Here, $\omega_\mathrm{E} = \gamma H_\mathrm{E}$, $\omega_\mathrm{A} = \gamma\frac{K_2}{M_\mathrm{Fe}}$, T is the spin lattice temperature, and $T_1 = 80\,\mathrm{K}$ and $T_2 = 90\,\mathrm{K}$ are the lower and upper temperature bounds of the Γ_{24} transition phase, respectively. The thermal excitations of the crystal-field-split ground states determine the equilibrium angle of the spin vector, $\phi_0(T) = \arcsin\left(\frac{T-T_2}{T_2-T_1}\right)^{\frac{1}{2}}$ (see also Figure 2.1). The last term in equation (2.9) describes the direct Zeeman coupling between the applied magnetic fields $\mathbf{B}_\mathrm{ext}$ and $\mathbf{B}_\mathrm{THz}$ and the spin system.
The interaction of the THz electric field with the spin system leads to an additional modification of the magnetic potential by $W_\mathrm{el}(\phi)$ (see equation (2.7)). In lowest order, $W_\mathrm{el}(\phi)$ scales quadratically with $\mathbf{E}_\mathrm{THz}$ and $\mathbf{G}$ and has the form

$$W_\mathrm{el}(\phi) = \sum_{i,k,l,m} g_{iklm}\mathbf{G}_\mathrm{l}\mathbf{G}_\mathrm{m}E_\mathrm{THz,i}E_\mathrm{THz,k}, \tag{2.10}$$

where g_{iklm} are the components of the nonlinear magnetoelectric susceptibility tensor $\hat{\mathbf{g}}$, that is defined by the crystal symmetry. For $TmFeO_3$, which belongs to the orthorombic space group D^{16}_{2h} [Sri95], $\hat{\mathbf{g}}$ in the Voigt notation [Gro18] is given by [Bai16a]:

$$\hat{\mathbf{g}} = \begin{pmatrix} g_{11} & g_{12} & g_{13} & 0 & 0 & 0 \\ g_{21} & g_{22} & g_{23} & 0 & 0 & 0 \\ g_{31} & g_{32} & g_{33} & 0 & 0 & 0 \\ 0 & 0 & 0 & g_4 & 0 & 0 \\ 0 & 0 & 0 & 0 & g_5 & 0 \\ 0 & 0 & 0 & 0 & 0 & g_6 \end{pmatrix}. \tag{2.11}$$

Taking into account that the antiferromagnetic vector $\mathbf{G}$ lies in the crystallographic x-z-plane such that $\mathbf{G} = \big(\cos\phi,\ 0,\ \sin\phi\big)$, $W_{\mathrm{el}}(\phi)$ can be written as

$$W_{\mathrm{el}}(\phi) = f(\mathbf{E}) + \mathcal{E}\sin^2\phi + \frac{1}{2}g_5 E_{\mathrm{THz,x}} E_{\mathrm{THz,z}}, \tag{2.12}$$

where $f(\mathbf{E}) = g_{11}E^2_{\mathrm{THz,x}} + g_{12}E^2_{\mathrm{THz,y}} + g_{13}E^2_{\mathrm{THz,z}}$ and

$$\mathcal{E} = \chi_{\mathrm{x}}E^2_{\mathrm{THz,x}} + \chi_{\mathrm{y}}E^2_{\mathrm{THz,y}} + \chi_{\mathrm{z}}E^2_{\mathrm{THz,z}} \tag{2.13}$$

with $\chi_{\mathrm{x}} = g_{12} = -g_{11}$, $\chi_{\mathrm{y}} = g_{22} - g_{11}$ and $\chi_{\mathrm{z}} = g_{33} - g_{13}$. As the function $f(\mathbf{E})$ does not depend on the magnetic phase of the crystal, it can be neglected at this point. Equation (2.12) effectively describes how the THz electric field couples to the Fe^{3+} spins in $TmFeO_3$ and how it modifies their magnetic potential. Nonetheless, the described interaction mechanism is not material-specific but rather arises from the D^{16}_{2h} symmetry of the crystal. In $TmFeO_3$, the coupling is mediated by the electronic excitation within the Tm^{3+} ground state, which results in an anisotropy torque that in turn leads to a coherent spin motion. In general, the interaction can also be carried by other elementary excitations such as phonons [Afa19] or excitons.
Now, according to the Lagrange formalism, the equation of motion for the spin angle, ϕ, accounting for a THz-induced change of the magnetic potential energy, can be derived from the differential equation

$$\frac{\mathrm{d}}{\mathrm{d}t}\left(\frac{\partial L}{\partial \dot{\phi}}\right) - \frac{\partial L}{\partial \phi} + \frac{\partial R}{\partial \dot{\phi}} = 0. \tag{2.14}$$

With equations (2.7), (2.8), (2.9) and (2.12), the equation of motion assumes the form of a generalized sine-Gordon equation:

$$\begin{aligned} \ddot{\phi} + \beta\omega_{\mathrm{E}}\dot{\phi} + 4\omega_{\mathrm{E}}\omega_{\mathrm{A}}\sin\phi\cos\phi\left(\frac{T-T_2}{T_2-T_1} + \sin^2\phi\right) \ &= \\ \gamma\dot{B}_{\mathrm{THz,y}} - \frac{H_{\mathrm{D}}}{H_{\mathrm{E}}}\gamma\omega_{\mathrm{E}}\Big[\,(B_{\mathrm{ext,z}} + B_{\mathrm{THz,z}})\sin\phi + (B_{\mathrm{ext,x}} + B_{\mathrm{THz,x}})\cos\phi\Big] \\ -\frac{\omega_{\mathrm{E}}\omega_{\mathrm{A}}}{K_2}\left(2\mathcal{E}\sin\phi\cos\phi + g_5\cos 2\phi\ E_{\mathrm{THz,x}}E_{\mathrm{THz,z}}\right). \end{aligned} \tag{2.15}$$

Solving equation (2.15) with the initial conditions

$$\phi(t=0) = \phi_0(T) \quad \text{and} \quad \dot{\phi} = 0, \tag{2.16}$$

uniquely describes the coherent magnetization dynamics of the q-fm magnon mode induced by an intense THz pulse. Thereby, the excitation of the Tm^{3+} ions by the intense THz electric near field abruptly modifies $W(\phi)$, which shifts both the position, ϕ_0, and the depth of the potential minimum (Figure 2.14b, inset). These non-adiabatic changes then give rise to a displacive and an impulsive anisotropy torque, which scale quadratically with the applied THz electric field [Bai16a], in conceptual analogy to reference [Gar96]. Moreover, as these anisotropy torques are proportional to $\propto \sin\phi_0 \cos\phi_0$, they are only non-zero in the Γ_{24} transition phase, while their relative strength is maximal in the middle of the temperature interval between T_1 and T_2. The terms linear in the THz magnetic field component describe the excitation of the q-fm mode based on the Zeeman torque.
For the numerical simulations, the effective magnetic potential, $W(\phi)$, is calibrated by the experiment with bulk $TmFeO_3$. Additionally, an external magnetic field along the z-axis ($\alpha = 0$) of $\mathbf{B}_{\text{ext},0} = 150\,\text{mT}$ is included, which is compatible with the experimentally determined value. According to the experimental geometry, the THz electric field is aligned perpendicular to the crystallographic x-axis. Consequently, $E_{\text{THz,x}} = 0$ and $B_{\text{THz,y}} = B_{\text{THz,z}} = 0$. Moreover, as shown in reference [Bai16a], the spin dynamics in the high-field regime are dominated by the THz-induced nonlinear anisotropy torque. Thus, also the interaction of the spins with the THz magnetic field component, $B_{\text{THz,x}}$, which is oriented along the crystallographic x-axis, is neglected in the calculations. The equation of motion then reads

$$\begin{aligned} \ddot{\phi} - C^2\nabla^2\phi \;=\; & -\gamma_{\text{D}}\dot{\phi} + 4\omega_{\text{E}}\omega_{\text{A}}\cos\phi\sin\phi \times \left(\eta + \sin^2\phi\right) \\ & +\kappa\;\sin\phi\cos\phi\;\epsilon_0 n_{\text{sub}} c\alpha_{\text{eff}}\mathbf{E}^2_{\text{THz}} - \frac{H_{\text{D}}}{H_{\text{E}}}\gamma\omega_{\text{E}}\mathbf{B}_{\text{ext}}\sin\phi. \end{aligned} \tag{2.17}$$

Here, γ_{D} is the experimentally determined spin damping. The excitation by the crystal field transitions is modeled by both an impulsive and a displacive anisotropy torque, accounting for an increase of the angular velocity, $\dot{\phi}$, and a shift of the equilibrium spin angle, ϕ_0, respectively. The impulsive excitation is implemented by

the term proportional to the constant κ, which couples the spin dynamics to the instantaneous THz power density $\epsilon_0 n_{\mathrm{sub}} c \alpha_{\mathrm{eff}} \mathbf{E}^2_{\mathrm{THz}}$. Here, ϵ_0 is the vacuum permittivity, n_{sub} is the refractive index of $TmFeO_3$, c is the speed of light, and α_{eff} is the effective THz absorption coefficient [Zha16]. To account for the displacive term, a strong THz-induced excitation of the crystal field transitions is implemented, which leads to an increase of the population density $\Delta\rho(t)$ of the excited states of the Tm^{3+} ions. This is described by the excitation parameter $\eta = \frac{(\rho(T)+\Delta\rho(t))-\rho_2}{\rho_2-\rho_1}$, where $\rho(T)$, ρ_1, and ρ_2 are the equilibrium population densities of the crystal-field split states at the temperature T, T_1, and T_2, respectively. The THz-induced change of the population density leads to an abrupt change of the magnetic potential, $W(\phi)$, of the iron spins, resulting in a displacive anisotropy torque. Quantitatively, one calculates

$$\Delta\rho(t) = \Gamma \int_{-\infty}^{\infty} \frac{\epsilon_0 n_{\mathrm{sub}} c \alpha_{\mathrm{eff}}}{\hbar \omega_{\mathrm{CFT}}} \mathbf{E}^2_{\mathrm{THz}}(t') dt', \tag{2.18}$$

where Γ is a coupling parameter, $\hbar$ is Planck's constant, and ω_{CFT} is the resonance frequency of the electric dipole-active Tm^{3+} ground state transition [Koz90]. Finally, the term $C^2\nabla^2\phi$ accounts for the interaction between different magnetic domains of the sample, where C is the spin-wave velocity that sets the maximal speed of a domain boundary. In the orthoferrites, $C = 2{\cdot}10^6$ cm s^{-1}[Zve79, Che78]. Thus, on the ≈ 1 ps timescale of this experiment, the regions of the sample exposed to the THz fields of different strengths can be assumed to be practically non-interacting as the magnetic excitations travel a distance of 10 nm during this time. This distance is also much smaller than the characteristic spatial scale of the THz near-field of > 1 µm. Therefore the term $C^2\nabla^2\phi$ is neglected in the numerical simulations.

Figure 2.14b illustrates two typical spin trajectories obtained by solving equation (2.17) for two exemplary near-field transient extracted from the FEM calculations (see section 2.3) featuring different peak electric-field amplitudes. For a peak near field of $E_{\mathrm{NF}} = 6\,\mathrm{MV\,cm^{-1}}$, the spins carry out a coherent oscillation around ϕ_0 with a maximal excursion of $\Delta\phi = 15.8°$. A field of $E_{\mathrm{NF}} = 10\,\mathrm{MV\,cm^{-1}}$, in contrast, allows the spins to overcome the potential barrier at $t = 3.4$ ps, and relax into a new equilibrium position ϕ_1, which corresponds to a spin rotation by $\approx 90°$. Thereby, as soon as the spins leave the parabolic potential trough in the vicinity of their starting position $\phi_0 = -49.8°$, their motion is slowed down and defined by the potential

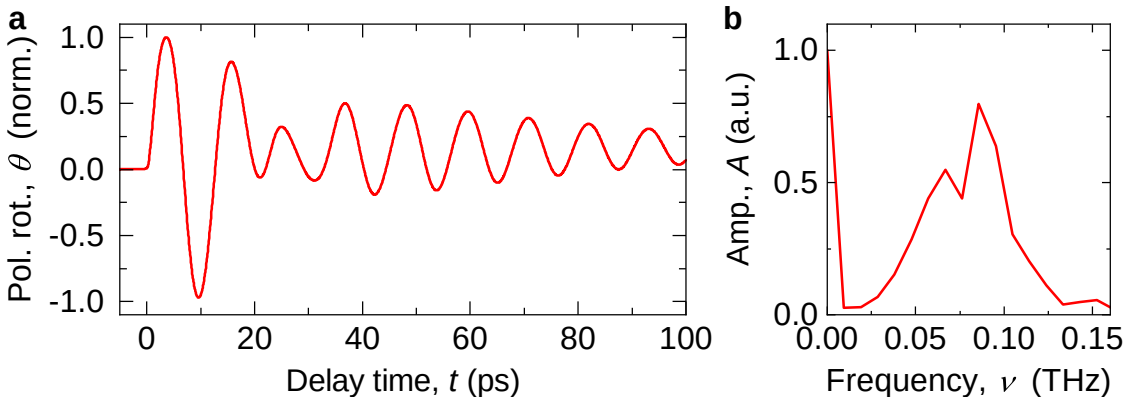

Figure 2.15 | Qualitative simulation of the beating signature. **a**, Polarization rotation calculated by superimposing the responses shown in Figure 2.14b, that is, spins oscillating in the equilibrium potential minimum at ϕ_0 (relative weight, 0.8) and spins driven into the neighboring local minimum at ϕ_1 (relative weight, 0.2). **b**, Amplitude spectra of the time-domain data shown in **a**.

curvature along the trajectory into the adjacent local minimum, $\phi_1 = 49.8°$. During this highly anharmonic motion, the spins acquire a characteristic phase relative to spins oscillating with a low amplitude around ϕ_0. At a delay of $t = 9.7\,\mathrm{ps}$ this phase amounts to $\approx 180°$. Once the spins have reached their maximum positive deflection, they oscillate back, which still drives them through anharmonic regions of the potential in the target valley around ϕ_1. Because of damping, however, they do not overcome the potential barrier a second time but rather stay in the new minimum. Owing to this enduring, strongly anharmonic motion, the spins accumulate even more phase retardation such that the red and blue trajectories in Figure 2.14b oscillate in phase again, around $t \approx 25\,\mathrm{ps}$.

To link these spin dynamics with the measured polarization rotation, the local dynamics of the spin deflection angle, ϕ, are calculated by solving equation (2.17) separately for each near-field cell using the corresponding THz near-field transient extracted from the FEM calculations (see paragraph 2.3). As confirmed by polarimetry, the THz-induced change of the magnetization leads to a rotation of the near-infrared probe polarization. A switch-off analysis shows that the Faraday rotation is almost exclusively caused by the ferromagnetic component of the magnetization, while the dynamics of the antiferromagnetic response plays a minor role. Consequently, the microscopic Faraday rotation is obtained by projecting the ferro-

magnetic vector, $\mathbf{F}(\phi)$, of each cell onto the wave vector of the near-infrared probe beam, $\mathbf{k}_{\mathrm{NIR}}$ (see Figure 2.14a). By simply superimposing the Faraday contributions of the two exemplary spin trajectories in Figure 2.14b, the pronounced beating feature at a delay time of $t \approx 25\,\mathrm{ps}$ of the magneto-optical signal (see Figure 2.15) can already be associated with the phase slip occurring during spin switching.
For a quantitative analysis, the overall polarization rotation is obtained by summing up all the locally induced Faraday signals from the entire probe volume, weighed by the intensity distribution of the probe beam. Thereby, in the direction parallel to the capacitor plates, a diameter of 6 µm (FWHM) is used, whereas, in the orthogonal direction, a diameter of 2 µm (FWHM) is utilized in order to account for diffraction effects near the capacitive plates. In the non-perturbative regime, the spin trajectory depends sensitively on the exact location in the near-field region of the antenna. Although calibrating electric near fields in excess of $\approx 10\,\mathrm{MV\,cm^{-1}}$ is challenging [Liu12, Lan14], the total polarization rotation is fairly robust against variations of the maximum near fields occurring in the close vicinity of the capacitive plates.
Figure 2.16a shows the calculated polarization rotations, θ, for $E_{\mathrm{THz}} = 0.4\,\mathrm{MV\,cm^{-1}}$ and $1.0\,\mathrm{MV\,cm^{-1}}$ as a function of the delay time, t. For the measurement with a far-field THz peak amplitude of $E_{\mathrm{THz}} = 0.4\,\mathrm{MV\,cm^{-1}}$, the best agreement (Figure 2.16a, blue curve) is obtained by using the experimentally determined spin dephasing rate $\gamma_{\mathrm{D}} = 45\,\mathrm{GHz}$, as well as the following fit parameters: $\omega_{\text{q-fm}}/2\pi = 88.7\,\mathrm{GHz}$, $\kappa = 3.58{\cdot}10^{8}\ \mathrm{m^2\,W^{-1}\,s^2}$, and $\Gamma = 2.49{\cdot}10^{10}\ \mathrm{m^3\,s}$. For the THz peak field amplitude of $E_{\mathrm{THz}} = 1.0\,\mathrm{MV\,cm^{-1}}$ (Figure 2.16a, red curve), some of the parameters are slightly adjusted to $\omega_{\text{q-fm}}/2\pi = 90.0\,\mathrm{GHz}$, $\kappa = 1.02{\cdot}10^{8}\ \mathrm{m^2\,W^{-1}\,s^2}$, and $\Gamma = 1.01{\cdot}10^{10}\ \mathrm{m^3\,s}$. Moreover, magnon-magnon scattering can effectively be accounted for by introducing a momentum-dependent damping of the spin system. The calculations quantitatively reproduce all experimental features, including the quasi-monochromatic magnon oscillation, for low fields (Figure 2.16a, blue curve), as well as the phase retardation of the first magnon oscillation period and the pronounced beating at $t \approx 25\,\mathrm{ps}$, at large THz fields (Figure 2.16a, red curve). In addition to that, the model unambiguously connects the asymmetric splitting of the q-fm resonance and the broad low-frequency components (Figure 2.16b) to THz-driven all-coherent spin switching.

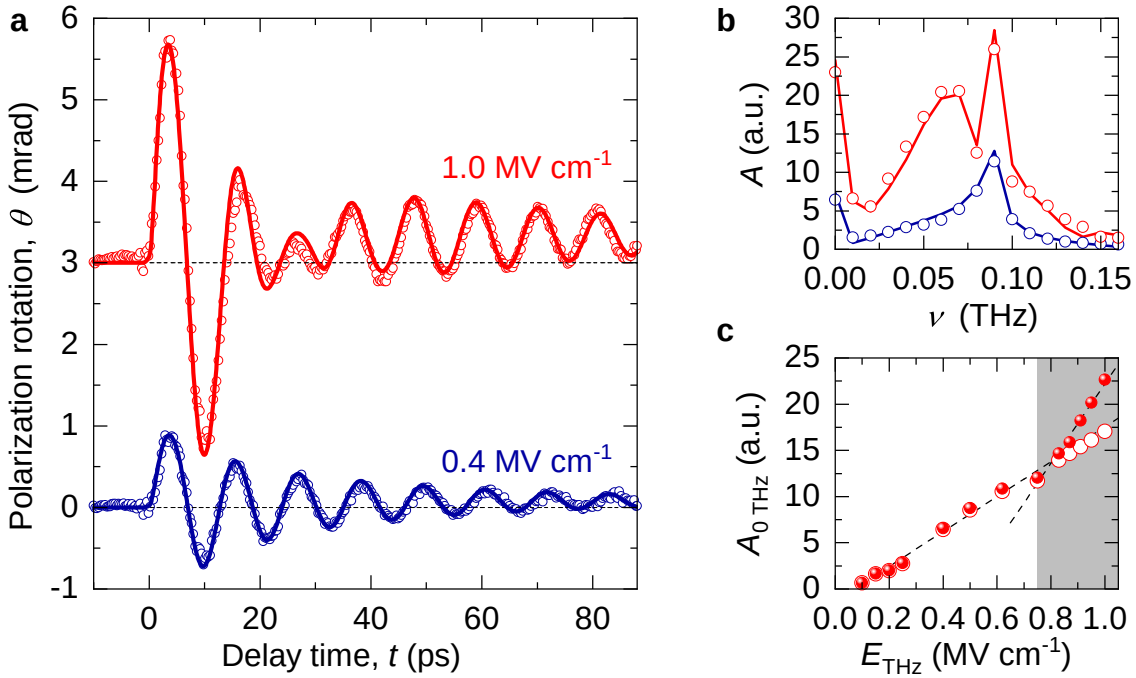

Figure 2.16 | Calculated THz-induced spin dynamics. **a**, Calculated polarization rotation, θ, in the antenna feed gap for an incident THz electric peak-field amplitude of $E_{\mathrm{THz}} = 0.4\,\mathrm{MV\,cm^{-1}}$ (dark blue curve) and $E_{\mathrm{THz}} = 1.0\,\mathrm{MV\,cm^{-1}}$ (red curve) as a function of the delay time, t, for a lattice temperature of $T = 83.0\,\mathrm{K}$, normalized to the experimental peak value. The experimental data are plotted as circles. **b**, Amplitude spectra of the time-domain data shown in **a**. **c**, Calculated scaling of the spectral amplitude of the long-lived offset, $A_{0\ \mathrm{THz}}$, for no misalignment (red circles) and a misalignment angle of the near-infrared $\mathbf{k}_{\mathrm{NIR}}$-vector out of the y-z-plane of 1.25° (red spheres). In the spin-switching regime ($E_{\mathrm{THz}} > 0.75\,\mathrm{MV\,cm^{-1}}$, gray-shaded area) the calculations reproduce the increased slope of $A_{0\ \mathrm{THz}}$ observed in the experiment (Figure 2.12c and figure 2.13b). Dashed lines, guides to the eye.

Figure 2.17 displays the results of a switch-off analysis considering three scenarios including the full calculation (solid lines), only the displacive (dashed lines), and only the impulsive contribution (dashed-dotted lines). For a THz field amplitude of $E_{\mathrm{THz}} = 0.4\,\mathrm{MV\,cm^{-1}}$, the sum of displacive and impulsive contributions approximates the full calculation. Conversely, the strong-field dynamics at $E_{\mathrm{THz}} = 1.0\,\mathrm{MV\,cm^{-1}}$ are only rendered correctly by the full calculation, which further corroborates the nonlinear character of the spin dynamics in this regime. In all cases, a purely displacive effect yields an exclusively positive magneto-optical signal

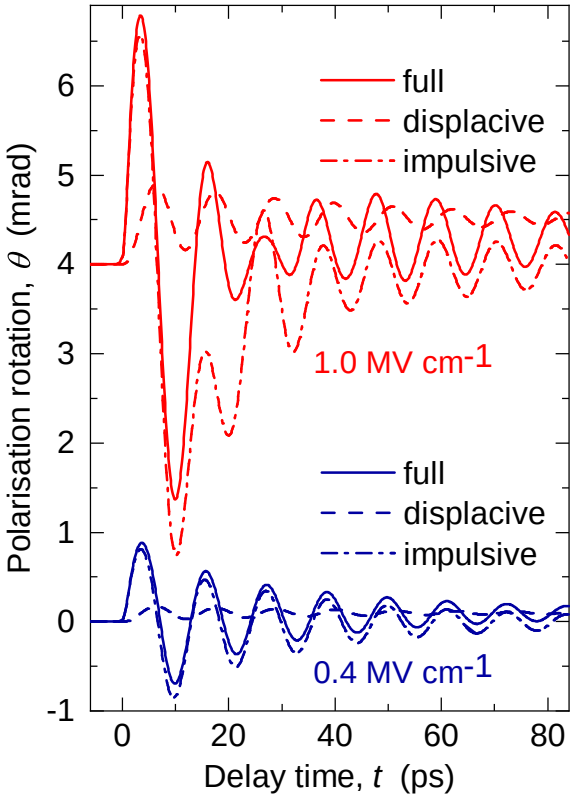

Figure 2.17 | Simulated magneto-optical response for different driving forces. Calculated polarization rotation, *theta*, expected from the antenna structures for a THz far-field amplitude of $E_{\mathrm{THz}} = 0.4\,\mathrm{MV\,cm^{-1}}$ (dark blue curves) and $E_{\mathrm{THz}} = 1.0\,\mathrm{MV\,cm^{-1}}$ (red curves). Calculations including only the displacive (dashed lines) or impulsive (dashed-dotted lines) anisotropy torque do not fit the experimental data. For the switch off analysis, the parameters, Γ, for the displacive and, κ, for the impulsive torque of the full calculation (solid lines) are used. The curves are offset and normalized to the experimental peak value.

and a non-zero signal offset, while the impulsive component is responsible for the strong oscillatory component.

The calculation also confirms that the switched spins can be directly read out. As seen in Figure 2.12 and Figure 2.13, increasing E_{THz} leads to a long-lived signal offset. This is caused by two distinct mechanisms: (i) THz excitation of Tm^{3+} ions slightly shifts the position of the potential minimum (Figure 2.14b, inset). (ii) A transfer of spins over the barrier can also change the net magneto-optical signal if $\mathbf{k}_{\mathrm{NIR}}$ is tilted out of the y-z-plane (Figure 2.16a). Assuming a tilt angle of 1.25°, all measured transients can be fitted in the time domain. For the corresponding fit parameters, $A_{0\,\mathrm{THz}}$ traces the experimental field scaling (Figure 2.12c), including the slow increase below the switching threshold of $E_{\mathrm{THz}} > 0.75\,\mathrm{MV\,cm^{-1}}$, and the steep slope above (Figure 2.16c, red spheres). In contrast, a calculation with identical fit parameters but a tilt angle of 0° yields a slow increase of $A_{0\,\mathrm{THz}}$ for all field strengths (see Figure 2.16c, red circles). From this comparison, the slow increase can be attributed to the shift of the potential minimum whereas the steep

slope observed for finite tilt angles can be directly related to the spin transfer over the barrier.

As the generalized sine-Gordon equation is solved separately for each near-field cell, it is also possible to visualize the local differences of the THz-induced magnetization dynamics in the antenna near field, with subcycle resolution. Figure 2.18 illustrates snapshots of the spatially resolved spin angle, ϕ, for three characteristic delay times, t (see "1", "2", and "3" in Figure 2.18a), and the maximum experimental THz far-field amplitude of $E_{\mathrm{THz}} = 1.0\,\mathrm{MV\,cm^{-1}}$. The THz-induced ballistic spin motion starts out with the largest spin deflection near the capacitive metal plates, where the field enhancement is maximal. Already after a delay time of $t = 1.3\,\mathrm{ps}$ the first spins cross the potential barrier, which separates the two stable states centered at $\phi_0 = -49.8°$ and $\phi_1 = 49.8°$, respectively (see also Figure 2.3b). The critical electric near field, necessary for spin switching is given by $E_{\mathrm{NF}} = 7.8\,\mathrm{MV\,cm^{-1}}$.

Irrespective of the exact peak electric near field, the THz-induced spin dynamics can be divided into two characteristic regimes:

(i) For a THz electric near field of $E_{\mathrm{NF}} < 7.8\,\mathrm{MV\,cm^{-1}}$, the spins perform an almost harmonic oscillation around their initial spin orientation, ϕ_0 (see also Figure 2.14b, blue trajectory).

(ii) For a THz electric near field exceeding the threshold of $E_{\mathrm{NF}} = 7.8\,\mathrm{MV\,cm^{-1}}$, the spins are driven over the barrier into the adjacent potential minimum, where they perform an anharmonic motion and relax into the new stable state ϕ_1 (see also Figure 2.14b, red trajectory).

As shown in Figure 2.18b-d, the inhomogeneous electric-field enhancement in the antenna near field entails that most of the spins close to the capacitative plates and the sample surface are transferred to a new stable state, whereas below $z = -1.0\,\mu\mathrm{m}$ the threshold for switching is not reached. Moreover, the phase between the different spin trajectories constantly changes with time. Thereby, after $t = 9.7\,\mathrm{ps}$ most of the spins, that reside in different potential minima, are oscillating out of phase (see Figure 2.18b). As a consequence, one can find a global minimum in the calculated polarization rotation, θ (Figure 2.18a, label "1"). At $t = 27.2\,\mathrm{ps}$, the spins have settled in their respective potential minima and a domain structure has formed (see Figure 2.18c). Due to the phase retardation that the switched spins gain during

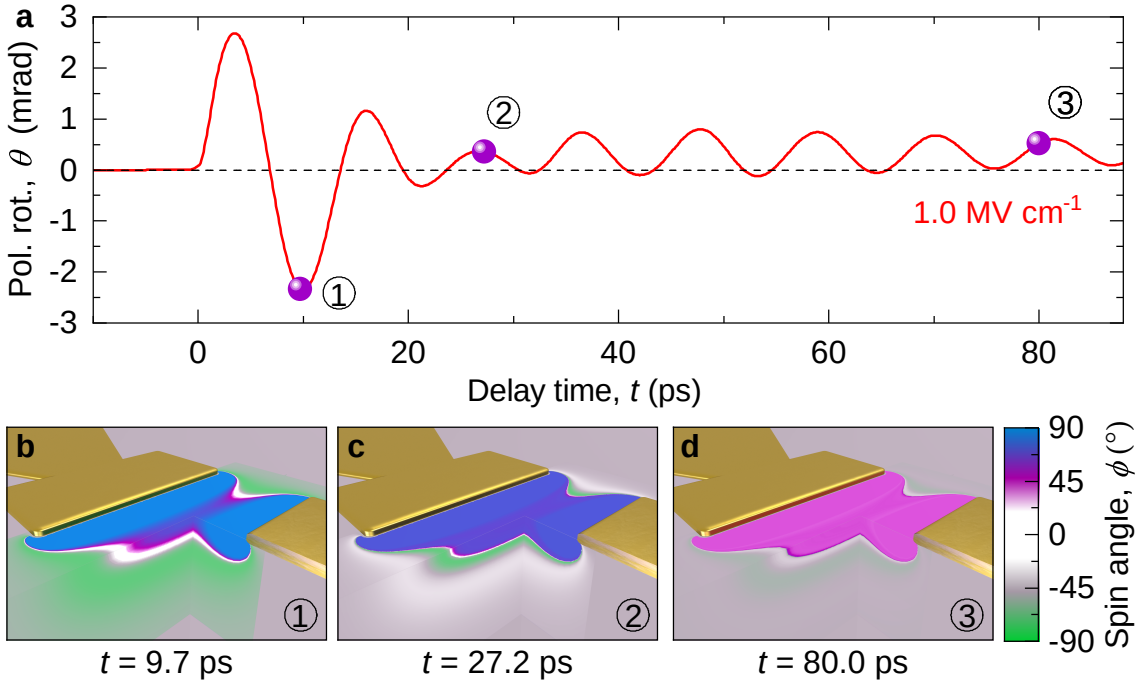

Figure 2.18 | Time-resolved spin switching. **a**, Calculated polarization rotation, θ, in the antenna feed gap for an incident THz electric peak-field amplitude $E_{\mathrm{THz}} = 1.0\,\mathrm{MV\,cm^{-1}}$ as a function of the delay time, t, normalized to the experimental peak value. The violet spheres labeled with "1", "2", and "3" indicate the delay times at which the snapshots of the spin dynamics in panels **b**, **c**, and **d** are taken, respectively. **b**, **c**, **d**, Spin angle, ϕ, in the three principal planes x-y, x-z, and y-z in the near field of the bowtie antenna for different time steps after the excitation by a THz pulse with a peak electric far-field amplitude of $E_{\mathrm{THz}} = 1.0\,\mathrm{MV\,cm^{-1}}$. The THz-induced spin dynamics lead to a permanent reorientation of the magnetization in a large near-field volume (violet volume).

their anharmonic motion in their new potential minimum ϕ_1 (see also Figure 2.14b, red trajectory), the two spin sub-ensembles are oscillating in phase now, which in turn results in the characteristic beating feature in the polarization rotation signal observed around $t \approx 25\,\mathrm{ps}$ (Figure 2.18a, label "2"). For even longer delay times $t > 80\,\mathrm{ps}$ (Figure 2.18d), the two domain borders sharpen even further as the coherent spin precessions have decayed within $\approx 40\,\mathrm{ps}$. On a much longer timescale, the spins tunnel back to the equilibrium orientation (not shown). In the experiment, this final relaxation step was enforced by the external magnetic bias field, $\mathbf{B}_{\mathrm{ext}}$.

2.6 Subcycle ballistic spin control in tailored magnetic potentials

Based on the theoretical model described in the previous section, the experimentally observed characteristic phase flip, the asymmetric splitting of the q-fm magnon resonance, and the long-lived offset of the Faraday signal are identified as hallmarks of coherent spin switching into adjacent potential minima. Beyond that, the combination of the numerical FEM calculations of the local near-field enhancement in the custom-tailored antenna structures with the efficient electric-field control of the magnetic anisotropy in $TmFeO_3$ provides superior insights into the microscopic magnetization dynamics, that guide the spins throughout the entire phase space. Based on this microscopic understanding of the THz-induced spin dynamics, the spin trajectory can now be shaped by tailoring the magnetic potential, while keeping the peak THz far-field amplitude constant at $E_{\mathrm{THz}} = 1.0\,\mathrm{MV\,cm^{-1}}$.
As a first control parameter, the crystal temperature is lowered to $T = 82.5\,\mathrm{K}$, where the barrier height, w, separating the two stable spin states ϕ_0 and ϕ_1, is slightly increased (Figure 2.19a). Consequently, the switching dynamics are decelerated and the beating signature in the experimentally detected Faraday rotation signal, θ, is delayed to $t = 45$ ps (Figure 2.19e, red curve). Meanwhile, the spectrum remains qualitatively similar (Figure 2.19f, red curve). The barrier height can also be raised by rotating the external magnetic bias field, $\mathbf{B}_{\mathrm{ext}}$, by an angle $\alpha = 15°$ about the optical axis (see Figure 2.10a and Figure 2.19b), resulting in a shift of the beating feature to a delay time of $t = 55\,\mathrm{ps}$ (Figure 2.19e, dark red curve). Thereby, the potential shoulder at $\phi = -115°$ is lowered (Figure 2.19b), which enables large-amplitude oscillations throughout a slightly wider potential trough, causing a weak red-shift of the spectrum. The q-fm magnon resonance is now centered around $\omega_{\text{q-fm}} = 0.085$ THz (see Figure 2.19f, dark red curve). For $\alpha = 60°$ (Figure 2.19c), the dynamics are strongly altered (Figure 2.19e, f, brown curves). After the spins are driven up the potential barrier at $\phi = 0°$ during the first half cycle, the non-switching spins oscillate back through the wide potential minimum that is extended by the shoulder at $\phi = -115°$. This results in a strong red-shift of the q-fm magnon center frequency to $\omega_{\text{q-fm}} = 0.050\,\mathrm{THz}$. On the potential shoulder, the projection $\mathbf{k}_{\mathrm{NIR}} \cdot \mathbf{F}(\phi)$ drops below its initial value at ϕ_0 and becomes negative for $\phi < -90°$

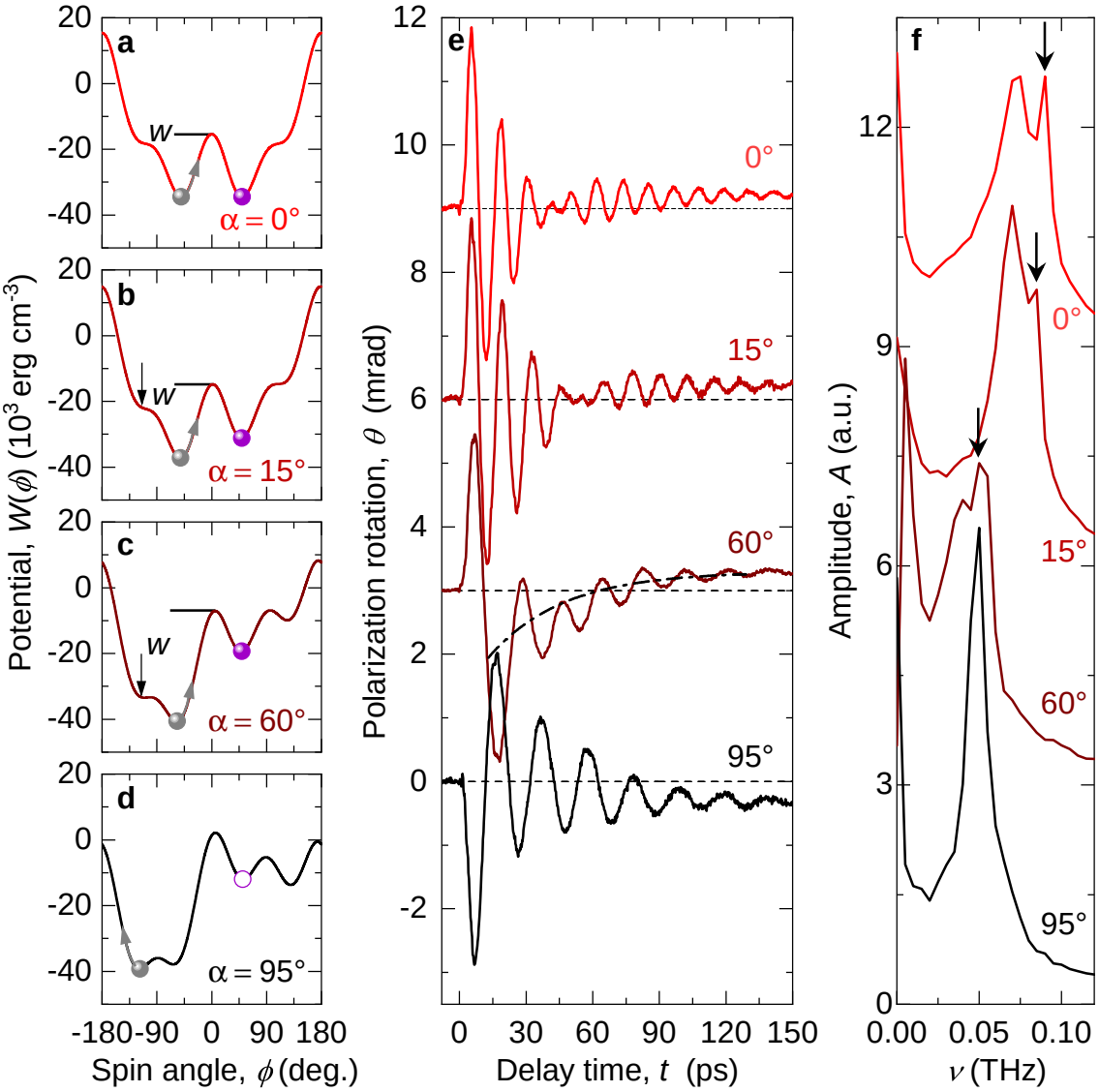

Figure 2.19 | Ballistic navigation of spins. a-d, Magnetic potential, $W(\phi)$, for a lattice temperature of $T = 82.5\,\mathrm{K}$ and various orientations α of the static external magnetic bias, $\mathbf{B}_{\mathrm{ext}}$. w, potential barrier height relevant for switching; black arrows, potential shoulder associated with the red-shift. Gray spheres and arrows, initial spin orientation and direction after excitation; violet spheres, final orientation of switched spins. **e**, Polarization rotation, θ, as a function of the delay time, t, for the potentials shown in **a-d** and a THz peak far-field amplitude of $E_{\mathrm{THz}} = 1.0\,\mathrm{MV\,cm^{-1}}$. Dashed-dotted curve, transient negative polarization rotation. **f**, Amplitude spectra of the time-domain data shown in e. The black arrows mark the computed center frequencies.

(see Figure 2.20a), which leads to a transient negative offset of the Faraday signal (Figure 2.19e, dashed-dotted line) until the oscillations of the unswitched spins have decayed in the starting local potential minimum. Still, a sufficiently large fraction of spins reaches the target valley (Figure 2.19c, violet sphere), leading to a beating feature. Finally, $\alpha = 95°$ sets a new starting position and direction of acceleration (Figure 2.19d and Figure 2.20b, gray sphere and arrow), which causes a reversal of the transient polarization rotation signal and offset (Figure 2.19e). The wide potential minimum leads to a reduced center frequency reproduced by calculating the single spin dynamics (Figure 2.19f, black arrows). The large barrier to the neighboring valley (Figure 2.19d, violet circle) inhibits switching completely and no beating is observed.

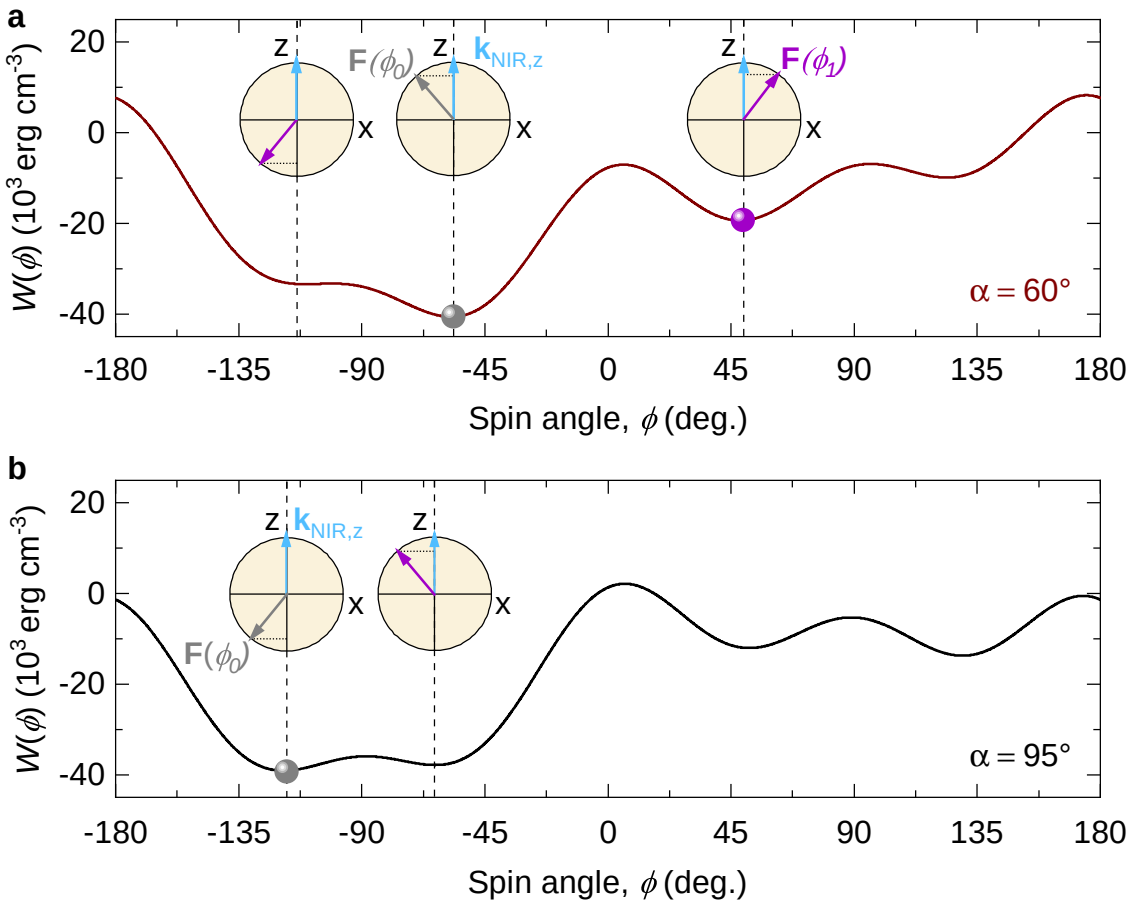

Figure 2.20 | Faraday signal for spin dynamics in different magnetic potentials. **a**, Magnetic potential, $W(\phi)$ (brown curve), for a lattice temperature of $T = 82.5\,\mathrm{K}$ and an angle of $\mathbf{B}_{\mathrm{ext}}$, $\alpha = 60°$, as shown in Figure 2.19c. Gray (violet) sphere, initial (switched) spin state. Insets: projection (gray dotted horizontal lines) of the magnetization $\mathbf{F}(\phi)$ (arrows) onto the near-infrared wave vector, $\mathbf{k}_{\mathrm{NIR,z}}$ (light blue arrow), for different angles, ϕ. For $\phi < \phi_0$, the projection drops below its initial value and becomes negative for $\phi < -90°$, causing a negative transient Faraday signal (Figure 2.19e). For $\phi_0 < \phi < \phi_1$, $\mathbf{k}_{\mathrm{NIR}}{\cdot}\mathbf{F}(\phi) > \mathbf{k}_{\mathrm{NIR}}{\cdot}\mathbf{F}(\phi_0)$, resulting in the positive initial half cycle of the Faraday rotation signal (Figure 2.19e). **b**, Magnetic potential, $W(\phi)$, for $\alpha = 95°$ (black curve) as shown in Figure 2.19d. For $\phi < \phi_0$, the initial spin deflection leads to $\mathbf{k}_{\mathrm{NIR}}{\cdot}\mathbf{F}(\phi) < \mathbf{k}_{\mathrm{NIR}}{\cdot}\mathbf{F}(\phi_0)$, causing a negative onset of the first oscillation period (Figure 2.19e, black curve).

2.7 Prospects of THz-driven minimally dissipative spin memories

In this chapter, coupling spins in $TmFeO_3$ with the locally enhanced THz electric field of custom-tailored antenna structures allows for the first time to observe ultrafast THz-induced spin switching directly in the time domain. This achievement opens up a qualitatively new regime of ultrafast all-coherent spin control throughout the entire phase space, which manifests in a number of unique hallmarks in the optical signal (see paragraph 2.4). These include the occurrence of a phase flip analogous to the famous Rabi flops in a two-level system, anharmonic changes of the spin precession frequency during the first oscillation half cycle, a splitting of the magnon resonance, similar to Rabi flopping, and a long-lived offset of the Faraday rotation, which shows a characteristic threshold to overcome the potential barrier and reads out the switched magnetization state.

To put this fundamentally new concept of THz-driven all-coherent control of the

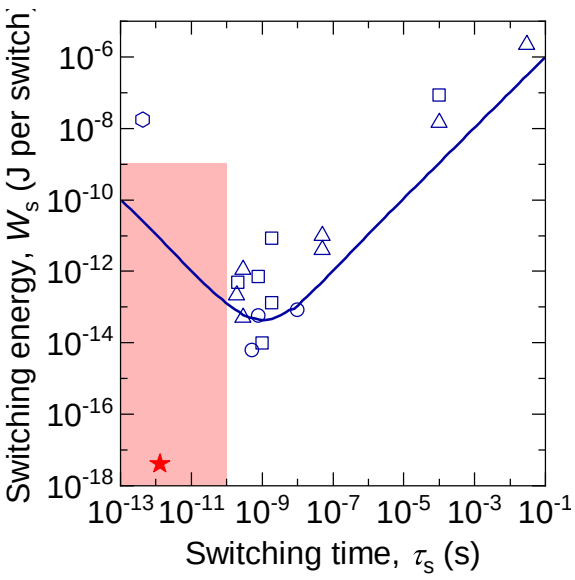

Figure 2.21 | Figures of merit of all-optical switching schemes. Summary of selected switching times, τ_s, and energies, W_s, of opto-magnetic devices based on magnetic tunnel junctions (hexagon) and electrically switchable spin valves using STT (triangles), SOT (squares) and electric-field-induced switching (circles). The red star indicates the calculated results for THz-driven spin switching in $TmFeO_3$ reported in this chapter. Blue solid line, calculated switching energy for STT switching with a characteristic switching time of $t_c = 1\,\text{ns}$ and a static switching energy of $W_c = 10\,\text{fJ}$ [Kim19]. Red-shaded area, desired specifications for future opto-magnetic technologies. Adapted from [Kim19].

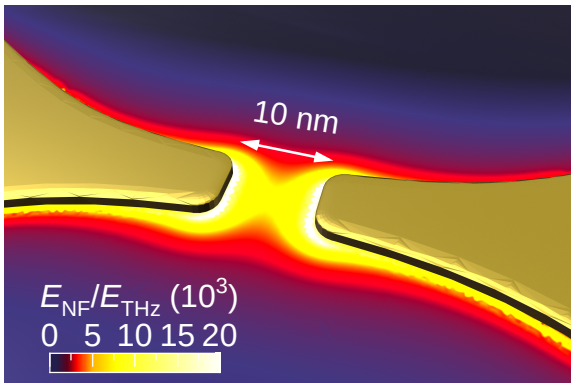

Figure 2.22 | Electric near field of a THz nanoantenna. Enhancement factor $E_{\mathrm{NF}}/E_{\mathrm{THz}}$ of the near-field peak amplitude, E_{NF}, compared to the THz electric far field, E_{THz}, calculated by finite-element-method simulations for a real THz waveform in the near field of an antenna structure with a feed gap of 10 nm. Assuming a switching threshold of $\approx 10\,\mathrm{MV\,cm^{-1}}$, a far-field amplitude of only $1\,\mathrm{kV\,cm^{-1}}$ is sufficient to drive coherent spin switching by 90° in the center of the antenna structure.

electron's spin in relation with already existing all-optical switching schemes and opto-magnetic devices it has to be evaluated concerning the three technological most important figures of merit: the switching speed, the accompanying dissipation, and the scalability [Kim19, Ved20]. Figure 2.21 gives an overview of the reachable switching times, τ_{s}, and the corresponding switching energies, W_{s}, per switch for selected optically switchable magnetic tunnel junctions and spin valves. Thereby, spin-transfer torque, spin-orbit torque, and electric-field-induced switching (see Figure 2.21, blue symbols) are included in the consideration [Kim19]. The results indicate that at long timescales, the switching energy scales linearly with the switching time. For timescales of $\tau_{\mathrm{s}} < 1\,\mathrm{ns}$, however, faster switching comes with a significant increase of the dissipated energy. This trend is in agreement with the calculated switching energy for spin transfer torque switching (see Figure 2.21, blue solid line), which follows the expression $W_{\mathrm{s}}(\tau_{\mathrm{s}}) = W_{\mathrm{c}}\left(2 + \frac{\tau_{\mathrm{s}}}{t_{\mathrm{c}}} + \frac{t_{\mathrm{c}}}{\tau_{\mathrm{s}}}\right)$, where W_{c} is the static switching energy and t_{c} is the characteristic timescale for switching dynamics [Kim19].

From the numerical calculations of the THz-induced spin dynamics (see section 2.5) a switching time of only $\tau_{\mathrm{s}} = 1.3\,\mathrm{ps}$ can be extracted for the highest THz electric near-field amplitudes. Nonetheless, in this specific implementation of a THz-driven anisotropy torque, one can estimate that already the absorption of approximately one THz photon energy per spin suffices for switching (see Appendix C). Moreover, the energy dissipation in the spin system is even smaller. To overcome the potential

barrier, which separates two neighboring stable states, only an energy on the order of 1 µeV per spin is necessary. This scheme is, thus, highly scalable. Future storage devices based on this THz-driven switching mechanism could also exploit the excellent spatial definition of custom-tailored antenna structures to switch magnetic bits of a diameter of only 10 nm. As shown in Figure 2.22, such optimized antennas with nanoscale gaps provide field enhancement factors of 10^4 and more and may be driven by all-electronic on-chip THz sources [Sen18]. The switching energy for a bit of the size 10 nm × 10 nm × 10 nm only amounts to $W_\mathrm{s} = 4.12\,\mathrm{aJ}$, which is orders of magnitude lower as compared to the other ultrafast switching schemes (see Figure 2.21, red star). Owing to the absence of magnetic stray fields, these cells could be densely packed, similar to vortex core structures in ferromagnetic thin films [Van06]. Furthermore, the readout of the spin state could be combined with spintronic approaches [Jun16, Ole18].

The results presented in this chapter not only provide a solution to a key challenge of femtomagnetism, which is ultrafast spin switching close to the Landauer limit, they may also be the key to practical implementations of novel energy efficient spin memories. As the THz light pulses operate at the intrinsic energy scales of the magnetic excitations, such spin memories could operate at THz clock rates, and ultimately low dissipation, whereas nanogap antennas simultaneously allow very high bit densities.

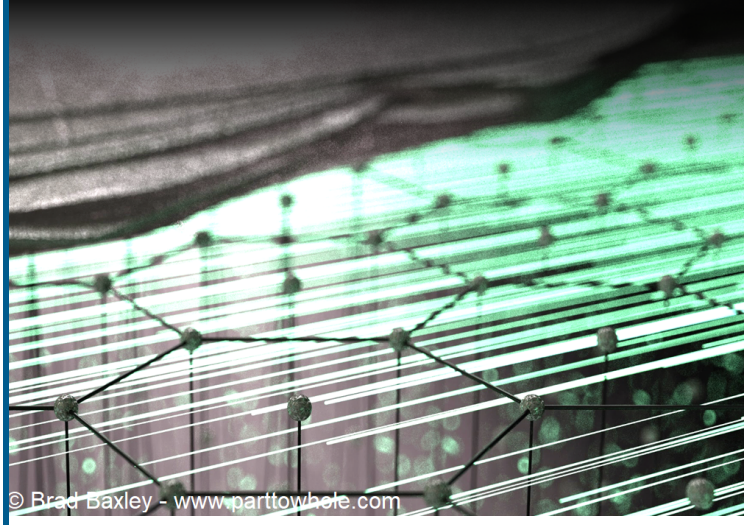

3

Ballistic, lightwave-driven electron dynamics in topological insulators

The fact that the speed of processors has stagnated around 3 GHz for more than a decade is a clear indication that, on the long run, contemporary digital electronics based on metal-oxide-semiconductor field-effect transistors (MOSFETs) may not be able to fulfill the needs of modern challenges like 'Big Data' or the 'Internet of Things'. Consequently, future high-speed information processing technology cannot be a simple improvement of already existing technology - it requires disruptive innovations concerning both the general way how information is processed as well as the underlying material platform [Mar14, Sha20].

In the 1960s, the development of mode-locked lasers pushed the research field of ultrafast optical spectroscopy to unprecedented timescales [Sha99]. In the following decade, optical techniques have been developed that amplify and compress laser pulses [Str85, Die06], generate different frequencies by nonlinear mixing schemes [Boy03], or attosecond laser pulses by non-perturbative processes [Cor07]. This enables the observation and control of elementary dynamics of solids such as magnons [Kam11, Bai16a, Bai16b, Sch19], phonons [Por14] or plasmons [Hub17] on their intrinsic timescale of a few femtoseconds [Ros02]. Just recently, it has even been

possible to resolve the time delay of electron emission in the photoelectric effect on the zeptosecond timescale [Gru20].

Besides that, intense electromagnetic light fields themselves can be used to drive ultrafast carrier dynamics in solids [Bra00, Sch13, Sch14]. Harnessing the oscillating electric field of light as an alternating voltage bias to control electron motion inside a solid is at the heart of the research field known as *lightwave electronics* [Sch14, Vam14, Hig14, Hoh15, Gar16, Lan17, Liu17, Yos17, Lan18b, Rei18b]. In particular, phase-locked electromagnetic single- or few-cycle waveforms in the THz spectral range are a versatile tool to control the translational motion of crystal electrons with a temporal resolution much shorter than one single oscillation period of the carrier wave [Hub01, Kam13, Hoh15]. As THz photon energies are well below typical electronic resonances in solids [Kam13], these phase-stable electromagnetic waveforms can be used as precisely adjustable bias voltages. As their electric field is only applied for a few femtoseconds, THz electric peak field amplitudes on the order of atomic binding potentials can be reached without destroying the sample [Sel08]. In this high-field regime, exciting new coherent quantum phenomena like field-induced phase transitions [Liu12], coherent control of dark excitons [Lei08], or interband Rabi flopping [Müc01, Jun12] are observed.

Moreover, lightwave electronics might offer a way to increase computing capabilities by a massive scale-up of clock frequencies. Utilizing the carrier wave of light as an a.c. bias field to switch on and off electric currents would facilitate electronic devices at optical clock rates. The finite band mass and ultrafast scattering in conventional dielectrics, however, limit the velocity and the excursion of the accelerated electrons. Thus, such lightwave electronic devices would still suffer from high energy losses. The material class of topological insulators bears the potential to solve this dilemma. While these novel materials are insulating or semiconducting in their bulk form, they feature conductive states on the surface with a Dirac-like energy dispersion [Zha09, Xia09], and rather long scattering times compared to sub- or few-femtosecond timescales usually present in semiconductors [Has10, Rei18b].

In this chapter, the electric field of intense single- and few-cycle THz waveforms is used to ballistically drive Dirac electrons in the surface band of the topological insulator bismuth telluride (Bi_2Te_3), while the dynamics is simultaneously traced by time- and angle-resolved photoemission spectroscopy (ARPES), with subcycle

resolution. The corresponding inertia-free surface currents reach peak densities of $28.3\,\mathrm{A\,cm^{-1}}$ with ballistic mean free paths of several nanometers. By applying THz electric field amplitudes in excess of $1\,\mathrm{MV\,cm^{-1}}$, even strong light-matter interaction, involving lightwave-driven intraband and interband dynamics, can be resolved directly in the band structure and on a subcycle timescale. For the first time, this allows for the visualization of the microscopic electron dynamics that lead to non-perturbative nonlinearities such as high-harmonic generation in solids and paves the way to practical, topological-insulator-based lightwave electronic devices operating at optical clock rates.

3.1 Lightwave-driven quasiparticle dynamics in semiconductors

The way how a material responds to an external perturbation by a light field depends critically on the frequency and on the intensity of the electromagnetic wave. In general, once light is incident on a solid, its electric and magnetic field components exert forces on the electrons and on the ion cores, which lead to a polarization of the material [Boy03]. In the optical spectral region, the electric dipole interaction is much stronger than the magnetic one. Thus, the optical response is dominated by the Coulomb force

$$\mathbf{F}_\mathrm{c}(t) = e \cdot \mathbf{E}(t), \tag{3.1}$$

driven by the electric field component $\mathbf{E}(t)$ of the lightwave [Kam13]. For small electron displacements within the atomic Coulomb potential landscape, the material response scales linearly with the applied electric field and, consequently, is dominated by the refractive index of the material [Boy03, Hec17]. Yet, the development of intense ultrashort laser sources opened up a completely new playground of light-matter interaction. Without damaging the material, electric fields that can compete with the inner atomic binding potentials of $E_\mathrm{a} \approx 1\,\mathrm{V\,\mathring{A}^{-1}}$ can be applied for a short amount of time [Die06]. As a result, carrier dynamics can be studied and controlled on ultrashort timescales [Sch13, Lan16, Rei18b], and even field-induced non-perturbative nonlinear optical phenomena such as high-harmonic generation can be observed [Chi01, Ghi11, Sch14, Hoh15, Lan17].

3.1.1 Light-matter interaction in the strong-field regime

Whereas for low electric field amplitudes it is appropriate to describe light-matter interaction in a photon-like picture, in the so-called strong-field regime, where the strength of the electric light field approaches the magnitude of intra-atomic potentials, the lightwave is rather interpreted as a classical, quasi-static bias field [Kel65]. A well-established figure of merit that helps to separate these two regimes of multi-photon processes and field-driven effects is the Keldysh parameter [Kel65]

$$\gamma = \omega \frac{\sqrt{m_\mathrm{e} E_\mathrm{gap}}}{eE_0}, \tag{3.2}$$

which relates the maximum electric field amplitude, E_0, and the angular frequency, ω, of the incident lightwave to the electronic resonance, E_gap, of the material. Here, m_e and e are the electron's mass and charge, respectively.

For a Keldysh parameter much greater than unity, $\gamma \gg 1$, the ponderomotive energy that the electron gains during lightwave acceleration is smaller than the resonance energy. Thus, charges can only be excited across the band gap by absorbing one or more photons simultaneously. In this scenario, which occurs for high frequencies and low electric fields, the light-matter interaction has to be described as a multi-photon process.

Conversely, for low frequencies and high electric peak fields, $\gamma \lessapprox 1$. In this regime, the lightwave can be seen as a classical external bias field that spatially distorts the potential landscape and field-driven effects taking place on a subcycle scale dominate. As a result, electrons can gain sufficient energy in the electric field to overcome E_gap and tunnel through the forbidden band gap into empty states of the conduction band. This phenomenon is known as Landau-Zener tunneling [Zen34, Kel65].

While the electronic interband resonances of typical semiconductors are on the order of a few electron volts [Gru10], electromagnetic radiation with a low center frequency is required to obtain a Keldysh parameter significantly smaller than unity. Thereby, in particular intense lightwaves in the THz spectral window with photon energies of only a few meV are ideally suited to drive strong-field processes in a solid [Kam13]. Even in the vicinity of an external electric bias field, however, the electron motion is

also significantly affected by the material itself. Due to the periodicity of the crystal lattice and the interaction with all other charged particles in the solid, the electron wavefunction cannot simply be described by a plane wave as it is the case for a free electron in vacuum. In a solid, the electron wavefunction also obeys the crystal periodicity and can be described by delocalized Bloch waves of the form [Blo29]

$$\Psi_{\mathrm{n},\mathbf{k}} = u_{\mathrm{n},\mathbf{k}}(\mathbf{r}) \cdot \mathrm{e}^{i\mathbf{k}\cdot\mathbf{r}}, \tag{3.3}$$

where n denotes the band index, $\mathbf{k}$ the wave vector and $\mathbf{r}$ the position of the electron in real space. These Bloch waves consist of a lattice-periodic part, $u_{\mathrm{n},\mathbf{k}}(\mathbf{r})$, and a plane wave. The corresponding eigenstates, $E_{\mathrm{n}}(\mathbf{k})$, of the system form continuous energy bands known as the band structure of the material [Gro18]. Note, that $\mathbf{k}$ indeed describes the motion of electrons in the solid, owing to the translational symmetry of the crystal lattice, however, $\hbar\mathbf{k}$ is not the actual electron momentum, but the so-called crystal momentum.
Also the shape of the energy band influences the response of the carriers to the external electric field. More precisely, the real space velocity, $\mathbf{v}_{\mathrm{n}}$, of the electron within the band n is directly linked to the energy dispersion of the band by the group velocity [Blo29, Zen34]

$$\mathbf{v}_{\mathrm{n}} = \frac{1}{\hbar}\,\nabla_{\mathbf{k}} E_{\mathrm{n}}(\mathbf{k}). \tag{3.4}$$

Here, $\hbar = h/2\pi$ is the reduced Planck constant. For a given wave vector $\mathbf{k}$, the electron moves with a constant velocity $\mathbf{v}_{\mathrm{n}}$, even if no external electric field is applied. Yet, in conventional undoped semiconductors, the highest occupied band, the so-called valence band, is completely filled with electrons, whereas the lowest unoccupied band, the conduction band, is completely empty. Thus, in equilibrium, there are no mobile electrons that contribute to an electric current. Moreover, even if electrons are excited across the band gap, the states in the conduction band are symmetrically occupied, which cancels a collective charge transport.
In order to drive a charge current, an external electric field has to be applied, which then generates an imbalance of occupied states with positive and negative wave vectors. This acceleration of the crystal electrons is best described in reciprocal

space by Bloch's acceleration theorem [Blo29]:

$$\hbar \frac{\mathrm{d}\mathbf{k}}{\mathrm{d}t} = -e\ \mathbf{E}(t). \tag{3.5}$$

The electric field, $\mathbf{E}(t)$, changes the crystal momentum, $\mathbf{k}$, moving the electrons continuously through the band structure (see Figure 3.1a). Once the electrons reach the edge of the Brillouin zone, the Bloch wave gets Bragg-reflected and enters the unit cell from the other side again. Without scattering, the electrons could continue their motion and repeatedly traverse the Brillouin zone (see Figure 3.1a, blue and red arrows). This periodic movement occurring both in reciprocal as well as in real space is known as Bloch oscillations [Blo29, Zen34]. For a solid featuring a cubic unit cell with a lattice constant of a, the period of the Bloch oscillation is given by [Zen34]

$$\tau_\mathrm{B} = \frac{h}{eE_\mathrm{ext}a}. \tag{3.6}$$

Thus, a constant electric field E_ext can lead to an oscillating electron motion, that can serve as a source of electromagnetic radiation [Lar97] at the frequency $\nu_\mathrm{B} = \tau_\mathrm{B}^{-1}$. As a result, Bloch oscillations have been proposed as an essential part of the generation mechanism of high-order harmonics in solids [Gol08, Gol11]. Yet, Bloch oscillations can cause high-harmonic generation only if the external electric field bias is strong enough to non-resonantly excite a substantial amount of electrons from the valence band into the initially empty conduction band. Furthermore, this lightwave-driven interband polarization that is mediated by the dipole matrix element d_cv (see Figure 3.1b) can serve as source for radiation as well [Gol08, Gol11, Sch14, Hoh15].
For quite some time it had generally been assumed, that Bloch oscillations could never be observed in bulk semiconductors. The reason for that is the rapid Coulomb scattering of dense many-body electron systems in semiconductors, which is on a timescale of only a few femtoseconds [Bec88, Lei99, Vu04]. To reach the edge of the Brillouin zone before the electrons scatter and destroy the coherence of the system, one would have to apply d.c. electric fields that exceed dielectric breakdown voltages of conventional semiconductors. Thus, for many years, the quantum mechanical phenomenon of Bloch oscillations could only be observed in artificial periodic structures like semiconductor superlattices [Fel92, Was93] or superconduct-

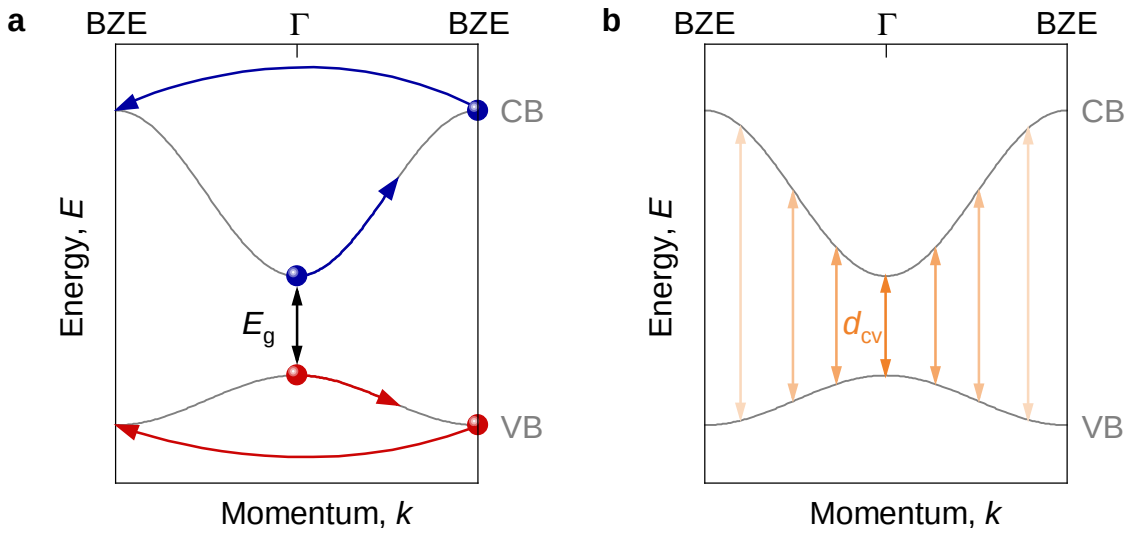

Figure 3.1 | Lightwave-driven intraband acceleration and interband excitation in a solid. **a**, Applying an external electric field leads to the acceleration of electrons (blue sphere) and holes (red sphere) through the conduction band (CB) and valence band (VB), respectively. At the edge of the Brillouin zone (BZE), the carriers get Bragg-reflected and Bloch oscillations occur. E_g, band gap separating valence and conduction band. **b**, In the strong-field regime, an external applied light field can also induce non-resonant excitations from the valence band (VB) to the conduction band (CB) (orange arrows). The transitions are mediated by the dipole matrix element, d_{cv}, and can occur at every point in the Brillouin zone, where d_{cv} is non-zero.

ing Josephson junction arrays [Del03]. The situation changed, however, since it is possible to generate intense THz pulses with peak electric fields in excess of $108\,\mathrm{MV\,cm^{-1}}$ [Sel08]. With a Keldysh parameter still smaller than unity, these intense low-frequency waveforms drive large electron excursions in momentum space within only a few femtoseconds before scattering occurs. As a consequence, a dielectric breakdown can be avoided although the material is exposed to atomically strong electric peak fields. Moreover, owing to the low photon energies, resonant absorption in the system is strongly suppressed, which significantly limits the energy dissipation. In particular, intense, single-cycle or few-cycle THz pulses with an inherently stable carrier-envelope phase facilitated the control of low-energy elementary excitations in solids [Kam13, Sch19] and possess the potential for the observation of many other elusive coherent phenomena [Sal19, Jun20]. For THz electric fields in excess

of $1\,\mathrm{MV\,cm^{-1}}$ e.g. a ballistic charge transport through a significant fraction of the Brillouin zone of a bulk semiconductor is possible [Kue10]. Thus, the oscillating electric field of intense THz waveforms is the ideal tool for lightwave electronics [Ghi11, Sch14, Vam14, Hig14, Hoh15, Lan16, Lan17, Yos17, Haf18].

3.1.2 THz lightwave acceleration in semiconductors

An essential process in strong-field light-matter interaction is the purely field-driven off-resonant excitation of carriers from one energy band to another [Bra00]. In bulk semiconductors, this process can generate mobile electrons in the conduction band, which can subsequently be accelerated by the lightwave (see Figure 3.1). Thereby, the intraband acceleration and interband polarization are not only simultaneously driven and continuously modified by the lightwave [Ros02], they are also closely intertwined with each other. As a consequence, the emission of high-order harmonics is governed by their complex interplay [Gol08, Gol11, Vam14, Sch14, Lan17], whereas in the strong-field regime even the non-perturbative coupling of several energy bands has to be taken into account to correctly describe the microscopic carrier dynamics [Hoh15].

In recent years, numerous experiments showed, that intense few-cycle THz pulses are ideally suited to accelerate quasiparticles in solids [Hoh15, Lan16, Lan18b]. Thereby, their oscillating electric field serves as an ultrafast bias voltage to drive intraband currents on the femtosecond timescale and controls the translational motion of the electron across the entire Brillouin zone. As a consequence, even in bulk semiconductors like gallium selenide, dynamical Bloch oscillations have been observed, which manifest themselves in the emission of high-harmonics as shown in reference [Sch14]. To show the capabilities of lightwave acceleration, these experiments shall be briefly reviewed in the following.

The intense multi-THz transients used for ligthwave acceleration are generated by means of difference frequency generation in a nonlinear gallium selenide crystal as described in detail in paragraph 3.4.1. Figure 3.2a illustrates the electro-optically detected multi-THz waveform with a center frequency of 30 THz, a pulse duration of 109 fs and an electric peak field amplitude of $E_{\mathrm{THz}} = 72\,\mathrm{MV\,cm^{-1}} = 0.72\,\mathrm{V\,Å^{-1}}$. The corresponding Keldysh parameter has a value of $\gamma = 0.13$ [Lan14], which pro-

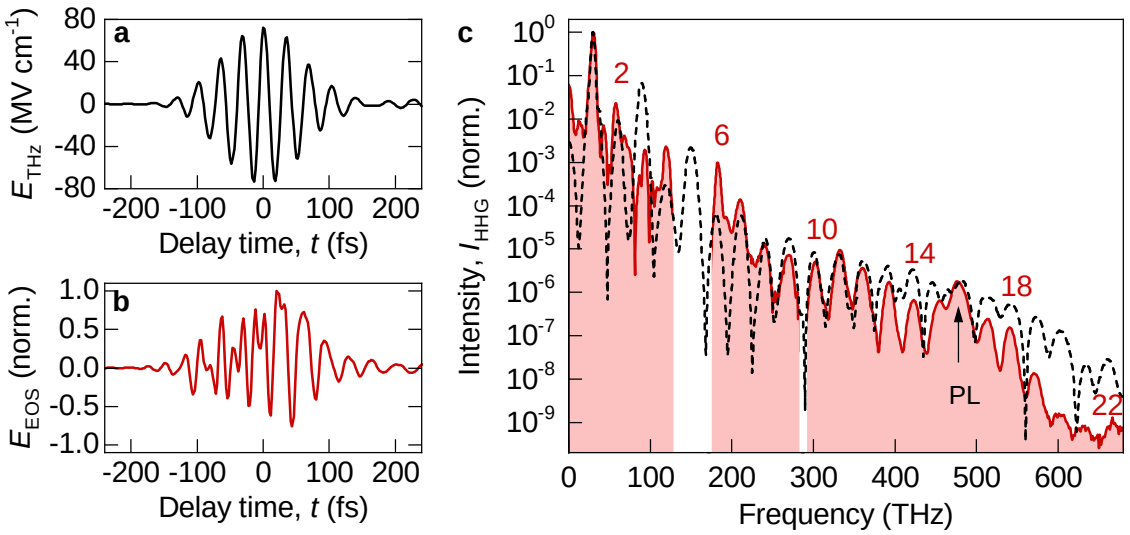

Figure 3.2 | High-harmonic generation from bulk gallium selenide. **a**, THz electric field, E_{THz}, recorded by electro-optic sampling with an gallium selenide detector crystal with a thickness of 40 µm. The waveform features a peak electric field amplitude of 72 MV cm^{-1}, a pulse duration of 109 fs and a center frequency of 30 THz. **b**, Electro-optically detected signal, E_{EOS}, after interaction with the gallium selenide sample with a thickness of 220 µm under an angle of incidence of 70°. **c**, High-harmonics intensity spectrum, I_{HHG} (red shaded area), emitted from the gallium selenide crystal driven by the THz transient shown in **a**. The spectrum features even and odd orders up to the 22nd harmonic. Black dashed line, high-harmonic spectrum calculated by a five-band model based on the semiconductor Bloch equations. PL, photoluminescence peak of gallium selenide. Data taken from reference [Sch14].

vides the ideal platform for coherent quasiparticle acceleration [Gol08, Gol11]. This atomically strong lightwave is now focused into a bulk crystal of the semiconductor gallium selenide with a thickness of 220 µm. The transmitted waveform, E_{EOS}, detected by electro-optic sampling in a silver gallium sulphide detector crystal with a thickness of 100 µm (see Figure 3.2b) clearly differs from the incident THz waveform. A Fourier analysis of this signal reveals, that the fundamental wave is superimposed with newly generated frequency components originating from optical rectification and the second harmonic of the driving field (see Figure 3.2c, left). Recording the emitted radiation with spectrometers reveals odd and even high-order harmonics up to the 22$^{\mathrm{nd}}$ order (see Figure 3.2c). Thus, the spectrum spans the entire THz-to-

visible spectral range and even shows orders above the fundamental band gap of the semiconductor (marked with "PL" in Figure 3.2c), which almost coincides with the 16^{th} harmonic order. Covering in total 12.7 optical octaves from 0.1 to 675 THz, this spectrum sets a new record bandwith for tabletop THz sources. The existing plateau-like region in the high harmonics intensity spectrum is a hallmark of the non-perturbative character of the underlying microscopic electron dynamics.

An elegant way of accurately describing lightwave-driven carrier dynamics in solids are the semiconductor Bloch equations, which consider the full k-dependent band structure of the material, the acceleration of the electron within one band, and the coherent interband polarization driven by the light field [Kir12]. Using the cluster expansion approach also enables the implementation of many-body effects. In order to appropriately describe the microscopic dynamics that lead to the high-harmonic emission shown in Figure 3.2, our theory collaborators *Ulrich Huttner*, *Daniel Golde*, and *Stephan W. Koch* from the University of Marburg, *Mackillo Kira* from the University of Michigan, and *Torsten Meier* from the University of Paderborn developed a full quantum mechanical model based on the semiconductor Bloch equations, including three valence and two conduction bands to account for THz-induced dynamical band mixing.

The black dashed curve in Figure 3.2 indicates the corresponding calculated high-harmonic spectrum based on this five-band model. The calculation quantitatively reproduces the experimentally detected spectrum with even and odd order harmonics as well as their relative intensities especially in the plateau region. This excellent agreement between experiment and theory further underlines the suitability of the model to trace the microscopic electron dynamics that are driven by the intense THz transient and lead to the emitted high-order harmonic radiation. Figure 3.3a shows the calculated THz-induced carrier density, n_{e} (Figure 3.3a, red shaded area), in the first conduction band on the timescale of the THz-driving field, E_{THz}, which has an internal peak field amplitude of $E_{\text{THz}} = 11\,\text{MV}\,\text{cm}^{-1}$ (Figure 3.3a, black solid line). The number of electrons that are off-resonantly excited to the conduction band peaks at the field crests of the THz driving waveform of negative polarity. This is a direct result of the five-band model, which allows for coherent interband transitions between several bands. Depending on the polarity of the excitation channel, the contributions can interfere either constructively, for negative field crests, or

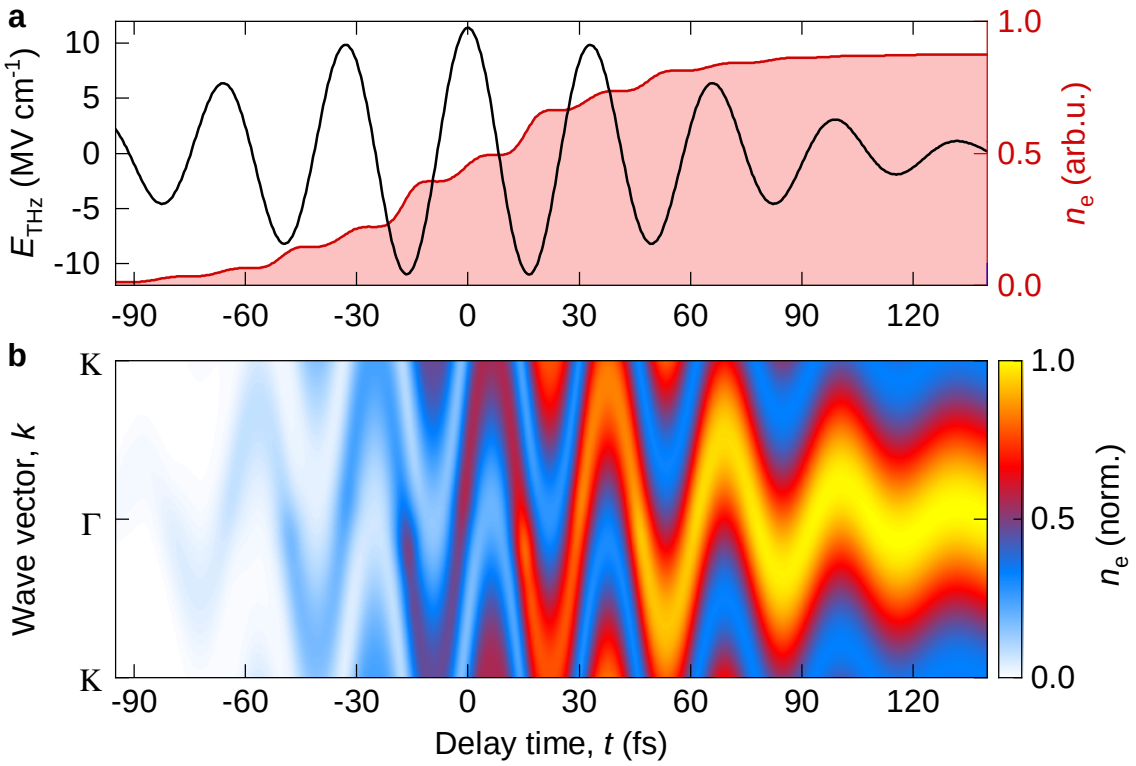

Figure 3.3 | Microscopic carrier dynamics accompanying the high-harmonic generation in gallium selenide. **a**, Calculated carrier density in the first-conduction band of gallium selenide, n_e (red shaded area), on the timescale of the THz driving field, E_{THz} (black solid line). A larger density of electrons is generated at the negative field crests. **b**, Calculated temporal dynamics of the electron distribution in reciprocal space (color code) during high-harmonic generation driven by the intense THz waveform shown in **a** with an internal peak electric field of 11 MV cm^{-1}. The carriers are accelerated through the entire Brillouin zone performing dynamical Bloch oscillations. Data taken from reference [Sch14].

destructively, for a positive polarity [Sch14, Hoh15]. Independent of the sign of the driving field, the electrons are simultaneously accelerated in the conduction band by the transient field bias of the multi-THz waveform as depicted in the contour plot in Figure 3.3b. Under the influence of the large THz electric field of up to $E_{THz} = 11\,\mathrm{MV\,cm^{-1}}$, the electron wave packet, initially created close to the Γ-point in reciprocal space, is driven through the entire Brillouin zone. During the most intense half cycles, the electrons are sufficiently accelerated to reach the edge of the Brillouin zone, where they are Bragg-reflected and perform a complete Bloch cycle

within only a few femtoseconds. These all-coherent intraband dynamics involving dynamical Bloch oscillations together with the coherent off-resonant interband excitation can be identified as the driving mechanism behind the detected high-harmonic emission.
The calculations impressively demonstrate that intense multi-THz transients are able to coherently accelerate and redistribute carriers in a bulk semiconductor on a subcycle timescale. Nonetheless, in this high-field regime of light-matter interaction, the extent of lightwave-driven charge control is limited since the atomically-strong electric fields drive an inseparable combination of inter- and intraband dynamics with mutual interactions. To reach a higher level of control, it would be desirable to disentangle these two processes without affecting the coherence of the light-matter interaction. Indeed, this can be realized in a two-pulse experiment: first, an optical pulse resonantly excites carriers above the band gap into a well-defined initial state. An additional THz waveform then drives the intraband acceleration [Hoh15, Lan16]. Thereby, the electric field of the THz transient is adjusted such that the electron wave packet is significantly deflected in momentum space, but Zener tunneling is suppressed. With this scheme, specific resonances or quasiparticles in solids like excitons [Che14, Hoh15, Lan16], trions [Kir06] or dropletons [AH14] can be selectively addressed. By systematically tuning the frequency and the electric field amplitude of the driving THz waveform, it is even possible to all-optically probe the electronic bands in reciprocal space by super-resolution lightwave tomography [Bor20].

3.1.3 Lightwave quantum control

Accelerating electrons through a solid not only changes their wave vector. In general, also the lattice periodic part, $u_{\mathrm{n},\mathbf{k}}(\mathbf{r})$, of the Bloch wavefunction (see equation (3.3)), which encodes the orbital structure of lattice atoms and thus comprises internal quantum attributes such as Berry curvature, the spin or valley pseudospin, is k-dependent [Xia10]. Thus, by changing the momentum of the crystal electrons, also the electronic properties of the material can be altered. This, in turn, influences the electron dynamics itself and also leaves signatures in the optical readout [Yan15, Ban17, Liu17, You17, Yos19]. Ultimately, these quantum attributes can also be controlled by strong lightwaves as shown in references [Lan18b] and [Lan18a] for

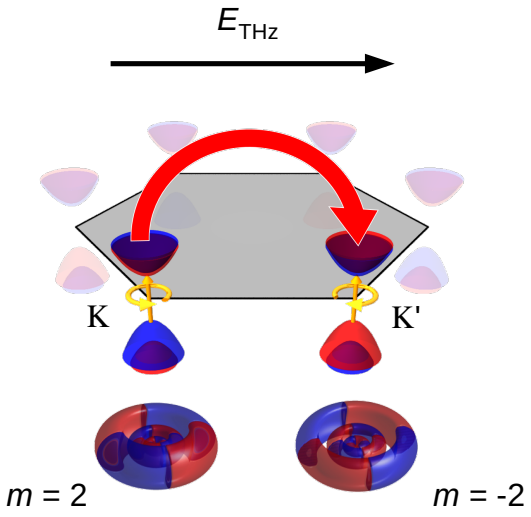

Figure 3.4 | Lightwave quantum control in a monolayer of tungsten diselenide. Hexagonal Brillouin zone of monolayer tungsten diselenide with the spin-split valence and conduction band edges at the inequivalent K and K′ points. The main orbital contributions to the top of the valence bands, as calculated from density functional theory, are shown below (the red-blue color scale depicts the sign of the imaginary part). Upon lightwave acceleration, the intense multi-THz field, E_{THz}, drives electron-hole pairs from the K to the K′ valley. Data taken from [Lan18b].

the valley pseudospin in a monolayer of the semiconductor tungsten diselenide. Monolayers of transition metal dichalcogenides (TMDs) such as tungsten diselenide are direct band gap semiconductors featuring a hexagonal Brillouin zone with two inequivalent but degenerate band minima at their corners, which are known as K and K′ valleys (see Figure 3.4) [Xia12, Xu14, Sch16]. In the vicinity of the K and K′ points in reciprocal space, the lattice-periodic part of the electronic wave function, $u_{\mathrm{n},\mathbf{k}}(\mathbf{r})$, of the valence band mainly consists of contributions of the atomic $5d$ orbitals of tungsten atoms, which have a magnetic quantum number $m = 2$ and $m = -2$, respectively [Xu14]. Such a sign flip of the magnetic quantum number implies that the wave functions at K and K′ are time-reversal pairs of each other. As the same also holds for the conduction band wave functions at K and K′, the valleys can be selectively addressed by circularly polarized light with opposite helicity (see Figure 3.4, yellow arrows) [Xia12, Xu14, Mak12, Jon13]. A spin-like quantity called the *valley pseudospin* now describes, in which of the two degenerate valleys the electron resides. Moreover, as the valley coherence is even conserved in steady-state photoluminescence experiments [Mak12, Jon13], this valley degree of freedom is suggested as a promising information carrier for future quantum electronics [Sch16, Ye17]. In Langer *et al.* [Lan18b], we now combined the advantages of this research field called *valleytronics* with the concept of lightwave electronics: by utilizing the electric field

of an intense multi-THz waveform (see Figure 3.4, black arrow) as an ultrafast bias voltage, previously photo-injected electron-hole pairs were accelerated from one valley to the other (see Figure 3.4, red arrow), which effectively switches their valley pseudospin on a subcycle timescale.
In this way, the coherent electron-hole pairs were excited by a near-infrared preparation pulse, which was resonantly tuned to the excitonic interband polarization of the tungsten diselenide monolayer. Subsequently, a multi-THz transient with a center frequency of $\nu_{\mathrm{THz}} = 40\,\mathrm{THz}$ and a electric peak field amplitude of $E_{\mathrm{THz}} = 18\,\mathrm{MV\,cm^{-1}}$ ballistically drove the excitonic polarization, which lead to a real-space acceleration followed by a recollision of the constituent electron and hole [Kir12, Lan16]. These coherent dynamics resulted in the observation of so-called *high-order sidebands* [Zak12, Lan16] that accompany the excitonic interband resonance. As is apparent from Figure 3.5a, the high-order sideband spectrum from the monolayer (Figure 3.5, red shaded area) qualitatively differs from the one generated in the tungstens diselenide bulk crystal (Figure 3.5, black shaded area). The different valley pseudospin in the K and K′ valleys imparts different helicities on the sideband radiation resulting from recombination in the respective valleys. This circumstance breaks the symmetry for positive and negative THz field polarities and caused the generation of the odd-order sidebands.
Now, to directly demonstrate that the valley degree of freedom can be completely flipped by the THz waveform, a circularly polarized excitation pulse (see Figure 3.5b, black dots) selectively excited electron-hole pairs into the K valley. If the electron-hole recollisions predominantly occur in the same valley where they were injected, the emitted high-order sideband emission is supposed to have the same helicity as the near-infrared excitation pulse. Figure 3.5b shows the detected high-order sideband intensity of the orders $n = 4$ to 7 as a function of the polarization angle, θ. In stark contrast to the excitation pulse (Figure 3.5b, black dots), the measurement revealed strongly elliptically polarized sidebands whereas the respective principal axis were aligned at a large angle of θ, almost perpendicular to the THz driving field. Here, the polarization axes of the multi-THz transient defines $\theta = 0°$.
Based on the semiconductor Bloch equations, a full quantum mechanical model that describes the electron-hole recollision in the tungsten diselenide monolayer including also many-body correlations was developed by *Peter Hawkins*, *Ulrich Huttner*,

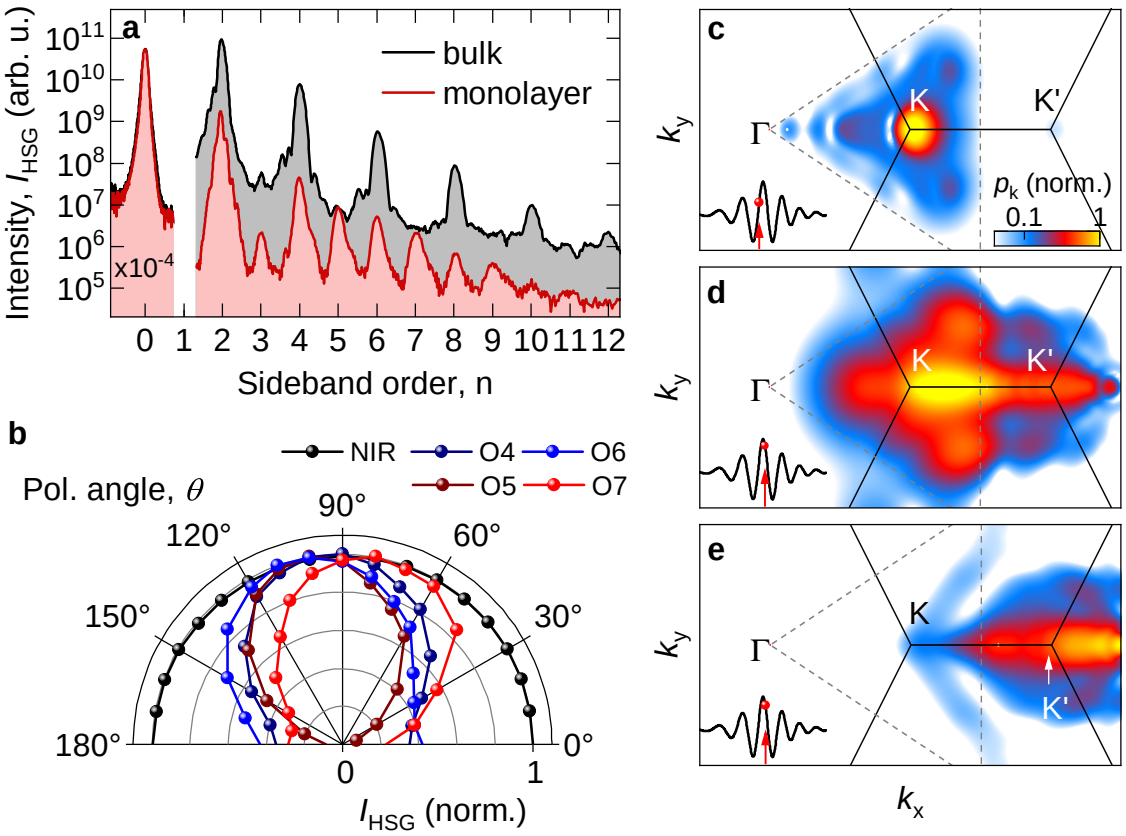

Figure 3.5 | Lightwave valleytronics in monolayer tungsten diselenide. **a**, High-order sideband intensity, I_{HSG}, measured from bulk (thickness 60 µm, black) and monolayer tungsten diselenide (red) driven by a multi-THz transient with a center frequency of $\nu_{\mathrm{THz}} = 40\,\mathrm{THz}$ and a electric peak field amplitude of $E_{\mathrm{THz}} = 18\,\mathrm{MV\,cm^{-1}}$. The monolayer spectrum features even- and odd-order sidebands with comparable intensities. The frequency axis of the bulk spectrum has been shifted by 9 THz owing to the different excitation frequencies. **b**, Measured high-order sideband intensity, I_{HSG}, of individual sideband orders (colored data points) as a function of the polarization angle, θ. Electron-hole pairs are selectively excited in the K valley by a resonant, circularly polarized near-infrared excitation pulse (black data points). The THz-driving field has a center frequency of $\nu_{\mathrm{THz}} = 40\,\mathrm{THz}$ and a electric peak field amplitude of $E_{\mathrm{THz}} = 23\,\mathrm{MV\,cm^{-1}}$. **c**, **d**, **e**, Calculated coherent electron-hole polarization, p_{k}, in reciprocal space (color code). The coherent electron-hole pairs are initially injected at the K point. The multi-THz waveform (inset, $E_{\mathrm{THz}} = 23\,\mathrm{MV\,cm^{-1}}$) ballistically accelerates the quasiparticles towards the K′ point and thereby allows for a control of the valley pseudospin. Employing a 5-fs excitation pulse leads to a intervalley transfer of 96 %, demonstrating a complete flip of the valley pseudospin on a sub-cycle timescale. Black lines, unit cell. Data taken from [Lan18b].

Johannes T. Steiner and *Stephan W. Koch* from the University of Marburg and *Mackillo Kira* from the University of Michigan. The quantum mechanical computations in two dimensions quantitatively reproduce the polarization state of the sideband orders and connect it with a coherent lightwave-driven intraband transport from the K to the K′ valley. This ultrafast intervalley transport leads to a superposition of high-order sideband radiation of both valleys contributing opposite helicities to the overall sideband emission. Thus, the ellipticity of the resulting polarization is a measure of the yield of the intervalley transfer, whereas the orientation of the principal axis is set by the relative phase of the wave functions in the K and K′ valley. The fact that the different orders peak at slightly different polarization angles could be attributed to different dynamical and geometric phases the electron-hole pairs acquire during the lightwave acceleration in a band [Ban17, You17].

For a clear visualization of the the lightwave-driven intervalley transport, the coherent, two-dimensional electron-hole polarization, p_{k}, which is proportional to the density of coherent electron-hole pairs, was calculated in reciprocal space (see Figure 3.5c,d,e). Near a zero-crossing of the THz driving field (see Figure 3.5c, inset), the electrons and holes reside in the vicinity of the K point, where they were injected. The following half cycle accelerates the quasiparticels towards larger k values, whereas p_{k} spreads into the K′ valley within only a few femtoseconds (see Figure 3.5d). As the polarization in the K valley is continuously refilled by the circularly polarized near-infrared excitation pulse, the coherent electron-hole polarization still peaks in the K valley. Nonetheless, a significant fraction of electron-hole pairs is transferred to the K′ valley, which leads to the observed elliptical polarization of the optical readout (see Figure 3.5b). Calculations of p_{k} for a THz peak electric field of $E_{\mathrm{THz}} = 23\,\mathrm{MV\,cm^{-1}}$ and a much shorter near-infrared preparation pulse with a duration of 5 fs, which excites electron-hole pairs at a well-defined phase of the THz carrier wave, even lead to a transfer rate of 96 % (see Figure 3.5e). This was the first demonstration of lightwave-driven valley pseudospin flipping on sub-cycle timescales.

In conclusion, these experiments proved that lightwave acceleration can also be used to control internal quantum attributes of the crystal electrons, which are encoded in the lattice periodic part $u_{\mathrm{n},\mathbf{k}}(\mathbf{r})$ of the Bloch wave function. Thus, lightwave electronics may lead to electronic devices at optical clock rates and furthermore bears the

potential to enable quantum logic operations at ultrafast timescales. Nonetheless, so far the finite band mass and ultrafast scattering in conventional semiconductors limit the velocity and the excursion of the accelerated electrons and hampers the development of actual lightwave-driven electronic devices. In the following section, the material class of topological insulators is introduced, whose peculiar electronic properties open up a realistic parameter space for dissipation-free lightwave-driven electronic devices operating at optical clock rates.

3.2 Topological insulators: platform for lightwave electronics

With their exceptional electronic properties, the material class of topological insulators provides interesting and exciting perspectives for the whole research field of lightwave electronics [Has10, Tok17]. Whereas these materials are insulating or semiconducting in their bulk form, the surface exhibits conductive states that are protected by time-reversal symmetry [Kan11, Van18]. Moreover, these surface states feature a linear, Dirac-like energy dispersion. In the case of three-dimensional topo-

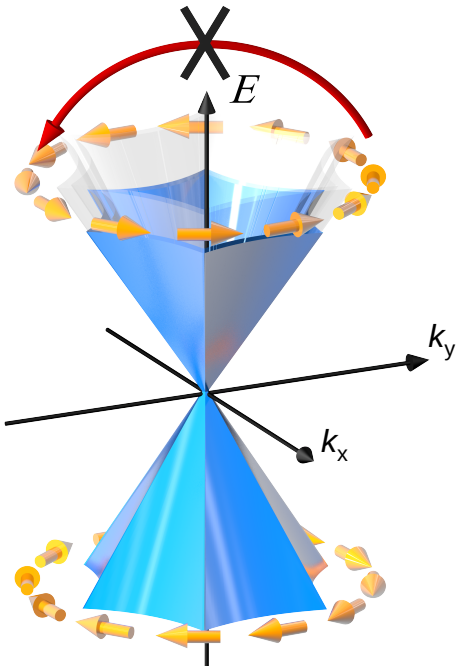

Figure 3.6 | Topologically protected surface state of three-dimensional topological insulators. The Dirac cone, characteristic for the Dirac like dispersion of the surface state of topological insulators, is filled up to the Fermi level (blue). Due to the helical spin texture (orange arrows), direct electron backscattering in the surface band is forbidden (red arrow).

logical insulators like Bi_2Te_3, this leads to a Dirac cone at the $\overline{\Gamma}$-point in reciprocal space (see Figure 3.6) [Fu07b, Zha09].
The existence of these surface states is guaranteed by the topology of the band structure, which makes them robust against defects or non-magnetic impurities [Has10]. In addition to that, so-called *spin-momentum locking* leads to a helical spin texture in the Dirac cone (see Figure 3.6, orange arrows) [Hsi09]. Owing to this coupling of the propagation direction of the electrons and its spin state, charges in the topological surface state are expected to have rather long scattering and dephasing times compared to the few-femtosecond timescales usually present in semiconductors [Haj12, Rei14].
These properties render topological insulators the ideal material platform for ultrafast low-loss electronics and applications in quantum computing [Tok17]. Besides that, also other fascinating phenomena such as Floquet-Bloch states [Wan13, Mah16], Dirac plasmons [Di 13], Majorana fermions [Fu08] or strong optical nonlinearities [Gio16] are associated with this novel state of matter. In the following, the theoretical foundations of topologically protected surface states are briefly summarized. After that, the structural and electronic properties of the three-dimensional topological insulator Bi_2Te_3, that is used for the experiments presented in this chapter, are studied in detail.

3.2.1 Concept of topologically protected states

The state of a material is commonly characterized by the underlying symmetries and order parameters [Van18]. The lattice periodicity of the crystal lattice, for example, leads to the formation of continuous energy bands and an energy gap, that separates the occupied valence band and unoccupied conduction band of an intrinsic semiconductor or insulator (see Figure 3.7a) [Gro18]. As described by Landau's theory [Lan37], a phase transitions can be classified by the broken symmetries in the different states. Thus, changing the symmetry of a crystal structure can drastically alter its electronic properties. In particular in the regime of strong light-matter interaction, optical nonlinearities depend crucially on the crystal orientation [Boy03], which can also be detected in the optical readout [Lan17, Lan18b].
The inherently broken symmetry at the sample surface can lead to the emergence of

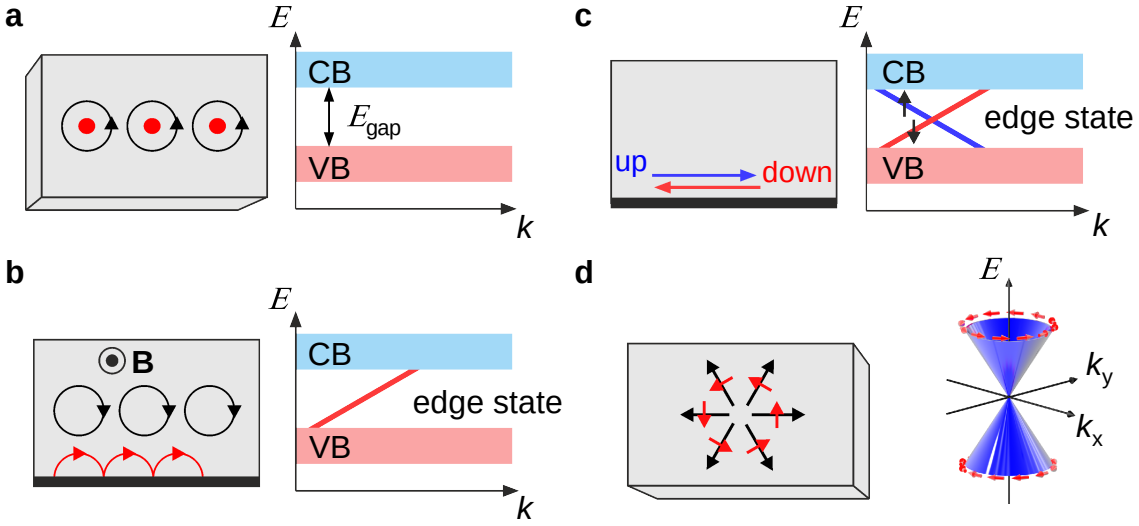

Figure 3.7 | Electronic states of matter. **a**, In an intrinsic semiconductor or insulator, the crystal electrons are localized around their atomic cores (left, red dots). The valence (VB) and conduction band (CB) are separated by an energy gap, E_{gap}. **b**, In the quantum Hall effect, a magnetic field, **B**, oriented perpendicular to a two-dimensional electron gas, forces the electrons on circular orbits (left, black circles). At the sample boundary, skipping cyclotron orbits (left, red circles) emerge, leading to a conducting edge state that connects the valence band and the conduction band. **c**, For the quantum spin hall effect or a two-dimensional topological insulator, metallic, spin-polarized edge states emerge. **d**, In a three-dimensional topological insulator, conducting edge states support an electronic motion in any direction (left, black arrows). The orientation of the electron spin (red arrows) is coupled to the momentum, k, of the electron. The dispersion of the surface state has a Dirac-cone structure. Adapted from reference [Kan11].

surface bands as already described by *Shockley* [Sho39]. The states that emerge on the surface of topological insulators, however, have a different origin: they occur as a result of a change of the topological order parameter at the interface [Kos73, Has10, Van18]. Thereby, the categorization of a material according to its topological phase rather refers to protected symmetries, which allowed a description of the quantum Hall effect [Von80, Tho82]. Here, a two-dimensional electron gas is placed in a strong out-of-plane magnetic field, **B** (see Figure 3.7b). Owing to the Lorentz force, the electrons perform a circular motion with a fixed rotational direction (Figure 3.7, black circles) [Dav09], which leads to the formation of quantized

Landau levels that can be viewed as a band structure of the system [Has10, Kan11]. Thus, inside the two-dimensional electron gas, the situation is pretty similar to an ordinary insulator, where the electrons are localized around their atomic cores and the occupied and empty states are separated by an energy gap (see Figure 3.7a). At the edge of the system, however, the orbits are interrupted as the electron hits the boundary. This results in so-called *skipping orbits* as shown in Figure 3.7b and leads to the formation of a conducting edge channel that lies in the bulk band gap [Has10]. Owing to the external magnetic field, electron transport in this conducting channel is only allowed in one direction. Thus, there are no states that support propagation in the opposite direction, which makes these states insensitive to disorder or defects [Has10]. This is also apparent from Figure 3.7b, where for an edge state with momentum $\hbar k$, there is no state with the same energy at $-\hbar k$. The electrons in this edge channels can propagate without dissipation and exhibit a quantized, so-called *Hall conductance* which is proportional to a topological invariant, the Chern number of the system, that uniquely characterizes this quantum Hall state [Gro18, Van18]. In quantum spin Hall insulators, which have been theoretically proposed in 2005 [Kan05], the role of the strong magnetic field is taken by spin-orbit coupling [Kan11]. This links the intrinsic angular momentum of the electron with its orbital motion and leads to a strong spin- and momentum-dependent force in these materials that mimics the Lorentz force induced by an out-of-plane magnetic field. Similar to the quantum Hall state (see Figure 3.7b), this leads to quantized energy states and a band gap separating the occupied and empty bulk states (see Figure 3.7c). As the sign of the spin-orbit force, which acts on the electrons, depends on their spin orientation, the resulting metallic edge states in the bulk band gap are spin-polarized [Kan05, Gro18]. In other words, spin 'up' and spin 'down' electrons are propagating in opposite directions (see Figure 3.7c. left). Thus, the quantum spin Hall effect can be interpreted as two copies of the quantum Hall effect [Qi10]. Due to the absence of a magnetic field, however, time-reversal symmetry is not broken in the quantum spin Hall state. Consequently, a spin-up electron with momentum $\hbar k$, that scatters at a non-magnetic impurity, is converted into a spin-down electron at $-\hbar k$. *Spin-momentum locking* strongly suppresses any backscattering and allows for a dissipationless, spin-polarized transport in the edge channels. The time-reversal invariance in quantum spin Hall insulators also implies, that the two edge channels are

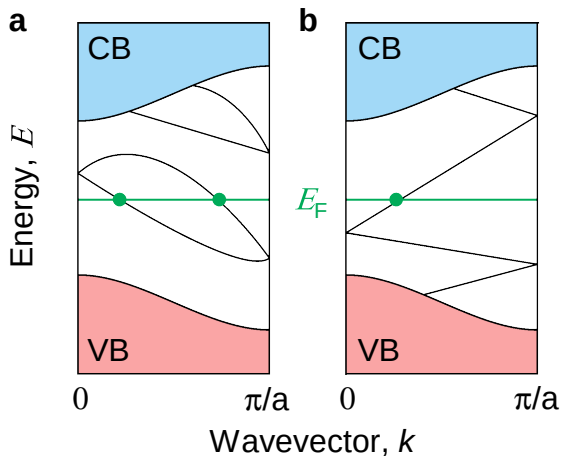

Figure 3.8 | Kramers theorem in time-reversal invariant states. **a**, Electronic dispersion between two boundary Kramers degenerate points located at $k = 0$ and $k = \pi/a$, where a is the lattice constant of the crystal. The number of surface states crossing the Fermi energy, E_F, can be either **a** even or **b** odd. An odd number of crossings leads to topologically protected edge states that are connecting the bulk valence (VB) and conduction (CB) band. Adapted from reference [Has10].

so-called *Kramers pairs*. In particular, the Kramers' theorem states, that the edge states have to be twofold degenerate at the time-reversal invariant momentum points (TRIM) at $k = 0$ and $k = \pi/a$ in reciprocal space (see Figure 3.8) [Kan05, Has10]. Here, a is the lattice constant. Away from these points, the degeneracy is lifted by the spin-orbit interaction, which allows for two different ways to connect the TRIM points: (i) the edge states intersect the Fermi level, E_F, in one half of the Brillouin zone an even number of times, and consequently no conducting states connect the bulk valence and conduction band (see Figure 3.8a). (ii) the Fermi level, E_F, is intersected between the two TRIM points an odd number of times (see Figure 3.8b). In this case, conducting quantum spin Hall edge states exist, that connect the bulk valence and conduction band. The nature of this time-reversal invariant system can be characterized by the $\mathbb{Z}_2$ topological invariant [Has10, Van18, Gro18]. As a fundamental consequence, at the interface of two materials with different topological $\mathbb{Z}_2$ invariants gapless states that are *topologically protected* must exist. Therefore, quantum spin Hall insulators are also referred to as two-dimensional topological insulators [Qi10, Has10].

Although spin-orbit coupling is present in every material, not all of them are topological insulators. Nonetheless, recent studies showed that about 30 % of all materials in nature are topological [Ver19, Zha19]. Especially compounds composed of elements with a large atomic number like mercury (Hg) or bismuth (Bi), exhibit a large spin-orbit interaction, which can lead to nontrivial topological phases [Has10, Gro18]. So

already one year after the discovery of the quantum spin Hall state [Kan05] in 2006, the realization of topologically protected edge states in mercury telluride-cadmium telluride semiconductor quantum wells has been proposed [Ber06], which could be experimentally confirmed in 2007 [Kön07]. Thereby, the occurrence of these conducting edge states in these systems is based on a band inversion.
In cadmium telluride, the conduction band has a s-like symmetry, whereas the valence band is mainly composed of contributions from electronic p-orbitals [Qi10]. Since the spin-orbit interaction in heavy elements like mercury, tellurium or bismuth, is so strong, the trivial band ordering of the valence and conduction band is inverted and the p-like band lies above the s-like band. By placing a sheet of mercury-telluride with an inverted band structure between two layers of cadmium telluride with an ordinary band ordering, metallic states have to emerge at the interface that connect the two band structures with each other [Qi10, Has10]. Thereby, the two edge channels allow for a dissipationless spin-polarized charge transport, whereas the layers themselves show no conductance [Kön07, Gro18].
As illustrated in Figure 3.7c the two spin-polarized edge states of a two-dimensional topological insulator that cross at the TRIM point (see Figure 3.8b) at $k = 0$ feature a linear dispersion relation, similar to massless Dirac fermions in quantum field theory [Qi10]. Thus, the Dirac equation can also be used to describe the quantum spin Hall states, which also allows for a generalization to three dimensions [Zha09]. This three-dimensional topological insulator is then characterized by four $\mathbb{Z}_2$ topological invariants [Van18] and the surface states are forming a topologically protected two-dimensional conducting layer that allows for an electron motion in any direction. The dispersion relation has the shape of a Dirac cone (see Figure 3.7d), whereas the TRIM point is at the tip of the cone [Qi10]. Again, owing to the conserved time-reversal symmetry, electrons with momentum $\hbar k$ and $-\hbar k$ need to have opposite spin orientations [Has10]. Thus, the spin of the electron rotates with k around the Fermi surface (see Figure 3.7d) leading to a helical spin texture.
Spin-momentum locking, which suppresses electronic backscattering, together with the Dirac-like dispersion (see Figure 3.6) suggesting a very high Fermi velocity render three-dimensional topological insulators the ideal platform for minimally dissipative, lightwave-driven electronic applications.

3.2.2 The three-dimensional topological insulator Bi_2Te_3

The first theoretically predicted three-dimensional topological insulator has been the semiconducting alloy bismuth antimonide $Bi_{1-x}Sb_x$, which is supposed to exhibit a topological character in a special range of x [Fu07a]. And indeed, ARPES experiments have verified that this compound exhibits an odd number of surface states that are crossing the Fermi energy [Hsi08]. However, the surface structure turns out to be rather complicated and the bulk band gap is smaller than 20 meV [Jai59]. Thus, there has been an extensive search for large-gap stoichiometric materials that feature topologically protected states with no alloying disorder [Xia09].
Based on theoretical predictions [Zha09], the so-called second generation of three-dimensional topological insulator materials including the pure compounds Bi_2Se_3, Sb_2Te_3 and Bi_2Te_3 was discovered [Moo09]. It tuns out that these materials have a relatively large bulk energy gap on the order of 100 - 300 meV and feature a single gapless Dirac cone in the center of the surface Brillouin zone [Zha09, Xia09]. This significantly increases the potential for practical electronic applications as topological effects might even be observed at room temperature and zero magnetic field [Che09, Has10].
The semiconductor compound Bi_2Te_3, which is used for the experiments in this chapter, shows a strong spin-orbit interaction and features a rhombohedral D_{3d}^5 ($R3m$) crystal structure with the lattice parameters $a = 4.386$ Å and $c = 30.497$ Å [Nak63]. The unit cell consists of five atomic layers arranged along the crystallographic z-axis as Te-Bi-Te-Bi-Te quintuple layers (see Figure 3.9a) [Zha09, Yav11]. Each layer exhibits a triangular lattice structure (see Figure 3.9b), which can be classified according to the atomic position as A, B, or C. As indicated in Figure 3.9c, within a quintuple layer, two tellurium (gray spheres) and two bismuth (bronze spheres) atoms are equivalent, the central tellurium atom acts as the inversion center of the structure [Zha09]. Whereas the atomic layers are covalently bonded, adjacent quintuple layers interact only weakly and are separated by a van der Waals gap. Thereby, the quintuple blocks have a height of ≈ 1 nm and feature a hexagonal symmetry (see Figure 3.9b). Note that the weak van-der-Waals bonding between adjacent quintuple layers, allows for the preparation of clean surfaces by mechanical exfoliation as described further below.

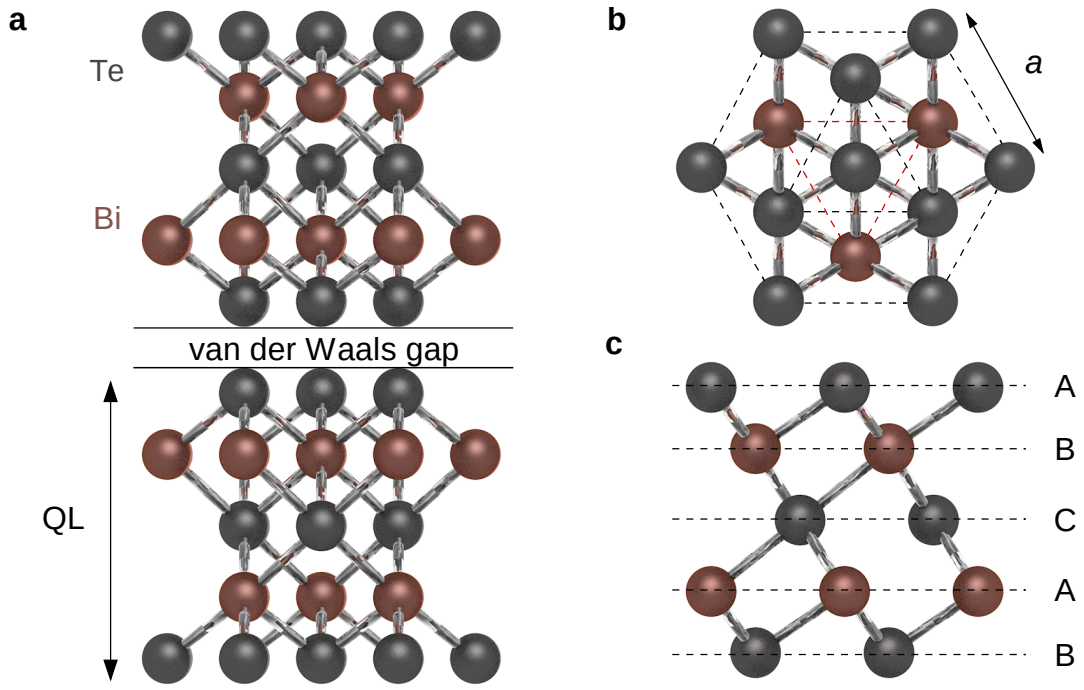

Figure 3.9 | Crystal structure of the topological insulator Bi_2Te_3. **a**, The Bi_2Te_3 crystal consists of single quintuple layers (QL), which are separated by a van der Waals gap. Within one layer, the alternating layers of tellurium (gray spheres) and bismuth (bronze spheres) are covalently bound together. **b**, Top view of a quintuple layer along the crystallographic z-direction showing the hexagonal lattice structure of the Bi_2Te_3 crystal. Atoms residing in the same crystal plane are connected by dashed lines. a, lattice constant of Bi_2Te_3. **c**, Side view of a quintuple layer. Along the crystallographic z-direction the stacking order of the tellurium and bismuth layers is ABCAB. The respective crystal planes are indicated by the dashed lines.

In analogy to the two-dimensional topological insulator mercury telluride, the topologically nontrivial nature of Bi_2Te_3 results from a reversed band order close the Fermi energy. In particular, the strong spin-orbit interaction in combination with chemical bonding and crystal-field splitting causes an inversion of the bulk conduction and valence band at the Γ-point in reciprocal space [Zha09]. This band inversion can be associated with a nontrivial $\mathbb{Z}_2$ invariant and results in gapless, topologically protected surface states at the interface to a trivial insulator with an ordinary band

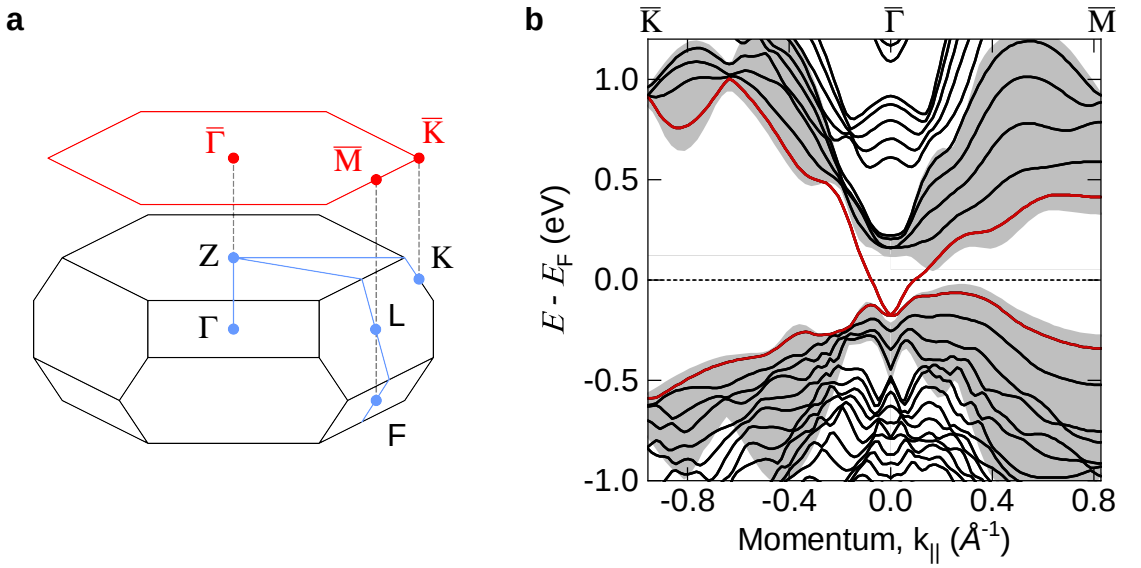

Figure 3.10 | Brillouin zone and calculated band structure of Bi_2Te_3. **a**, Brillouin zone of the three-dimensional topological insulator Bi_2Te_3 with a D^5_{3d} ($R3m$) crystal structure. The high-symmetry points of the three-dimensional bulk are connected by blue solid lines. The two-dimensional Brillouin zone of the (111) surface with the high-symmetry points $\overline{\Gamma}$, $\overline{\mathrm{M}}$, and $\overline{\mathrm{K}}$ is shown in red. Gray dashed lines, projections from bulk to surface. Adapted from reference [Zha09]. **b**, Electronic structure, E, of Bi_2Te_3 as a function of the in-plane momentum, $k_{||}$, calculated by density function theory considering five quintuple layers. A single surface state at the $\overline{\Gamma}$-point in reciprocal space (red solid line) disperses in the bulk band gap. Gray shaded area, bulk band projections.

ordering. Figure 3.10a shows a schematic illustration of the Brillouin zone of the Bi_2Te_3 bulk crystal (black solid lines) as well as the two-dimensional Brillouin zone of the (111) surface (red solid lines) studied in the experiments in this chapter. The surface Brillouin zone features a hexagonal structure with the high-symmetry points $\overline{\Gamma}$, $\overline{\mathrm{M}}$, and $\overline{\mathrm{K}}$. The corresponding electronic structure of Bi_2Te_3 obtained by density functional theory calculations considering five quintuple layers is presented in Figure 3.10b. The calculations are performed by our collaborator *Suguru Ito* from the University of Marburg using the Quantum ESPRESSO software [Gia09].
The topological surface state forming a single Dirac cone at $k = 0$, is apparent in the bulk band gap (see Figure 3.10b, red solid line). Thereby, the spin-polarized bands cross at the $\overline{\Gamma}$-point in reciprocal space, whereas the Dirac point is $\approx 180\,\mathrm{meV}$

below the Fermi level, E_F. The energy dispersion of the surface states close to E_F can be approximated by

$$E(\mathbf{k}) \;=\; \pm\hbar v_F|\mathbf{k}|, \tag{3.7}$$

where v_F is the Fermi velocity defined by the slope of the band. Along the high-symmetry directions $\overline{\Gamma}$-$\overline{K}$ and $\overline{\Gamma}$-$\overline{M}$, the Fermi velocity is $v_F = 4.1 \cdot 10^5\ \mathrm{m\,s^{-1}}$ and $v_F = 3.4 \cdot 10^5\ \mathrm{m\,s^{-1}}$, respectively. This is in agreement with the values experimentally obtained in section 3.4.3. With a bulk band gap of $\approx 150\,\mathrm{meV}$ [Mic14], topological behavior should be observed even at room temperature [Che09, Has10].
Although Bi_2Te_3 is supposed to be insulating in its bulk form, previous experiments revealed an intrinsic n-doping owing to charged tellurium vacancies [Wie16, Che09]. As a consequence, the Fermi level lies above the Dirac point in the bulk band gap and the occupied topological surface states can be studied by photoemission experiments. Thereby, spin-polarized ARPES has demonstrated the peculiar spin-texture of the Dirac cone (see Figure 3.6 and references [Hsi09, Kur16]).
Moreover, owing to the spin-momentum locking, the decay time of electron dynamics in topological insulators is on the order of $\approx 1\,\mathrm{ps}$ [Haj12, Rei14]. For a Fermi level in the bulk conduction band, scattering times of up to 400 ps are observable [Sum17]. In this case, no electron-hole pairs can be generated, which significantly reduces the amount of decay channels. In addition to that, both electron-electron scattering, which is very efficient in metals [Ech04], and electron-phonon scattering is strongly suppressed in the topologically protected surface band due to the linear dispersion and spin-momentum locking [Rei14]. The resulting extremely long scattering times in combination with the Dirac like energy dispersion of the topological surface states in Bi_2Te_3, allow for the observation of ballistic carrier dynamics driven by intense THz waveforms as shown in section 3.3.2 and 3.4.
The Bi_2Te_3 samples used for the experiments of this chapter are fabricated by the modified Bridgman method [Kok14]. By choosing an appropriate solidification condition, a gradation in the carrier concentration was realized in an ingot naturally forming a p-n junction. As the surface sensitive photoemission experiments require a clean and well-ordered surface, the Bi_2Te_3 sample is cleaved *in situ* by the Scotch tape method [Nov05, CG14] in ultra-high vacuum at a pressure of only $4{\cdot}10^{-11}$ mbar. The sample orientation was determined by low-energy electron diffraction.

3.3 Subcycle observation of THz-driven Dirac currents in Bi_2Te_3

To reveal the unique electronic properties of the topologically protected surface states of compounds like Bi_2Te_3, an experimental probe that couples mainly to the surface is indispensable. Electron spectroscopy already proved to be the ideal tool to probe electronic states in the surface region [Hüf03, Kan11]. In particular, angle-resolved photoelectron spectroscopy facilitated the experimental verification of the first three-dimensional topological insulators [Hsi08]. Now, by combining this technique with the concept of lightwave acceleration, for the first time, THz-driven electron dynamics of Dirac fermions can be directly traced in the topological surface state of Bi_2Te_3 and on a subcycle timescale. The results open a new chapter in lightwave electronics, where currents induced with optical carrier waves can be directly traced in the band structure itself.

3.3.1 Band structure mapping by angle-resolved photoelectron spectroscopy

The band structure of a solid describes the crystal electrons' nontrivial energy-momentum relation and governs their key physical and electronic properties. Energy gaps, for example, distinguish insulators from metals whereas the band slope sets the velocity of the crystal electrons [Gro18]. Thus, a full reconstruction of the energy bands is crucial for both fundamental materials sciences and applications. With angle-resolved photoelectron spectroscopy (ARPES) the occupied part of band structures can be mapped out by measuring the kinetic energy of photoemitted electrons as a function of their momenta [Dam04, Hüf03].

The basic mechanism behind this experimental technique is the photoelectric effect, that was first reported by Hertz back in 1887 [Her87] and was conclusively explained by Einstein [Ein05]. According to the photoelectric effect, electrons can be liberated out of a solid by absorbing a high-energy photon with a sufficiently large energy, $E_{\mathrm{ph}} = h\nu$, where ν is the frequency of the lightwave. Figure 3.11a shows the schematic energy diagram of this photoemission process. A crystal electron is excited from an initial state, E_{i}, below the Fermi level, E_{F}, to a final state, E_{f}, above

the vacuum level, E_v [Hüf03, Wei02]. According to the energy conservation law,

$$E_\mathrm{f} - E_\mathrm{i} \;=\; h\nu \tag{3.8}$$

by detecting the kinetic energy of the photoreleased electron, E_kin, with an electron energy analyzer, the initial energy, E_i, relative to the Fermi level, can be determined by

$$E_\mathrm{i} = E_\mathrm{F} + E_\mathrm{kin} - h\nu + \Phi. \tag{3.9}$$

Here, Φ is the work functions of the material. The intensity of the photoemission depends on the density of states of the initial and final state as well as their dipole matrix elements [Pen76, Hüf03]. Therefore, the detection of the kinetic energy spectrum of the photoemitted electrons allows for the determination of the electronic band structure of the solid. Moreover, as the mean free path of electrons with energies between 10 eV and 100 eV inside a solid is typically below 1 nm [Sea79], the photoelectron spectroscopy is inherently surface sensitive, which makes it ideally suited to study the nature of the topological surface states of three-dimensional topological insulators.
During the photoexcitation process, the momentum conservation law is valid [Dam04]:

$$\hbar\mathbf{k}_\mathrm{f} - \hbar\mathbf{k}_\mathrm{i} = \hbar\mathbf{k}_\mathrm{ph}, \tag{3.10}$$

where $\hbar\mathbf{k}_\mathrm{f}$ is the momentum in the final state and $\hbar\mathbf{k}_\mathrm{i}$ denotes the crystal momentum of the electron inside the material. $\hbar\mathbf{k}_\mathrm{ph}$ is the momentum of the incoming photon. For photon energies below 100 eV, which are typically used for ARPES, $\hbar k_\mathrm{ph}$ is much smaller than the characteristic Brillouin zone dimension of a solid [Dam04]. Thus, it can be neglected in the photoemission process and $\hbar\mathbf{k}_\mathrm{f} - \hbar\mathbf{k}_\mathrm{i} = 0$. The absolute value of $\mathbf{k}_\mathrm{f} = \mathbf{k}$ can be derived from the measured kinetic energy,

$$|\mathbf{k}| = \frac{1}{\hbar}\sqrt{2m_\mathrm{e}E_\mathrm{kin}}. \tag{3.11}$$

As a consequence of the abrupt potential change at the sample surface, the electron momentum perpendicular to the sample surface, $k_\perp$, changes during photoemission [Hüf03]. In contrast, owing to the translational symmetry in the surface, the

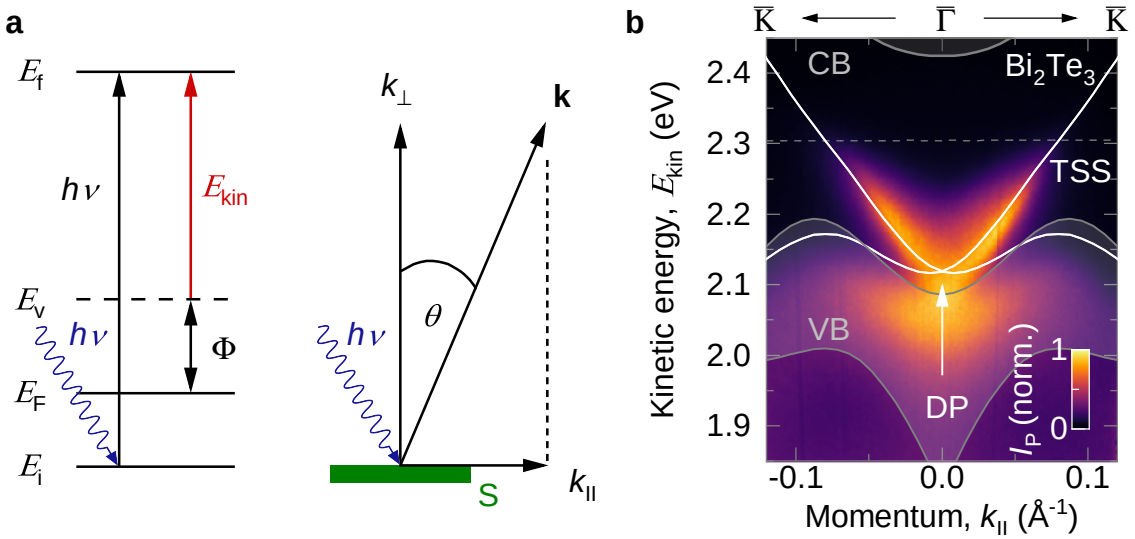

Figure 3.11 | Angle-resolved photoelectron spectroscopy (ARPES). a, Energy and momentum conservation upon photoemission. A high-energy photon, $h\nu$ (blue), excites an electron from an initial state, E_i, below the Fermi level, E_F, to the final state, E_f, above the vacuum state, E_v. Depending on the binding energy in the solid, the photoemitted electron features a specific kinetic energy, E_{kin}. Φ indicates the work function of the material. During this process, the parallel momentum, $k_{||}$, of the electrons emitted from the sample (S) is conserved. The perpendicular component, $k_\perp$, changes according to the energy conservation law. The electrons are emitted upon the angle, θ, relative to the surface normal with the momentum, **k**. **b**, Angle-resolved photoemission spectrum, I_P, of Bi_2Te_3 along the $\overline{\Gamma}$-$\overline{K}$-direction for a excitation light pulse with a photon energy of 6.42 eV. The topologically protected surface state (TSS) exhibiting the characteristic V-shaped dispersion is located in the energy gap between the bulk valence band (VB) and conduction band (CB). The surface state is filled up to the Fermi level (gray dashed line) that lies 200 meV above the Dirac point (DP). White solid line, topological surface state calculated by density function theory considering five quintuple layers; gray shaded area, bulk band projections (see also Figure 3.10b).

momentum parallel to the surface, $k_{||}$, is conserved. Thus, by measuring the emission angle, θ, the parallel electron momentum of the crystal electron inside the solid at the time of the photoemission can be determined:

$$k_{||} = |\mathbf{k}| \sin\theta = \frac{1}{\hbar}\sqrt{2m_e E_{kin}} \sin\theta. \tag{3.12}$$

By detecting the kinetic energy spectrum of the photoemitted electrons in an angle-resolved fashion, it is possible to simultaneously track the in-plane wave vector, $k_{||}$, of the electrons as well as their initial binding energy, E_i. This reveals the complete energy dispersion relation of the electrons inside the solid, which is their band structure [Dam04, Hüf03].
Figure 3.11b shows the angle-resolved photoemission spectrum, I_P, of the three-dimensional topological insulator Bi_2Te_3 along the crystallographic $\overline{\Gamma}$-$\overline{\mathrm{K}}$-direction recorded with a photon energy of $h\nu = 6.42\,\mathrm{eV}$. In agreement with density functional theory calculations (see also Figure 3.10b and reference [Zha09]), gapless surface states emerge at the $\overline{\Gamma}$-point in reciprocal space, where the parallel momentum, $k_{||}$, is zero. The energy-momentum map shows both the topologically protected surface state with the characteristic Dirac-like dispersion as well as the bulk valence band. The unoccupied conduction band is not visible in the experiment. The Fermi energy lies in the bulk band gap and 200 meV above the Dirac point. The linear dispersion of the surface state indicates a Fermi velocity of $v_\mathrm{F} = 4.1\,\mathrm{Å\,fs^{-1}}$ in quantitative agreement with theory calculations (Figure 3.11b, white solid line). Owing to the spectral bandwidth of the excitation light pulse, the photoemission maps feature a finite energy resolution, which leads to a broadening of the energy bands.
The measurements demonstrate the capabilities of ARPES, that allows for impressive insights into the electronic structure of solids. An interesting perspective is to combine photoemission with light excitation or lightwave acceleration. In this way, also the previously unoccupied states can by dynamically mapped out, which enables a complete characterization of the electronic structure of the material.

3.3.2 Subycycle videography of THz-driven Dirac currents

By utilizing ultrashort laser pulses, time-resolved ARPES has been able to trace the dynamics of photoinjected currents at surfaces as a small imbalance of carriers moving in opposite directions [Güd07]. In topological insulators, ARPES has been utilized to reveal light-induced Floquet states [Mah16] and interband transitions [Kur16]. Furthermore, attosecond metrology has been able to measure subcycle time delays in the momentum-integrated photoemission from surfaces [Nep15]. In the following, the electric field of intense THz pulses with a center frequency of

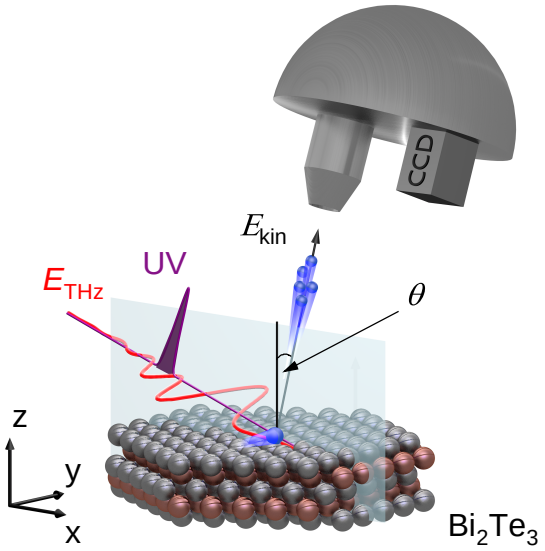

Figure 3.12 | Concept of subcycle THz ARPES Electrons (blue sphere) in the topologically protected surface state of Bi_2Te_3 (crystal lattice, bronze spheres, Bi atoms; gray spheres Te atoms) are accelerated by an intense, linear *s*-polarized THz field, E_{THz} (red waveform) and subsequently photoemitted by an ultrashort p-polarized UV pulse (violet). The kinetic energy, E_{kin}, and emission angle, θ, of the liberated electrons are measured by a hemispherical electron analyzer to determine the binding energy and the parallel momentum k_y of the electrons in the topological surface band along the $\overline{\Gamma}$-$\overline{K}$-direction. The plane of incidence (x-z-plane) is indicated by a transparent rectangle.

1 THz is used to drive coherent intraband dynamics in the topological surface state of Bi_2Te_3. The results, which have been published in *Nature* [Rei18b] and discussed in detail in reference [Rei18a], are briefly reviewed in this section to set the stage for the novel experiments presented in section 3.4.

The single crystal of Bi_2Te_3, which is oriented along the $\overline{\Gamma}$-$\overline{K}$-direction, is kept in an ultrahigh-vacuum chamber in order to retain a clean and well-ordered surface. To accelerate the Dirac fermions in the topological surface band, a strong THz electric field, E_{THz}, with a center frequency of 1 THz, that is linearly polarized parallel to the sample surface, is focused onto the Bi_2Te_3 crystal (see Figure 3.12). More specifically, according to Bloch's acceleration theorem (see equation (3.3)), the electron occupation is supposed to be shifted in momentum space along the field direction. Simultaneously, the transient electron distribution in momentum space is probed by time- and angle-resolved photoelectron spectroscopy. For this purpose, a time-delayed ultraviolet (UV) laser pulse (see Figure 3.12, violet pulse) with a pulse duration of 100 fs and a center wavelength of 201 nm is used to photorelease electrons out of the sample surface. With the help of an electrostatic hemispherical electron analyzer equipped with a charge-coupled device detector, the kinetic energy, E_{kin},

of the photoemitted electrons is recorded as a function of the emission angle, θ. In this way, the relation between the energy, E_{kin}, and the in-plane momentum, k_{y}, of the crystal electrons inside the material can be determined as demonstrated in the previous section. On their way to the detector, the photoemitted electrons also interact with the THz field in the vacuum, such that the apparent band structure is effectively offset in energy and momentum. Since the duration of the ultraviolet probe pulse is much shorter than the oscillation period of the THz driving field, this streaking effect can be used to sample the electric field close to the surface as explained in greater detail in section 3.4.2.

The electric field of the *s*-polarized THz pulses is oriented along the *y*-direction in which our electron analyzer detects the electron momentum, $\hbar k_{\mathrm{y}}$. Whereas the momentum streaking is used to directly probe the instantaneous THz electric field (see Figure 3.13d, e, f and section 3.4.2), the *s*-polarized, in-plane electric field component may effectively accelerate electrons in the topologically protected surface band before they are photoemitted.

Figures 3.13a, b and c show snapshots of photoemission spectra for three characteristic delay times, t, and a THz electric peak field amplitude of $E_{\mathrm{THz}} = 2.4 \pm 0.5\,\mathrm{kV\,cm^{-1}}$. Before the arrival of the THz transient at $t = -1.86\,\mathrm{ps}$ (see Figures 3.13a), the left and the right branch of the Dirac cone are occupied up to the same Fermi energy, E_{F}, which is $\approx 200\,\mathrm{meV}$ above the Dirac point. The corresponding Fermi momentum is $k_{\mathrm{F}} = 0.075\,\mathrm{\AA}^{-1}$. The characteristic V-shaped dispersion proves the presence of the quasirelativistic topological surface state with a Fermi velocity of $v_{\mathrm{F}} = 4.1\,\mathrm{\AA\,fs^{-1}}$. When the THz field is applied, the occupation becomes asymmetric as is apparent from Figures 3.13b and c taken at a delay time $t = 0.14\,\mathrm{ps}$ slightly after the positive THz field maximum and $t = 0.64\,\mathrm{ps}$ right after the negative crest, respectively. The opposite shift of the population for opposite THz field polarity hallmarks an ultrafast displacement of the Fermi circle in momentum space. This represents the first direct observation of electron currents driven by the carrier wave of an ultrashort electromagnetic pulse in the band structure of a solid, in general, and of Dirac currents, in particular.

Microscopically, the transient THz electric field accelerates the electrons out of equilibrium, while elastic and inelastic scattering limits their ballistic motion. A quantitative agreement between the momentum distribution extracted from the data

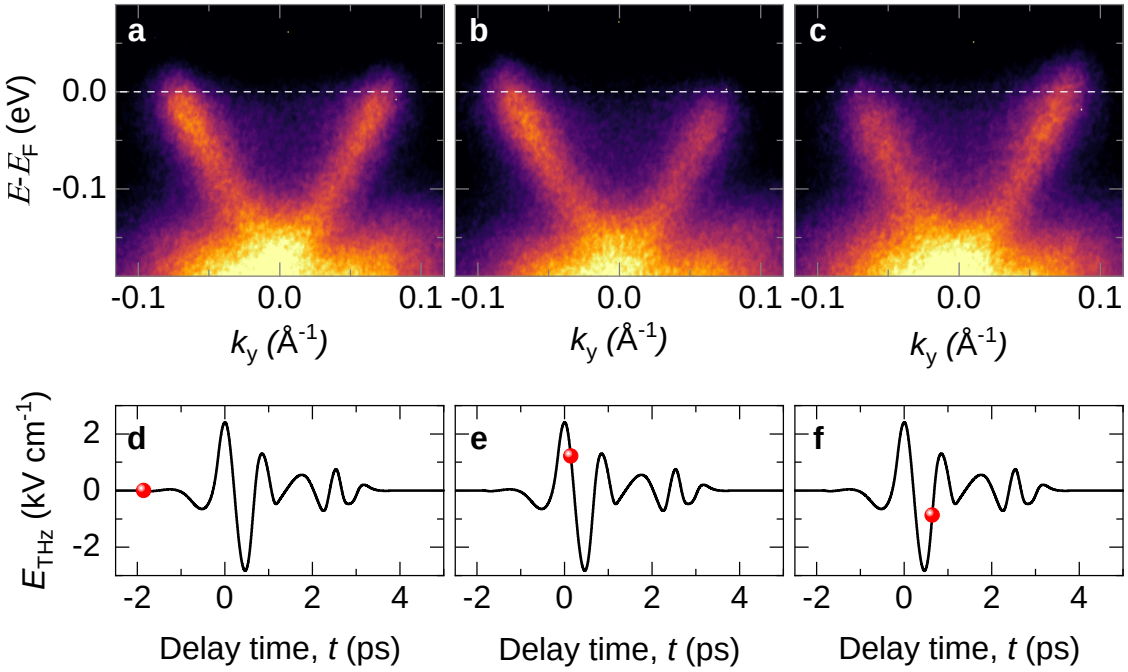

Figure 3.13 | Acceleration of the electrons in the surface band by a *s*-polarized THz waveform. a, **b**, **c**, Photoemission maps before the arrival of the THz field (t = -1.86 ps) (**a**), just after the first positive THz field crest (t = 0.14 ps) (**b**), and right after the negative maximum of the THz electric field (t = 0.64 ps) (**c**). White dashed line, Fermi level for the unperturbed system. **d**, **e**, **f**, THz electric field, E_{THz}, parallel to the surface as reconstructed from the transient momentum shift of the photoelectrons. The red spheres indicate the delay times at which the photoemission maps in panels **a**, **b**, and **c** are taken, respectively.

(see reference [Rei18b]) and a semiclassical Boltzmann model is only achieved if the relevant scattering times are kept above 1 ps. In combination with the relativistic band dispersion, these long scattering times foster extremely large current densities. Even for the moderate THz electric fields of $E_{\mathrm{THz}} = 2.4 \pm 0.5\,\mathrm{kV\,cm^{-1}}$, a large displacement of the Fermi circle is observed, that leads to a maximum momentum shift of $\Delta k = 0.005\,\mathrm{Å}^{-1}$. This corresponds to a peak surface current density of up to $2\,\mathrm{A\,cm^{-1}}$.

Figure 3.14b displays the subcycle evolution of the current density, $j(t)$, together with the instantaneous THz electric field, $E_{\mathrm{THz}}(t)$. The dynamics bear the fingerprint of ballistic acceleration: $j(t)$ increases monotonically during the onset of the

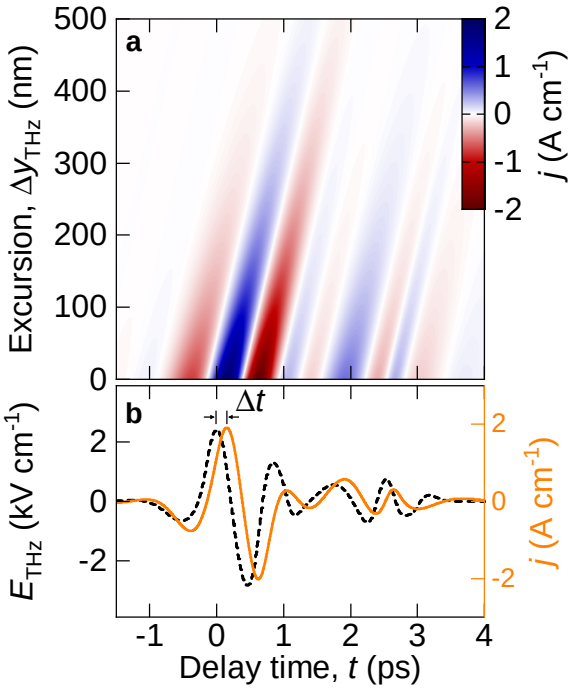

Figure 3.14 | Local current density in Bi_2Te_3. **a**, Calculated current density, j (color scale), as a function of the delay time, t, and the electron excursion, Δy_{THz}, in the surface layer of Bi_2Te_3. The excursion was evaluated employing the extracted scattering times of the charge carriers in the topologically protected surface state. The intense THz fields ballistically drive Dirac fermions over several 100 nm. **b**, Temporal evolution of the current density, $j(t)$, calculated for scattering times of 1 ps (orange solid line). The THz driving field extracted from the experiment (dashed black curve) shows a delay, Δt.

first intense THz half cycle. While $E_{THz}(t)$ decreases for $t > 0$ ps, $j(t)$ keeps rising and reaches its maximum at $t = 0.14$ ps, shortly before the reversal of the THz driving field. This behavior, which also occurs for all other THz half cycles, is only expected when the influence of scattering on the Dirac current is weak. The extracted scattering rates exceed coherence times previously observed for lightwave-driven electron dynamics in dielectrics and semiconductors [Hoh15, Lan16, Gar16, Liu17] by orders of magnitude and attest to a reduced scattering phase space owing to spin-momentum locking.

These unique transport dynamics of topological Dirac fermions elevate carrier wave electronics to the next, fully ballistic level. In contrast to massive quasiparticles populating the parabolic bands of conventional dielectrics, the acceleration of quasirelativistic topological surface states is inertia free as the group velocity of Dirac fermions is very high from the outset. Hence, THz-accelerated Dirac fermions may coherently propagate over several 100 nm before undergoing scattering (see Figure 3.14a). This scale exceeds electron excursions in dielectrics [Hoh15, Lan16, Gar16, Liu17] as well as the typical diameters of gate regions of contemporary transistors by orders of magnitude. Therefore, future electronic devices based on three-dimensional topo-

logical insulators may allow for an all-coherent electron transfer at THz clock rates whereas the underlying subcycle currents might become accessible to complementary real-space measurements [Kas15, Kie20].

3.4 Topological lightwave-electronics at optical clock rates

The novel concept of subcycle ARPES demonstrated in the last paragraph provides the most straightforward way of studying lightwave acceleration as carrier dynamics can be traced directly in the band structure. Thereby, the coherent Dirac currents observed in the surface band of Bi_2Te_3 are driven by THz pulses with peak electric field amplitudes of only a few $\mathrm{kV\,cm^{-1}}$. The experiments presented in this section are intended to shine light onto the complex quantum motion of Dirac electrons that are accelerated by intense, phase-stable lightwaves in the mid-infrared spectral range featuring peak electric fields, which can compete with inner-atomic binding potentials [Sel08, Sch14, Hoh15, Lan17]. Applying such intense multi-THz light pulses to conventional semiconductors and dielectrics leads to the observation of non-perturbative nonlinearities like high-harmonic generation [Ghi11, Sch14, Hoh15]. According to theory, the underlying electron dynamics is governed by a complex interplay of intraband acceleration and interband excitation and also includes quantum path interferences between several bands (see also section 3.1.2 and reference [Kir06, Sch14, Hoh15, Lan17]).
Now, by combining time-resolved ARPES with an intense multi-THz driving field exceeding $1\,\mathrm{MV\,cm^{-1}}$, the microscopic carrier dynamics can be traced on a subcycle timescale and in the band structure itself. The experiments presented in this section have been performed in a close collaboration with *Suguru Ito*, *Jens Güdde* and *Ulrich Höfer* from the University of Marburg.

3.4.1 Experimental setup for multi-THz subcycle ARPES

Intense, phase-stable few-cycle pulses in the multi-THz spectral region have already been utilized to accelerate electrons through a solid [Sch14, Lan17], recollide electron-hole pairs [Zak12, Lan16] and even switch internal quantum attributes

such as the valley pseudospin [Lan18b], on ultrashort timescales. Following these processes on their natural timescale provides unique insights into strong-field light-matter interaction [Hoh15, Lan16]. Especially in materials with a nontrivial electronic structure such as topological insulators, a full subcycle band structure analysis is required to understand the complex lightwave-driven electron motion. The novel optical setup established in this thesis utilizes intense, multi-THz transients with peak electric fields in excess of $1\,\mathrm{MV\,cm^{-1}}$ to drive coherent carrier dynamics in the three-dimensional topological insulator Bi_2Te_3, while simultaneously tracing it directly in reciprocal space by time-resolved ARPES.

Generation of ultrashort probe pulses

The time-resolved detection of lightwave-driven carrier dynamics requires ultrashort probe pulses with a pulse duration much shorter than one oscillation period of the driving waveform [Hoh15, Lan16]. In the case of driving fields in the multi-THz spectral region, the duration of these ultrashort probe pulses has to be on the order of only a few femtoseconds. The time-bandwidth-product, which reads $\Delta\tau\Delta\nu \geq 0.441$ for a Gaussian pulse profile [Die06], links the pulse duration $\Delta\tau$ and the spectral bandwidth $\Delta\nu$ of a light pulse. Thus, such ultrashort gating pulses need to have a broadband spectrum.

A well established method for spectral broadening is the so-called *supercontinuum* or *white-light generation* [Alf06]. Thereby, octave-spanning spectra, which have a high spatial and temporal coherence and stability, are generated by focusing intense light pulses into a nonlinear transparent medium [Bra09]. The microscopic driving mechanism behind this phenomenon is governed by a complex interplay of numerous nonlinear processes such as self-phase modulation, self-steepening, self-focusing and filamentation [Alf06, Ber07, Cou07, Bra09]. Above a certain threshold of the intensity, however, effects like multi-photon absorption, multi-filamentation and plasma formation destroy the overall spatio-temporal coherence and limit a further increase of the supercontinuum power [Che16]. An optical breakdown can even lead to a damage of the material [Cou07, Lu14]. As a consequence, the pulse energy of bulk continua remains below a microjoule [Lu14].

In this chapter, the coherent carrier dynamics induced by an intense multi-THz

driving field shall be probed by time-resolved ARPES on a subcycle timescale. For the photoemission of Dirac electrons out of the topological surface state of Bi_2Te_3, ultrashort gating pulses in the UV spectral range are required, which also feature a duration of only a few femtoseconds. For this purpose, very intense, ultrashort near-infrared pulses are generated by a *multi-plate continuum* (MPC) generation scheme [Lu14, Che16, Lu19], which are subsequently converted to a center wavelength of $\lambda_{UV} = 413\,\text{nm}$ by second-harmonic generation [Boy03]. The multi-plate continuum process is based on sequential spectral broadening within thin plates, which are strategically placed at or near the beam waist of a weakly focused near-infrared laser beam. By limiting the thickness of the nonlinear medium, one can still seize the effect of self-phase modulation to obtain a broad spectrum, but the pulse exits the crystal before (multi-)filamentation or damage of the material occurs. In general, this cascaded spectral broadening can be repeated as long as the pulse power and intensity is above the threshold for filamentation. The resulting intense, broadband continua also exhibit an excellent spectral and temporal coherence [Lu14, Che16].

Figure 3.15 shows a schematic illustration of the experimental setup used for the generation of ultrashort gating pulses. The near-infrared laser pulses from the titanium-sapphire amplifier system (see section 2.2), which feature a pulse duration of $\tau = 31\,\text{fs}$, are focused by a calcium fluoride lens (L) with a focal length of $f = 100\,\text{cm}$. The pulse energy can be controlled by a half-wave plate ($\lambda/2$) and a thin film polarizer (P), whereas the focusing condition is fine-tuned with the help of an adjustable iris aperture (A1). In the following, four crystalline quartz plates, two of them with a thickness of 200 µm and two with a thickness of 100 µm, are placed at Brewster's angle at the beam waist of the focused near-infrared beam. This configuration facilitates the largest spectral broadening while simultaneously maintaining the transversal Gaussian mode profile. While the pump spectrum features a full-width at half maximum of the intensity of 36.3 nm (see Figure 3.16a, black solid line), the multi-plate continuum generated by self-phase modulation within the thin quartz plates (see Figure 3.16a, red shaded area) is significantly broader and exhibits a spectral bandwidth of 70 nm (see Figure 3.16a, black dashed line). To maximize the generated spectral width while avoiding optical damage and filamentation inside the quartz plates, the near-infrared pump pulse energy is tuned to 100 µJ. The

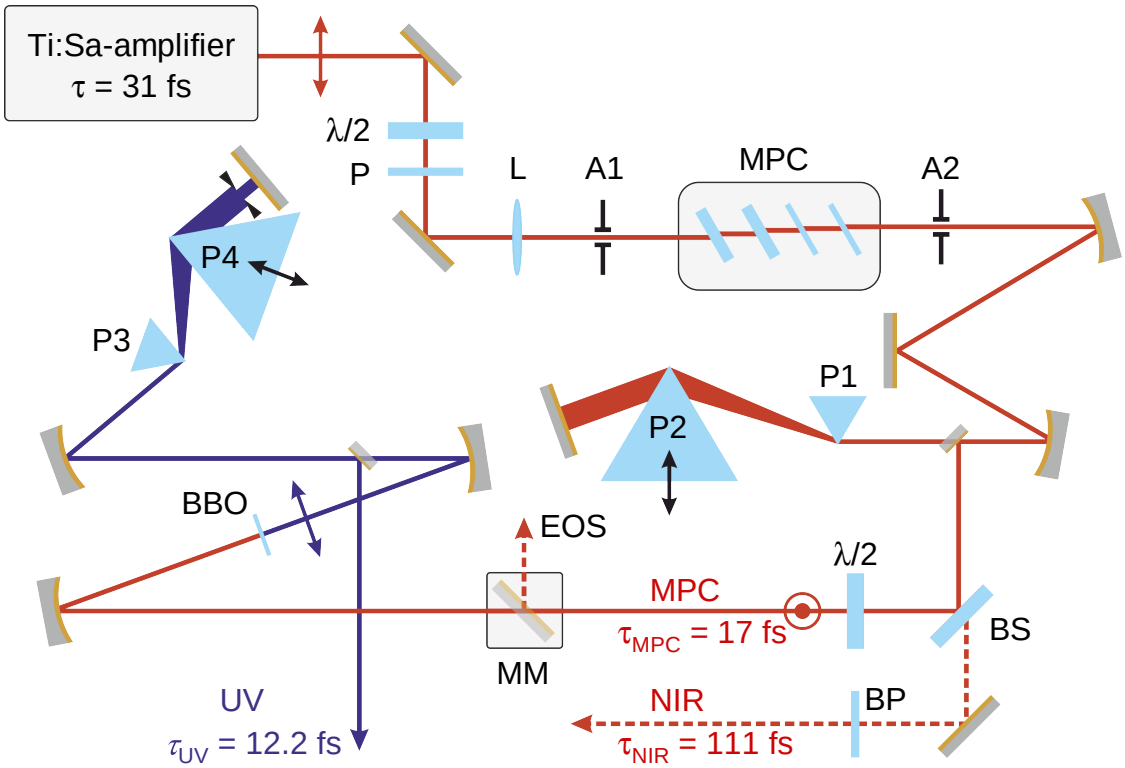

Figure 3.15 | Experimental setup for the generation of ultrashort gating pulses. A half-wave plate ($\lambda/2$) and a polarizer (P) control the pulse energy of the horizontally polarized laser pulses from the Ti:sapphire laser system with a pulse duration of $\tau = 31\,\mathrm{fs}$. The lens L focuses the beam, whereas the aperture A1 defines the focus condition. The bandwidth of the near-infrared pulses is broadened by self-phase modulation in four crystalline quartz plates, which are placed in the focus under Brewster's angle. The resulting multi-plate continuum (MPC) (see Figure 3.16a) is spatially cut by aperture A2 and collimated by a spherical mirror. After compression in the prism compressor consisting of the prisms P1 and P2, the pulses have a pulse duration of $\tau_{\mathrm{MPC}} = 17\,\mathrm{fs}$ as determined by SHG-FROG measurements (see Appendix D). A 90 % beamsplitter BS divides the beam in a weak probe arm (NIR, red dashed line), and a strong generation arm (MPC, red solid line), used for second-harmonic generation in the nonlinear BBO crystal (thickness, 30 µm). The polarization of the MPC beam is rotated by a half-wave plate ($\lambda/2$) to be vertical. The generated second-harmonic pulses (blue solid line) are centered around $\lambda_{\mathrm{UV}} = 413\,\mathrm{nm}$ (see Figure 3.16b). After compression in the prism compressor consisting of the prisms P3 and P4, they feature a pulse duration of $\tau_{\mathrm{UV}} = 12.2\,\mathrm{fs}$ (see Figure 3.17). A removable fused silica window (MM) splits off a small fraction of the MPC beam to serve as gating pulses for the electro-optic detection of the multi-THz waveforms (see Figure 3.19). The weak near-infrared arm (NIR) is spectrally cut by a bandpass filter (BP) with a center wavelength of 790 nm and a bandwidth of 10 nm. SHG-FROG measurements reveal a pulse duration of $\tau_{\mathrm{NIR}} = 111\,\mathrm{fs}$.

generated white-light pulses are spatially cut with aperture A2 and subsequently collimated by a spherical mirror. After that, they are guided into a double-pass prism compressor, which is designed to compensate the group-velocity dispersion or temporal chirp, which is imprinted on the multi-plate continuum pulses during the propagation through the crystalline quartz plates. For this purpose, a spherical mirror focuses the beam through two UV fused silica prisms (P1 and P2) on a planar end mirror placed in the focal plane. By propagating through the prisms, the low-frequency part of the spectrum passes more material and thus experiences a larger delay than the high-frequency components. Depending on the position of prism P2, the material passage and consequently the compensation of the imprinted temporal chirp can be fine tuned. After passing the prism compressor and the spherical mirror in the reverse direction with a slight vertical offset, the re-collimated MPC beam is picked off. The multi-plate continuum contains a pulse energy of 25 µJ and features an intensity FWHM of $\tau_{\mathrm{MPC}} = 17\,\mathrm{fs}$, which makes it a useful tool for the time-resolved detection of multi-THz waveforms by electro-optic sampling (see Figure 3.19). The exact pulse width has been determined using second-harmonic generation frequency-resolved optical gating (SHG-FROG) (see Appendix D).
Next, the main part of the multi-plate continuum, which is reflected at a 90:10 beamsplitter, is frequency-doubled by second-harmonic generation [Boy03]. For this purpose, the beam is transmitted through a half-wave plate ($\lambda/2$) that rotates the polarization by 90° and subsequently focused into a β-barium borate (BBO) crystal with a thickness of 30 µm. Owing to its high optical nonlinearity, a high damage threshold and the relatively flat dispersion in the near-infrared spectral range, BBO is the ideal material for second-harmonic generation [Eim87]. To ensure minimal reflection losses and phase matching under normal incidence, the thin nonlinear crystal is cut at an angle of 29.2° with respect to its optical axis. Figure 3.16b shows the resulting ultraviolet spectrum with a center wavelength of $\lambda_{\mathrm{UV}} = 413\,\mathrm{nm}$ and a full-width at half maximum of the intensity of 24 nm, corresponding to a bandwidth-limited pulse duration of 10 fs.
On their way to the sample, the ultrashort UV probe pulses propagate through an indium-tin-oxide-coated fused silica window, which serves as a dichroic beam combiner of the UV pulses and the multi-THz waveforms. Furthermore, both laser pulses enter the ultra-high vacuum chamber through a diamond window with a thickness

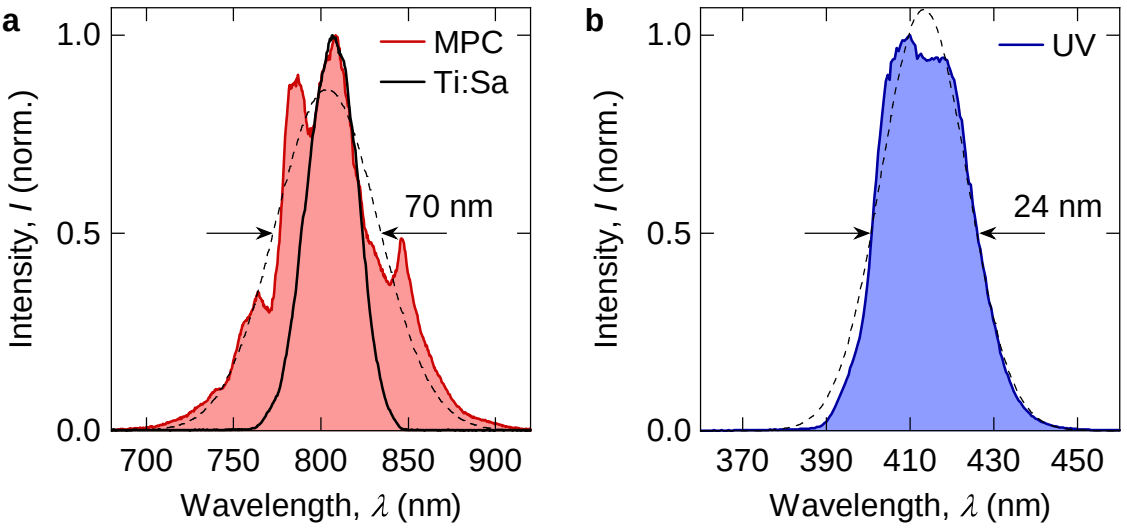

Figure 3.16 | Spectra of the ultrashort gating pulses. **a**, Spectrum of the multi-plate continuum (red shaded area) generated by self-phase modulation within four crystalline quartz plates. Whereas the spectrum of the fundamental near-infrared pulses from the titanium-saphhire amplifier system (black solid line) exhibits a bandwidth of only 36.3 nm, the multi-plate continuum spectrum has a FWHM of the intensity of 70 nm (black dashed line). Both spectra are centered around $\lambda_c = 807$ nm. **b**, Spectrum of the ultrashort ultraviolet gating pulses with a center wavelength of $\lambda_{UV} = 413$ nm and a FWHM of the intensity of 24 nm.

of 1065 µm. This leads to a temporal chirp, which significantly increases the pulse duration of the ultrashort UV probe pulses. Thus, another double-pass prism compressor consisting of the two UV fused silica prisms (P3 and P4) is implemented to allow for a precise dispersion management.

In order to obtain a bandwidth-limited UV pulse duration at the sample position inside the ARPES chamber, the pulses are characterized outside the vacuum chamber by cross-correlation frequency resolved optical gating (XFROG). To mimic the group-delay dispersion imprinted on the ultrashort probe pulses in the real experiment, the UV beam is transmitted through a indium-tin-oxide-coated fused silica window with a thickness of 1 mm and a diamond window with a thickness of 1065 µm. The near-infrared beam, which is transmitted at the beam splitter BS (see Figure 3.15, red-dashed line), is spectrally cut by using a band pass filter with a center wavelength of $\lambda_c = 790$ nm and a bandwidth of 10 nm. An SHG-FROG measurement of the near-infrared beam reveals a pulse duration of $\tau_{NIR} = 111$ fs

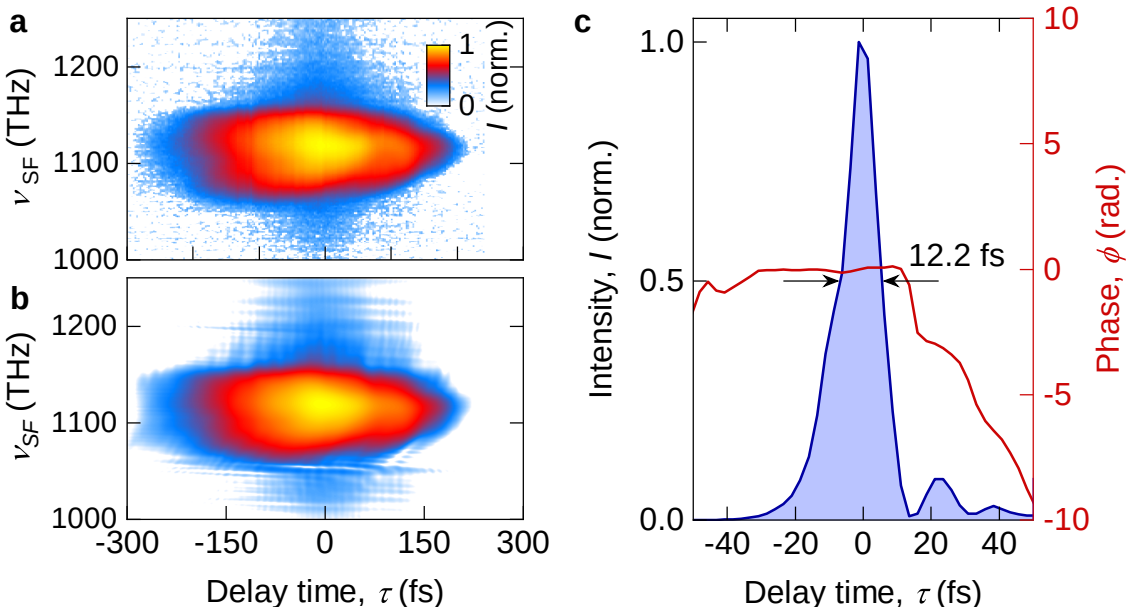

Figure 3.17 | Characterization of the ultrashort UV gating pulses. a, Measured XFROG trace. The intensity of the sum-frequency, $I(\tau, \nu_{SF})$, of the ultrashort UV and the near-infrared gating pulses is shown as a false color plot and as a function of the sum-frequency, ν_{SF}, and the relative delay time, τ, between the two pulses. **b**, Computed XFROG trace by a numerical reconstruction algorithm. Color scale, see **a**. **c**, Reconstructed intensity envelope of the UV gating pulses (blue shaded area) with a FWHM pulse duration of $\tau_{UV} = 12.2\,\text{fs}$. Red solid line, temporal phase, ϕ.

(see Appendix D). Subsequently, the UV pulse and the near-infrared pulse are spatially superimposed with a dichroic beam combiner and focused into a BBO crystal with a thickness of 10 µm to generate their sum-frequency as a nonlinear cross-correlation signal [Boy03]. For phase-matching purposes, the BBO crystal is cut at an angle of 44.3° with respect to its optical axis. Detecting the sum-frequency intensity, $I(\tau, \nu_{SF})$, as a function of the delay times, τ, between the UV pulse and the near-infrared gating pulse, and the sum-frequency, ν_{SF}, yields a full two-dimensional spectrogram as shown in Figure 3.17a. Thereby, $\tau = 0$ indicates the optimal temporal overlap of the two pulses, where $I(\tau, \nu_{SF})$ peaks. An iterative numerical algorithm [Kan93, Kan99, Wya08, Mon10] deconvolves both pulses and retrieves the temporal shape of the unknown UV pulse. As is apparent from Figure 3.17a and b, the reconstructed sum-frequency trace resembles the measured one to a very high degree of congruency, which denotes a valid extraction of the temporal structure of

the pulses. Figure 3.17c depicts the retrieved intensity envelope of the ultrashort UV pulse, which reveals a FWHM pulse duration of $\tau_{\mathrm{UV}} = 12.2 \pm 1.0\,\mathrm{fs}$ and a very flat temporal phase, ϕ. Thus, the optimization of the pulse dispersion with the help of the double-pass compressor yields nearly bandwidth-limited UV pulses with a pulse energy of up to 2 µJ, which are ideally suited as an ultrashort probe for the lightwave-driven carrier dynamics in Bi_2Te_3.

Generation of intense, phase-stable multi-THz waveforms

The second ingredient for the subcycle observation of lightwave-driven Dirac currents are intense few-cycle light pulses in the multi-THz spectral region. Figure 3.18 shows the experimental setup, that is capable of generating intense multi-THz transients with center frequencies between 20 and 60 THz and pulse energies of up to $E_{\mathrm{p,THz}} = 5\,\mu\mathrm{J}$. The starting point is the titanium-sapphire amplifier system that has been explained in greater detail in section 2.2. Now, the ultrashort laser pulses with a center wavelength of $\lambda_{\mathrm{c}} = 807\,\mathrm{nm}$ and a pulse energy of $E_{\mathrm{p}} = 4.4\,\mathrm{mJ}$ are used to operate a dual double-stage optical parametric amplifier (OPA), where the light is converted to longer wavelengths. For the purpose of wavelength tunability, a small part of the incoming radiation is focused into a sapphire crystal to generate a broadband white-light continuum, which is then selectively amplified in two consecutive parametric processes. The spectral components of the generated white-light continuum are temporally chirped on purpose by the propagation through a zinc selenide window. By varying the temporal overlap of the white-light seed and the intense titanium-sapphire pump pulses in the nonlinear bismuth borate (BiBO) crystals, different wavelengths can be selectively amplified within the nonlinear $\chi^{(2)}$-process of optical parametric amplification [Tza12, Pet10]. The commercial OPA system has two output arms, which provide ultrashort signal pulses with an independently tunable center wavelength between 1.1 µm and 1.7 µm and pulse energies of up to 0.5 mJ, each. As the two beams originate from the same supercontinuum, they are perfectly phase-correlated and can therefore be used for the generation of inherently, phase-stable multi-THz pulses [Sel08]. For this purpose, the two frequency-detuned near-infrared pulses from the signal outputs of the dual OPA are mixed in a nonlinear generation crystal [Sel08, Sch14]. According to the nonlinear $\chi^{(2)}$-process of

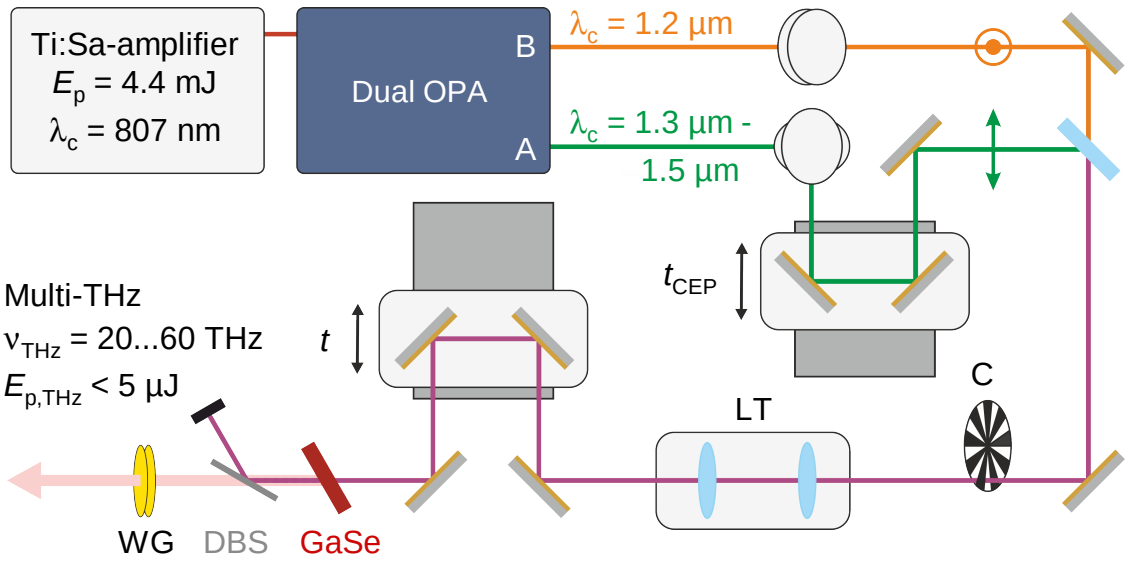

Figure 3.18 | Schematic of the generation of intense multi-THz waveforms. The double stage optical parametric amplifier is seeded with the near-infrared pulses from the titanium-sapphire laser system with a center wavelength of 807 nm, and a pulse energy of 4.4 mJ. The two output arms A (green solid line) and B (orange solid line) are phase-correlated and can be tuned independently of each other between 1.1 µm and 1.7 µm. Once guided over a polarization rotating periscope and a variable delay line t_{CEP}, arm A is superimposed with arm B through a dichroic mirror. The lens telescope LT consisting of two calcium fluoride lenses decreases the beam diameter of the superimposed beams by a factor of three. In the gallium selenide (GaSe) generation crystal with a thickness of 434 µm, the two beams interact with each other according to the nonlinear process of difference frequency generation. With the help of a dichroic beam splitter (DBS), namely a Germanium wafer, the fundamental beams are separated from the generated THz pulses. Depending on the phase matching angle, multi-THz transients with a center frequency, ν_{THz}, between 20 and 60 THz and pulse energies, $E_{p,THz}$, of up to 5 µJ are generated. A second delay line in the THz generation arm controls the temporal overlap, t, between the THz pump and the UV probe pulse, used for the subcycle multi-THz ARPES experiments presented in section 3.4.3.

difference frequency generation (DFG), the two waves cause a beating in the nonlinear polarization, which oscillates at their difference frequency [Boy03]. If the pulses used for the DFG are phase-correlated, the emitted pulses are inherently phase-stable, whereas the carrier-envelope phase of the generated THz pulses can be precisely controlled by changing the phase of one of the generation pulses.

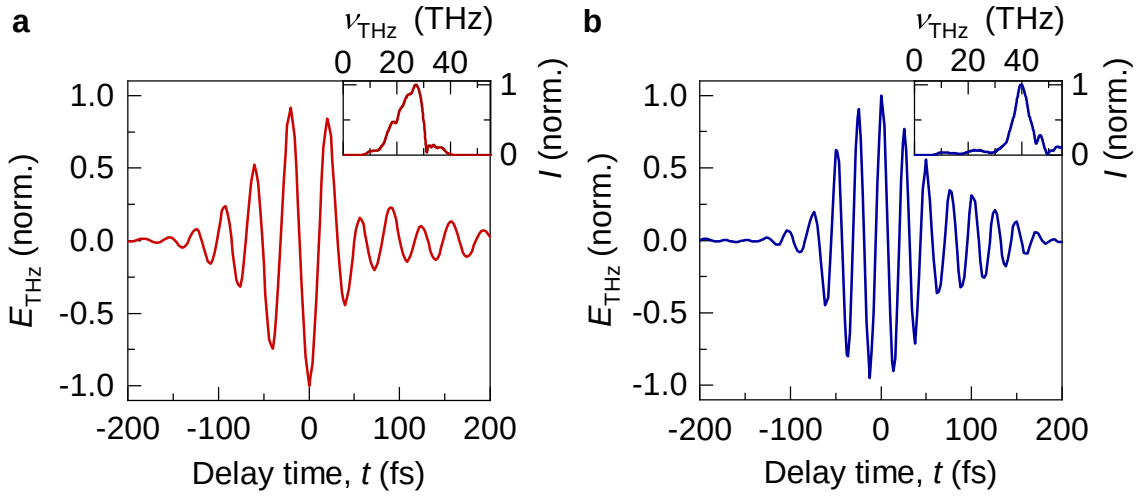

Figure 3.19 | Characterization of the multi-THz transients. Electro-optically detected multi-THz fields, E_{THz}, as a function of the delay time, t, for different phase matching conditions of the gallium selenide generation crystal. Inset: Corresponding spectral amplitude of the THz waveforms showing a center frequency of **a** 27 THz and **b** 40 THz.

To generate the intense, phase-stable pulses in the multi-THz region, which are utilized for the subcycle experiments performed in this chapter, the two OPA outputs are detuned in such a way, that their frequency difference exactly matches the desired THz center frequency. To obtain multi-THz transients with a center frequency between 20 THz and 60 THz the signal branch B is set to a center wavelength of 1.2 µm, whereas the OPA output A is variably tuned between 1.3 µm and 1.5 µm. A polarization-rotating periscope in the beam path of signal branch A rotates the polarization of the pulses of arm A by 90°, such that the two near-infrared beams are perpendicularly polarized with respect to each other. This ensures the type-II phase-matching condition for DFG in the nonlinear generation crystal [Boy03]. In order to control the temporal overlap, t_{CEP}, of the two pump pulses and, hence, also the carrier-envelope phase, ϕ_{CEP}, of the generated multi-THz-transients, the OPA arm A is guided over a variable delay line. Afterwards, the two beams are collinearly superimposed with the help of a dichroic mirror. A second delay line in the THz generation arm sets the temporal overlap, t, between the multi-THz pump and the UV probe pulse used for the subcycle multi-THz ARPES experiments presented in section 3.4.3.

A lens telescope (LT) consisting of two calcium fluoride lenses decreases the beam diameter by a factor of three, before the generation pulses co-propagate through a gallium selenide emitter crystal with a thickness of 434 µm. With its large nonlinearity and a broad transparency range, gallium selenide serves as the ideal, widely tunable source for high-intensity, mid-infrared waveforms [Sel08, Sch14]. Thereby, the center frequency of the emitted multi-THz radiation can be fine-tuned by rotating the nonlinear crystal, which in turn changes the phase matching condition. The fundamental near-infrared pump pulses and the generated THz radiation are separated by a dichroic beam splitter (DBS). For this purpose, a germanium wafer is put in the beam path under the Brewster angle for the multi-THz pulses. At room temperature, the band gap energy of germanium is 0.67 eV, which corresponds to a frequency of about 160 THz. Thus, the low-frequency THz radiation is completely transmitted, whereas the near-infrared pump light is fully reflected or absorbed. In this way, intense multi-THz waveforms with a variable center frequency, ν_{THz}, between 20 THz and 60 THz and pulse energies of up to $E_{\mathrm{p,THz}} = 5\,\mu\mathrm{J}$ can be generated.

Figure 3.19 shows the electric field, E_{THz}, of typical few-cycle THz transients detected by electro-optic sampling (see section 2.2). Thereby, a small fraction of the multi-plate continuum beam, which is split off by a fused silica window (see Figure 3.15, MM), serves as an ultrashort probe. The corresponding amplitude spectra (see Figure 3.19, insets) exhibit a center frequency of $\nu_{\mathrm{THz}} = 27\,\mathrm{THz}$ and $\nu_{\mathrm{THz}} = 40\,\mathrm{THz}$, respectively. Independent of the center frequency, the generated multi-THz pulses exhibit a full width at half maximum of their intensity envelope of about $\tau_{\mathrm{THz}} = 70\,\mathrm{fs}$. With their electric fields as large as several $\mathrm{MV\,cm^{-1}}$ and a precisely adjustable carrier-envelope phase, these intense, phase-stable multi-THz waveforms are the perfect tool for the strong-field lightwave control of Dirac currents in Bi_2Te_3.

Time-resolved ARPES under strong THz-fields

In the following, the intense multi-THz waveforms are supposed to serve as an ultrafast bias voltage to accelerate electrons in the surface state of the topological insulator Bi_2Te_3, whereas the ultrashort UV pulses simultaneously release electrons out of the sample surface by two-photon photoemission [Wei02, Güd07, Rei14]. Figure 3.20

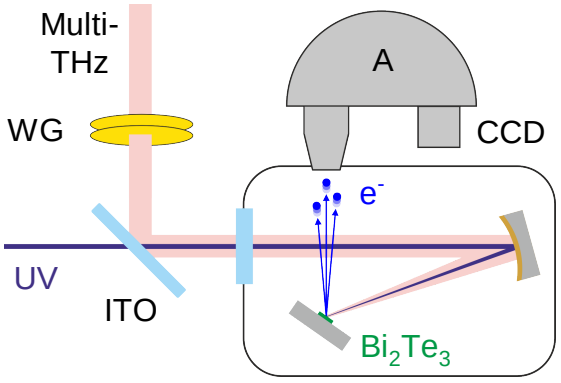

Figure 3.20 | Schematic of the multi-THz ARPES setup. Before the UV probe (blue solid line) and the multi-THz pump beam (red solid line) are coupled into the ARPES chamber, they are spatially superimposed with the help of an indium-tin-oxide-coated fused silica window (ITO). A pair of wire-grid polarizers (WG) controls the pulse energy and the polarization state of the multi-THz pulses. After transmission through the diamond window of the vacuum chamber, a spherical mirror focuses the two beams onto the Bi_2Te_3 sample. The kinetic energy and the emission angle of the photoemitted electrons (e^-) are measured by a hemispherical electron analyzer (A).

shows a schematic of the newly developed experimental setup for angle-resolved photoelectron spectroscopy with subcycle resolution. Here, an indium-tin-oxide-coated fused silica window serves as a dichroic beam combiner and is used to spatially overlap the intense multi-THz pump pulses with the UV probe pulses. Their temporal overlap, t, can be varied with the help of a mechanical delay stage in the multi-THz beam path (see Figure 3.18). In the experiment, a pair of wire-grid polarizers (WG), precisely controls the peak field amplitude and the polarization state of the multi-THz waveform. The fluence of the UV light is set by a continuously variable neutral density filter wheel, such that space charge effects are suppressed [Zho05]. Subsequently, the temporally and spatially overlapped multi-THz pump and p-polarized UV probe pulses are transmitted through a diamond window with a thickness of 1065 µm into a μ-metal shielded ultra-high vacuum chamber at a base pressure of $4 \cdot 10^{-11}$ mbar. A spherical UV-grade aluminum mirror with a focal length of $f = 75$ mm mounted in the ultra-high vacuum chamber is used to focus both beams under an angle-of-incidence of 53° onto the Bi_2Te_3 sample.
The electrons (e^-), emitted by two-photon photoemission, are then collected perpendicular to the plane of light incidence by a hemispherical electron analyzer (A) with

a display-type detector (CCD). The energy resolution of the setup is $\approx 130\,\mathrm{meV}$, which is mainly limited by the bandwidth of the ultrashort UV probe pulses. Energy and momentum shifts of photoelectrons can be determined with an accuracy of $3\,\mathrm{meV}$ and $0.004\,\mathrm{Å}^{-1}$, respectively.

3.4.2 THz-field reconstruction by photoelectron streaking

The novel experimental setup introduced in the last paragraph makes it possible to directly observe how the carrier wave of an intense multi-THz pulse accelerates Dirac fermions in the band structure of the topological surface state of Bi_2Te_3. Figure 3.21a shows a schematic illustration of the general experimental concept. The ultrashort UV probe pulses (blue) with a pulse duration of $\tau_{\mathrm{UV}} = 12.2 \pm 1.0\,\mathrm{fs}$ and a center wavelength of $\lambda_{\mathrm{UV}} = 413\,\mathrm{nm}$ are used to release electrons out of the surface of a single-crystal of Bi_2Te_3 (see section 3.2.2) by two-photon photoemission. An electrostatic hemispherical electron analyzer, equipped with a charge-coupled device (CCD) detector, then images the relation between the kinetic energy and the momentum, $k_y = k_{||}$, of the photoelectrons parallel to the sample surface. In addition to that, a strong multi-THz electric field, E_{THz}, is focused onto the surface to accelerate the Dirac fermions, which is expected to shift the electron occupation in momentum space along the field direction (see Figure 3.21b). In addition, the photoemitted electrons can also interact with the intense multi-THz field in the vacuum. Depending on the polarization of the multi-THz waveform, this acceleration of the photoemitted electrons can change their kinetic energy as well as their parallel momentum. As shown in Figure 3.21c, owing to this so-called *streaking effect*, the photoemission map appears offset in E as well as in k_y. As the pulse duration of the UV probe pulse is much smaller than the oscillation period of the multi-THz driving field, the THz electric field components perpendicular and parallel to the sample surface can be determined by tracking the lightwave-induced energy streaking, E_{streak}, and momentum streaking, k_{streak}, similar to the sampling of near-infrared lightwaves by attosecond pulses [Nep15].
In the work by Reimann *et al.* [Rei18b], it has been shown, that the relative strength of intraband acceleration and streaking in vacuum can be controlled by the THz polarization. Thereby, a *p*-polarized THz electric field (see Figure 3.21a, orange

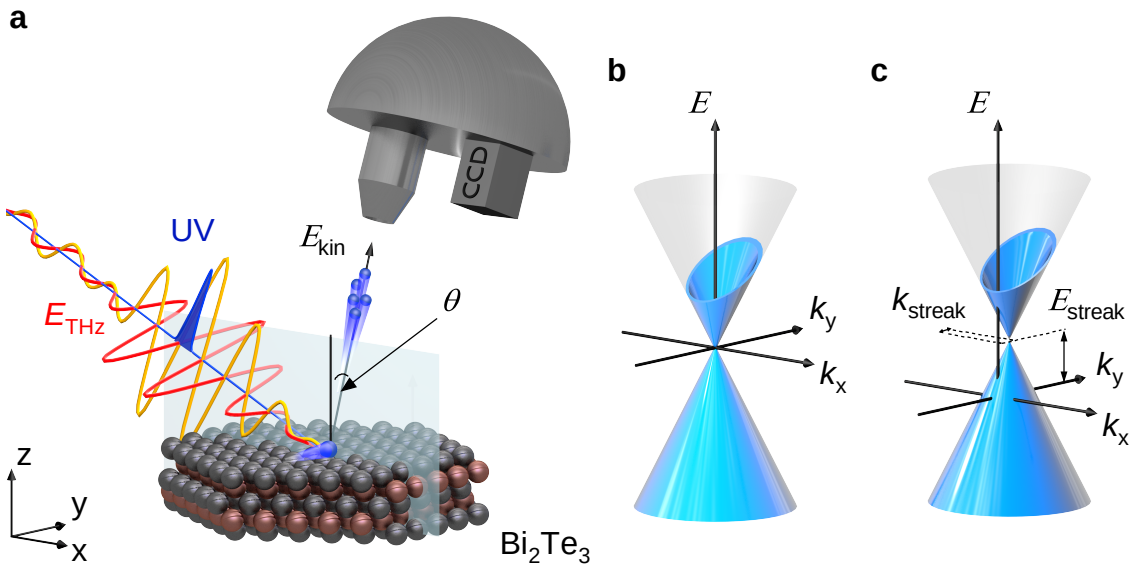

Figure 3.21 | Concept of subcycle multi-THz ARPES. a, Electrons (blue sphere) in the topological surface state of Bi_2Te_3 (crystal lattice; bronze spheres, Bi atoms; gray spheres, Te atoms) are accelerated by an intense linearly polarized multi-THz field, E_{THz} (red waveform, *s*-polarization; orange waveform, *p*-polarization) and are photoemitted by a short time-delayed *p*-polarized UV pulse (blue). The kinetic energy, E_{kin}, and the emission angle, θ, of the liberated electrons are measured by a hemispherical electron analyzer to determine the binding energy and the parallel momentum, $k_{||} = k_y$, of the electrons in the topological surface band along the $\overline{\Gamma}$-$\overline{K}$-direction. The plane of incidence (x-z-plane) is indicated by a transparent rectangle. **b**, Lightwave acceleration of electrons in the Dirac cone can shift the Fermi surface. **c**, The interaction of the photoemitted electrons with the electric field of the multi-THz waveform in vacuum can lead to a streaking of the photoemission spectra with an energy shift, E_{streak}, and/or a momentum shift, k_{streak}, of the apparent band structure.

waveform) causes a pronounced energy streaking of the photoemitted electrons, but cannot effectively accelerate Dirac fermions in the surface bands. On the other hand, an intense *s*-polarized multi-THz waveform (see Figure 3.21a, red waveform), which is oriented along the y-direction, in which the electron analyzer detects the electron momentum, $\hbar k_y$, may accelerate electrons in the topologically protected surface state. Consequently, for the time-resolved ARPES experiments presented in paragraph 3.4.3, the polarization of the intense multi-THz waveforms is precisely aligned parallel to the sample surface. In this geometry, the energy streaking is

negligible and momentum streaking is strongly suppressed, owing to the screening of the THz field parallel to the surface [Rei18b]. Nonetheless, the acceleration of the photoemitted electrons by the intense multi-THz electric field, $E_{||}(t)$, in the vacuum still leads to a measurable change of the parallel momentum:

$$k_{\mathrm{streak}}(t) = -\frac{e}{\hbar}\int_{t}^{\infty} E_{||}(t')\mathrm{d}t'. \tag{3.13}$$

Here, t indicates the time, when the electrons are photoemitted from the surface. This transient momentum streaking, $k_{\mathrm{streak}}(t)$, is independent of the binding energy and the parallel momentum, $k_{||}$, of the electrons inside the material and solely depends on the effective THz electric field, $E_{||}(t)$, parallel to the sample surface. Consequently, $k_{\mathrm{streak}}(t)$ can be used to directly trace the instantaneous multi-THz field parallel to the sample surface [Rei18b]:

$$E_{||}(t) \;=\; \frac{\hbar}{e}\,\frac{\mathrm{d}}{\mathrm{d}t}k_{\mathrm{streak}}(t). \tag{3.14}$$

Here, $\frac{\mathrm{d}}{\mathrm{d}t}k_{\mathrm{streak}}(t)$ is the time derivative of the transient momentum shift of the whole photoemission spectrum. Remarkably, even in the presence of a residual p-polarized field component, amplitude and phase of the s-polarized multi-THz waveform can be unambiguously reconstructed from this momentum streaking, as it is exclusively caused by the THz electric field component parallel to the sample surface. Moreover, owing to continuity conditions at the interface, the extracted electric field, $E_{||}(t)$, is equivalent with the multi-THz electric field, $E_{\mathrm{THz}}(t)$, inside the material. Thus, momentum streaking provides an accurate and direct way of determining the actual strength of the acceleration field that acts on the Dirac electrons in the topological surface state.

Figure 3.22a and b display angle-resolved photoemission spectra, $I_{\mathrm{P}}(k_y, E_{\mathrm{kin}})$, for two different delay times, t, between the ultrashort UV probe pulse and the multi-THz driving field, which is in this case predominantly s-polarized, but features a small residual p-component. At a delay time, $t = -138\,\mathrm{fs}$, before the arrival of the multi-THz pulse (see Figure 3.22a), the characteristic V-shaped dispersion of Dirac fermions is faintly visible, which indicates the presence of a topological surface state. The bulk valence band manifests as the broad dispersion at lower energies and fea-

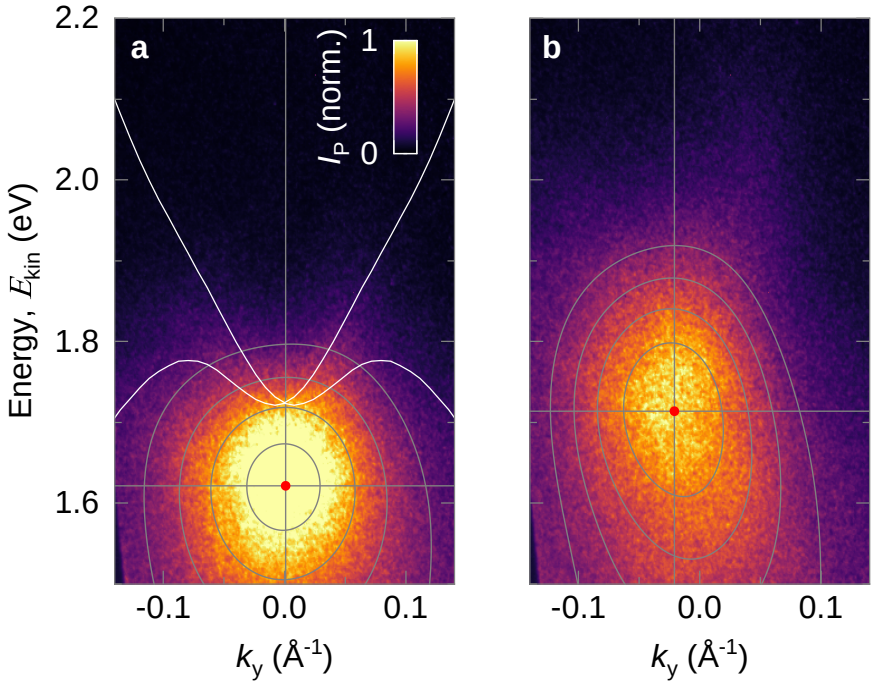

Figure 3.22 | THz-induced streaking of photoelectrons. **a**, Photoemission map taken before the arrival of the THz field ($t = -138\,\mathrm{fs}$) and **b**, at a time delay of $t = 17\,\mathrm{fs}$ after the arrival of the maximum THz electric field. The spectra exhibit a clear energy and momentum streaking induced by the multi-THz field, whereas $E_{\mathrm{streak}} = 0.09\,\mathrm{eV}$ and $k_{\mathrm{streak}} = -0.02\,\mathrm{Å}^{-1}$, respectively. Red dot, intensity maximum of the photoemission spectrum. Gray solid lines, contour lines indicating points with the same intensity. The white solid lines in **a** indicate the topological surface state calculated by density function theory (see also Figure 3.10b).

tures an intensity maximum at $k_y = 0$ and a kinetic energy of $E_{\mathrm{kin}} = 1.62\,\mathrm{eV}$ (see Figure 3.22a, red dot in the center of the contour lines). The Fermi velocity, that can be deduced from the linear dispersion of the Dirac cone, is $v_{\mathrm{F}} = 4.1\,\mathrm{Å\,fs}^{-1}$. As a result of the interaction of the photoemitted electrons with the intense THz electric field in vacuum, at a delay time $t = 17\,\mathrm{fs}$ (see Figure 3.22b), the entire band structure is offset in energy and parallel momentum. This shifts the intensity maximum to $k_y = 0.02\,\mathrm{Å}^{-1}$ and $E_{\mathrm{kin}} = 1.71\,\mathrm{eV}$ (see Figure 3.22b, red dot in the center of the contour lines). For a quantitative reconstruction of the temporal evolution of the electric field parallel to the sample surface, the THz-induced momentum streaking, k_{streak}, is determined by tracing the intensity maximum of the photoemission

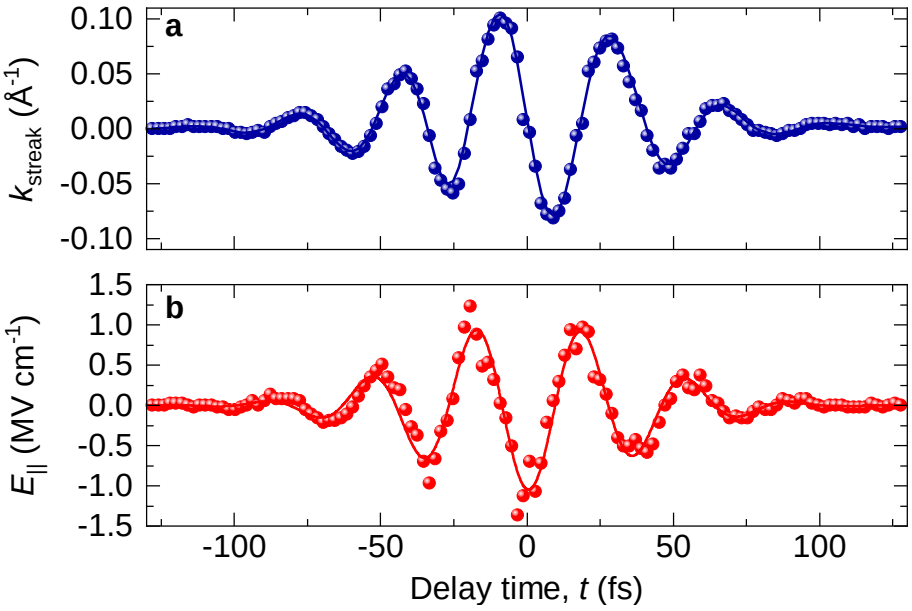

Figure 3.23 | Reconstruction of the THz electric field by momentum streaking. **a**, Parallel momentum streaking, k_{streak}, of the photoemission spectra as a function of the delay time, t, between the multi-THz driving field and the ultrashort UV probe pulse (blue data points). Blue solid line, guide to the eye. **b**, Temporal evolution of the electric field amplitude, $E_{||}(t)$, parallel to the sample surface (red data points) reconstructed from momentum streaking. Red solid line, least mean square fit of the experimental data.

map for each delay time t (see Figure 3.23a). According to equation (3.14), the instantaneous THz-electric field amplitude parallel to the sample surface, $E_{||}(t)$ (see Figure 3.23b), which is equivalent with the multi-THz electric field, $E_{\mathrm{THz}}(t)$, inside the material (see Figure 3.24d-f), can be calculated from the extracted momentum streaking, $k_{\mathrm{streak}}(t)$. Taking into account the averaging effect owing to the finite pulse duration of the UV probe pulse, the retrieved multi-THz waveform exhibits a peak electric field amplitude of $E_{||} = 1.06 \pm 0.10\,\mathrm{MV\,cm^{-1}}$. The corresponding amplitude spectrum shows a center frequency of $\nu_{\mathrm{THz}} = 27.6\,\mathrm{THz}$ (not shown). The fact that the reconstructed multi-THz transient coincides with the waveform determined by electro-optic sampling outside the UHV chamber (see Figure 3.19a), further corroborates the reliability of the field retrieval by streaking. In the next paragraph, these intense multi-THz transients are used to drive both intraband and interband dynamics in the topological insulator Bi_2Te_3. To obtain a clear view at these coherent,

lightwave-driven dynamics inside the material, all photoemission spectra presented in the following are corrected by the THz-induced energy and momentum shift.

3.4.3 Subcyle observation of lightwave-driven intra- and interband dynamics in Bi_2Te_3

Besides the acceleration of the electrons in vacuum, an *s*-polarized THz field can also effectively act on the carriers in the material (see section 3.3.2). Now, the intense multi-THz waveforms with a center frequency of $\nu_{\mathrm{THz}} = 27.6\,\mathrm{THz}$ and electric peak fields exceeding $1\,\mathrm{MV\,cm^{-1}}$ are utilized to coherently drive Dirac electrons within only a few femtoseconds through large fraction of the Brillouin zone. Along the crystallographic $\overline{\Gamma}$-$\overline{\mathrm{M}}$-direction, this coherent acceleration leads to a lightwave-driven charge transfer from surface to bulk states. For an intense THz driving field with a center frequency of $\nu_{\mathrm{THz}} = 40\,\mathrm{THz}$ both a large intraband acceleration as well as an interband excitation are observed directly in reciprocal space.
In order to trace this lightwave-driven carrier dynamics on a subcycle timescale, the UV probe pulses, used to photorelease the electrons out of the surface, have to be shorter than one oscillation period of the multi-THz waveform. As a consequence, these ultrashort pulses feature a broad spectral distribution (see Figure 3.16b, blue shaded area), which limits the energy resolution of the corresponding ARPES spectra. A well-established method to improve the visualization of the band dispersion in photoemission maps is taking the second derivative of the data [Sat01, Qia06, Kim06, Ric10]. Nonetheless, the absolute position of the band features obtained with this analysis method often differ from the actual position in the detected energy-momentum images. Therefore, in this section the so-called *curvature method* is applied to the photoemission maps, which significantly increases the sharpness of the dispersing features of the ARPES intensity image plot, while maintaining their absolute position [Zha11].
In general, in one dimension, the curvature, $C(x)$, associated with a function $f(x)$ can be written as [Zha11]

$$C(x) \sim \frac{\frac{\mathrm{d}^2}{\mathrm{d}x^2} f(x)}{(1 + \left[\frac{\mathrm{d}}{\mathrm{d}x} f(x)\right]^2)^{\frac{3}{2}}}. \tag{3.15}$$

In the case of ARPES spectra, $f(x)$ may correspond to the photoemission intensity and x represents the normalized momentum or energy. As these experimental variables are only defined to an arbitrary factor, equation (3.15) can be rewritten as [Zha11]

$$C(x) \sim \frac{\frac{\mathrm{d}^2}{\mathrm{d}x^2} f(x)}{(C_0 + \left[\frac{\mathrm{d}}{\mathrm{d}x} f(x)\right]^2)^{\frac{3}{2}}}, \tag{3.16}$$

where C_0 is a scaling parameter. Depending on the specific value of C_0, relative variations of the curvature can be highlighted, which significantly increases the visualization of band features in the photoemission maps.
In particular, for $C_0 \gg \left[\frac{\mathrm{d}}{\mathrm{d}x} f(x)\right]^2$, $C(x)$ gives the same result as the second derivative method, whereas for $C_0 \ll \left[\frac{\mathrm{d}}{\mathrm{d}x} f(x)\right]^2$, the curvature $C(x)$ can be expressed as

$$C(x) \sim \frac{\frac{\mathrm{d}^2}{\mathrm{d}x^2} f(x)}{\left[\frac{\mathrm{d}}{\mathrm{d}x} f(x)\right]^3}. \tag{3.17}$$

In this case, $C(x)$ diverges at the extrema of $f(x)$, and the peak position of $C(x)$ approaches the actual peak position of $f(x)$. As the detected ARPES intensity map is a function of energy and momentum, the curvature analysis is extended to two dimensions (for details see reference [Zha11]). Thereby, the photoemission maps are additionally smoothened by a single moving average filter with a box size of 80×80 pixels. C_0 is defined such that the analysis reliably tracks the real band structure, while simultaneously singularities are avoided. This significantly increases the visibility of the dynamics in the topological surface state of Bi_2Te_3 and also improves the relative intensity between the V-shaped dispersion of the topological surface band and the broad distribution of the bulk conduction band (see Figure 3.22a and Figure 3.24a). Applying the curvature method to the subcycle THz-ARPES data recorded with an energy resolution of 45 meV (see section 3.3.2) shows, that the analysis reliably traces the temporal evolution of the lightwave-driven electron deflection in reciprocal space while it overestimates its absolute amplitude (see Appendix E). Therefore, the transient electron excursions extracted from the photoemission spectra, that have been analyzed by the curvature method, are corrected by a constant scaling factor.

Figure 3.24a, b, and c show corrected photoemission spectra along the crystallographic $\overline{\Gamma}$-$\overline{\mathrm{K}}$-direction of Bi_2Te_3 for three different delay times, t, between the s-polarized multi-THz driving field and the UV probe pulse. The reconstructed in-plane electric field amplitude, $E_{\mathrm{THz}}(t)$, of the multi-THz waveform features an electric peak field of $E_{\mathrm{THz}} = 1.06 \pm 0.1\,\mathrm{MV\,cm^{-1}}$ (see Figure 3.24, d-f), whereas the corresponding amplitude spectrum exhibits a center frequency of $\nu_{\mathrm{THz}} = 27.6\,\mathrm{THz}$ (not shown). The recorded photoemission spectrum before the arrival of the intense multi-THz pulse ($t = -138\,\mathrm{fs}$) presented in Figure 3.24a illustrates an undisturbed, in k_y symmetrical, equilibrium distribution of the electrons in the upper, occupied part of the topological surface state. The Dirac point is located 200 meV below the Fermi level. Furthermore, the Fermi velocity $v_{\mathrm{F}} = 4.1\,\mathrm{Å\,fs^{-1}}$ and the Fermi wave vector $k_{\mathrm{F}} = 0.075\,\mathrm{Å}^{-1}$, which can be extracted from the ARPES data, are in agreement with previous studies [Rei18b, Zha09]. The white solid line indicates the energy dispersion of the topologically protected surface state as obtained by density functional theory calculations, whereas the gray shaded area marks the corresponding surface projection of the bulk conduction band (see also Figure 3.10b).

Figure 3.24b displays an ARPES snapshot for a delay time of $t = -9\,\mathrm{fs}$, at the zero-crossing after a positive field maximum of the multi-THz driving field (see Figure 3.24e, red dot). The photoemission spectrum shows a clear asymmetry of the intensity in the topological surface state near the Fermi energy, which directly corresponds to a change of the band occupation. For negative values of k_y, the electron distribution is shifted to higher energies and larger parallel momentum, whereas for the positive k_y-direction, the distribution is significantly shifted to smaller energies and parallel momenta. The photoemission spectrum in Figure 3.24c depicts a snapshot of the dynamics at the delay time, $t = 9\,\mathrm{fs}$, which is at the zero-crossing after a negative field maximum (see Figure 3.24f, red dot). Also in this case, the photoemission spectrum exhibits an asymmetry of the intensity in the topological surface state, but in the opposite direction as compared to Figure 3.24b. Thus, the left branch of the Dirac cone is almost completely unoccupied, whereas the population of the surface state for positive k_y is raised up to 300 meV above the Fermi level.

The origin of the observed transient shift of the occupation to higher and lower values of the parallel momentum is a lightwave-driven acceleration of the charge carriers in momentum space according to Bloch's acceleration theorem (see equation (3.5)).

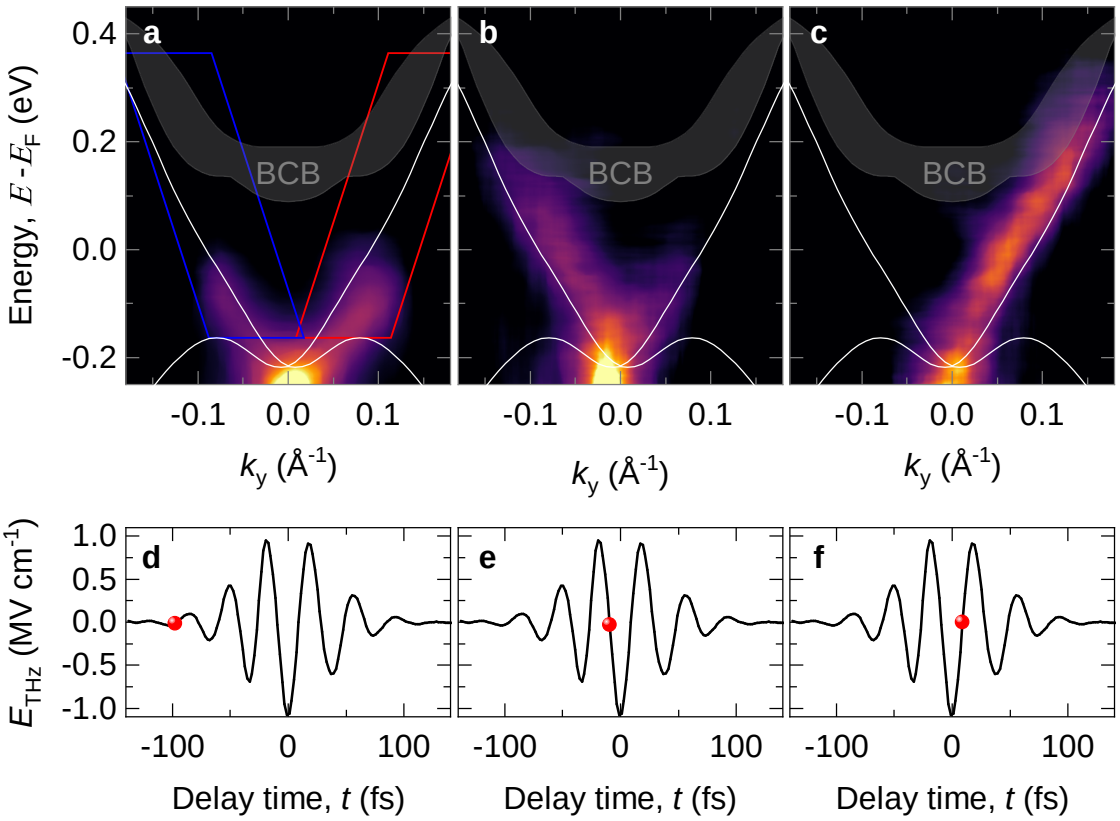

Figure 3.24 | Intraband acceleration of Dirac electrons under strong lightwave biasing along the $\overline{\Gamma}$-$\overline{\mathrm{K}}$-direction. **a**, Static photoemission map before the arrival of the multi-THz field, E_{THz} ($t = -98\,\mathrm{fs}$). White solid lines, topological surface state calculated by density function theory (see also Figure 3.10b). Gray shaded area, bulk conduction band projection. **b**, **c** Photoemission maps for a delay time $t = -9\,\mathrm{fs}$ (**b**) and $t = 9\,\mathrm{fs}$ (**c**) between the multi-THz driving field, E_{THz}, and the UV probe pulse. Depending on the sign of the strong lightwave bias, the electron population in the topological surface band is shifted towards negative (**b**) or positive (**c**) values of the parallel momentum, k_y. **d**, **e**, **f**, Reconstructed in-plane electric field, E_{THz}, of the multi-THz driving waveform with a center frequency of $\nu_{\mathrm{THz}} = 27.6\,\mathrm{THz}$ and a peak electric field of up to $1.06 \pm 0.1\,\mathrm{MV\,cm^{-1}}$. The red spheres indicate the delay times, t, at which the photoemission maps in panels **a**, **b**, and **c** are taken, respectively.

This asymmetric occupation of the Dirac cone corresponds to an imbalance in the number of electrons moving in opposite directions and hallmarks an ultrafast displacement of the Fermi circle in momentum space. For a quantitative analysis of the

THz-induced redistribution of electrons in the topologically protected surface state, the photoemission intensity in the Dirac cone is integrated along k_y for each delay time, t, between the multi-THz acceleration field and the ultrashort UV probe pulse. Thereby, the red and blue parallelograms in Figure 3.24a indicate the integration areas for positive and negative parallel momenta, k_y, respectively. The resulting electron energy distribution function follows a Fermi-Dirac statistic [Rei18b] and allows us to determine the THz-induced energy shift, ΔE, with respect to the undisturbed, equilibrium energy $E = \hbar v_\mathrm{F} k_\mathrm{F}$. As the topological surface state exhibits a linear Dirac dispersion, the transient deflection, Δk, of the parallel momentum, k_y, can then be calculated according to the formula

$$\Delta k = \frac{\Delta E}{\hbar v_\mathrm{F}}. \tag{3.18}$$

Figure 3.25a displays the temporal evolution of the lightwave-induced momentum shift, $\Delta k(t)$, together with the instantaneous multi-THz driving field, $E_\mathrm{THz}(t)$, which has been determined by momentum streaking (Figure 3.25a, black solid line). With a Fermi velocity of $v_\mathrm{F} = 4.1\,\text{Å}\,\mathrm{fs}^{-1}$, along the $\overline{\Gamma}$-$\overline{\mathrm{K}}$-direction, a maximal THz-induced momentum deflection of $\Delta k = 0.073 \pm 0.006\,\text{Å}^{-1}$ is obtained for the multi-THz field with a center frequency of $\nu_\mathrm{THz} = 27.6\,\mathrm{THz}$ and a peak electric field amplitude of $E_\mathrm{THz} = 1.06 \pm 0.10\,\mathrm{MV\,cm^{-1}}$. Similar to previous experiments with a THz waveform centered at $\nu_\mathrm{THz} = 1\,\mathrm{THz}$ (see section 3.3.2), the maximal deflection in reciprocal space is reached at the zero-crossings of the driving field (see Figure 3.25, vertical dashed lines). This subcycle delay between the multi-THz field crests and the maximum of the THz-induced momentum shift, Δk, is a direct fingerprint of the ballistic lightwave-driven acceleration of the Dirac electrons, resulting from the extremely long scattering times in the topological surface state that are exceeding 1 ps [Rei18b]. Consequently, as described by Bloch's acceleration theorem (see equation (3.5)), Δk follows the vector potential of the driving field, V_THz (see Figure 3.25b). The absolute value of Δk is 15 times larger as compared to the previous experiment with a THz driving field centered at 1 THz. As a consequence, at a delay time of $t = 9\,\mathrm{fs}$ (see Figure 3.24c), one branch of the Dirac cone is completely depopulated, whereas in positive k_y-direction the electron distribution is shifted up to a parallel momentum of $k_y = 0.148 \pm 0.006\,\text{Å}^{-1}$. Thereby, the lightwave-driven

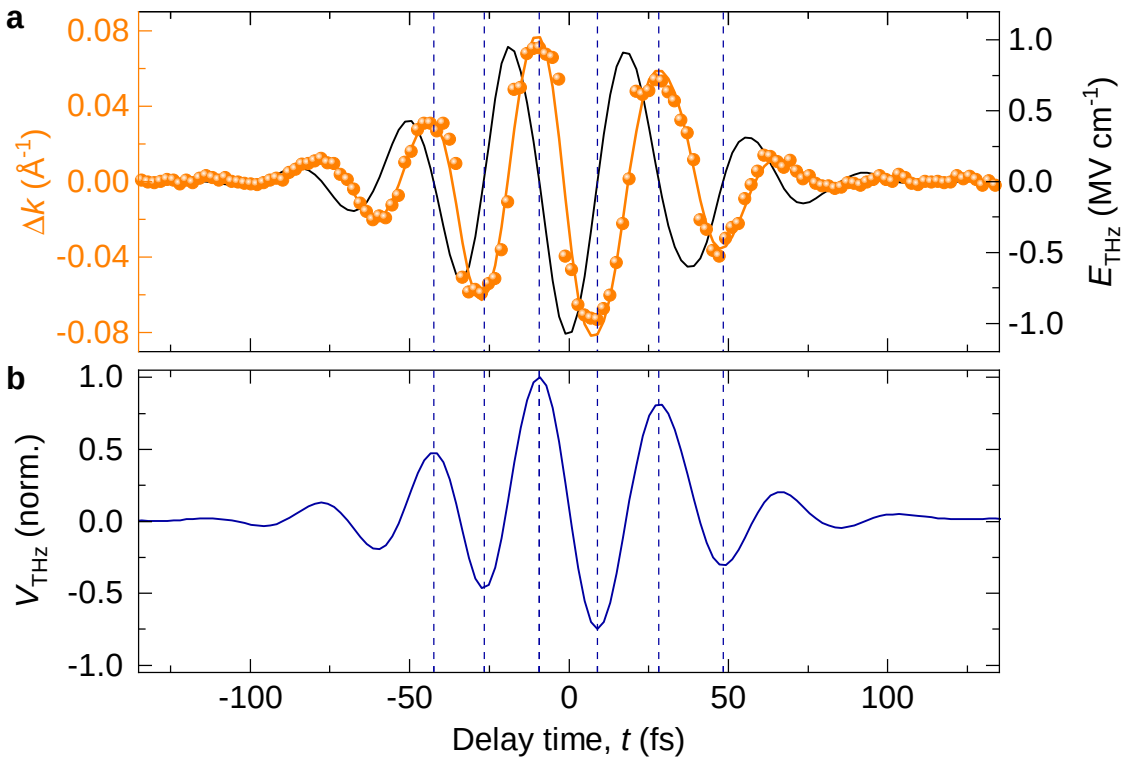

Figure 3.25 | Dynamics of the lightwave-acceleration in the topological surface band of Bi_2Te_3. **a**, Temporal evolution of the momentum deflection, Δk, as a function of the delay time, t, extracted from the photoemission intensity distributions (orange data points) featuring a maximum momentum shift of $\Delta k = 0.073\,\text{Å}^{-1}$. Orange solid line, least mean square fit of the data. Black solid line, electric field, E_{THz}, of the multi-THz waveform with a peak electric field of $E_{\text{THz}} = 1.06 \pm 0.1\,\text{MV cm}^{-1}$. **b**, Normalized vector potential of the multi-THz driving field, V_{THz}, as a function of the delay time, t. As indicated by the vertical dashed lines, the momentum deflection, Δk, peaks at the zero-crossings of the driving field, which is at the maxima of V_{THz}.

acceleration of electrons through the Dirac point abruptly reverses their group velocity, which can lead to large optical nonlinearities (see section 3.5).

Although the electron analyzer only images the dynamics in momentum space along one specific crystallographic direction, the acceleration direction given by the externally applied multi-THz field leads to an asymmetric distribution across the whole Dirac cone (see Figure 3.21b amd reference [Rei18b]). The observed lightwave-driven intraband acceleration along the $\overline{\Gamma}$-$\overline{\text{K}}$-direction can be associated with a non-

vanishing ballistic photocurrent flowing in the positive or negative y-direction on the sample surface. The corresponding THz-induced current density, $j(t)$, can be derived from the experimentally observed transient momentum shift, $\Delta k(t)$, by the formula [Rei18b]

$$j(t) \;=\; -ev_{\mathrm{F}}k_{\mathrm{F}}\frac{\Delta k(t)}{4\pi}. \tag{3.19}$$

With a Fermi momentum of $k_{\mathrm{F}} = 0.075\,\text{Å}^{-1}$, a Fermi velocity of $v_{\mathrm{F}} = 4.1\,\text{Å}\,\text{fs}^{-1}$ and a maximal momentum deflection of $\Delta k = 0.073 \pm 0.006\,\text{Å}^{-1}$, the current density reaches values of up to $j = 28.3 \pm 2.3\,\text{A}\,\text{cm}^{-1}$. As this coherent carrier dynamics is limited to the atomically thin surface layer, which has a thickness of only 1 nm, the corresponding bulk current density reaches values of up to 56 nA, per atom. Within one half-cycle of the multi-THz driving field, this inertia-free lightwave-driven Dirac current may coherently propagate over a distance of at least 8 nm. The associated low dissipation rate of this ballistic, THz-induced surface current together with the large coherence length, which is on the order of the typical gate width of state-of-the-art electronic transistors, makes lightwave-driven, topological-insulator-based electronic devices operating at multi-THz clock rates a realistic perspective. Furthermore, the scattering times of Dirac fermions in the topological surface state, which are on the order of 1 ps, are large enough to preserve the quantum memory of the accelerated electrons between successive cycles of the driving field. This also sparks hope for ultimate strong-field quantum control in topological insulators.

Accelerating Dirac electrons with intense multi-THz waveforms with peak electric fields exceeding $1\,\text{MV}\,\text{cm}^{-1}$ leads to a large redistribution of electrons in momentum space. As is apparent from Figure 3.24c, after the most intense half-cycle of the multi-THz driving field, the Dirac electrons of the topological surface state are shifted up to a parallel momentum of $k_y = 0.148\,\text{Å}^{-1}$, which corresponds to more than one tenth of the entire Brillouin zone. As already explained in section 3.1.3, the acceleration of electrons not only changes their wave vector, it can also modify the lattice periodic part of the Bloch wavefunctions (see equation (3.3)). Especially for large excursions in reciprocal space, anharmonicities or broken symmetries in the crystal lattice as well as internal quantum attributes like Berry curvature might thus influence the lightwave-driven carrier dynamics in reciprocal space. This, in turn,

leaves signatures in the optical readout which renders processes like high-harmonic generation a useful tool to investigate electron dynamics in a solid in an all-optical way [Ban17, Liu17, You17, Lan17, Lan18b, Yos19].

Just recently, in Borsch *et al.* [Bor20], we showed that even an all-optical, fully three-dimensional tomography of the electronic structure is possible by a systematic analysis of the high-order sideband emission from a monoloayer of tungsten diselenide. Now, by combining time-resolved ARPES with intense multi-THz fields, microscopic electron dynamics can be studied, for the first time, under strong lightwave bias directly in the band structure. Therefore, both the crystal orientation as well as the center frequency of the multi-THz driving field, are varied in the following experiments.

As a first step, the Bi_2Te_3 crystal is rotated, such that the *s*-polarized multi-THz driving field is oriented along the crystallographic $\overline{\Gamma}$-$\overline{\mathrm{M}}$-direction. Figure 3.26 illustrates the corresponding corrected photoemission spectra, for two different delay times, t. The intense multi-THz waveform exhibits a center frequency of $\nu_{\mathrm{THz}} = 27.6\,\mathrm{THz}$ and a peak electric field of $E_{\mathrm{THz}} = 1.04 \pm 0.10\,\mathrm{MV\,cm^{-1}}$ (see Figure 3.26c and d, black solid line). At a delay time of $t = -84\,\mathrm{fs}$, before the arrival of the intense multi-THz field (see Figure 3.26a), the V-shaped dispersion of the topological surface state, located at the $\overline{\Gamma}$-point in reciprocal space, is clearly visible. In agreement with density functional theory calculations (white solid line), the Fermi velocity features a value of $v_{\mathrm{F}} = 3.4\,\mathrm{Å\,fs^{-1}}$ and is, hence, smaller compared to the crystallographic $\overline{\Gamma}$-$\overline{\mathrm{K}}$-direction. The Dirac cone is symmetrically occupied for positive and negative momenta, whereas the Fermi level lies $\approx 200\,\mathrm{meV}$ above the Dirac point. The corresponding Fermi wave vector is again, $k_{\mathrm{F}} = 0.075\,\mathrm{Å^{-1}}$.

Figure 3.26b illustrates a snapshot of the photoemission spectrum at $t = 7\,\mathrm{fs}$, which is at the zero-crossing after the most intense negative half cycle of the multi-THz driving field (see Figure 3.26d, red dot). The lightwave acceleration of the Dirac electrons in the topological surface state leads to a clear asymmetry of the photoemission intensity. Thereby, the left branch of the topological surface state is almost completely depopulated, whereas in positive k_y-direction the occupation is shifted up to 100 meV above the Fermi level. This corresponds to a transient momentum shift of $\Delta k = 0.046 \pm 0.004\,\mathrm{Å^{-1}}$. Moreover, the photoemission spectra show that for a large parallel momentum, k_y, a significant part of the electrons is transferred to

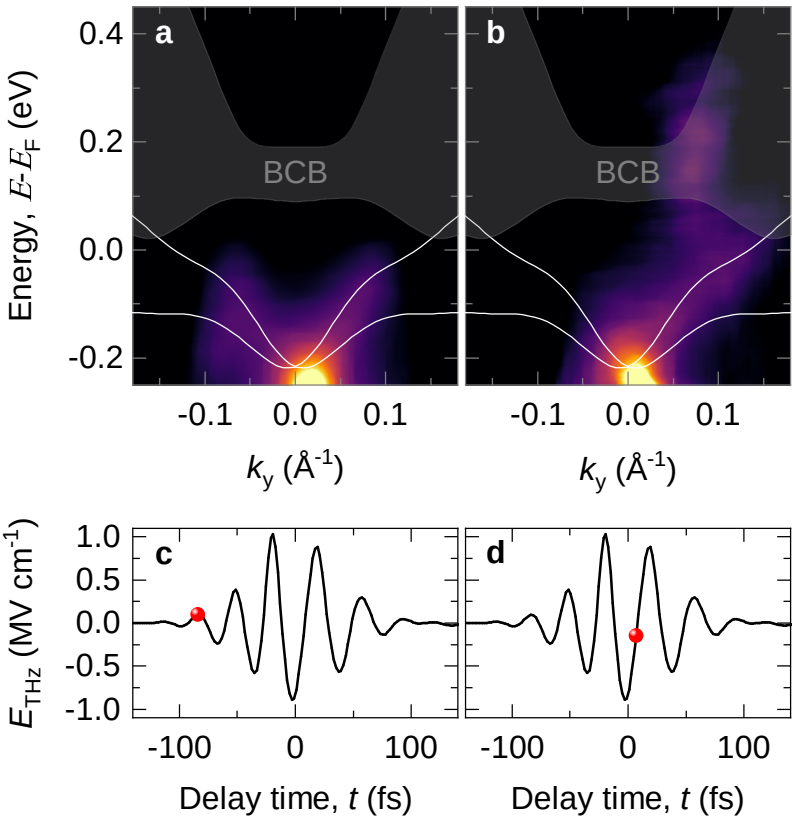

Figure 3.26 | Lightwave acceleration of Dirac electrons along the $\overline{\Gamma}$-$\overline{\mathrm{M}}$-direction. **a**, Photoemission spectrum along the crystallographic $\overline{\Gamma}$-$\overline{\mathrm{M}}$-direction before the arrival of the intense, *s*-polarized multi-THz field, E_{THz}. The white solid lines indicate the topological surface states calculated by density function theory (see also Figure 3.10b). The gray shaded area represents the respective bulk conduction band projection. **b**, Photoemission map taken at a delay time $t = 7\,\mathrm{fs}$ between the multi-THz transient, E_{THz}, and the UV probe pulse. The strong lightwave bias leads to an intraband acceleration of the Dirac electrons and simultaneously drives a charge transfer to the bulk conduction band (BCB). **c**, **d**, Reconstructed in-plane electric field, E_{THz}, of the multi-THz driving waveform with a peak electric field amplitude of up to $E_{\mathrm{THz}} = 1.04 \pm 0.1\,\mathrm{MV\,cm^{-1}}$. Red spheres, delay times, t, at which the photoemission maps in panels **a** and **b** are taken, respectively.

the bulk conduction band (Figure 3.26b, gray shaded area). According to the density functional theory calculations along the $\overline{\Gamma}$-$\overline{\mathrm{M}}$-direction (see also Figure 3.10b), the topologically protected surface states energetically overlap with bulk states for $\left|k_y\right| > 0.15\,\mathrm{Å}^{-1}$. The lightwave-driven acceleration of the Dirac fermions shifts the

electron distribution in the topological surface band up to a parallel momentum of $k_y = 0.121 \pm 0.004\,\text{Å}^{-1}$. The recorded subcycle ARPES map suggests that this facilitates a charge transfer from the topologically protected surface state to the bulk conduction band. Previous time-resolved ARPES studies have discussed interband transitions from surface to bulk states in topological insulators owing to optical excitation [Haj12, Haj14, Kur16, Soi19]. So far, however, a lightwave-driven charge transfer from a topologically nontrivial surface state to a topologically trivial bulk state has not been observed on a subcycle timescale. In the absence of spin-momentum locking, the scattering times in the topologically trivial Bi_2Te_3 bulk conduction band are supposed to be significantly shorter than in the topological surface state. Consequently, the THz-induced bulk population should significantly influence the coherence of the optical readout. In the future, a systematic analysis of the exact scattering times as well as the transfer rate between the two bands might help to further characterize the electronic properties of three-dimensional insulators under strong lightwave bias, which is essential for future optoelectronic applications.

The experiments show, how a strong lightwave bias leads to a strong intraband acceleration of the Dirac electrons in the topologically protected surface state of Bi_2Te_3. Along the crystallographic $\overline{\Gamma}$-$\overline{\text{M}}$-direction, the dynamics even allows for a lightwave-driven charge transfer into the bulk conduction band. Yet, direct interband excitation is not apparent from the subcycle ARPES experiments with a multi-THz waveform centered at $\nu_{\text{THz}} = 27\,\text{THz}$. To gain further insights into the interplay between intraband acceleration and interband excitation under strong lightwave bias, the center frequency of the intense multi-THz driving field is now tuned to $\nu_{\text{THz}} = 41.0\,\text{THz}$. With a corresponding photon energy of $\approx 170\,\text{meV}$, the THz lightwave should be able to efficiently excite carriers across the bulk band gap of Bi_2Te_3 of $\approx 150\,\text{meV}$ [Mic14].
In the course of this experiment, the Bi_2Te_3 crystal is oriented such that the multi-THz field is polarized along the high-symmetry $\overline{\Gamma}$-$\overline{\text{K}}$-direction, where previously a pure lightwave-driven intraband acceleration has been observed (see Figure 3.24). The multi-THz high-field source (see section 3.4.1) is set to efficiently generate intense, few-cycle waveforms centered at $\nu_{\text{THz}} = 41.0\,\text{THz}$. The in-plane electric field,

$E_{\mathrm{THz}}(t)$, extracted from momentum streaking exhibits a peak amplitude of $E_{\mathrm{THz}} = 0.54 \pm 0.05\,\mathrm{MV\,cm^{-1}}$ (see Figure 3.27c and d). Figure 3.27a and b display two snapshots of the photoemission spectra taken before the arrival of the intense multi-THz light pulse ($t = -104\,\mathrm{fs}$) and at the zero-crossing after the most intense negative half-cycle of the THz driving field ($t = 13\,\mathrm{fs}$), respectively. At the delay time $t = -104\,\mathrm{fs}$ (Figure 3.27a), the left and the right branch of the Dirac cone are occupied up to the same Fermi energy and Fermi momentum ($k_{\mathrm{F}} = 0.075\,\mathrm{\AA}^{-1}$).
When the multi-THz electric field bias is applied (see Figure 3.27b), the occupation becomes strongly asymmetric and the electron distribution in the topological surface state is shifted to positive parallel momenta, k_y. Moreover, the photoemission spectrum shows a significant electron population in the bulk conduction band at the $\overline{\Gamma}$-point in reciprocal space. This suggests, that the intense multi-THz field coherently accelerates Dirac electrons in the topological surface band and simultaneously excites carriers across the bulk band gap.
Remarkably, the ARPES spectrum in Figure 3.27b visualizes two fundamentally different light-matter coupling mechanisms at the same time. Whereas the resonant interband excitation can be associated with a perturbative quantum absorption, the simultaneously observed lightwave acceleration is a prime example for non-perturbative light-matter interaction. Yet, with time-resolved ARPES these intriguing strong-field dynamics can be traced directly in the band structure and on a sub-cycle timescale. Moreover, the experiments, for the first time, make the microscopic electron dynamics behind non-perturbative nonlinearities such as the high-harmonic generation in solids experimentally accessible [Gol08, Gol11, Sch14, Hoh15, Lan17].

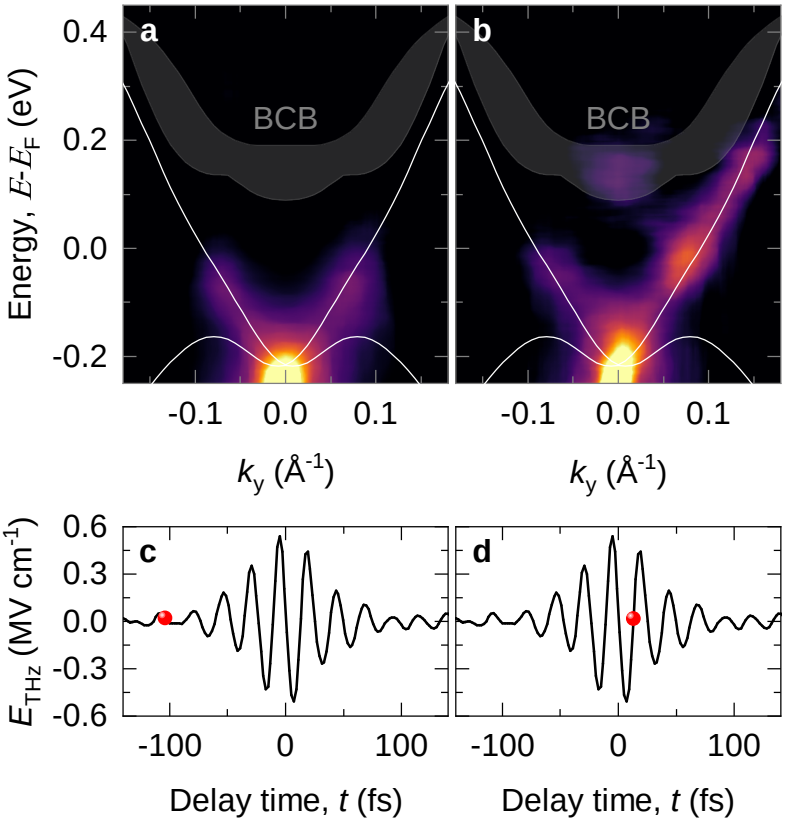

Figure 3.27 | Lightwave-driven intraband and interband dynamics in Bi_2Te_3. **a**, Static photoemission map along the crystallographic $\overline{\Gamma}$-$\overline{\mathrm{K}}$-direction before the arrival of the intense, *s*-polarized multi-THz field, E_{THz}. White solid line, topological surface states calculated by density function theory (see also Figure 3.10b). Gray shaded area, corresponding bulk conduction band projection. **b**, Photoemission spectrum recorded at a delay time $t = 13\,\mathrm{fs}$ between the multi-THz transient, E_{THz}, with a center frequency of $\nu_{\mathrm{THz}} = 41.0\,\mathrm{THz}$ and the ultrashort UV gating pulse. The intense multi-THz field drives a coherent intraband acceleration in the Dirac cone and simultaneously excites electrons into the bulk conduction band (BCB). **c**, **d**, Reconstructed in-plane electric field, E_{THz}, of the multi-THz driving waveform with a peak electric field amplitude of up to $E_{\mathrm{THz}} = 0.54 \pm 0.05\,\mathrm{MV\,cm^{-1}}$. Red spheres, delay times, t, at which the photoemission maps in panels **a** and **b** are taken, respectively.

3.5 High-harmonic generation in Bi_2Te_3

The time-resolved ARPES experiments presented in the last section provide qualitatively new insights into strong-field light matter interaction. By applying multi-THz electric fields in excess of $1\,\mathrm{MV\,cm^{-1}}$, within only a few femtoseconds, Dirac electrons inside the topological surface state of Bi_2Te_3 are ballistically steered through more than one tenth of the entire Brillouin zone (see Figure 3.24). Depending on the frequency of the driving field and the orientation of the Bi_2Te_3 crystal, this intraband acceleration can also be accompanied by a lightwave driven interband excitation (see Figure 3.26) or a direct transition into the bulk conduction band (see Figure 3.27). In conventional semiconductors and dielectrics, such coherent electron dynamics manifests in the emission of high-order harmonics [Chi01, Sch14, Hoh15, Siv17, Haf18, Yos17, Lan17]. Owing to their unique electronic properties featuring massless Dirac electrons, which can be ballistically driven over large distances, and the fact that the strongest optical nonlinearity occurs in the vicinity of the center of the Brillouin zone [Gio16], three-dimensional topological insulators are supposed to serve as a prime medium for efficient high-harmonic generation. Moreover, it has been predicted, that topological invariants might leave characteristic fingerprints in the polarization of the corresponding high-harmonic emission, which would probe the topology of the material in an all-optical way [Bau18, Sil19].
To test, how the distinct lightwave-driven subcycle electron dynamics observed by time-resolved ARPES affect the optical readout, multi-THz waveforms with a center frequency of $\nu_{\mathrm{THz}} = 28\,\mathrm{THz}$ and $\nu_{\mathrm{THz}} = 43\,\mathrm{THz}$, respectively, are applied to a Bi_2Te_3 crystal oriented along the crystallographic $\overline{\Gamma}$-$\overline{\mathrm{K}}$-direction. Thereby, a parabolic mirror with a focal length of $f = 5\,\mathrm{cm}$ focuses the intense multi-THz waveforms under an angle of 45° onto the Bi_2Te_3 sample. Accounting for the refractive index of Bi_2Te_3 of $n_{\mathrm{Bi_2Te_3}} = 9.2$ [Aus58] as well as the experimental angle of incidence of 45°, a peak electric field amplitude inside the Bi_2Te_3 crystal of $E_{\mathrm{THz}} = 1.16\,\mathrm{MV\,cm^{-1}}$ and $E_{\mathrm{THz}} = 1.04\,\mathrm{MV\,cm^{-1}}$ is obtained, respectively. The emitted radiation is collimated and detected with a spectrograph coupled to a thermoelectrically cooled silicon charge-coupled device (CCD) camera. Subsequently, the recorded spectra are corrected for the diffraction efficiency of the grating and the quantum efficiency of the detector.

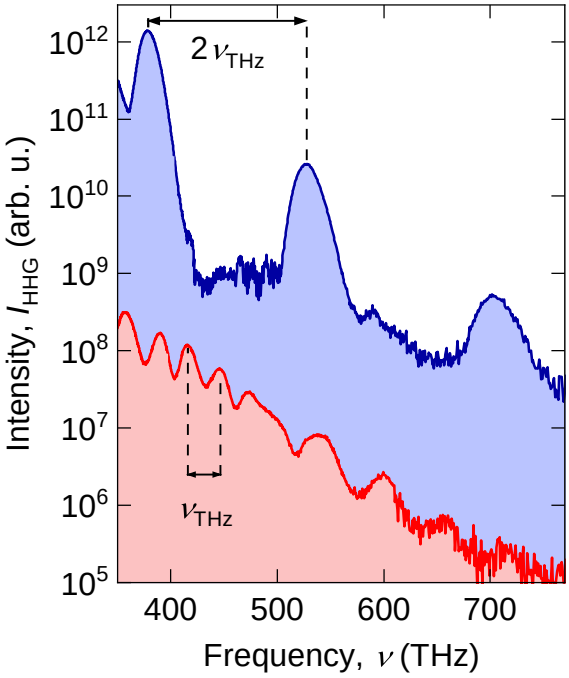

Figure 3.28 | High-harmonic generation in Bi_2Te_3. High-harmonic intensity spectrum, I_{HH}, measured in reflection geometry for a THz-driving waveform with a center frequency of $\nu_{THz} = 28\,THz$ (red shaded area) and $\nu_{THz} = 43\,THz$ (blue shaded area) and a peak electric field amplitude of $E_{THz} = 1.16\,MV\,cm^{-1}$ and $E_{THz} = 1.04\,MV\,cm^{-1}$, respectively. The upper spectrum is vertically offset by a factor of 50 for clarity.

Figure 3.28 shows that the THz-induced electron dynamics in the Bi_2Te_3 crystal, in fact, lead to the generation of high-order harmonics of the driving field. The high-harmonic spectra, I_{HH}, detected for the two different THz driving waveforms cover the whole infrared, visible, and near-ultraviolet window. In the case of a THz driving frequency of $\nu_{THz} = 43\,THz$, however, the emission is dominated by odd-order harmonics spaced by twice the THz-driving frequency (Figure 3.28, blue shaded area), whereas for $\nu_{THz} = 28\,THz$, even and odd order harmonics are emitted with comparable strength (Figure 3.28, red shaded area).

As the inversion symmetry of the Bi_2Te_3 crystal is only broken at the surface, the emergence of even-order harmonics for $\nu_{THz} = 28\,THz$ suggests that the high-harmonic radiation stems from lightwave-driven dynamics in the topologically protected surface state. This can be directly proved by the subcycle ARPES experiments performed with similar experimental parameters (see section 3.4.3). The photoemission spectra presented in Figure 3.24 reveal that a THz-driving field with a photon energy below the bulk band gap solely accelerates Dirac electrons in the topologically protected surface state. As the largest optical nonlinearity occurs right in the center of the Brillouin zone [Gio16], even a weak external driving field causes

an extremely anharmonic response. Driving Dirac fermions through the vicinity of the $\overline{\Gamma}$-point, abruptly reverses their group velocity [Bra16, Yos17, Che20], which results in the efficient generation of broadband high-frequency electromagnetic radiation.
Conversely, multi-THz pulses whose photon energy is larger than the bulk band gap are also able to resonantly excite electrons into the bulk conduction band as illustrated in Figure 3.27. In this case, both electrons in the topological surface state and in the bulk conduction band are accelerated by the strong multi-THz electric field. Owing to the large absorption length of $\approx 100\,\mathrm{nm}$, however, the lightwave-driven dynamics in the inversion symmetry bulk crystal dominates the optical response, which leads to the generation of only odd-order harmonics. Consequently, by choosing a driver frequency below the bulk band gap, high-harmonics are selectively driven in the surface state resulting in the observation of even- and odd-order harmonics. Beyond that, a detailed analysis of the polarization state of these high-order harmonics reveals anomalous components that can be attributed to the influence of the Berry curvature of the topological surface state as will be explained in detail in the upcoming doctoral thesis of my colleague *Christoph Schmid*. Besides that, the demonstrated strong-field ballistic control of topologically protected surface states opens a unique laboratory to test fundamental predictions of relativistic quantum physics like Zitterbewegung [Jun20], Floquet physics [Fai97, Has10, Wan13] or axion dynamics [Nen20].

4 Summary

In this thesis, single- and few-cycle light pulses in the terahertz spectral regime have been utilized to coherently control the electron's spin [Sch19], as well as its translational motion [Rei18b] on ultrashort time scales and with minimal energy dissipation. The presented results point out a promising route towards future ultrafast, minimally dissipative information technology based on coherent lightwave-control.

In order to switch spins on ultrashort timescales and with minimal energy dissipation, the advantages of the electric-field control of the magnetic anisotropy in the prototypical antiferromagnetic $TmFeO_3$ are combined with the local THz near-field enhancement of optical antenna structures. As the orbital angular momentum of the Tm^{3+} ground state singlets is coupled to the Fe^{3+} spins, a thermal re-population of the Tm^{3+} energy levels also modifies the strength and the direction of the magnetic anisotropy. Ultrashort light pulses in the THz spectral range can be utilized to abruptly modify this anisotropy potential by optically driving electric dipole transitions between crystal field-split states of the electronic ground state of the Tm^{3+} ions. The resulting lightwave-induced non-adiabatic changes of the magnetic anisotropy give rise to a displacive and an impulsive torque, which cause coherent magnetization dynamics, whose amplitude scales quadratically with the applied THz electric field [Bai16a].
Coupling spins in $TmFeO_3$ with the locally enhanced THz electric field of custom-tailored bowtie antenna structures bypasses the diffraction limit and maximizes the achievable THz amplitude. In a pump-probe scheme, intense single-cycle THz pulses with a center frequency of 1 THz and a tunable far-field amplitude of up to

$E_{\mathrm{THz}} = 1.0\,\mathrm{MV\,cm^{-1}}$ excite the $TmFeO_3$ crystal from the backside. The subsequent THz-induced magnon oscillations are probed on a subcycle timescale by recording the polarization rotation imprinted on a co-propagating near-infrared probe pulse by the magneto-optic Faraday effect. In the absence of an antenna and for the highest THz electric fields, the coherent magnon oscillations cause a maximum rotation angle of the probe polarization of 0.5 mrad, corresponding to a spin deflection angle of 3.5°. When the probe pulse is positioned in the center of the antenna feed gap, even a much weaker far-field of $E_{\mathrm{THz}} = 0.4\,\mathrm{MV\,cm^{-1}}$ leads to a polarization rotation of 0.9 mrad, while the magnetization dynamics resembles the spin precession observed in the unstructured crystal. Above a threshold far-field amplitude of $E_{\mathrm{THz}} = 0.75\,\mathrm{MV\,cm^{-1}}$, however, a qualitatively new behavior emerges. The period of the first full cycle of the magnetization oscillation gets distinctly stretched, an unprecedented phase flip occurs in the coherent polarization rotation signal, which corresponds to an asymmetric splitting of the magnon resonance in the frequency domain, and the magneto-optical response features a long-lived offset that persists up to nanoseconds.

With the help of numerical simulations of the microscopic THz-induced spin dynamics, it is possible to fathom the origin of the observed features in the polarization rotation signal. The calculations show, that above a critical near-field amplitude of $E_{\mathrm{NF}} = 7.8\,\mathrm{MV\,cm^{-1}}$, the spins are ballistically driven over a potential barrier into a new stable state. Remarkably, the first spins in the antenna near-field region already cross the potential barrier after a delay time of 1.3 ps. By summing up all locally induced Faraday signals from the probed near-field volume, every feature of the coherent polarization rotation signal is quantitatively reproduced both for the experiments below and above the threshold electric far-field amplitude of $E_{\mathrm{THz}} = 0.75\,\mathrm{MV\,cm^{-1}}$. Consequently, the stretching of the first oscillation cycle, the beating of the Faraday signal, and the spectral splitting of the magnon resonance observed above this threshold can unambiguously be identified as the fingerprints of all-coherent non-perturbative spin trajectories between adjacent minima of the magnetic potential energy. Moreover, it becomes apparent that the long-lived offset in the Faraday signal directly reads out the switched spin state. Going one step further, based on this microscopic understanding of the THz-induced spin dynamics, the spin trajectories can be shaped by custom-tailoring the magnetic potential. In

particular, by changing the lattice temperature or the external magnetic bias field while keeping the peak THz far-field amplitude constant at $E_{\mathrm{THz}} = 1.0\,\mathrm{MV\,cm^{-1}}$, the switchable spin states can be selected, or spin switching can be inhibited completely.
The experiments mark a novel regime of ultrafast all-coherent spin control throughout the entire phase space. Furthermore, for the first time, lightwave-driven spin switching can be observed on a subcycle time scale, which results in the observation of a number of unique hallmarks in the coherent polarization rotation signal. In this specific implementation of a THz-driven anisotropy torque, the absorbed energy of approximately one THz photon per spin suffices for switching whereas the energy dissipation in the spin system is on the order of 1 µeV per spin. This makes the scheme highly scalable. Beyond that, future storage devices could also exploit the excellent spatial definition of the antenna structures, which can be scaled down to a size of 10 nm. This sets the stage for novel spin memories operating at THz clock rates, and ultimately low dissipation close to the Landauer limit [Lan61].

The carrier wave of intense single and few-cycle light pulses in the THz regime can also be utilized to coherently control the translational motion of electrons in a solid. This concept of ballistic lightwave acceleration of charges has lead to the observation of dynamical Bloch oscillations which manifest in the emission of high-order harmonic radiation [Sch14, Hoh15]. Also, internal quantum attributes like the valley pseudospin can be coherently controlled on a subcycle timescale by a lightwave-driven intraband acceleration of carriers in a monolayer of the transition metal dichalcogenide tungsten diselenide [Lan18b]. Hence, using the carrier wave of light as an a.c. bias voltage may pave the way to future ultrafast electronics and ultimate quantum control. Nonetheless, the finite band mass and ultrafast scattering in conventional dielectrics limit the velocity and the excursion of the accelerated electrons, causing also substantial energy losses.
With their unique electronic properties, the material class of topological insulators may lift these constraints and bring actual lightwave electronic devices into reach. Owing to strong spin-orbit interaction, compounds like bismuth telluride (Bi_2Te_3) are insulating or semiconducting in their bulk form, while conductive states emerge at the sample surface. The linear, Dirac-like dispersion and the reduced scatter-

ing rate, caused by spin-momentum locking, renders these surface states promising for ultrafast low-loss electronics. Moreover, as their existence is guaranteed by the topology of the band structure, they are robust against defects or impurities which further increases the potential for practical electronic applications.
To actually observe how an intense lightwave accelerates the carriers in momentum space, time-resolved angle-resolved photoelectron spectroscopy (trARPES) is applied to record complete subcycle band structure movies of the lightwave-driven dynamics. In a first set of experiments, single-cycle THz pulses with a center frequency of 1 THz and peak electric field amplitudes of only $E_{\mathrm{THz}} = 2.4\,\mathrm{kV\,cm^{-1}}$ are utilized to ballistically accelerate Dirac electrons in the topological surface band of Bi_2Te_3. From the experiment, scattering times in the topological surface state of at least one picosecond can be determined. Together with the high Fermi velocity of the Dirac electrons, these extremely large coherence times facilitate a non-dissipative propagation of the lightwave-driven surface current over several hundred nanometers. This record scale exceeds the gate width of contemporary electronic circuitry by orders of magnitude and makes future lightwave-driven low-loss electronic devices a real perspective. Owing to spin-momentum locking, the ballistic Dirac currents also carry a spin current, which could enable spintronics up to optical clock rates.
Now, by applying THz waveforms with peak electric field amplitudes on the order of a few $\mathrm{MV\,cm^{-1}}$, also coherent phenomena in the regime of strong-field light-matter interaction can be studied directly in the band structure and on a subcycle timescale. Thereby, intense, phase-stable multi-THz waveforms with a tunable center frequency between 20 and 60 THz and electric peak field amplitudes above $1\,\mathrm{MV\,cm^{-1}}$ serve as the ideal tool for the strong-field control of the topologically protected surface states. To trace the coherent carrier dynamics directly in the band structure, co-propagating ultrashort UV probe pulses with a duration of 12.2 fs simultaneously photorelease electrons out of the sample surface.
Along the crystallographic $\overline{\Gamma}$-$\overline{\mathrm{K}}$-direction, the intraband acceleration by a multi-THz waveform with a center frequency of 27.6 THz and a peak electric field of $E_{\mathrm{THz}} = 1.06\,\mathrm{MV\,cm^{-1}}$ leads to a maximal momentum shift of $\Delta k = 0.073\,\mathrm{\AA^{-1}}$, reached at the zero-crossings of the driving field. The associated inertia-free surface current amounts up to $28.3\,\mathrm{A\,cm^{-1}}$, corresponding to a bulk current density of up to 56 nA, per atom. Within one half-cycle of the multi-THz driving field, this ballistic

Dirac current can coherently propagate over a distance of at least 8 nm, which is on the order of the typical gate width of state-of-the-art electronic transistors.
Conversely, if the multi-THz driving waveform with a peak electric field amplitude of $E_{\mathrm{THz}} = 1.04\,\mathrm{MV\,cm^{-1}}$ is orientated along the $\overline{\Gamma}$-$\overline{\mathrm{M}}$-direction, the lightwave-induced dynamics are qualitatively different. Although the maximum THz-induced momentum shift only amounts up to $\Delta k = 0.046\,\mathrm{\AA}^{-1}$, the coherent intraband acceleration leads to a lightwave-driven charge transfer from the topological surface band to the bulk conduction band. The carrier dynamics are also significantly altered if one increases the frequency of the driving field. Intense multi-THz waveforms featuring a center frequency of 41.0 THz and a peak electric field amplitude of $E_{\mathrm{THz}} = 0.54\,\mathrm{MV\,cm^{-1}}$ coherently accelerate Dirac electrons in the topological surface band along the crystallographic $\overline{\Gamma}$-$\overline{\mathrm{K}}$-direction, and simultaneously drive resonant interband transition across the bulk bandgap. This marks the first subcycle observation of lightwave-driven intra- and interband dynamics in the band structure itself and will help to answer key open questions in lightwave electronics. A fascinating example represents the analysis of the high-harmonic generation from the topological surface state of Bi_2Te_3, which has also been demonstrated in the scope of this thesis. Also other fundamental predictions of relativistic quantum physics like Zitterbewegung [Jun20], Floquet physics [Fai97, Has10, Wan13], or axion dynamics [Nen20] might become experimentally accessible in the future.
The novel subcycle multi-THz ARPES setup established in this thesis offers unprecedented insights into light-matter interaction by resolving the coherent lightwave-driven dynamics directly in momentum space and on a subcycle timescale. Nonetheless, so far, the rather low photon energy of the ultrashort UV probe pulses used for photoemission limits the accessible momentum space to a small fraction of the Brillouin zone. In a next step, the current UV gate pulses with a photon energy of about 3 eV will be replaced by a new light source that provides vacuum-UV pulses with a photon energy above 20 eV and a pulse duration on the order of ten femtoseconds. In this case, the accessible momentum range will be large enough to photoemit electrons from the entire first Brillouin zone. In combination with the intense multi-THz driving waveforms featuring peak electric fields of several $\mathrm{MV\,cm^{-1}}$, it will be possible to trace lightwave-driven electron dynamics throughout the entire Brillouin zone and on the femtosecond time scale. Ultimately, even subcycle band

structure movies of Bloch oscillating electrons are imaginable, which will help to gain a comprehensive understanding of strong-field phenomena like high-harmonic or high-order sideband generation in solids. Furthermore, once the subcycle ARPES setup is able to resolve the entire Brillouin zone, also electron dynamics in materials, whose fundamental bandgap is not at the center or even at the corners of the Brillouin zone, become experimentally accessible. This for example bears the potential to visualize quasiparticle collisions [Lan16] or lightwave valleytronics [Lan18b] directly in the band structure and on a subcycle time scale.

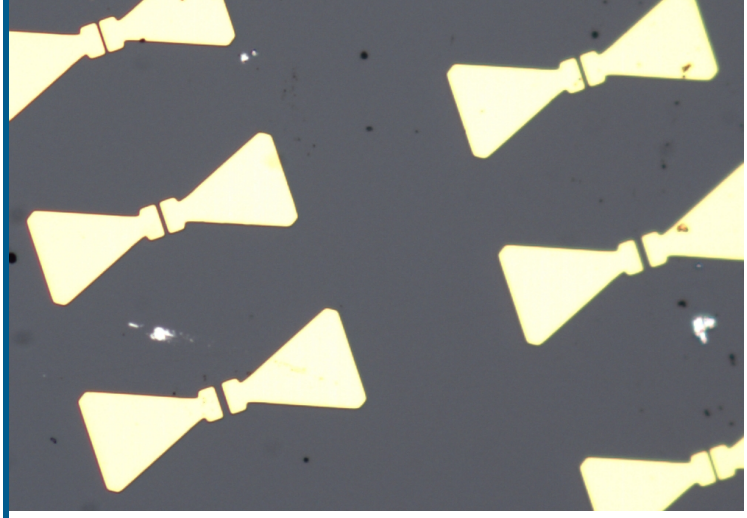

A

Fabrication of optical antenna structures on $TmFeO_3$

For the experiments presented in chapter 2, custom-tailored antenna structures are fabricated on top of a $TmFeO_3$ crystal with a thickness of 60 µm, which has been cut perpendicular to one of the optical axis. For this purpose, the sample has been processed with a positive resist system. Table A.1 summarizes the parameters of the structuring process of the bowtie antennas.

In a first step, the surface of the $TmFeO_3$ crystal is cleaned with acetone and propanol. Then, the sample is placed in a spin coater to apply the electron beam sensitive positive resist AR6200.13 (CSAR 62). In order to harden the resist, the coated substrate is placed on a hot plate. After that, a conductive lacquer (SX AR-PC5000/90.2) is applied and the sample is transferred into a vacuum chamber, where the antenna structures can be written by electron beam lithography. Notably, the use of this conductive lacquer after the actual resist coating prevents space charge effects during the writing process, which ensures an accuracy of 0.5 µm. Afterwards, the conductive lacquer is removed by dipping the sample into deionized water. Subsequently, the substrate is put into a developer solution for 65 s and then cleaned in deionized water. With the help of an electron beam evaporator, a

Spin coating of positive resist	
Type	AR6200.13 (CSAR 62)
Duration (seconds)	50
Revolutions per minute	5000
Acceleration steps	1000
Bake out	
Temperature (°C)	150
Duration (seconds)	60
Spin coating of conductive lacquer	
Type	SX AR-PC 5000/90.2
Duration (seconds)	50
Revolutions per minute	4000
Acceleration steps	800
Parameters of the electron beam lithography	
Acceleration voltage (kV)	20
Aperture (µm)	30
Dose (µC/cm^2)	60
Remove conductive lacquer	
Type	deionized water
Duration (seconds)	120
Development	
Type	AR600-546
Duration (seconds)	65
Stop in Isopropanol (seconds)	5
Evaporation	
Titanium (Thickness; rate)	10 nm; 0.7 Å s^{-1}
Gold (Thickness; rate)	100 nm; 1.5 Å s^{-1}
Lift-off	
Type	Remover PG

Table A.1: Parameters for the fabrication of custom-tailored antenna structures on $TmFeO_3$. Durations, revolutions per minute and acceleration steps refer to the settings of the spin coater, which is used to apply the positive resist and the conductive lacquer. For the bake out, the $TmFeO_3$ is put on a customary hot plate. The thin titanium and gold films are deposited on the sample with the help of a commercial electron beam evaporator.

10 nm-thick layer of titanium and a 100 nm-thick gold film are deposited onto the structured $TmFeO_3$ crystal. Finally, the sample is placed in a bath of Remover PG to lift-off all resist, which has not been exposed to the electron beam.

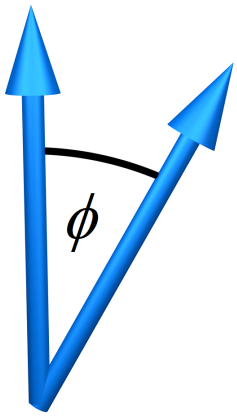

B

Estimate of the magnetization deflection in the near-field volume

In the case of unstructured bulk $TmFeO_3$, the total polarization rotation, θ, results from approximately equal contributions across the entire sample thickness of 60 µm. In order to calibrate the relation between θ and the spin angle ϕ, a full switching of the magnetization (change of $\phi = 180°$) is enforced by reversing the external static magnetic bias field $\mathbf{B}_{\text{ext}}$. This scenario rotates the probe polarization by 24 mrad. Consequently, a polarization rotation of $\theta = 0.5$ mrad, as induced by a THz amplitude of 1.0 MV cm^{-1} in the antenna-free sample, corresponds to a transient spin excursion of $\Delta\phi = 3.5°$. Taking into account the quadratic dependence of $\Delta\phi$ on the electric field amplitude, the polarization rotation, θ, is linked to the THz peak electric field, E_{peak}, by

$$\theta = \xi \times \mathrm{L} \times E_{\text{peak}}^2, \tag{B.1}$$

where L is the crystal length, $\xi = 472\,\text{mrad}\,\text{cm}\,(\text{MV})^{-2}$ is the coupling constant, and $E_{\text{peak}} = 0.42\,\text{MV}\,\text{cm}^{-1}$ is the peak electric THz amplitude averaged over the length of the unstructured $TmFeO_3$ sample. In the antenna-covered structure, the magneto-optical signal can be divided into two contributions:

(a) the antenna near-field region extending down to a depth of 13 µm below the

antenna, where electric fields strongly exceeding the far-field amplitude are encountered (Figure 2.11, red-shaded area)

(b) a bulk part, where the electric field assumes an average value of $0.3\,\mathrm{MV\,cm^{-1}}$ (Figure 2.11, blue-shaded area).

Accordingly, the polarization rotation by the bulk part is

$$\theta_\mathrm{b} \;=\; \xi \times \;47\,\mu\mathrm{m} \;\times\; 0.3\,\mathrm{MV\,cm^{-1}} = 0.2\,\mathrm{mrad}, \tag{B.2}$$

such that 0.7 mrad of the total magneto-optical signal result from the near-field volume. This contribution corresponds to an average spin deflection angle of $\Delta\phi \;=\; 24°$.

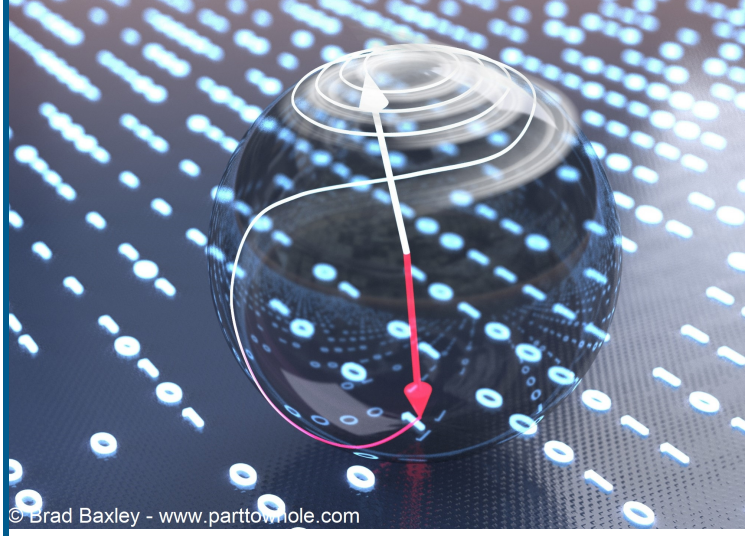

C

Estimation of the spin switching energy

The Poynting theorem dictates that the absorbed electro-magnetic power density $P(t)$ is given by

$$P(t) = j(t)E(t), \tag{C.1}$$

where $j(t)$ is the effective current density describing dissipative processes in a material and $E(t)$ is the oscillating electric field. The full energy absorbed per unit volume is therefore

$$W_{\text{abs}} = \int_{-\infty}^{\infty} j(t)E(t)dt. \tag{C.2}$$

By taking the Fourier transforms

$$j(t) = \frac{1}{2\pi}\int_{-\infty}^{\infty} \tilde{j}(\omega)e^{i\omega t}d\omega \tag{C.3}$$

and

$$E(t) = \frac{1}{2\pi}\int_{-\infty}^{\infty} \tilde{E}(\omega')e^{i\omega' t}d\omega', \tag{C.4}$$

where ω is the frequency, and substituting them into equation C.2 we obtain

$$W_{\text{abs}} = \frac{1}{2\pi}\int_{-\infty}^{\infty} \tilde{j}(\omega)\tilde{E}(-\omega)d\omega. \tag{C.5}$$

The current density is connected to the electric field by the effective conductivity $\sigma(\omega) = \frac{\tilde{j}(\omega)}{\tilde{E}(\omega)}$ such that

$$W_{\mathrm{abs}} = \frac{1}{2\pi}\int_{-\infty}^{\infty}\sigma(\omega)\tilde{E}(\omega)\tilde{E}(-\omega)d\omega = \frac{1}{2\pi}\int_{-\infty}^{\infty}\sigma(\omega)|\tilde{E}(\omega)|^2 d\omega. \tag{C.6}$$

In the case of crystal-field split ground state transitions of $TmFeO_3$ in the temperature interval between 80 K and 90 K, where the imaginary part of the dielectric function ϵ_2 is much smaller than its real part ϵ_1 [Zha16], the effective conductivity can be approximated by $\sigma = \epsilon_0 n_{\mathrm{sub}} c\alpha_{\mathrm{eff}}$. Here, $n_{\mathrm{sub}} = 4.92$ is the refractive index of $TmFeO_3$, and $\alpha_{\mathrm{eff}} \approx 4000\,\mathrm{m}^{-1}$ is the effective THz absorption coefficient obtained from data of reference [Zha16], taking into account the spectral shape of our THz pulse. We obtain

$$W_{\mathrm{abs}} = \frac{1}{2\pi}\epsilon_0 n_{\mathrm{sub}} c\alpha_{\mathrm{eff}}\int_{-\infty}^{\infty}|\tilde{E}(\omega)|^2 d\omega, \tag{C.7}$$

which can be rewritten in the time domain (compare equations C.2 and C.5) as

$$W_{\mathrm{abs}} = \epsilon_0 n_{\mathrm{sub}} c\alpha_{\mathrm{eff}}\int_{-\infty}^{\infty}E^2(t)dt. \tag{C.8}$$

The absorbed energy density in the rare-earth system for a near-field THz transient with a peak electric field of $E_{\mathrm{NF}} = 7.8\,\mathrm{MV\,cm^{-1}}$, which exceeds the threshold for spin switching, is $W_{\mathrm{abs}} = 20\,\mathrm{J\,cm^{-3}}$. $TmFeO_3$ crystallizes in a distorted perovskite structure with a unit cell volume of $V_{\mathrm{uc}} = 2.22{\times}10^{-28}\ \mathrm{m}^3$ (lattice constants, $a = 525\,\mathrm{pm}$, $b = 557\,\mathrm{pm}$, and $c = 758\,\mathrm{pm}$) [Lea68], which contains 4 Fe^{3+} spins. Thus, an upper bound for the absorbed energy in the rare-earth system per spin is given by

$$W_{\mathrm{spin}} = W_{\mathrm{abs}} \times \frac{V_{\mathrm{uc}}}{4} = 7.15\,\mathrm{meV}, \tag{C.9}$$

which is on the order of the energy of one THz photon. The dissipation by the spin system is even smaller: The energy required to overcome the potential barrier, separating two neighboring potential minima (see Figure 2.3 and Figure 2.16), normalized by the number of spins in the switched volume is on the order of 1 µeV. This value can, thus, be regarded as an upper limit for the maximal energy dissipated by one spin upon switching.

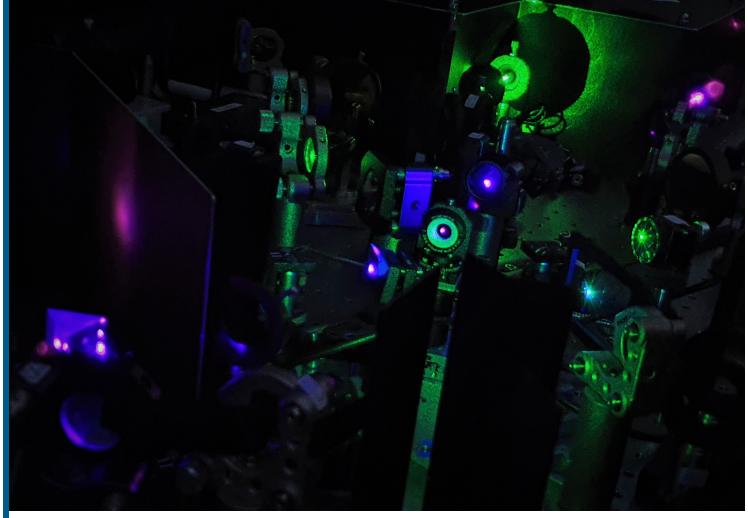

D

Characterization of ultrashort gating pulses

A well established and very powerful tool to characterize ultrashort laser pulses in amplitude and phase is *frequency-resolved optical gating* (FROG) [Kan93, Kan99, Mon10]. The conceptional idea of this technique is to temporally gate the test pulse $E(t)$ with a reference pulse $E_{\mathrm{G}}(t)$ and subsequently measuring the spectrum, ν, of this gated pulse as a function of the delay time, τ [Mon10], between the test and the gate pulse. This gives a two-dimensional signal, known as the spectrogram of the pulse

$$I(\tau,\nu) \propto \left| \int E(t)E_{\mathrm{G}}(t-\tau)\exp^{-i2\pi\nu t}\,\mathrm{d}t \right|. \tag{D.1}$$

Reconstructing this two-dimensional map with an iterative numerical algorithm allows to extract the spectral phase and amplitude of the test pulse, $E(t)$ [Kan93, Kan99].

To fully characterize the ultrashort near-infrared pulses obtained by multi-plate continuum generation, second-harmonic generation frequency-resolved optical gating (SHG-FROG) [Mon10] is used. Therefore, the multi-plate continuum beam is split into two identical replicas, whereas one of them is guided over a variable delay line in order to vary the temporal overlap, τ, between the two pulses. Subsequently, the two copies are spatially superimposed again and focused into a BBO crystal with a thickness of 10 µm to generate their sum-frequency, ν_{SF}. Detecting the intensity of ν_{SF} as a function of the delay time, τ, yields the two-dimensional spectrogram,

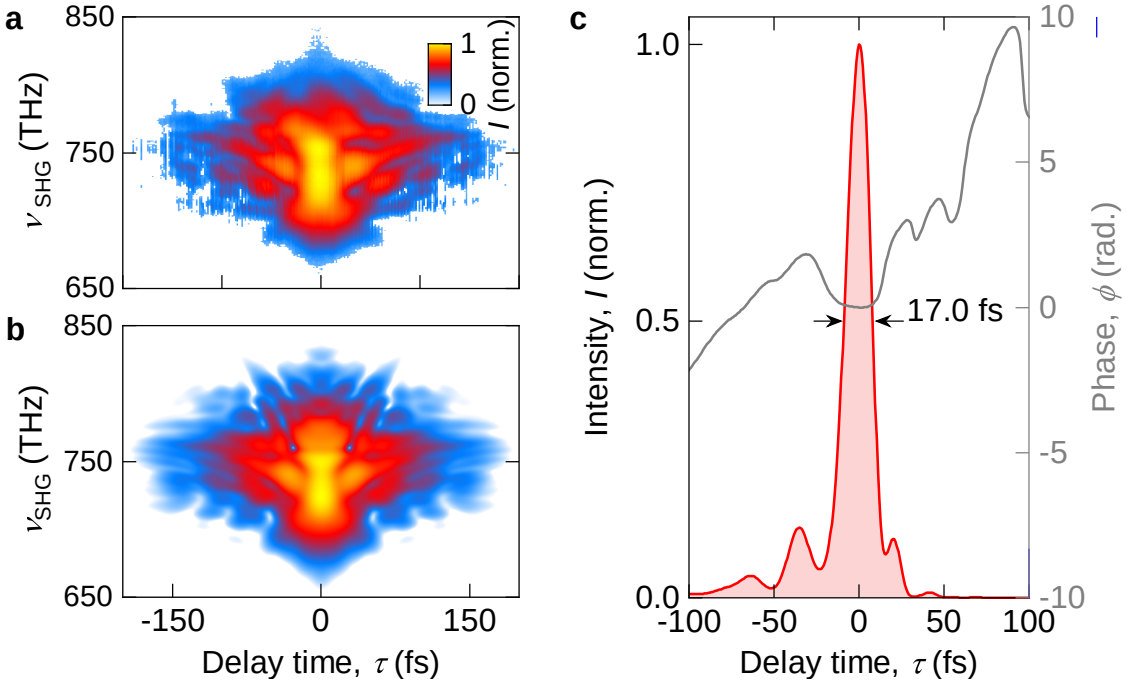

Figure D.1 | Characterization of the ultrashort multi-plate continuum pulses. a, Measured SHG-FROG trace. The spectrally resolved intensity of the second harmonic-frequency, $I(\tau, \nu_{\mathrm{SHG}})$, of the ultrashort multi-plate continuum pulses shown as a false color plot and as a function of the sum-frequency, ν_{SHG}, and the relative delay time, τ, between the two pulses. **b**, Computed SHG-FROG trace by a numerical reconstruction algorithm. Color scale, see **a**. **c**, Reconstructed intensity envelope of the multi-plate continuum pulses (red shaded area) with a FWHM pulse duration of $\tau_{\mathrm{MPC}} = 17.0\,\mathrm{fs}$. Grey solid line, temporal phase, ϕ.

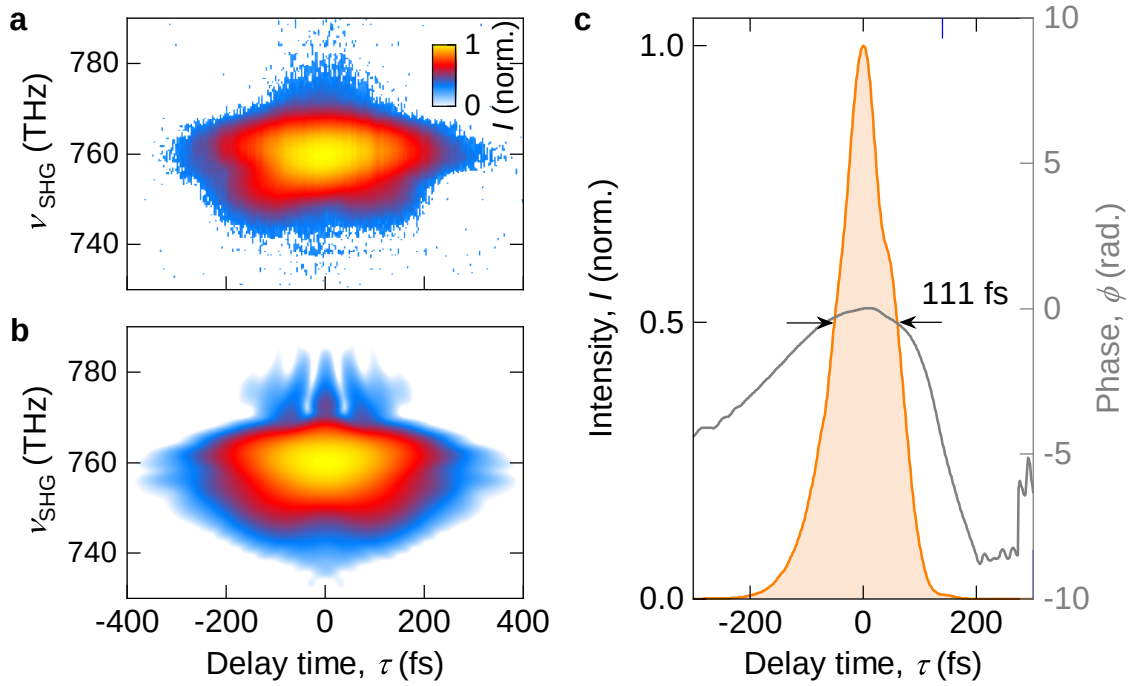

Figure D.2 | Characterization of the near-infrared probe pulses. **a**, Measured SHG-FROG trace. Intensity of the second harmonic-frequency, $I(\tau, \nu_{SHG})$, of the near-infrared pulses shown as a false color plot and as a function of the sum-frequency, ν_{SHG}, and the relative delay time, τ, between the two pulses. **b**, Computed SHG-FROG trace by a numerical reconstruction algorithm. Color scale, see a. **c**, Reconstructed intensity envelope of the near-infrared pulses (orange shaded area) with a FWHM pulse duration of $\tau_{NIR} = 111$ fs. Grey solid line, temporal phase, ϕ.

$I(\tau, \nu_{SHG})$, displayed in Figure D.1a. Thereby, at $\tau = 0$, the two copies are perfectly temporally overlapped and $I(\tau, \nu_{SHG})$ peaks. Figure D.1b displays the corresponding reconstructed sum-frequency trace calculated by an iterative numerical algorithm [Kan99, Wya08]. The good agreement between the measured (Figure D.1a) and reconstructed (Figure D.1b) intensity spectrograms permits a valid extraction of the temporal structure, $I(\tau)$, and phase, $\phi(t)$ of the multi-plate continuum pulse, which is depicted in Figure D.1c. This gives a FWHM pulse duration of $\tau_{MPC} = 17$ fs. Figure D.2 summarizes the SHG-FROG measurement of the near-infrared gating pulse (see Figure 3.15, red dashed line) used for the characterization of the ultrashort UV probe pulses, which are necessary for the time-resolved ARPES experiments. The near-infrared pulses exhibit a pulse duration of $\tau_{NIR} = 111$ fs.

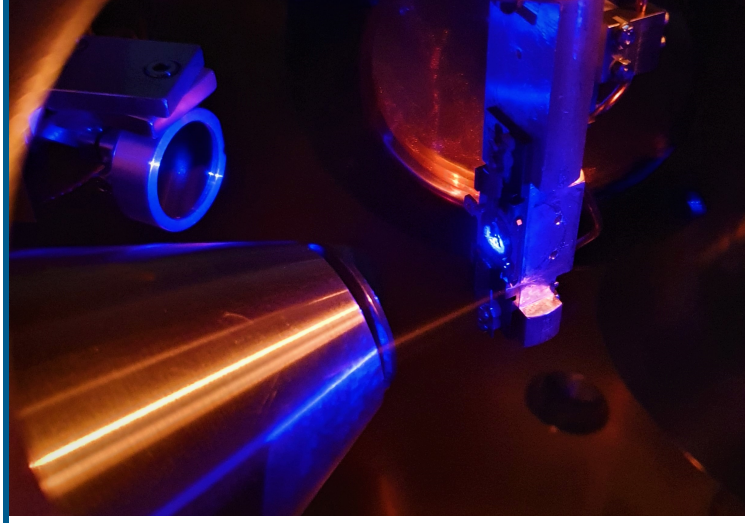

E

Influence of the curvature method on the photoemission spectra

In general, taking the second derivative of a photoemission map highlights veiled peak structures in the spectra [Sat01, Qia06, Ric10]. The two-dimensional curvature method not only significantly sharpens dispersive features in static spectroscopic images, it also maintains their absolute position [Zha11]. However, at the same time, this procedure can also introduce artifacts. To test its influence on the results that can be extracted from the time-resolved ARPES experiment, the curvature method is applied to the data presented in section 3.3.2 and published in Reimann *et al.* [Rei18b]. Thereby, a THz waveform with a center frequency of $\nu_{\mathrm{THz}} = 1\,\mathrm{THz}$ and an in-plane electric peak field strength of $E_{\mathrm{THz}} = 2.4 \pm 0.5\,\mathrm{kV\,cm^{-1}}$ is used to accelerate Dirac electrons within the topological surface state of Bi_2Te_3. Simultaneously, the lightwave induced carrier dynamics are probed by time-resolved ARPES using a *p*-polarized UV probe pulse with a center wavelength of $\lambda_{\mathrm{UV}} = 201\,\mathrm{nm}$ and a bandwidth of $\Delta\lambda = 2.8\,\mathrm{nm}$. This results in an energy resolution of 45 meV, whereas energy and momentum shifts of the photoelectrons can be determined with an accuracy of 3 meV and $0.004\,\mathrm{\AA}^{-1}$, respectively. Figure E.1a shows the corresponding static photoemission spectrum of Bi_2Te_3 taken along the crystallographic

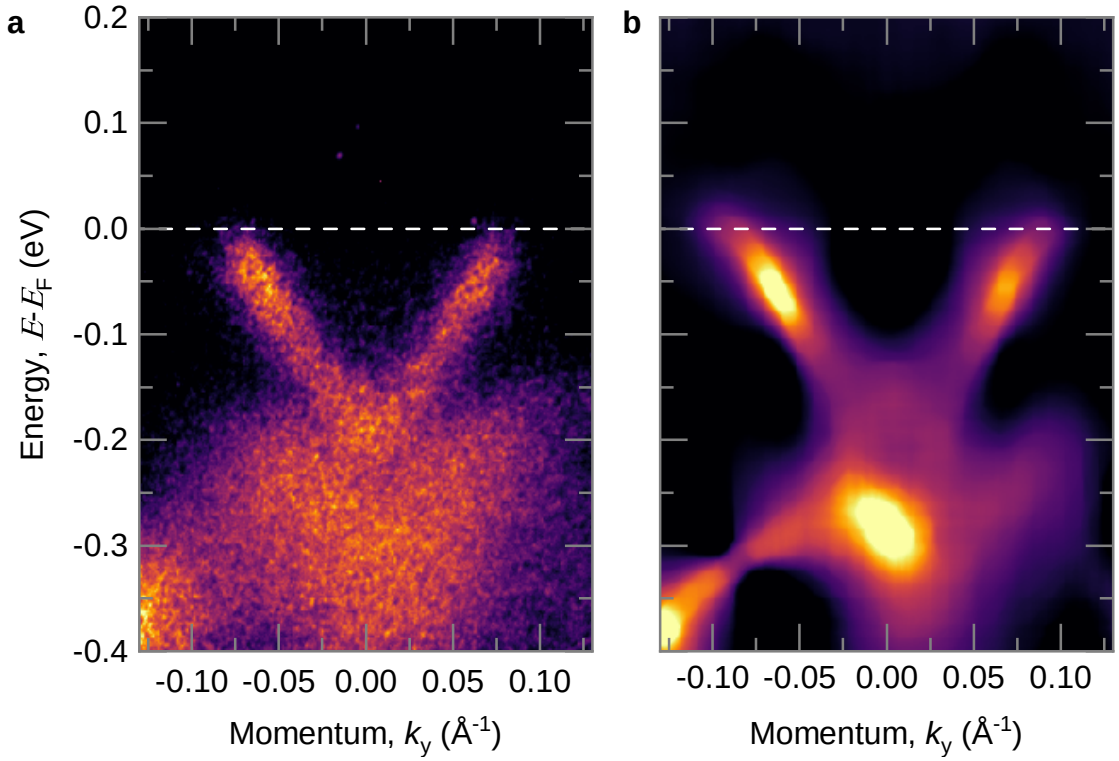

Figure E.1 | Static photoemission maps a, Static photoemission map of Bi_2Te_3 taken along the $\overline{\Gamma}$-$\overline{\mathrm{K}}$-direction with a UV pulse, that features a center wavelength of $\lambda_{\mathrm{UV}} = 201\,\mathrm{nm}$ and a bandwidth of $\Delta\lambda = 2.8\,\mathrm{nm}$. **b**, Corresponding photoemission map, smoothened by a simple moving average filter with a box size of 80×80 pixels and subsequently analyzed using the two-dimensional curvature method. The white dashed line indicates the Fermi Energy, E_{F}

$\overline{\Gamma}$-$\overline{\mathrm{K}}$-direction. The characteristic V-shaped dispersion of the Dirac cone at the $\overline{\Gamma}$-point in reciprocal is clearly visible. The Dirac point is $\approx 200\,\mathrm{meV}$ below the Fermi level, E_{F}, whereas the bulk valence band manifests itself in a broad intensity distribution at lower energies.

Figure E.1b shows the corresponding corrected ARPES image, which has been smoothened by a simple moving average filter with a box size of 80×80 pixels and subsequently analyzed by using the two-dimensional curvature method. This analysis is now repeated for every delay time, t, between the THz pump pulse and the UV probe pulse. Then, the lightwave-driven current density is calculated from the transient momentum shift, which can be extracted from the photoemission spectra

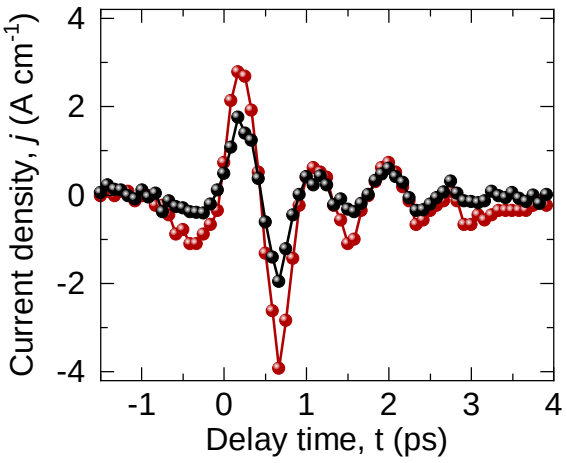

Figure E.2 | Quantitative comparison of the THz-driven electric current within the surface band. Temporal evolution of the current density, $j(t)$, extracted from the photoemission intensity distributions that have been smoothened by a simple moving average filter with a box size of 80×80 pixels and subsequently sharpened by the curvature method (red data points) compared to the current density obtained from the uncorrected photoemission map (black data points).

(see section 3.4.3 and reference [Rei18b] for details). Figure E.2 displays the resulting temporal evolution of the THz-driven Dirac current, $j(t)$, as a function of the delay time, t, extracted from the photoemission spectra sharpened by the curvature method (red data points) and the experimentally measured ARPES maps (black data points), respectively. It is clearly visible, that the current density extracted from the photoemission spectra, which have been analyzed by the two-dimensional curvature method, qualitatively reproduces the dynamics obtained from the uncorrected photoemission maps. Nonetheless, the curvature analysis overestimates the absolute value of the current density. Consequently, the values obtained from the corrected photoemission spectra are scaled by a factor of 0.537 to quantitatively match the experimental data.

F

List of publications

Publications in peer-reviewed journals

▷ C. P. Schmid, L. Weigl, P. Grössing, V. Junk, C. Gorini, **S. Schlauderer**, S. Ito, M. Meierhofer, N. Hofmann, D. Afanasiev, J. Crewse, K. A. Kokh, O. E. Tereshchenko, J. Güdde, F. Evers, J. Wilhelm, K. Richter, U. Höfer, and R. Huber
Tunable non-integer high-harmonic generation in a topological insulator
Nature, accepted.

▷ M. Borsch, C. P. Schmid, L. Weigl, **S. Schlauderer**, N. Hofmann, C. Lange, J. T. Steiner, S. W. Koch, R. Huber, M. Kira
Super-resolution lightwave tomography of electronic bands in quantum materials
Science **370**, 1204-1207 (2020).

▷ **S. Schlauderer**, C. Lange, S. Baierl, T. Ebnet, C. P. Schmid, D. C. Valovcin, A. K. Zvezdin, A. V. Kimel, R. V. Mikhaylovskiy, and R. Huber
Temporal and spectral fingerprints of ultrafast all-coherent spin switching
Nature **569**, 383-387 (2019).

▷ J. Reimann, **S. Schlauderer**, C. P. Schmid, F. Langer, S. Baierl, K. A. Kokh, O. E. Tereshchenko, A. Kimura, C. Lange, J. Güdde, U. Höfer, and R. Huber

Subcycle observation of lightwave-driven Dirac currents in a topological surface band
Nature **562**, 396-400 (2018).

▷ F. Langer, C. P. Schmid, **S. Schlauderer**, M. Gmitra, J. Fabian, P. Nagler, C. Schüller, T. Korn, P. G. Hawkins, J. T. Steiner, U. Huttner, S. W. Koch, M. Kira, and R. Huber
Lightwave valleytronics in a monolayer of tungsten diselenide
Nature **557**, 76-80 (2018).

▷ X. Ding, M. Haertelt, **S. Schlauderer**, M. S. Schuurman, A. Y. Naumov, D. M. Villeneuve, A. R. W. McKellar, P. B. Corkum, and A. Staudte
Ultrafast Dissociation of Metastable CO^{2+} in a Dimer
Physical Review Letters **118**, 153001 (2017).

Reports at international conferences and workshops

▷ **S. Schlauderer**, C. Lange, C. P. Schmid, A. K. Zvezdin, A. V. Kimel, R. V. Mikhaylovskiy and R. Huber
Minimally dissipative all-coherent spin switching at terahertz clock rates
The 22nd International Conference on Ultrafast Phenomena (UP 2020), Shanghai, China, November 2020.

▷ **S. Schlauderer**, C. Lange, C. P. Schmid, A. K. Zvezdin, A. V. Kimel, R. V. Mikhaylovskiy and R. Huber
Minimally dissipative magnetization control at terahertz clock rates
The International Magnetics Conference (INTERMAG 2020), Montréal, Canada, May 2020, **invited talk**.

▷ **S. Schlauderer**, C. Lange, C. P. Schmid, A. K. Zvezdin, A. V. Kimel, R. V. Mikhaylovskiy and R. Huber
Subcycle observation of terahertz-driven all-coherent spin switching in an antiferromagnet

Winter School on Ultrafast Processes in Condensed Matter (WUPCOM) 2020, Reit im Winkl, Germany, March 2020.

▷ **S. Schlauderer**, C. P. Schmid, F. Langer, C. Lange, S. W. Koch, M. Kira, A. V. Kimel, R. V. Mikhaylovskiy, J. Reimann, J. Güdde, U. Höfer, R. Huber
Terahertz subcycle control of charge, spin & pseudospin
12^{th} International Photonics and OptoElectronics Meetings (POEM 2019), Wuhan, China, November 2019, **invited talk**.

▷ **S. Schlauderer**, C. P. Schmid, F. Langer, C. Lange, S. W. Koch, M. Kira, A. V. Kimel, R. V. Mikhaylovskiy, J. Reimann, J. Güdde, U. Höfer,and R. Huber
Terahertz charge, spin and pseudospin control faster than a cycle of light
International conference on Ultrafast Spectroscopy of Correlated Quantum Materials (USCQM-2019), Liyang, China, July 2019, **invited talk**.

▷ **S. Schlauderer**, J. Reimann, C. P. Schmid, F. Langer, S. Baierl, K. A. Kokh, O. E. Tereshchenko, A. Kimura, C. Lange, J. Güdde, R. Huber and U. Höfer
Subcycle observation of lightwave-driven Dirac currents in a topological surface band
CLEO/Europe - EQEC, Munich, Germany, June 2019.

▷ **S. Schlauderer**, C. Lange, S. Baierl, T. Ebnet, C. P. Schmid, D. C. Valovcin, A. K. Zvezdin, A. V. Kimel, R. V. Mikhaylovskiy and R. Huber
Subcycle observation of terahertz-driven minimally dissipative spin switching
2019 Conference on Lasers and Electro-Optics (CLEO:2019), San José, USA, May 2019.

▷ **S. Schlauderer**, C. P. Schmid, F. Langer, C. Lange, P. G. Hawkins, S. W. Koch, M. Kira, A. V. Kimel, R. V. Mikhaylovskiy, J. Reimann, J. Güdde, U. Höfer, and R. Huber
Terahertz-driven all-coherent charge, spin and pseudospin control on a subcycle time scale

2^{nd} Photonic and OptoElectronic Materials Conference (POEM 2019), London, United Kingdom, April 2019, **invited talk**.

▷ **S. Schlauderer**, C. Lange, S. Baierl, T. Ebnet, C. P. Schmid, A. K. Zvezdin, A. V. Kimel, R. V. Mikhaylovskiy, and R. Huber
Ultrafast Terahertz-driven spin switching in an antiferromagnet
DPG Frühjahrstagung, Regensburg, Germany, April 2019.

▷ **S. Schlauderer**, J. Reimann, C. P. Schmid, F. Langer, S. Baierl, K. A. Kokh, O. E. Tereshchenko, A. Kimura, C. Lange, J. Güdde, R. Huber and U. Höfer
THz-driven Dirac currents in a topological surface band
8^{th} International conference on Optical Terahertz Science and Technology (OTST 2019), Santa Fe, USA, March 2019.

▷ **S. Schlauderer**, C. Lange, S. Baierl, T. Ebnet, A. K. Zvezdin, A. V. Kimel, R. V. Mikhaylovskiy and R. Huber
Time-resolved observation of THz driven magnetic switching in an antiferromagnet
2019 Joint MMM-INTERMAG Conference, Washington D.C., USA, January 2019.

▷ **S. Schlauderer**, F. Langer, C. P. Schmid, C. Lange, D. Peller, T. L. Cocker, J. Repp, J. T. Steiner, U. Huttner, P. G. Hawkins, S. W. Koch, M. Kira and R. Huber
Subcycle dynamics of terahertz lightwave electronics
International Workshop Attosecond Physics at the Nanoscale, Daejeon, South Korea, November 2018, **invited talk**.

▷ **S. Schlauderer**, F. Langer, C. P. Schmid, M. Gmitra, J. Fabian, P. Nagler, C. Schüller, T. Korn, P. G. Hawkins, J. T. Steiner, U. Huttner, S. W. Koch, M. Kira, and R. Huber
Lightwave control of the valley pseudospin in a 2D semiconductor
14^{th} International Conference on Nonlinear Optics and Excitation Kinetics in Semiconductors (NOEKS 14), Berlin, Germany, September 2018, **invited talk**.

▷ **S. Schlauderer**, F. Langer, C. P. Schmid, M. Gmitra, J. Fabian, P. Nagler, C. Schüller, T. Korn, P. G. Hawkins, J. T. Steiner, U. Huttner, S. W. Koch, M. Kira, and R. Huber
Lightwave valleytronics in monolayers of transition metal dichalcogenides
Workshop "Frontiers of photonics, plasmonics and electronics with 2D nano systems", Erice, Italy, July 2018.

▷ **S. Schlauderer**, F. Langer, C. P. Schmid, M. Gmitra, J. Fabian, P. Nagler, C. Schüller, T. Korn, P. G. Hawkins, J. T. Steiner, U. Huttner, S. W. Koch, M. Kira, and R. Huber
Lightwave valleytronics in a monolayer of tungsten diselenide
Winter School on Ultrafast Processes in Condensed Matter (WUPCOM) 2018, Reit im Winkl, Germany, March 2018.

Conference Proceedings

▷ **S. Schlauderer**, C. P. Schmid, F. Langer, C. Lange, S. W. Koch, M. Kira, A. V. Kimel, R. V. Mikhaylovskiy, J. Reimann, J. Güdde, U. Höfer, and R. Huber
Terahertz subcycle control of charge, spin & pseudospin
International Photonics and OptoElectronics Meeting 2019,
doi: 10.1364/TSA.2019.TW5B.2.

▷ J. Reimann, C. P. Schmid, **S. Schlauderer**, F. Langer, C. Lange, P. G. Hawkins, J. T. Steiner, U. Huttner, S. W. Koch, M. Kira, J. Güdde, U. Höfer, and R. Huber
Lightwave control of Dirac electrons and the valley pseudospin
Nonlinear Optics 2019, doi: 10.1364/NLO.2019.NF2A.1.

▷ C. P. Schmid, F. Langer, **S. Schlauderer**, M. Gmitra, J. Fabian, P. Nagler, T. Korn, C. Schüller, P. G. Hawkins, J. T. Steiner, U. Huttner, S. W. Koch, M. Kira, and R. Huber
Lightwave valleytronics at multi-terahertz clock rates

2019 Conference on Lasers and Electro-Optics Europe & European Quantum Electronics Conference (CLEO/Europe-EQEC), doi: 10.1109/CLEOE-EQEC.2019.8872908.

▷ **S. Schlauderer**, J. Reimann, C. P. Schmid, F. Langer, S. Baierl, K. A. Kokh, O. E. Tereshchenko, A. Kimura, C. Lange, J. Güdde, R. Huber, and U. Höfer
Subcycle observation of lightwave-driven Dirac currents in a topological surface band
2019 Conference on Lasers and Electro-Optics Europe & European Quantum Electronics Conference (CLEO/Europe-EQEC), doi: 10.1109/CLEOE-EQEC.2019.8873027.

▷ J. Reimann, **S. Schlauderer**, C. P. Schmid, F. Langer, S. Baierl, K. A. Kokh, O. E. Tereshchenko, A. Kimura, C. Lange, J. Güdde, U. Höfer, and R. Huber
Subcycle band structure movie of lightwave-driven Dirac currents
CLEO: QELS_Fundamental Science 2019,
doi: 10.1364/CLEO_QELS.2019.FTh1B.4.

▷ M. Borsch, B. J. Girodias, J. T. Steiner, S. W. Koch, C. P. Schmid, **S. Schlauderer**, F. Langer, R. Huber, and M. Kira
Lightwave Driven Valleytronic Qubit Flip
CLEO: Science and Innovations 2019, doi: 10.1364/CLEO_AT.2019.JTh4F.2.

▷ **S. Schlauderer**, C. Lange, S. Baierl, T. Ebnet, C. P. Schmid, D. C. Valovcin, A. K. Zvezdin, A. V. Kimel, R. V. Mikhaylovskiy, R. Huber
Subcycle observation of terahertz-driven minimally dissipative spin switching
CLEO: QELS_Fundamental Science 2019,
doi: 10.1364/CLEO_QELS.2019.FTh1B.2.

▷ C. P. Schmid, **S. Schlauderer**, F. Langer, M. Gmitra, J. Fabian, P. Nagler, C. Schüller, T. Korn, P. G. Hawkins, J. T. Steiner, U. Huttner, M. Borsch, B. Girodias, S. W. Koch, M. Kira, and R. Huber
Valleytronics on the subcycle timescale

CLEO: Applications and Technology 2019,
doi: 10.1364/CLEO_AT.2019.JTu4M.2.

▷ C. P. Schmid, D. Peller, F. Langer, **S. Schlauderer**, C. Lange, T. L. Cocker, J. Repp, J. Reimann, J. Güdde, U. Höfer, S. W. Koch, M. Kira, and R. Huber
Terahertz lightwave electronics and valleytronics
SPIE Ultrafast Phenomena and Nanophotonics XXIII, 1091606 2019, doi: 10.1117/12.2507634.

▷ F. Langer, C. P. Schmid, **S. Schlauderer**, P. Nagler, C. Schüller, T. Korn, M. Gmitra, J. Fabian, P. G. Hawkins, U. Huttner, J. T. Steiner, S. W. Koch, M. Kira, and R. Huber
Electron-hole collisions in an atomically thin semiconductor
Journal of Physics: Conference Series, 1220 012001 (2019), doi: 10.1088/1742 6596/1220/1/012001.

▷ F. Langer, **S. Schlauderer**, C. P. Schmid, C. Lange, D. Peller, T. L. Cocker, J. Repp, J. T. Steiner, U. Huttner, P. G. Hawkins, S. W. Koch, M. Kira, and R. Huber
Controlling electronic quantum motion on subcycle and atomic scales
CLEO: QELS_Fundamental Science 2018,
doi: 10.1364/CLEO_QELS.2018.FM3F.1.

▷ F. Langer, C. P. Schmid, **S. Schlauderer**, P. Nagler, C. Schüller, T. Korn, M. Gmitra, J. Fabian, P. G. Hawkins, J.T. Steiner, U. Huttner, S. W. Koch, M. Kira, and R. Huber
Terahertz Quasiparticle Acceleration: From Electron-Hole Collisions To Lightwave Valleytronics
2018 43rd International Conference on Infrared, Millimeter, and Terahertz Waves (IRMMW-THz), doi: 10.1109/IRMMW-THz.2018.8510268.

▷ C. P. Schmid, F. Langer, **S. Schlauderer**, M. Gmitra, J. Fabian, P. Nagler, C. Schüller, T. Korn, P. G. Hawkins, J. T. Steiner, U. Huttner, S. W Koch, M. Kira, and R. Huber
Lightwave control of the valley pseudospin in a monolayer of tung-

sten diselenide
XXI International Conference on Ultrafast Phenomena 2018 (UP 2018), doi: 10.1051/epjconf/201920505011.

▷ P. G. Hawkins, J. T. Steiner, U. Huttner, F. Langer, C. P. Schmid, **S. Schlauderer**, S. W. Koch, R. Huber, and M. Kira
Harmonic sideband generation in monolayer transition metal dichalcogenides
CLEO: QELS_Fundamental Science 2017,
doi: 10.1364/CLEO_QELS.2017.FM3D.7.

▷ F. Langer, M. Hohenleutner, C. P. Schmid, **S. Schlauderer**, U. Huttner, S. W. Koch, M. Kira, and R. Huber
THz-driven strong-field dynamics in solids: High-harmonic generation and quasiparticle collisions
2017 IEEE Photonics Conference (IPC), 523-524 (2017) doi: 10.1109/IPCon.2017.8116205.

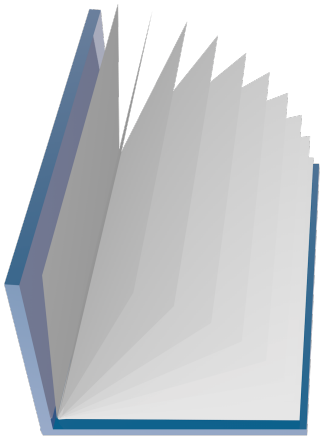

Bibliography

[Afa19] D. Afanasiev, J. R. Hortensius, B. A. Ivanov, A. Sasani, E. Bousquet, Y. M. Blanter, R. V. Mikhaylovskiy, A. V. Kimel, and A. D. Caviglia, *Light-driven ultrafast phonomagnetism*, arXiv (2019).

[AH14] A. E. Almand-Hunter, H. Li, S. T. Cundiff, M. Mootz, M. Kira, and S. W. Koch, *Quantum droplets of electrons and holes*, Nature **506**, 471–475 (2014).

[Alf06] R.R. Alfano, *The Supercontinuum Laser Source*, 2nd ed., Springer, 2006.

[Aus58] I. G. Austin, *The optical properties of bismuth telluride*, Proceedings of the Physical Society **72**, 545–552 (1958).

[Bac98] C. H. Back, R. Lopusnik, J. Fassbender, and B. Hillebrands, *Magnetization reversal in ultrashort magnetic field pulses*, Physical Review Letters **81**, 3251 (1998).

[Bac99] C. H. Back, R. Allenspach, W. Weber, S. S. P. Parkin, D. Weller, E. L. Garwin, and H. C. Siegmann, *Minimum Field Strength in Precessional Magnetization Reversal*, Science **285**, 864–868 (1999).

[Bac04] C. H. Back and D. Pescia, *Applied physics: Speed limit ahead*, Nature **428**, 808 (2004).

[Bai16a] S. Baierl, M. Hohenleutner, T. Kampfrath, A. K. Zvezdin, A. V. Kimel, R. Huber, and R. V. Mikhaylovskiy, *Nonlinear spin control by terahertz-driven anisotropy fields*, Nature Photonics **10**, 715–718 (2016).

[Bai16b] S. Baierl, J. H. Mentink, M. Hohenleutner, L. Braun, T. M. Do, C. Lange, A. Sell, M. Fiebig, G. Woltersdorf, T. Kampfrath, and R. Huber, *Terahertz-Driven Nonlinear Spin Response of Antiferromagnetic Nickel Oxide*, Physical Review Letters **117**, 197201 (2016).

[Bal85] A. M. Balbashov, A. A. Volkov, G.V. Kozlov, S. P. Lebedev, A. A. Mukhin, A. Yu. Pronin, A. S. Prokhorov, and A. M. Prokhorov, *Observation in TmFeO3 of direct electronic transitions inside the principal multiplet of a rare-earth ion*, JETP Letters **42**, 564–567 (1985).

[Ban17] H. B. Banks, Q. Wu, D. C. Valovcin, S. Mack, A.C. Gossard, L. Pfeiffer, R. B. Liu, and M. S. Sherwin, *Dynamical birefringence: Electron-hole recollisions as probes of berry curvature*, Physical Review X **7**, 41042 (2017).

[Bar48] J. Bardeen and W. H. Brattain, *The Transistor, a semiconductor triode*, Physical Review **74**, 230–231 (1948).

[Bau17] M. Baumgartner, K. Garello, J. Mendil, C. O. Avci, E. Grimaldi, C. Murer, J. Feng, M. Gabureac, C. Stamm, Y. Acremann, S. Finizio, S. Wintz, J. Raabe, and P. Gambardella, *Spatially and time-resolved magnetization dynamics driven by spin-orbit torques*, Nature Nanotechnology **12**, 980–986 (2017).

[Bau18] D. Bauer and K. K. Hansen, *High-Harmonic Generation in Solids with and without Topological Edge States*, Physical Review Letters **120**, 177401 (2018).

[Bea96] E. Beaurepaire, J. C. Merle, A. Daunois, and J. Y. Bigot, *Ultrafast spin dynamics in ferromagnetic nickel*, Physical Review Letters **76**, 4250–4253 (1996).

[Bec88] P. C. Becker, H. L. Fragnito, C. H.Brito Cruz, R. L. Fork, J. E. Cunningham, J. E. Henry, and C. V. Shank, *Femtosecond photon echoes from band-to-band transitions in GaAs*, Physical Review Letters **61**, 1647–1649 (1988).

[Bel75] K. P. Belov, A. K. Zvezdin, R. Z. Levitin, A. S. Markosyan, B. V. Mill, A. A. Mukhin, and A. P. Perov, *Spin-flip transitions in cubic magnets . Magnetic phase diagram of terbium-yttrium iron garnets*, Soviet Physics JETP **41 (3)**, 590–596 (1975).

[Ber06] B. A. Bernevig, T. L. Hughes, and S.-C. Zhang, *Quantum Spin Hall Effect and Topological Phase Transition in HgTe Quantum Wells*, Science **314**, 1757–1762 (2006).

[Ber07] L. Bergé, S. Skupin, R. Nuter, J. Kasparian, and J. P. Wolf, *Ultrashort filaments of light in weakly ionized, optically transparent media*, Reports on Progress in Physics **70**, 1633–1713 (2007).

[Blo29] F. Bloch, *Über die Quantenmechanik der Elektronen in Kristallgittern*, Zeitschrift für Physik **52**, 555–600 (1929).

[Bor20] M. Borsch, C. P. Schmid, L. Weigl, S. Schlauderer, N. Hofmann, C. Lange, J. T. Steiner, S. W. Koch, R. Huber, and M Kira, *Super-resolution lightwave tomography of electronic bands in quantum materials*, Science **370**, 1204–1207 (2020).

[Boy03] B. Boyd, *Nonlinear Optics*, 3rd ed., Academic Press, 2003.

[Bra00] T. Brabec and F. Krausz, *Intense few-cycle laser fields: Frontiers of nonlinear optics*, Reviews of Modern Physics **72**, 545–591 (2000).

[Bra09] M. Bradler, P. Baum, and E. Riedle, *Femtosecond continuum generation in bulk laser host materials with sub-μJ pump pulses*, Applied Physics B: Lasers and Optics **97**, 561–574 (2009).

[Bra16] L. Braun, G. Mussler, A. Hruban, M. Konczykowski, T. Schumann, M. Wolf, M. Münzenberg, L. Perfetti, and T. Kampfrath, *Ultrafast photocurrents at the surface of the three-dimensional topological insulator Bi_2Se_3*, Nature Communications **7**, 1–9 (2016).

[CG14] A. Castellanos-Gomez, M. Buscema, R. Molenaar, V. Singh, L. Janssen, H. S. J. Van Der Zant, and G. A. Steele, *Deterministic transfer of two-*

dimensional materials by all-dry viscoelastic stamping, 2D Materials **1**, 011002 (2014).

[Che78] M. V. Chetkin and A. de la Campa, *Maximum velocity of a domain wall in a weak ferromagnet*, JETP Letters **27**, 157–160 (1978).

[Che09] Y. L. Chen, J. G. Analytis, J.-H. Chu, Z. K. Liu, S.-K. Mo, X. L. Qi, H. J. Zhang, D. H. Lu, X. Dai, Z. Fang, S. C. Zhang, I. R. Fisher, Z. Hussain, and Z.-X. Shen, *Experimental Realization of a Three-Dimensional Topological Insulator, Bi_2Te_3*, Science **325**, 178–181 (2009).

[Che14] A. Chernikov, T. C. Berkelbach, H. M. Hill, A. Rigosi, Y. Li, O. B. Aslan, D. R. Reichman, M. S. Hybertsen, and T. F. Heinz, *Exciton binding energy and nonhydrogenic Rydberg series in monolayer WS_2*, Physical Review Letters **113**, 076802 (2014).

[Che16] Y.-C. Cheng, C.-H. Lu, Y.-Y. Lin, and A. H. Kung, *Supercontinuum generation in a multi-plate medium*, Optics Express **24**, 7224 (2016).

[Che20] B. Cheng, N. Kanda, T. N. Ikeda, T. Matsuda, P. Xia, T. Schumann, S. Stemmer, J. Itatani, N. P. Armitage, and R. Matsunaga, *Efficient Terahertz Harmonic Generation with Coherent Acceleration of Electrons in the Dirac Semimetal Cd_3As_2*, Physical Review Letters **124**, 117402 (2020).

[Chi01] A. H. Chin, O. G. Calderón, and J. Kono, *Extreme midinfrared nonlinear optics in semiconductors*, Physical Review Letters **86**, 3292–3295 (2001).

[Coc16] T. L. Cocker, D. Peller, P. Yu, J. Repp, and R. Huber, *Tracking the ultrafast motion of a single molecule by femtosecond orbital imaging*, Nature **539**, 263–267 (2016).

[Coe09] J. M. D. Coey, *Magnetism and Magnetic Materials*, Cambridge University Press, 2009.

[Cor07] P. B. Corkum and F. Krausz, *Attosecond science*, Nature Physics **3**, 381–387 (2007).

[Cou07] A. Couairon and A. Mysyrowicz, *Femtosecond filamentation in transparent media*, Physics Reports **441**, 47–189 (2007).

[Cun02] S. T. Cundiff, *Phase stabilization of ultrashort optical pulses*, Journal of Physics D: Applied Physics **35**, R43–R59 (2002).

[Dam04] A. Damascelli, *Probing the electronic structure of complex systems by ARPES*, Physica Scripta T **109**, 61–74 (2004).

[Dav09] J. H. Davies, *The physics of low-dimensional semiconductors*, Cambridge University Press, 2009.

[De 11] J. A. De Jong, A. V. Kimel, R. V. Pisarev, A. Kirilyuk, and Th. Rasing, *Laser-induced ultrafast spin dynamics in $ErFeO_3$*, Physical Review B - Condensed Matter and Materials Physics **84**, 1–8 (2011).

[Del03] J. Delahaye, J. Hassel, R. Lindell, M. Sillanpää, M. Paalanen, H. Seppä, and P. Hakonen, *Low-noise current amplifier based on mesoscopic Josephson junction*, Science **299**, 1045–1048 (2003).

[Di 13] P. Di Pietro, M. Ortolani, O. Limaj, A. Di Gaspare, V. Giliberti, F. Giorgianni, M. Brahlek, N. Bansal, N. Koirala, S. Oh, P. Calvani, and S. Lupi, *Observation of Dirac plasmons in a topological insulator*, Nature Nanotechnology **8**, 556–560 (2013).

[Die06] J.-C. Diels, *Ultrashort Laser Pulse Phenomena*, 2nd ed., Academic Press, 2006.

[Ech04] P. M. Echenique, R. Berndt, E. V. Chulkov, Th. Fauster, A. Goldmann, and U. Höfer, *Decay of electronic excitations at metal surfaces*, Surface Science Reports **52**, 219–317 (2004).

[Eib65] M. Eibschütz, *Lattice constants of orthoferrites*, Acta Crystallographica **19**, 337–339 (1965).

[Eim87] D. Eimerl, L. Davis, S. Velsko, E. K. Graham, and A. Zalkin, *Optical, mechanical, and thermal properties of barium borate*, Journal of Applied Physics **62**, 1968–1983 (1987).

[Ein05] A. Einstein, *Über eine Erzeugung und Verwandlung des Lichtes betreffenden heuristischen Gesichtspunkt*, Ann. Phys. **332**, 132–148 (1905).

[Fai97] F. H. M. Faisal and J. Z. Kamiński, *Floquet-Bloch theory of high-harmonic generation in periodic structures*, Physical Review A **56**, 748–762 (1997).

[Fel92] J. Feldmann, K. Leo, J. Shah, D. A. B. Miller, and J. E. Cunningham, *Optical investigation of Bloch oscillations in semiconductor superlattices*, Physical Review B **46**, 7252–7255 (1992).

[För11] M. Först, R. I. Tobey, S. Wall, H. Bromberger, V. Khanna, A. L. Cavalieri, Y. D. Chuang, W. S. Lee, R. Moore, W. F. Schlotter, J. J. Turner, O. Krupin, M. Trigo, H. Zheng, J. F. Mitchell, S. S. Dhesi, J. P. Hill, and A. Cavalleri, *Driving magnetic order in a manganite by ultrafast lattice excitation*, Physical Review B - Condensed Matter and Materials Physics **84**, 1–5 (2011).

[Fro04] D. P. Fromm, A. Sundaramurthy, P. James Schuck, G. Kino, and W. E. Moerner, *Gap-dependent optical coupling of single "Bowtie" Nanoantennas Resonant in the Visible*, Nano Letters **4**, 957–961 (2004).

[Fu07a] L. Fu and C. L. Kane, *Topological insulators with inversion symmetry*, Physical Review B **76**, 045302 (2007).

[Fu07b] L. Fu, C. L. Kane, and E. J. Mele, *Topological insulators in three dimensions*, Physical Review Letters **98**, 106803 (2007).

[Fu08] L. Fu and C. L. Kane, *Superconducting proximity effect and majorana fermions at the surface of a topological insulator*, Physical Review Letters **100**, 096407 (2008).

[Fül20] J. A. Fülöp, S. Tzortzakis, and T. Kampfrath, *Laser-Driven Strong-Field Terahertz Sources*, Advanced Optical Materials **8**, 1–25 (2020).

[Gal99] G. Gallot and D. Grischkowsky, *Electro-optic detection of terahertz radiation*, Journal of the Optical Society of America B **16**, 1204–1212 (1999).

[Gam09] S. J. Gamble, M. H. Burkhardt, A. Kashuba, R. Allenspach, S. S. P. Parkin, H. C. Siegmann, and J. Stöhr, *Electric field induced magnetic anisotropy in a ferromagnet*, Physical Review Letters **102**, 217201 (2009).

[Gar96] G. A. Garrett, T. F. Albrecht, J. F. Whitaker, and R. Merlin, *Coherent THz phonons driven by light pulses and the Sb problem: What is the mechanism?*, Physical Review Letters **77**, 3661–3664 (1996).

[Gar16] M. Garg, M. Zhan, T. T. Luu, H. Lakhotia, T. Klostermann, A. Guggenmos, and E. Goulielmakis, *Multi-petahertz electronic metrology*, Nature **538**, 359–363 (2016).

[Ger02] Th. Gerrits, H. A. M. Van den Berg, J. Hohlfeld, L. Bär, and Th. Rasing, *Ultrafast precessional magnetization reversal by picosecond magnetic field pulse shaping*, Nature **418**, 509–512 (2002).

[Ghi11] S. Ghimire, A. D. Di Chiara, E. Sistrunk, P. Agostini, L. F. Di Mauro, and D. A. Reis, *Observation of high-order harmonic generation in a bulk crystal*, Nature Physics **7**, 138–141 (2011).

[Gia09] P. Giannozzi, S. Baroni, N. Bonini, M. Calandra, R. Car, C. Cavazzoni, D. Ceresoli, G. L. Chiarotti, M. Cococcioni, I. Dabo, A. Dal Corso, S. De Gironcoli, S. Fabris, G. Fratesi, R. Gebauer, U. Gerstmann, C. Gougoussis, A. Kokalj, M. Lazzeri, L. Martin-Samos, N. Marzari, F. Mauri, R. Mazzarello, S. Paolini, A. Pasquarello, L. Paulatto, C. Sbraccia, S. Scandolo, G. Sclauzero, A. P. Seitsonen, A. Smogunov, P. Umari, and R. M. Wentzcovitch, *QUANTUM ESPRESSO: A modular and open-source software project for quantum simulations of materials*, Journal of Physics: Condensed Matter **21**, 395502 (2009).

[Gio16] F. Giorgianni, E. Chiadroni, A. Rovere, M. Cestelli-Guidi, A. Perucchi, M. Bellaveglia, M. Castellano, D. Di Giovenale, G. Di Pirro, M. Ferrario, R. Pompili, C. Vaccarezza, F. Villa, A. Cianchi, A. Mostacci, M. Petrarca, M. Brahlek, N. Koirala, S. Oh, and S. Lupi, *Strong nonlinear terahertz response induced by Dirac surface states in Bi_2Se_3 topological insulator*, Nature Communications **7**, 1–6 (2016).

[Gol08] D. Golde, T. Meier, and S. W. Koch, *High harmonics generated in semiconductor nanostructures by the coupled dynamics of optical inter- and intraband excitations*, Physical Review B **77**, 1–6 (2008).

[Gol11] D. Golde, M. Kira, T. Meier, and S. W. Koch, *Microscopic theory of the extremely nonlinear terahertz response of semiconductors*, Phys. Status Solidi B **248**, 863–866 (2011).

[Gri18] K. Grishunin, T. Huisman, G. Li, E. Mishina, Th. Rasing, A. V. Kimel, K. Zhang, Z. Jin, S. Cao, W. Ren, G.-H. Ma, and R. V. Mikhaylovskiy, *Terahertz Magnon-Polaritons in $TmFeO_3$*, ACS Photonics **5**, 1375–1380 (2018).

[Gro18] R. Gross and A. Marx, *Festkörperphysik*, 3rd ed., DeGruyter, 2018.

[Gru10] M. Grundmann, *The Physics of Semiconductors*, 2nd ed., Springer, 2010.

[Gru20] S. Grundmann, D. Trabert, K. Fehre, N. Strenger, A. Pier, L. Kaiser, M. Kircher, M. Weller, S. Eckart, L. Ph. H. Schmidt, F. Trinter, T. Jahnke, M. S. Schöffler, and R. Dörner, *Zeptosecond birth time delay in molecular photoionization.*, Science **370**, 339–341 (2020).

[Güd07] J. Güdde, M. Rohleder, T. Meier, S.W. Koch, and U. Höfer, *Time-Resolved Investigation of Coherently Controlled Electric Currents at a Metal Surface*, Science **318**, 1287–1291 (2007).

[Haf18] H. A. Hafez, S. Kovalev, J. C. Deinert, Z. Mics, B. Green, N. Awari, M. Chen, S. Germanskiy, U. Lehnert, J. Teichert, Z. Wang, K. J. Tielrooij, Z. Liu, Z. Chen, A. Narita, K. Müllen, M. Bonn, M. Gensch, and D. Turchinovich, *Extremely efficient terahertz high-harmonic generation in graphene by hot Dirac fermions*, Nature **561**, 507–511 (2018).

[Haj12] M. Hajlaoui, E. Papalazarou, J. Mauchain, G. Lantz, N. Moisan, D. Boschetto, Z. Jiang, I. Miotkowski, Y. P. Chen, A. Taleb-Ibrahimi, L. Perfetti, and M. Marsi, *Ultrafast surface carrier dynamics in the topological insulator Bi_2Te_3*, Nano Letters **12**, 3532–3536 (2012).

[Haj14] M. Hajlaoui, E. Papalazarou, J. Mauchain, L. Perfetti, A. Taleb-Ibrahimi, F. Navarin, M. Monteverde, P. Auban-Senzier, C. R. Pasquier, N. Moisan, D. Boschetto, M. Neupane, M. Z. Hasan, T. Durakiewicz, Z. Jiang, Y. Xu, I. Miotkowski, Y. P. Chen, S. Jia, H. W. Ji, R. J. Cava, and M. Marsi, *Tuning a Schottky barrier in a photoexcited topological insulator with transient Dirac cone electron-hole asymmetry*, Nature Communications **5**, 1–8 (2014).

[Han09] T. Hanke, G. Krauss, D. Träutlein, B. Wild, R. Bratschitsch, and A. Leitenstorfer, *Efficient nonlinear light emission of single gold optical antennas driven by few-cycle near-infrared pulses*, Physical Review Letters **103**, 257404 (2009).

[Has10] M. Z. Hasan and C. L. Kane, *Colloquium: Topological insulators*, Reviews of Modern Physics **82**, 3045–3067 (2010).

[Heb02] J. Hebling, G. Almasi, I. Kozma, and J. Kuhl, *Velocity matching by pulse front tilting for large area THz-pulse generation*, Optics Express **10**, 1161 (2002).

[Heb04] J. Hebling, A. G. Stepanov, G. Almási, B. Bartal, and J. Kuhl, *Tunable THz pulse generation by optical rectification of ultrashort laser pulses with tilted pulse fronts*, Applied Physics B: Lasers and Optics **78**, 593–599 (2004).

[Hec17] E. Hecht, *Optics*, 5th ed., Pearson, 2017.

[Her87] H. Hertz, *Ueber einen Einfluss des ultravioletten Lichtes auf die electrische Entladung*, Ann. Phys. **267**, 983–1000 (1887).

[Hig14] T. Higuchi, M. I. Stockman, and P. Hommelhoff, *Strong-field perspective on high-harmonic radiation from bulk solids*, Physical Review Letters **113**, 213901 (2014).

[Hir11] H. Hirori, A. Doi, F. Blanchard, and K. Tanaka, *Single-cycle terahertz pulses with amplitudes exceeding 1 MV/cm generated by optical rectification in $LiNbO_3$*, Applied Physics Letters **98**, 091106 (2011).

[Hoh15] M. Hohenleutner, F. Langer, O. Schubert, M. Knorr, U. Huttner, S. W. Koch, M. Kira, and R. Huber, *Real-time observation of interfering crystal electrons in high-harmonic generation*, Nature **523**, 572–575 (2015).

[Hor68] H. Horner and C. M. Varma, *Nature of spin-reorientation transitions*, Physical Review Letters **20**, 845–846 (1968).

[Hsi08] D. Hsieh, D. Qian, L. Wray, Y. Xia, Y. S. Hor, R. J. Cava, and M. Z. Hasan, *A topological Dirac insulator in a quantum spin Hall phase*, Nature **452**, 970–974 (2008).

[Hsi09] D. Hsieh, Y. Xia, D. Qian, L. Wray, J. H. Dil, F. Meier, J. Osterwalder, L. Patthey, J. G. Checkelsky, N. P. Ong, A. V. Fedorov, H. Lin, A. Bansil, D. Grauer, Y. S. Hor, R. J. Cava, and M. Z. Hasan, *A tunable topological insulator in the spin helical Dirac transport regime*, Nature **460**, 1101–1105 (2009).

[Hub01] R. Huber, F. Tauser, A. Brodschelm, M. Bichler, G. Abstreiter, and A. Leitenstorfer, *How many-particle interactions develop after ultrafast excitation of an electron-hole plasma*, Nature **414**, 286–289 (2001).

[Hub17] M. A. Huber, F. Mooshammer, M. Plankl, L. Viti, F. Sandner, L. Z. Kastner, T. Frank, J. Fabian, M. S. Vitiello, T. L. Cocker, and R. Huber, *Femtosecond photo-switching of interface polaritons in black phosphorus heterostructures*, Nature Nanotechnology **12**, 207–211 (2017).

[Hüf03] S. Hüfner, *Photoelectron Spectroscopy*, Springer Verlag, 2003.

[Jai59] A. L. Jain, *Temperature Dependence of the Electrical Properties of Bismuth-Antimony Alloys*, Physical Review **114**, 1518–1528 (1959).

[Jon13] A. M. Jones, H. Yu, N. J. Ghimire, S. Wu, G. Aivazian, J. S. Ross, B. Zhao, J. Yan, D. G. Mandrus, D. Xiao, W. Yao, and X. Xu, *Optical generation of excitonic valley coherence in monolayer WSe_2*, Nature Nanotechnology **8**, 634–638 (2013).

[Jun12] F. Junginger, B. Mayer, C. Schmidt, O. Schubert, S. Mährlein, A. Leitenstorfer, R. Huber, and A. Pashkin, *Nonperturbative interband response of a bulk InSb semiconductor driven off resonantly by terahertz electromagnetic few-cycle pulses*, Physical Review Letters **109**, 147403 (2012).

[Jun16] T. Jungwirth, X. Marti, P. Wadley, and J. Wunderlich, *Antiferromagnetic spintronics*, Nature Nanotechnology **11**, 231–241 (2016).

[Jun20] V. Junk, P. Reck, C. Gorini, and K. Richter, *Floquet oscillations in periodically driven Dirac systems*, Physical Review B **101**, 134302 (2020).

[Kam11] T. Kampfrath, A. Sell, G. Klatt, A. Pashkin, S. Mährlein, T. Dekorsy, M. Wolf, M. Fiebig, A. Leitenstorfer, and R. Huber, *Coherent terahertz control of antiferromagnetic spin waves*, Nature Photonics **5**, 31–34 (2011).

[Kam13] T. Kampfrath, K. Tanaka, and K. Nelson, *Resonant and nonresonant control over matter and light by intense terahertz transients*, Nature Photonics **7**, 680–690 (2013).

[Kan93] D. J. Kane and R. Trebino, *Characterization of Arbitrary Femtosecond Pulses Using Frequency-Resolved Optical Gating*, IEEE Journal of Quantum Electronics **29**, 571–579 (1993).

[Kan99] D. J. Kane, *Recent Progress Toward Real-Time Measurement of Ultrashort Laser Pulses*, IEEE Journal of Quantum Electronics **35**, 421–431 (1999).

[Kan05] C. L. Kane and E. J. Mele, *Z2 topological order and the quantum spin hall effect*, Physical Review Letters **95**, 146802 (2005).

[Kan11] C. Kane and J. Moore, *Topological insulators*, Physics World **24**, (02) 32 (2011).

[Kas15] C. Kastl, C. Karnetzky, H. Karl, and A. W. Holleitner, *Ultrafast helicity control of surface currents in topological insulators with near-unity fidelity*, Nature Communications **6**, 1–6 (2015).

[Kat04] Y. Kato, R. C. Myers, A. C. Gossard, and D. D. Awschalom, *Coherent spin manipulation without magnetic fields in strained semiconductors*, Nature **427**, 50–53 (2004).

[Kel65] L. V. Keldysh, *Ionization in the field of a strong electromagnetic wave*, Soviet Physics JETP **20**, 1307–1314 (1965).

[Key06] W. R. Keyes, *The Impact of Moore's Law*, IEEE Solid-State Circuits Society Newsletter **11**, 25–27 (2006).

[Kie20] J. Kiemle, P. Seifert, A. W. Holleitner, and C. Kastl, *Ultrafast and Local Optoelectronic Transport in Topological Insulators*, Physica Status Solidi B **2021**, 258, 2000033 (2020).

[Kil64] J. S. Kilby, *Miniaturized Electronic Circuits*, Texas Instruments, 1964.

[Kil76] J. S. Kilby, *Invention of the Integrated Circuit*, IEEE Transactions on Electron Devices **23**, 648–654 (1976).

[Kim04] A. V. Kimel, A. Kirilyuk, A. Tsvetkov, R. V. Pisarev, and Th. Rasing, *Laser-induced ultrafast spin reorientation in the antiferromagnet $TmFeO_3$*, Nature **429**, 850–853 (2004).

[Kim05] A. V. Kimel, A. Kirilyuk, P. A. Usachev, R. V. Pisarev, A. M. Balbashov, and Th. Rasing, *Ultrafast non-thermal control of magnetization by instantaneous photomagnetic pulses*, Nature **435**, 655–657 (2005).

[Kim06] B. J. Kim, H. Koh, E. Rotenberg, S. J. Oh, H. Eisaki, N. Motoyama, S. Uchida, T. Tohyama, S. Maekawa, Z. X. Shen, and C. Kim, *Distinct spinon and holon dispersions in photoemission spectral functions from one-dimensional $SrCuO_2$*, Nature Physics **2**, 397–401 (2006).

[Kim08] S. Kim, J. Jin, Y. Ji. Kim, I. Y. Park, Y. Kim, and S. W. Kim, *High-harmonic generation by resonant plasmon field enhancement*, Nature **453**, 757–760 (2008).

[Kim09] A. V. Kimel, B. A. Ivanov, R. V. Pisarev, P. A. Usachev, A. Kirilyuk, and Th. Rasing, *Inertia-driven spin switching in antiferromagnets*, Nature Physics **5**, 727–731 (2009).

[Kim12] K. W. Kim, A. Pashkin, H. Schäfer, M. Beyer, M. Porer, T. Wolf, C. Bernhard, J. Demsar, R. Huber, and A. Leitenstorfer, *Ultrafast transient generation of spin-density-wave order in the normal state of $BaFe_2As_2$ driven by coherent lattice vibrations*, Nature Materials **11**, 497–501 (2012).

[Kim18] T. H. Kim, P. Grünberg, S. H. Han, and B. K. Cho, *Precessional switching of antiferromagnets by electric field induced Dzyaloshinskii-Moriya torque*, Physical Review B **97**, 1–7 (2018).

[Kim19] A. V. Kimel and M. Li, *Writing magnetic memory with ultrashort light pulses*, Nature Reviews Materials **4**, 189–200 (2019).

[Kim20] A. V. Kimel, A. M. Kalashnikova, A. Pogrebna, and A. K. Zvezdin, *Fundamentals and perspectives of ultrafast photoferroic recording*, Physics Reports **852**, 1–46 (2020).

[Kir06] M. Kira and S. W. Koch, *Many-body correlations and excitonic effects in semiconductor spectroscopy*, Progress in Quantum Electronics **30**, 155–296 (2006).

[Kir10] A. Kirilyuk, A. V. Kimel, and Th. Rasing, *Ultrafast optical manipulation of magnetic order*, Reviews of Modern Physics **82**, 2731–2784 (2010).

[Kir12] M. Kira and S. W. Koch, *Semiconductor Quantum Optics*, Cambridge University Press, 2012.

[Kok14] K. A. Kokh, S. V. Makarenko, V. A. Golyashov, O. A. Shegai, and O. E. Tereshchenko, *Melt growth of bulk Bi_2Te_3 crystals with a natural p-n junction*, CrystEngComm **16**, 581–584 (2014).

[Kön07] M. König, S. Wiedmann, C. Brüne, A. Roth, H. Buhmann, L. W. Molenkamp, X.-L. Qi, and S.-C. Zhang, *Quantum Spin Hall Insulator State in HgTe Quantum Wells*, Science **318**, 766–771 (2007).

[Kos73] J. M. Kosterlitz and D. J. Thouless, *Ordering, metastability and phase transitions in two-dimensional systems*, Journal of Physics C: Solid State Physics **6**, 1181–1203 (1973).

[Koz90] G.V. Kozlov, A. A. Mukhin, Y. Yu. Pronin, A.S. Prokhorov, V. Zelezny, and J. Petzelt, *Observation of magnetic dipole and electric dipole electron transitions in the ground multiplet of the rare-earth ion in $TmFeO_3$*, JETP Letters **52**, 264–268 (1990).

[Kue10] W. Kuehn, P. Gaal, K. Reimann, M. Woerner, T. Elsaesser, and R. Hey, *Coherent ballistic motion of electrons in a periodic potential*, Physical Review Letters **104**, 146602 (2010).

[Kur16] K. Kuroda, J. Reimann, J. Güdde, and U. Höfer, *Generation of Transient Photocurrents in the Topological Surface State of Sb_2Te_3 by Direct Optical Excitation with Midinfrared Pulses*, Physical Review Letters **116**, 076801 (2016).

[Lan37] L. D. Landau, *On the theory of phase transitions*, Zh. Eksp. Teor. Fiz. **7**, 19–32 (1937).

[Lan61] R. Landauer, *Irreversibility and Heat Generation*, IBM Journal of Research and Development **5**, 183–191 (1961).

[Lan14] C. Lange, T. Maag, M. Hohenleutner, S. Baierl, O. Schubert, E. R. J. Edwards, D. Bougeard, G. Woltersdorf, and R. Huber, *Extremely nonperturbative nonlinearities in GaAs driven by atomically strong terahertz fields in gold metamaterials*, Physical Review Letters **113**, 227401 (2014).

[Lan16] F. Langer, M. Hohenleutner, C. P. Schmid, C. Poellmann, P. Nagler, T. Korn, C. Schüller, M. S. Sherwin, U. Huttner, S. T. Steiner, S. W. Koch, M. Kira, and R. Huber, *Lightwave-driven quasiparticle collisions on a subcycle timescale*, Nature **533**, 225–229 (2016).

[Lan17] F. Langer, M. Hohenleutner, U. Huttner, S. W. Koch, M. Kira, and R. Huber, *Symmetry-controlled temporal structure of high-harmonic carrier fields from a bulk crystal*, Nature Photonics **11**, 227–231 (2017).

[Lan18a] F. Langer, *Lightwave-driven quasiparticle acceleration*, Dissertation, University of Regensburg, 2018.

[Lan18b] F. Langer, C. P. Schmid, S. Schlauderer, M. Gmitra, J. Fabian, P. Nagler, C. Schüller, T. Korn, P. G. Hawkins, J. T. Steiner, U. Huttner, S. W. Koch, M. Kira, and R. Huber, *Lightwave valleytronics in a monolayer of tungsten diselenide*, Nature **557**, 76–80 (2018).

[Lar97] J. Larmor, *LXIII. On the theory of the magnetic influence on spectra; and on the radiation from moving ions* , The London, Edinburgh, and Dublin Philosophical Magazine and Journal of Science **44**, 503–512 (1897).

[Lea68] J. A. Leake, G. Shirane, and J. P. Remeika, *The magnetic structure of thulium orthoferrite, $TmFeO_3$*, Solid State Communications **6**, 15–17 (1968).

[Lei99] A. Leitenstorfer, S. Hunsche, J. Shah, M. C. Nuss, and W. H. Knox, *Ultrafast high-field transport in semiconductors*, Physica B: Condensed Matter **272**, 348–352 (1999).

[Lei08] S. Leinß, T. Kampfrath, K. v. Volkmann, M. Wolf, J. T. Steiner, M. Kira, S. W. Koch, A. Leitenstorfer, and R. Huber, *Terahertz coherent control of optically dark paraexcitons in Cu_2O*, Physical Review Letters **101**, 246401 (2008).

[Liu12] M. Liu, H. Y. Hwang, H. Tao, A. C. Strikwerda, K. Fan, G. R. Keiser, A. J. Sternbach, K. G. West, S. Kittiwatanakul, J. Lu, S. A. Wolf, F. G. Omenetto, X. Zhang, K. A. Nelson, and R. D. Averitt, *Terahertz-field-induced insulator-to-metal transition in vanadium dioxide metamaterial*, Nature **487**, 345–8 (2012).

[Liu17] H. Liu, Y. Li, Y. S. You, S. Ghimire, T. F. Heinz, and D. A. Reis, *High-harmonic generation from an atomically thin semiconductor*, Nature Physics **13**, 262–265 (2017).

[Liu18] H. Liu, C. Guo, G. Vampa, J. L. Zhang, T. Sarmiento, M. Xiao, P. H. Bucksbaum, J. Vučković, S. Fan, and D. A. Reis, *Enhanced high-harmonic*

generation from an all-dielectric metasurface, Nature Physics **14**, 1006–1010 (2018).

[Lu14] C.-H. Lu, Y.-J. Tsou, H.-Y. Chen, B.-H. Chen, Y.-C. Cheng, S.-D. Yang, M.-C. Chen, C.-C. Hsu, and A. H. Kung, *Generation of intense supercontinuum in condensed media*, Optica **1**, 10–12 (2014).

[Lu19] C.-H. Lu, W.-H. Wu, S.-H. Kuo, J.-Y. Guo, M.-C. Chen, S.-D. Yang, and A. H. Kung, *Greater than 50 times compression of 1030 nm Yb:KGW laser pulses to single-cycle duration*, Optics Express **27**, 15638 (2019).

[Mah16] F. Mahmood, C.-K. Chan, Z. Alpichshev, D. Gardner, Y. Lee, P. A. Lee, and N. Gedik, *Selective scattering between Floquet-Bloch and Volkov states in a topological insulator*, Nature Physics **12**, 306–310 (2016).

[Mak12] K. F. Mak, K. He, J. Shan, and T. F. Heinz, *Control of valley polarization in monolayer MoS_2 by optical helicity*, Nature Nanotechnology **7**, 494–498 (2012).

[Mar70] M. Marezio, J. P. Remeika, and P. D. Dernier, *The crystal chemistry of the rare earth orthoferrites*, Acta Crystallographica Section B Structural Crystallography and Crystal Chemistry **26**, 2008–2022 (1970).

[Mar14] I. L. Markov, *Limits on fundamental limits to computation*, Nature **512**, 147–154 (2014).

[Men15] J. H. Mentink, K. Balzer, and M. Eckstein, *Ultrafast and reversible control of the exchange interaction in Mott insulators*, Nature Communications **6**, 1–8 (2015).

[Mer19] P. Merkl, F. Mooshammer, P. Steinleitner, A. Girnghuber, K. Q. Lin, P. Nagler, J. Holler, C. Schüller, J. M. Lupton, T. Korn, S. Ovesen, S. Brem, E. Malic, and R. Huber, *Ultrafast transition between exciton phases in van der Waals heterostructures*, Nature Materials **18**, 691–696 (2019).

[Mic14] M. Michiardi, I. Aguilera, M. Bianchi, V. E. De Carvalho, L. O. Ladeira, N. G. Teixeira, E. A. Soares, C. Friedrich, S. Blügel, and P. Hofmann,

Bulk band structure of Bi_2Te_3, Physical Review B - Condensed Matter and Materials Physics **90**, 1–8 (2014).

[Mik14] R. V. Mikhaylovskiy, E. Hendry, V. V. Kruglyak, R. V. Pisarev, Th. Rasing, and A. V. Kimel, *Terahertz emission spectroscopy of laser-induced spin dynamics in $TmFeO_3$ and $ErFeO_3$ orthoferrites*, Physical Review B - Condensed Matter and Materials Physics **90**, 1–8 (2014).

[Mik15] R. V. Mikhaylovskiy, E. Hendry, A. Secchi, J. H. Mentink, M. Eckstein, A. Wu, R. V. Pisarev, V. V. Kruglyak, M. I. Katsnelson, Th. Rasing, and A. V. Kimel, *Ultrafast optical modification of exchange interactions in iron oxides*, Nature Communications **6**, 8190 (2015).

[Mon10] A. Monmayrant, *A newcomer's guide to ultrashort pulse shaping and characterization*, Journal of Physics B: Atomic, Molecular and Optical Physics **43**, 103001 (2010).

[Moo65] E. G. Moore, *Cramming more components onto integrated circuits*, Electronics **38**, 33–35 (1965).

[Moo09] J. Moore, *Topological insulators: The next generation*, Nature Physics **5**, 378–380 (2009).

[Moo10] J. E. Moore, *The birth of topological insulators*, Nature **464**, 194–198 (2010).

[Mor60] T. Moriya, *Anisotropic superexchange interaction and weak ferromagnetism*, Physical Review **120**, 91–98 (1960).

[Müc01] O. D. Mücke, T. Tritschler, M. Wegener, U. Morgner, and F. X. Kärtner, *Signatures of carrier-Wave Rabi Flopping in GaAs*, Physical Review Letters **87**, 057401 (2001).

[Muk91] A. A. Mukhin, A. Yu Pronin, A. S. Prokhorov, G. V. Kozlov, V. Zelezny, and J. Petzelt, *Submillimeter and far IR spectroscopy of magneto- and electrodipolar rare-earth modes in the orthoferrite $TmFeO_3$*, Physics Letters A **153**, 499–504 (1991).

[Nak63] S. Nakajima, *The crystal structure of $Bi_2Te_{3-x}Se_x$*, Journal of Physics and Chemistry of Solids **24**, 479–485 (1963).

[Née70] L. Néel, *Magnetism and local molecular field*, Nobel Lecture (1970).

[Něm18] P. Němec, M. Fiebig, T. Kampfrath, and A. V. Kimel, *Antiferromagnetic opto-spintronics*, Nature Physics **14**, 229–241 (2018).

[Nen20] D. M. Nenno, C. A. C. Garcia, J. Gooth, C. Felser, and P. Narang, *Axion physics in condensed-matter systems*, Nature Reviews Physics **2**, 682–696 (2020).

[Nep15] S. Neppl, R. Ernstorfer, A. L. Cavalieri, C. Lemell, G. Wachter, E. Magerl, E. M. Bothschafter, M. Jobst, M. Hofstetter, U. Kleineberg, J. V. Barth, D. Menzel, J. Burgdörfer, P. Feulner, F. Krausz, and R. Kienberger, *Direct observation of electron propagation and dielectric screening on the atomic length scale*, Nature **517**, 342–346 (2015).

[Ney02] O. Ney, M. Trzeciecki, and W. Hübner, *Femtosecond dynamics of spin-dependent SHG response from NiO (001)*, Applied Physics B: Lasers and Optics **74**, 741–744 (2002).

[Nic18] C. W. Nicholson, A. Lücke, W. G. Schmidt, M. Puppin, L. Rettig, R. Ernstorfer, and M. Wolf, *Beyond the molecular movie: dynamics of bands and bonds during a photoinduced phase transition*, Science **362**, 821–825 (2018).

[Nov05] K. S. Novoselov, D. Jiang, F. Schedin, T. J. Booth, V. V. Khotkevich, S. V. Morozov, and A. K. Geim, *Two-dimensional atomic crystals*, Proceedings of the National Academy of Sciences of the United States of America **102**, 10451–10453 (2005).

[Nov11] L. Novotny and N. Van Hulst, *Antennas for light*, Nature Photonics **5**, 83–90 (2011).

[Ole18] K. Olejník, T. Seifert, Z. Kašpar, V. Novák, P. Wadley, R. P. Campion, M. Baumgartner, P. Gambardella, P. Nemec, J. Wunderlich, J. Sinova, P. Kužel, M. Müller, T. Kampfrath, and T. Jungwirth, *Terahertz electrical*

writing speed in an antiferromagnetic memory, Science Advances **4**, 1–9 (2018).

[Ost12] T. A. Ostler, J. Barker, R. F. L. Evans, R. W. Chantrell, U. Atxitia, O. Chubykalo-Fesenko, S. El Moussaoui, L. Le Guyader, E. Mengotti, L. J. Heyderman, F. Nolting, A. Tsukamoto, A. Itoh, D. Afanasiev, B. A. Ivanov, A. M. Kalashnikova, K. Vahaplar, J. Mentink, A. Kirilyuk, Th. Rasing, and A. V. Kimel, *Ultrafast heating as a sufficient stimulus for magnetization reversal in a ferrimagnet*, Nature Communications **3**, 666 (2012).

[Pas13] A. Pashkin, A. Sell, T. Kampfrath, and R. Huber, *Electric and magnetic terahertz nonlinearities resolved on the sub-cycle scale*, New Journal of Physics **15**, 065003 (2013).

[Pea81] R. F. W. Pease, *Electron beam lithography*, Contemporary Physics **22**, 265 (1981).

[Pen76] J. B. Pendry, *Theory of photoemission*, Surface Science **57**, 679–705 (1976).

[Per06] C. A. Perroni and A. Liebsch, *Magnetization dynamics in dysprosium orthoferrites via the inverse Faraday effect*, Physical Review B - Condensed Matter and Materials Physics **74**, 1–10 (2006).

[Pet10] V. Petrov, M. Ghotbi, O. Kokabee, A. Esteban-Martin, F. Noack, A. Gaydardzhiev, I. Nikolov, P. Tzankov, I. Buchvarov, K. Miyata, A. Majchrowski, I. V. Kityk, F. Rotermund, E. Michalski, and M. Ebrahim-Zadeh, *Femtosecond nonlinear frequency conversion based on* BiB_3O_6, Laser and Photonics Reviews **4**, 53–98 (2010).

[Poe15] C. Poellmann, P. Steinleitner, U. Leierseder, P. Nagler, G. Plechinger, M. Porer, R. Bratschitsch, C. Schüller, T. Korn, and R. Huber, *Resonant internal quantum transitions and femtosecond radiative decay of excitons in monolayer* WSe_2, Nature Materials **14**, 889–893 (2015).

[Pop09] Yu. F. Popov, A. M. Kadomtseva, G. P. Vorob'ev, A. A. Mukhin, V. Yu. Ivanov, A. M. Kuz'Menko, A. S. Prokhorov, L. N. Bezmaternykh, and V. L. Temerov, *Observation of spontaneous spin reorientation in* $Nd_{1-x}Dy_x$

$Fe_3(BO_3)_4$ ferroborates with a competitive R-Fe exchange, JETP Letters **89**, 345–351 (2009).

[Por14] M. Porer, U. Leierseder, J. M. Ménard, H. Dachraoui, L. Mouchliadis, I. E. Perakis, U. Heinzmann, J. Demsar, K. Rossnagel, and R. Huber, *Non-thermal separation of electronic and structural orders in a persisting charge density wave*, Nature Materials **13**, 857–861 (2014).

[Qi10] X. L. Qi and S. C. Zhang, *The quantum spin Hall effect and topological insulators*, Physics Today **63**, 33–38 (2010).

[Qia06] D. Qian, L. Wray, D. Hsieh, L. Viciu, R. J. Cava, J. L. Luo, D. Wu, N. L. Wang, and M. Z. Hasan, *Complete d-band dispersion relation in sodium cobaltates*, Physical Review Letters **97**, 186405 (2006).

[Rei14] J. Reimann, J. Güdde, K. Kuroda, E. V. Chulkov, and U. Höfer, *Spectroscopy and dynamics of unoccupied electronic states of the topological insulators Sb_2Te_3 and Sb_2Te_2S*, Physical Review B - Condensed Matter and Materials Physics **90**, 1–5 (2014).

[Rei18a] J. Reimann, *Ladungsträgerdynamik und Photoströme im Dirac-Kegel topologischer Isolatoren*, Dissertation, University of Marburg, 2018.

[Rei18b] J. Reimann, S. Schlauderer, C. P. Schmid, F. Langer, S. Baierl, K. A. Kokh, O. E. Tereshchenko, A. Kimura, C. Lange, J. Güdde, U. Höfer, and R. Huber, *Subcycle observation of lightwave-driven Dirac currents in a topological surface band*, Nature **562**, 396–400 (2018).

[Ric10] P. Richard, K. Nakayama, T. Sato, M. Neupane, Y. M. Xu, J. H. Bowen, G. F. Chen, J. L. Luo, N. L. Wang, X. Dai, Z. Fang, H. Ding, and T. Takahashi, *Observation of dirac cone electronic dispersion in $BaFe_2As_2$*, Physical Review Letters **104**, 137001 (2010).

[Ros02] F. Rossi and T. Kuhn, *Theory of ultrafast phenomena in photoexcited semiconductors*, Reviews of Modern Physics **74**, 895–950 (2002).

[Sal19] P. Salén, M. Basini, S. Bonetti, J. Hebling, M. Krasilnikov, A. Y. Nikitin, G. Shamuilov, Z. Tibai, V. Zhaunerchyk, and V. Goryashko, *Matter manipulation with extreme terahertz light : Progress in the enabling THz technology*, Physics Reports **836-837**, 1–74 (2019).

[Sat01] T. Sato, T. Kamiyama, T. Takahashi, K. Kurahashi, and K. Yamada, *Observation of $d_{x^2-y^2}$-like superconducting gap in an electron-doped high- temperature superconductor*, Science **291**, 1517–1519 (2001).

[Sch10] J. A. Schuller, E. S. Barnard, W. Cai, Y. C. Jun, J. S. White, and M. L. Brongersma, *Plasmonics for extreme light concentration and manipulation*, Nature Materials **9**, 193–204 (2010).

[Sch13] A. Schiffrin, T. Paasch-Colberg, N. Karpowicz, V. Apalkov, D. Gerster, S. Mühlbrandt, M. Korbman, J. Reichert, M. Schultze, S. Holzner, J. V. Barth, R. Kienberger, R. Ernstorfer, V. S. Yakovlev, M. I. Stockman, and F. Krausz, *Optical-field-induced current in dielectrics*, Nature **493**, 70–74 (2013).

[Sch14] O. Schubert, M. Hohenleutner, F. Langer, B. Urbanek, C. Lange, U. Huttner, D. Golde, T. Meier, M. Kira, S. W. Koch, and R. Huber, *Sub-cycle control of terahertz high-harmonic generation by dynamical Bloch oscillations*, Nature Photonics **8**, 119–123 (2014).

[Sch16] J. R. Schaibley, H. Yu, G. Clark, P. Rivera, J. S. Ross, K. L. Seyler, W. Yao, and X. Xu, *Valleytronics in 2D materials*, Nature Reviews Materials **1**, 1–15 (2016).

[Sch19] S. Schlauderer, C. Lange, S. Baierl, T. Ebnet, C. P. Schmid, D. C. Valovcin, A. K. Zvezdin, A. V. Kimel, R. V. Mikhaylovskiy, and R. Huber, *Temporal and spectral fingerprints of ultrafast all-coherent spin switching*, Nature **569**, 383–387 (2019).

[Sea79] M. P. Seah and W. A. Dench, *Quantitative Electron Spectroscopy of Surfaces: A Standard Data Base for Electron Inelastic Mean Free Paths in Solids*, Surface and Interface Analysis **1**, 1–11 (1979).

[Sel08] A. Sell, A. Leitenstorfer, and R. Huber, *Phase-locked generation and field-resolved detection of widely tunable terahertz pulses with amplitudes exceeding 100 MV/cm.*, Optics letters **33**, 2767–2769 (2008).

[Sen18] K. Sengupta, T. Nagatsuma, and D. M. Mittleman, *Terahertz integrated electronic and hybrid electronicâ€“photonic systems*, Nature Electronics **1**, 622–635 (2018).

[Sha99] J. Shah, *Ultrafast Spectroscopy of Semiconductors and Semiconductor Nanostructures*, 2nd ed., Springer, 1999.

[Sha20] J. Shalf, *The future of computing beyond Moore's Law*, Philosophical Transactions Royal Society **378**, 20190061 (2020).

[Sho39] W. Shockley, *On the surface states associated with a periodic potential*, Physical Review **56**, 317–323 (1939).

[Sie19] F. Siegrist, J. A. Gessner, M. Ossiander, C. Denker, Y. P. Chang, M. C. Schröder, Al. Guggenmos, Y. Cui, J. Walowski, U. Martens, J. K. Dewhurst, U. Kleineberg, M. Münzenberg, S. Sharma, and M. Schultze, *Light-wave dynamic control of magnetism*, Nature **571**, 240–244 (2019).

[Sil19] R. E. F. Silva, A. Jiménez-Galán, B. Amorim, O. Smirnova, and M. Ivanov, *Topological strong-field physics on sub-laser-cycle timescale*, Nature Photonics **13**, 849–854 (2019).

[Siv17] M. Sivis, M. Taucer, G. Vampa, K. Johnston, A. Staudte, A. Yu. Naumov, D. M. Villeneuve, C. Ropers, and Corkum, *Tailored semiconductors for high-harmonic optoelectronics*, Science **357**, 303–306 (2017).

[Soi19] H. Soifer, A. Gauthier, A. F. Kemper, C. R. Rotundu, S. L. Yang, H. Xiong, D. Lu, M. Hashimoto, P. S. Kirchmann, J. A. Sobota, and Z. X. Shen, *Band-Resolved Imaging of Photocurrent in a Topological Insulator*, Physical Review Letters **122**, 167401 (2019).

[Sri95] G. Srinivasan and A. N. Slavin, *High frequency processes in magnetic materials*, World Scientific, 1995.

[Ste17] P. Steinleitner, P. Merkl, P. Nagler, J. Mornhinweg, C. Schüller, T. Korn, A. Chernikov, and R. Huber, *Direct Observation of Ultrafast Exciton Formation in a Monolayer of WSe_2*, Nano Letters **17**, 1455–1460 (2017).

[Str85] D. Strickland and G. Mourou, *Compression of amplified chirped optical pulses*, Optics Communications **56**, 219–221 (1985).

[Stu17] A. Stupakiewicz, K. Szerenos, D. Afanasiev, A. Kirilyuk, and A. V. Kimel, *Ultrafast nonthermal photo-magnetic recording in a transparent medium*, Nature **542**, 71–74 (2017).

[Sul20] P. Sulzer, K. Oguchi, J. Huster, M. Kizmann, T. L. M. Guedes, A. Liehl, C. Beckh, A. S. Moskalenko, G. Burkard, D. V. Seletskiy, and A. Leitenstorfer, *Determination of the electric field and its Hilbert transform in femtosecond electro-optic sampling*, Physical Review A **101**, 033821 (2020).

[Sum17] K. Sumida, Y. Ishida, S. Zhu, M. Ye, A. Pertsova, C. Triola, K. A. Kokh, O. E. Tereshchenko, A. V. Balatsky, S. Shin, and A. Kimura, *Prolonged duration of nonequilibrated Dirac fermions in neutral topological insulators*, Scientific Reports **7**, 1–7 (2017).

[Tho82] D. J. Thouless, M. Kohmoto, M. P. Nightingale, and M. den Nijs, *Quantized Hall Conductance in a Two-Dimensional Periodic Potential*, Physical Review Letters **49**, 405–408 (1982).

[Tok17] Y. Tokura, M. Kawasaki, and N. Nagaosa, *Emergent functions of quantum materials*, Nature Physics **13**, 1056–1068 (2017).

[Tre65] D. Treves, *Studies on orthoferrites at the Weizmann Institute of Science*, Journal of Applied Physics **36**, 1033–1039 (1965).

[Tse03] A. A. Tseng, K. Chen, C. D. Chen, and K. J. Ka, *Electron beam lithography in nanoscale fabrication: recent development*, IEEE Transactions on Electronics Packaging Manufacturing **26**, 141 (2003).

[Tud04] I. Tudosa, C. Stamm, A. B. Kashuba, F. King, H. C. Siegmann, J. Stöhr, G. Ju, B. Lu, and D. Weeler, *The ultimate speed of magnetic switching in granular recording media*, Nature **428**, 831–833 (2004).

[Tza12] P. Tzankov, O. Isaienko, I. Shumay, D. Stockwell, L. Xu, N. Moisan, and D. Boschetto, *Generation of Sub-50-fs Pulses in the Near Infrared by Optical Parametric Amplifiers Based on BIBO Crystals*, Conference on Lasers and Electro-Optics, 2012.

[Vam14] G. Vampa, C. R. McDonald, G. Orlando, D. D. Klug, P. B. Corkum, and T. Brabec, *Theoretical analysis of high-harmonic generation in solids*, Physical Review Letters **113**, 073901 (2014).

[Vam15] G. Vampa, T. J. Hammond, N. Thiré, B. E. Schmidt, F. Légaré, C. R. McDonald, T. Brabec, D. D. Klug, and P. B. Corkum, *All-Optical Reconstruction of Crystal Band Structure*, Physical Review Letters **115**, 193603 (2015).

[Van06] B. Van Waeyenberge, A. Puzic, H. Stoll, K. W. Chou, T. Tyliszczak, R. Hertel, M. Fähnle, H. Brückl, K. Rott, G. Reiss, I. Neudecker, D. Weiss, C. H. Back, and G. Schütz, *Magnetic vortex core reversal by excitation with short bursts of an alternating field*, Nature **444**, 461–464 (2006).

[Van18] D. Vanderbilt, *Berry Phases in Electronic Structure Theory: electric polarization, orbital magnetization and topological insulators*, Cambridge University Press, 2018.

[Vas06] A. N. Vasiliev and E. A. Popova, *Rare-earth ferroborates $RFe_3(BO_3)_4$*, Low Temperature Physics **32**, 735–747 (2006).

[Ved20] E. Y. Vedmedenko, R. K. Kawakami, D. D. Sheka, P. Gambardella, A. Kirilyuk, A. Hirohata, C. Binek, O. Chubykalo-Fesenko, S. Sanvito, B. J. Kirby, J. Grollier, K. Everschor-Sitte, T. Kampfrath, C. Y. You, and A. Berger, *The 2020 Magnetism Roadmap*, Journal of Physics D: Applied Physics **53**, 453001 (2020).

[Ver19] M. G. Vergniory, L. Elcoro, C. Felser, N. Regnault, B. A. Bernevig, and Z. Wang, *A complete catalogue of high-quality topological materials*, Nature **566**, 480–485 (2019).

[Von80] K. Von Klitzing, G. Dorda, and M. Pepper, *New et od for High-Accuracy Determination of th Fine-Structure Constant Based on Quantized Hall Resistance*, Physical Review Letters **45**, 494–497 (1980).

[Von18] A. Von Hoegen, R. Mankowsky, M. Fechner, M. Först, and A. Cavalleri, *Probing the interatomic potential of solids with strong-field nonlinear phononics*, Nature **555**, 79–82 (2018).

[Vu04] Q. T. Vu, H. Haug, O. D. Mücke, T. Tritschler, M. Wegener, G. Khitrova, and H. M. Gibbs, *Light-induced gaps in semiconductor band-to-band transitions*, Physical Review Letters **92**, 217403 (2004).

[Wad16] P. Wadley, B. Howells, J. Zelezny, C. Andrews, V. Hills, R. P. Campion, V. Novak, F. Freimuth, Y. Mokrousov, A. W. Rushforth, K. W. Edmonds, B. L. Gallagher, and T. Jungwirth, *Electrical switching of an antiferromagnet*, Science **351**, 587–591 (2016).

[Wan13] Y. H. Wang, H. Steinberg, P. Jarillo-Herrero, and N. Gedik, *Observation of Floquet-Bloch States on the Surface of a Topological Insulator*, Science **342**, 453–457 (2013).

[Was93] C. Waschke, H. G. Roskos, R. Schwedler, K. Leo, H. Kurz, and K. Köhler, *Coherent submillimeter-wave emission from Bloch oscillations in a semiconductor superlattice*, Physical Review Letters **70**, 3319–3322 (1993).

[Wei02] M. Weinelt, *Time-resolved two-photon photoemission from metal surfaces*, Journal of Physics Condensed Matter **14**, 1099–1141 (2002).

[Whi69] R. L. White, *Review of recent work on the magnetic and spectroscopic properties of the rare-earth orthoferrites*, Journal of Applied Physics **40**, 1061–1069 (1969).

[Wie16] B. Wiendlocha, *Resonant Levels, Vacancies, and Doping in Bi_2Te_3, Bi_2Te_2Se, and Bi_2Se_3 Tetradymites*, Journal of Electronic Materials **45**, 3515–3531 (2016).

[Wu95] Q. Wu and X. C. Zhang, *Free-space electro-optic sampling of terahertz beams*, Applied Physics Letters **67**, 3523 (1995).

[Wya08] A. Wyatt, *Frequency-resolved optical gating (FROG)*, MATLAB central file exchange, http://www.mathworks.com/matlabcentral/fileexchang (2008).

[Xia09] Y. Xia, D. Qian, D. Hsieh, L. Wray, A. Pal, H. Lin, A. Bansil, D. Grauer, Y. S. Hor, R. J. Cava, and M. Z. Hasan, *Observation of a large-gap topological-insulator class with a single Dirac cone on the surface*, Nature Physics **5**, 398–402 (2009).

[Xia10] D. Xiao, M. C. Chang, and Q. Niu, *Berry phase effects on electronic properties*, Reviews of Modern Physics **82**, 1959–2007 (2010).

[Xia12] D. Xiao, G. B. Liu, W. Feng, Xi. Xu, and W. Yao, *Coupled spin and valley physics in monolayers of MoS_2 and other group-VI dichalcogenides*, Physical Review Letters **108**, 196802 (2012).

[Xu14] Xi. Xu, W. Yao, D. Xiao, and T. F. Heinz, *Spin and pseudospins in layered transition metal dichalcogenides*, Nature Physics **10**, 343–350 (2014).

[Yan15] F. Yang and R. B. Liu, *Geometric diffusion of quantum trajectories*, Scientific Reports **5**, 1–9 (2015).

[Yav11] B. Yu. Yavorsky, N. F. Hinsche, I. Mertig, and P. Zahn, *Electronic structure and transport anisotropy of Bi_2Te_3 and Sb_2Te_3*, Physical Review B **84**, 165208 (2011).

[Ye17] Z. Ye, D. Sun, and T. F. Heinz, *Optical manipulation of valley pseudospin*, Nature Physics **13**, 26–29 (2017).

[Yos17] N. Yoshikawa, T. Tamaya, and K. Tanaka, *Optics: High-harmonic generation in graphene enhanced by elliptically polarized light excitation*, Science **356**, 736–738 (2017).

[Yos19] N. Yoshikawa, K. Nagai, K. Uchida, Y. Takaguchi, S. Sasaki, Y. Miyata, and K. Tanaka, *Interband resonant high-harmonic generation by valley polarized electro-hole pairs*, Nature Communications **10**, 1–7 (2019).

[You17] Y. S. You, D. A. Reis, and S. Ghimire, *Anisotropic high-harmonic generation in bulk crystals*, Nature Physics **13**, 345–349 (2017).

[Zak12] B. Zaks, R. B. Liu, and M. S. Sherwin, *Experimental observation of electron-hole recollisions*, Nature **483**, 580–583 (2012).

[Zen34] C. Zener, *A theory of the electrical breakdown of solid dielectrics*, Proceedings of the Royal Society of London. Series A **145**, 523–529 (1934).

[Zha09] H. Zhang, C.-X. Liu, X.-L. Qi, X. Dai, Z. Fang, and S.-C. Zhang, *Topological insulators in Bi_2Se_3, Bi_2Te_3 and Sb_2Te_3 with a single Dirac cone on the surface*, Nature Physics **5**, 438–442 (2009).

[Zha11] P. Zhang, P. Richard, T. Qian, Y. M. Xu, X. Dai, and H. Ding, *A precise method for visualizing dispersive features in image plots*, Review of Scientific Instruments **82**, 043712 (2011).

[Zha16] K. Zhang, K. Xu, X. Liu, Z. Zhang, Z. Jin, X. Lin, B. Li, S. Cao, and G. Ma, *Resolving the spin reorientation and crystal-field transitions in $TmFeO_3$ with terahertz transient*, Scientific Reports **6**, 23648 (2016).

[Zha19] T. Zhang, Y. Jiang, Z. Song, H. Huang, Y. He, Z. Fang, H. Weng, and C. Fang, *Catalogue of topological electronic materials*, Nature **566**, 475–479 (2019).

[Zho05] X. J. Zhou, B. Wannberg, W. L. Yang, V. Brouet, Z. Sun, J. F. Douglas, D. Dessau, Z. Hussain, and Z. X. Shen, *Space charge effect and mirror charge effect in photoemission spectroscopy*, Journal of Electron Spectroscopy and Related Phenomena **142**, 27–38 (2005).

[Zve79] A. K. Zvezdin, *Dynamics of domain walls in weak ferromagnets*, Pisma Zh. Exp. Teor. Fiz. **29**, 605–610 (1979).

Acknowledgements

Coming together is a beginning,
staying together is a progress,
and working together is success.

— Henry Ford

This thesis would not have been possible without the continuous support and help of numerous people. Here, I would like to particularly thank

- *Prof. Dr. Rupert Huber*, who has been a fantastic advisor and mentor throughout the last years. I especially want to thank him for sharing his passion for physics in general, the peerless support, and the trust he put in me. It was a real pleasure to tackle all these challenging projects together and turn them, also thanks to his inspiring ideas and absolute dedication in all scientific aspects, into reality. I am also grateful for his guidance concerning scientific writing, all the insightful and enlightening physical discussions, and the possibility to visit numerous, international conferences, where I could also share our joint work with the community.

- *Prof. Dr. Klaus Richter*, *Prof. Dr. Franz J. Gießibl*, and especially *Prof. Dr. Jörg Wunderlich* for taking the time to examine this work.

- *Dr. Fabian Langer* and *Dr. Sebastian Baierl* for getting me started in the lab at the beginning of my scientific career and sharing their knowledge and experience with me.

▷ *Christoph Schmid* for the great companionship in the kHz-lab and as a friend during the last years. I really appreciate that you never let me down and always found some time to help.

▷ *Prof. Dr. Christoph Lange* for the excellent cooperation, especially the theoretical support with modeling the THz-induced spin dynamics in the antenna near-field and helping to get the results published. This project would not have been such a success without your help.

▷ *Thomas Ebnet* for his contributions to the ultrafast spin switching project during his master's thesis.

▷ *Prof. Dr. Alexey V. Kimel*, *Dr. Rostislav V. Mikhaylovskiy*, and *Prof. Dr. Anatoly K. Zvezdin* for the great collaboration regarding the ultrafast spin switching project, providing the thulium orthoferrite samples, and many helpful physical discussions.

▷ *Josef Freudenstein* and *Manuel Meierhofer* for the superb support and teamwork in the lab and for taking over the quest to trace lightwave-driven dynamics directly in the band structure.

▷ *Prof. Dr. Ulrich Höfer*, *Prof. Dr. Jens Güdde*, *Dr. Johannes Reimann* and *Dr. Suguru Ito* for the fantastic collaboration on lightwave-driven Dirac currents, providing the bismuth telluride samples, the numerous fruitful discussions, and especially for introducing me to the world of angle-resolved photoemission spectroscopy. The way how we tackled this project is a prime example of scientific teamwork.

▷ *Prof. Dr. Mackillo Kira*, *Prof. Dr. Stephan W. Koch*, *Dr. Ulrich Huttner*, *Dr. Johannes T. Steiner*, *Dr. Peter Hawkins*, and *Markus Borsch* for the great theoretical support during the various joint projects on high-order harmonic and high-order sideband generation in solids.

▷ *Prof. Dr. Christian Schüller*, *Prof. Dr. Tobias Korn*, and *Dr. Philipp Nagler* for the collaboration on electron-hole recollisions in transition metal dichalcogenides, in particular for providing and characterizing the high-quality tungsten diselenide bulk and monolayer samples.

▷ *Martin Furthmeier* for his technical support, and always brewing such a delicious 'Zaubertrank' at our annual winter barbecue. There are rumors that this is the secret behind our success.

▷ *Ignaz Laepple* for his help with all issues related to electronics.

▷ *Imke Gronwald* for the guidance in the chemistry lab, the introduction to the e-beam lithography and the help by fabricating the antenna structures.

▷ *Ulla Franzke*, for her support in any kind of bureaucratic or administrative matters. Many thanks also for always being optimistic and brightening everybody's mood with a little gossip from time to time.

▷ all former and current *'Huber Buam'* for the excellent working atmosphere as well as the enjoyable time we had during and especially after work. I want to express my gratitude in particular to *Fabian Sandner*, who has become one of my closest friends in the last few years and proofed, that he is the best beer pong partner one can think of.

▷ my fellow students and friends *Dr. Fabian Mooshammer*, *Dr. Leonard Tutsch*, and *Tobias Lindner* for the companionship during our studies in Regensburg as well as the gorgeous times during our numerous travels all around the globe. I hope, more is about to come!

▷ my best friends *Pia Pollmann* and *René Nauthe* for the fun and memorable times we had together, and for supporting me in various ways along my path.

▷ my whole *family* and most importantly my *parents* for their constant encouragement and belief in me. Without your steady and reliable support throughout my entire life, I would not have made it so far!

▷ *Jasmin* for always reminding me what is important in life, and for becoming an essential part of it!

Special thanks to *Prof. Dr. Christoph Lange*, *Dr. Fabian Langer*,
Dr. Suguru Ito, *Manuel Meierhofer* and *Josef Freudenstein*
for proofreading this thesis.